UNIVERSITÉ DE GRENOBLE

THÈSE

Pour obtenir le grade de

DOCTEUR DE L'UNIVERSITÉ DE GRENOBLE

Spécialité : **Sciences de la Terre, de l'Univers et de l'Environnement**

Arrêté ministériel : 7 août 2006

Présentée par

Lamberto Adolfo INZA CALLUPE

Thèse dirigée par **Jérôme I. MARS**
et codirigée par **Jean-Philippe MÉTAXIAN et Christopher BEAN**

préparée au sein des **Laboratoires GIPSA-Lab et ISTerre**
et de **l'École Doctorale Terre, Univers, Environnement**

Compréhension des processus magmatiques et localisation de source sismo-volcanique avec des antennes sismiques multicomposantes

Thèse soutenue publiquement le **30 Mai 2013**,
devant le jury composé de :

Mr Patrick BACHELERY
PR Observatoire de Physique du Globe Clermont-Ferrand, Président
Mr Pascal LARZABAL
PR École Normale Supérieure CACHAN, Rapporteur
Mr Pierre BRIOLE
DR CNRS École Normale Supérieure Paris, Rapporteur
Mr Philippe LESAGE
M. de Conf., Université Savoie, Chambéry, Examinateur
Mr José MACHARE
DR Instituto Geofisico del Peru, Examinateur
Mr Jérôme I. MARS
PR Grenoble INP, Directeur de thèse
Mr Jean-Philippe MÉTAXIAN
CR IRD UJF ISTerre Université de Savoie, Co-Directeur de thèse
Mr Christopher BEAN
PR University College Dublin, Ireland, Co-Directeur de thèse



UNDERSTANDING MAGMATIC PROCESSES AND SEISMO-VOLCANIC SOURCE LOCALIZATION WITH MULTICOMPONENT SEISMIC ARRAYS

Acknowledgements

This thesis was supported by scholarship program of IRD since February 2010 until April 2013 (three years with an extension of three months), which allowed me to work at different laboratories as: SigmaPhy/Gipsa-Lab (Grenoble), volcano group/Isterre (Chambéry), Geophysics group University College Dublin - UCD (Ireland) and Volcano observatory Geophysical Institute of Peru.

Completion of this doctoral dissertation was possible with the support of several people. I am extremely grateful to my supervisor, Professor Jérôme Mars, the leader of the DIS/Gipsa-Lab department, whose expertise, patience, guidance, understanding have contributed considerably this thesis and above all, his unfailing trust made me feel confident about my job. Also my gratitude to my two co-supervisors, Dr. Jean-Philippe Métaxian and Professor Chris Bean for their valuable guidance, consistent encouragement which allowed me to improve my skill in volcano seismology. I also want to thank my thesis reviewers, whose their precise comments helped me further improve this manuscript, and the jury members for their relevant questions during the dissertation.

I would like to thank Christine Bigot for supporting during remote inscriptions. I appreciate the encouragement and support in many respects of Martin Möllohoff and his family. A big thanks to Aoife Brain and all the member from geophysics group at UCD. I appreciate all the team of Geological School, particularly soccer team.

A person with an amicable and positive disposition of Bernard Valette, I always remember the walks in the French Alps. Also my sincere gratitude to all members of volcano group Isterre/Chambery. I always remember the times of Latin party at Philippe and Edelmira home. Thanks to Dr. Orlando Macedo, Victor Montesinos, Roger Machacca and Riky for their support at IGP - Arequipa.

I thank Rodrigo, Jonathan, Gailene, Boris, Anis, Shahrbanoo and Razmig from Gipsa-Lab for their help. Finally, I owe a lot to my parents Tomas Inza and Juana Callupe, who encouraged and help me at every stage of my personal and academic life. I am very indebted to Luz Perpetua who supported me in every possible way and also my big family as Efrain, Lucy, Betty, Ketty, Cristel, Eduardo, Fred, Roxana, Luis, Leonardo, Luz Juanita, Patricia, Joaquin, Sofia, Valentina, Nestor Tomas and Marcela. At this point I finish remembering a saying in my original langage Quechua “Hatariyniykita qan kikiyki sumaqta chaskiy” (Make a commitment to yourself).

Summary

This dissertation with methodological and applicative aspect try to give an issue to the problem of seismo-volcanic source localization using sensor arrays. The attention is focused on monitoring the magmatic activity, which can be detected by seismic measurements around the volcanic area. Both scientific research and eruption hazard assessment follow the same goal of understanding the physical processes of the eruption using seismic measurements. Small-aperture sensor arrays have become a powerful tool for monitoring volcanic unrest in which the magma plumbing system beneath the volcano is active.

In this thesis, we study the seismo-volcanic source localization using data recorded by new sensor arrays composed of three-component (3C) seismometers. We will focus on the Ubinas stratovolcano, one of the most active volcano in Peru. We first formulate the geometry of seismic array networks to be deployed on volcano flanks. In this context, the Multiple Signal Classification (MUSIC) algorithm for source localization can be applicable to a non-uniformly spaced array, which is favorable for the complex topography of volcanoes. We develop a new approach (MUSIC-3C) based on the MUSIC method applied in the framework of plane wave and multicomponent sensors. This approach involves reformulating the problem in the new data recorded by arrays of sensors with 3C seismometers.

To investigate the performance of the MUSIC-3C method we use synthetic datasets designed from eight broadband isotropic seismic sources located beneath the crater floor at different depths. These datasets were generated using a 3D discrete numerical elastic lattice method from a digital elevation map of the Ubinas topography and an homogeneous velocity model. The fundamental scheme of the MUSIC-3C method exploits the fact of the cross-spectral matrix of 3C array data, corresponding to the first seismic signal arrivals, provides of useful vector components (slowness, back-azimuth and incidence angle) from the seismic source. Multiple 3C sensor arrays with small aperture (around 350 m) distributed over around the volcano provide the means for locating the position of seismic sources by crossing their slowness vectors. Application of the MUSIC-3C method on synthetic datasets shows the recovery of source positions. This analysis followed by comparison with classical methods, demonstrates that our approach has important advantages, such as estimations, of sources at different depths beneath the volcano and with less errors for epicenters.

Real data used in this study was collected during seismic measurements with two small-aperture 3C seismic arrays deployed at Ubinas volcano between May and July 2009, whose experiment conduced by volcanic teams of IRD-France (l'Institute de Recherche pour le Développment), Geophysics group

University College Dublin Ireland and Volcano staff of Geophysical Institute of Peru (IGP). We apply the MUSIC-3C algorithm to investigate wave fields associated with the magmatic activity of Ubinas volcano. These analysis evidence a complex mechanism of vulcanian eruptions in which their seismic sources are found at two separated sources located at depths of 300 m and 1100 m beneath the crater floor. This implies the reproduction of similar mechanisms into the conduit. Based on the eruptive mechanisms proposed for other volcanoes of the same type, we interpret the position of this sources as the limits of the conduit portion that was involved in the fragmentation process.

Recent improvements in portable seismic instruments have evolved during the last decade, and following the trends of technological developments of wireless communication in geophysical instruments now allow small aperture seismic arrays to be deployed as a seismo-volcanic monitoring method to process array data in real-time. A test experiment was carried out using a seismic telemetry system to remotely retrieve data from two 3C-sensor arrays deployed at Misti volcano 15 km far away the IGP observatory (Arequipa, Peru) during November-December 2011. To be realistic with the MUSIC-3C algorithm, we highlight results from source localizations in real-time during this experiment.

Compréhension des processus magmatiques et localisation de source sismo-volcanique avec des antennes sismiques multicomposantes

Résumé

Cette thèse, à la fois méthodologique et appliquée, a été financée par le programme de bourse IRD (l'Institut de Recherche pour le Développement). Elle concerne la localisation des sources liées à l'activité sismique volcanique. Cette tâche est cruciale pour mieux comprendre le mécanisme d'éruption volcanique. L'apparition émergente des capteurs sismiques à trois composantes (3C) permet d'utiliser des approches moderne de localisation, en particulier pour des séismes longue période liés à l'activité magmatique proche de la surface du volcan. Cette thèse se situe donc dans le contexte de la localisation de sources sismo-volcaniques enregistrées par de réseaux de capteurs. Une attention particulière est portée sur la surveillance de l'activité magmatique qui peut être détecté par des mesures sismiques autour du volcan. Les recherches scientifiques dans ce domaine et l'évaluation des risques éruptifs visent toujours le même objectif: á savoir comprendre les processus physiques de l'éruption. Les réseaux de capteurs sismiques déployés en antenne sismique sont devenus des outils puissants pour surveiller l'activité volcanique.

Dans cette thèse, nous étudions le problème de la localisation de sources, basée sur les données enregistrées par des réseaux de capteurs composés de sismomètres à trois composantes (3C). Nous nous concentrerons sur le stratovolcan Ubinas, l'un des plus actifs au Pérou (environ 5400 m d'altitude et possedant une grande caldeira de 1.4 km). Les éruptions de ce volcan historiques et récentes ont présenté un style majoritairement vulcanian caractérisé par des explosions de courte durée et violentes.

Dans ce rapport de these, nous avons d'abord formulé la géométrie des réseaux sismiques à déployer sur les flancs du volcan (Chapitre 2 entre les sections 2.2 et 2.4). Dans ce contexte, l'algorithme MUSIC (MUltiple SIgnal Classification Bienvenu and Kopp (1983); Schmidt (1986)), méthode classique pour la localisation de sources a été appliqué sur un réseau des capteurs. La principale innovation de cette thèse est le developpement d'une nouvelle approche (MUSIC-3C) basée sur la méthode MUSIC appliquée dans le cadre d'ondes planes et de signaux multicomposants, pour localiser les événements sismiques liés aux activités volcaniques. L'approche consiste à reformuler le problème en fonction des nouvelles données enregistrées par des réseaux de capteurs 3C.

Pour valider notre méthodologie, dans le Chapitre 2 section 2.5, nous analysons un ensemble de sources synthétiques propagées en tenant compte de la topographie du volcan Ubinas et avec un modèle de vitesse homogène, afin de tester la robustesse de l'algorithme MUSIC-3C. Dans cette expérience, les données synthétiques ont été générées pour plusieurs sources situées à différentes profondeurs sous le cratère Ubinas. Nous utilisons l'algorithme MUSIC-3C pour localiser ces sources en deux étapes. Tout d'abord, les vecteurs lenteur sont estimés, pour connaître l'azimut et l'angle d'incidence du front d'onde sismo-volcanique. Dans la seconde étape, pour délimiter spatialement la

localisation de la source, nous utilisons une approche probabiliste utilisant des vecteurs lenteur. Cette analyse, suivie d'une comparaison avec les méthodes classiques, montre que notre approche possede d'importants avantages par rapport aux méthodes classiques. On montre également que l'utilisation de plus de deux réseaux de capteurs améliore les résultats.

Après cette analyse sur données synthétiques, nous traitons des données réelles, dans le Chapitre 3, provenant d'une expérience de terrain menée au volcan Ubinas (Pérou) en 2009 par les équipes de recherche de l'IRD-France, projet VOLUME/UCD University College Dublin, l'Irlande et l'Institut de géophysique du Pérou (IGP). Cette mission a pour but d'enregistrer les tremblements de terre et les événements sismiques à partir de deux antennes sismiques déployées suivant une géométrie similaire à celle utilisée dans l'application synthétique décrit dan le Chapitre 1, section 1.4. Nous utilisons MUSIC-3C pour localiser les événements explosifs (type vulcanien), ce qui nous permet d'identifier et d'analyser les processus physiques des événements explosifs.

En plus nous avons proposé, une expérience impliquant des antennes sismiques pour la surveillance des volcans en temps réel, décrit dan le Chapitre 1, section 1.5. Une expérience de terrain sur le volcan Misti a également été menée en 2011 avec l'aide des équipes de recherche de l'IRD, le groupe de l'UCD et l'IGP, pour vérifier la pertinence de la méthode basée sur la télémétrie en temps réel avec des antennes sismiques.

Le méthode du goniomètre

Les signaux sismo-volcaniques sont la manifestation des phénoménes physiques complexes qui se produisent dans les systèmes magmatiques ou hydrothermaux du volcan. Ceux-ci se composent de deux grandes familles, les signaux volcano-tectonique et les signaux longues périodes (LP).

La surveillance volcanique effectuée avec des capteurs sismiques peut apporter une meilleure connaissance des processus physique du volcan.

L'antenne sismique est un dispositif de mesure composé d'une suite de sismomètres permettant d'enregistrer les ondes sismiques à la fois dans les domaines spatial et temporel. Les ondes sismiques sont des ondes élastiques qui se propagent dans toutes les directions à l'intérieur du sol. Nous ferons l'hypothése que les antennes sont suffisamment éloignés des sources pour observer des ondes planes au niveau des antennes. La direction d'arrivée à l'antenne peut être décrite par trois paramètres: le back-azimut θ, l'angle d'incidence ϕ et la vitesse apparante v_{app}. Considérons une antenne composée de N sismomètres deployées sur le flanc du volcan. Les ondes planes sont définis par le vecteur lenteur :

$$\mathbf{u}(\theta,\phi) = \frac{1}{v_a}\begin{bmatrix} -\cos(\theta)\sin(\phi) \\ -\sin(\theta)\sin(\phi) \\ -\cos(\phi) \end{bmatrix}$$

Les signaux reçu par l'antenne $\mathbf{W}(\mathbf{f})$ sont representées par leur formes matricielle par (Mars et al., 2004):

$$\mathbf{W}(\mathbf{f}) = \mathbf{A}(\theta,\phi)\mathbf{S}(\mathbf{f}) + \mathbf{B}(\mathbf{f})$$

où $\mathbf{A}(\theta,\phi)$ est la matrice directionnels d'onde plane $S(f)$ et $\mathbf{B}(\mathbf{f})$ est le bruit de mesure additif des capteurs supposées stationnaire blanc spatialement et temporellement. La matrice interspectrale de $\mathbf{W}(\mathbf{f})$ est défini par:

$$\Gamma_W = \mathbf{A}(\theta,\phi)\Gamma_S\mathbf{A}^H(\theta,\phi) + \Gamma_B$$

où Γ_W est les matrice interspectrale du signal reçu par l'antenne, Γ_S est la matrice interspectrale des sources et Γ_B est la matrice interspectrale de bruit.

La goniomètre appelle aussi la méthode MUSIC, qui procéde par la décomposition propre de la matrice interspectrale (covariance dans le domaine temporel) des signaux reçus. Il se base sur une decomposition en sous-espaces engendrés par les vecteurs propres de la matrice interspectrale. On suppose d'abord aucun bruit, la matrice interspectrale des signaux reçus (seulement des sources) exhibe une propriété forte importante lorsque le nombre de sources P est inférieure au nombre de capteurs N et lorsque la matrice interspectrale des sources est régulière, ce qui implique une corrélation nulle ou partielle entre les sources. Dans ces conditions, la matrice des vecteurs directionnels (steering vector) de dimensions PxN, a un rang plein selon les colonnes, pourvu que les N vecteurs directionnels soient linéairement indépendants, donc les sources sont localisées dans des angles différents. Les vecteurs sources génèrent un sous-espace de dimension P appelé sous-espace source. La matrice de covariance des signaux reçus sans bruit a donc un rang égal au nombre de sources, et de ce fait possède N-P valeurs propres nulles auxquelles correspondent des vecteurs propres formant un noyau de dimension N-P, appelé sous-espace bruit, qui est orthogonal à l'espace source. La décomposition propre d'une matrice fournit une base de l'espace engendrée par la matrice. Par la symétrie hermitienne semi-positive de toutes les matrices de covariance, les vecteurs propres sont orthogonaux et orthonormés. Par décomposition en valeurs propres associées rangées par ordre décroissant, nous avons

$$\widehat{\Gamma}_W = \sum_{n=1}^{N} \lambda_n \mathbf{u_n} \cdot \mathbf{u_n^H}$$

où $\lambda_1 \geq ... \geq \lambda_P \geq \lambda_{P+1} > ... > \lambda_N = \sigma^2$ sont les valeurs propres et $\mathbf{u_n}$ les vecteurs propres de la matrice interspectrale spatiale. Les méthodes à haute résolution reposent sur les propriétés particulières de la matrice interspectrale du signal. Ainsi, l'étude de son rang permet de séparer l'espace des données en deux sous-espaces: l'espace signal engendré par les fréquences correspondantes aux maxima d'énergie, et l'espace bruit qui est son complémentaire orthogonal.

Les méthodes haute résolution (HR) issues de cette décomposition en sous-espaces sont connues pour être plus robustes par rapport aux techniques de prédiction linéaire. La méthode MUSIC s'appuie sur l'espace bruit. Le choix du nombre de sources P résulte de l'étude de la courbe de décroissance des valeurs propres. Mais elles s'avèrent peu fiables en precence de bruit. Soit $\mathbf{G} = [\mathbf{u}_{P+1}, ..., \mathbf{u}_N]$ la matrice constituée des vecteurs propres associée aux N-P plus petites valeurs propres (N nombre des capteurs et P nombre de sources). Alors, le projecteur sur le sous-espace bruit est défini par:

$$\Pi^{\perp} = \mathbf{G}\mathbf{G}^{\mathbf{H}} = \sum_{k=K+1}^{N} \mathbf{u}_k \mathbf{u}_k^H$$

Nous définissons maintenant la fonction quadratique pour une fréquence donnée f_0 (bande étroite) qui représente l'onde plane, sera:

$$g(\theta, \phi) = \mathbf{A}^{\mathbf{H}}(\theta, \phi)\Pi^{\perp}(f_0)\mathbf{A}(\theta, \phi)$$

Nous verrons par la suite une version normalisée du vecteur directionnel $\mathbf{A}(\theta, \phi)$ dont l'écriture adoptée est $\frac{1}{\sqrt{N}}\mathbf{A}(\theta, \phi)$ (Miron et al., 2005). En pratique, il est préférable de maximiser l'inverse de $g(\theta, \phi)$. Nous pouvons dorénavant énoncer le critère d'optimisation de l'estimateur MUSIC comme suit:

$$\mathbf{G}(\theta) = \frac{1}{A^H(\theta)\Pi^{\perp}(\theta)A(\theta)}$$

où les P directions d'arrivées estimées sont alors données par :

$$\theta_P = arg(max(G(\theta)))$$

La principale différence entre la réseau de capteurs, une composante (1C) et trois composantes (3C) est le rapport signal sur bruit et l'analyse sans perte d'information. Le capteur trois composantes fonctionne comme au récepteur omnidirectionnel malgré le fait qu'elle a trois capteurs polarisé dans l'espace orthogonal. L'échantillon des données spatiales et temporelles 3C, (X est le composante Nord, Y est et Z le vertical), peut être exprimée par:

$$\mathbf{W3C}_m(f) = \left(\begin{bmatrix} X_{1,m} \\ \dots \\ X_{N,m} \end{bmatrix}, \begin{bmatrix} Y_{1,m} \\ \dots \\ Y_{N,m} \end{bmatrix}, \begin{bmatrix} Z_{1,m} \\ \dots \\ Z_{N,m} \end{bmatrix} \right)$$

qui peut s'écrire comme:

$$\mathbf{W3C}_m(f) = [X_m(f), Y_m(f), Z_m(f)]$$

Et la matrice interspectrale dans la bande spectrale du signal (M points autour de un pic de fréquence) est donné par:

$$\widehat{\Gamma}_{W3C} = \sum_{m=1}^{M} \xi \left\{ \mathbf{W3C}_m \, \mathbf{W3C}_m^{\mathbf{H}} \right\}$$

$$\widehat{\Gamma}_{W3C} = \frac{1}{M} \sum_{m=1}^{M} (\mathbf{X}_m \mathbf{X}_m^H + \mathbf{Y}_m \mathbf{Y}_m^H + \mathbf{Z}_m \mathbf{Z}_m^H)$$

Localisation de sources synthétiques

Pour analyser et calibrer l'algorithme MUSIC-3C (Chapitre 2, section 2.5), un ensemble de données synthétiques ont été générés en utilisant une méthode numérique 3D pour un modèle élastique maillé pour des ondes sismiques (O'Brien and Bean, 2004) couplé avec l'élévation de la topographie numérique Ubinas dans un milieu homogène. Elle se compose de 8 sources synthétiques simulés numériquement, au-dessous du cratère, avec des élévations des altitudes entre 1972 m et 4950 m. L'analyse des données synthétiques ont montrées que MUSIC-3C fourni les trois paramêtres de base (back-azimut, angle de incidence et vitesse apparent) permettant de définit la direction spatiale d'arrivé des ondes. L'ensemble des données synthétiques ont été généré pour les mêmes positions des deux antennes sismiques proposées pour l'expérience terrain fait à Ubinas en 2009, avec deux antennes sismiques, au nord (NUBI) et à l'ouest (WUBI) sur les flancs du volcan Ubinas. La Figure 1 montre une comparaison des résultats du back-azimut, de l'angle d'incidence et de la vitesse apparent, calculé à partir des antennes 3C (trois composantes) et 1C (composante verticale). Seule la méthode MUSIC-3C a apporté la solution correcte en estimant le back-azimut et l'angle d'incidence, en fonction de l'emplacement à des profondeurs différentes. Au contraire, pour MUSIC-1C (avec des composantes verticales uniquement), le back-azimut était le seul paramètre bien estimé mais plus grande erreur.

Pour représenter la localisation sur les cartes, une fonction densité de probabilité (FDP) de la position de la source a été dérivée à partir de la FDP de vecteurs lenteur estimés pour les deux antennes (Métaxian et al., 2002; Tarantola and Valette, 1982). La résolution en profondeur était d'environ 500 m pour NUBI antenne et 400 m pour WUBI antenne. Nous concluons que MUSIC-3C a fourni des estimations réalistes des hypocentres sismo-volcaniques (épicentre et la profondeur).

Activité Vulcanienne à Ubinas

Dans le chapitre 3, dans le but de connaître la physique du volcan Ubinas, nous étudions l'activité vulcanienne enregistrées à Ubinas. Plus de 16 explosions a été identifiées pendant la campagne terrain à Ubinas en 2009. La localisation de 16 explosions avec MUSIC-3C, en analysant un fenêtre de temps de 2 secondes au début des explosions, montrent deux sources arrivant quasi au même temps,

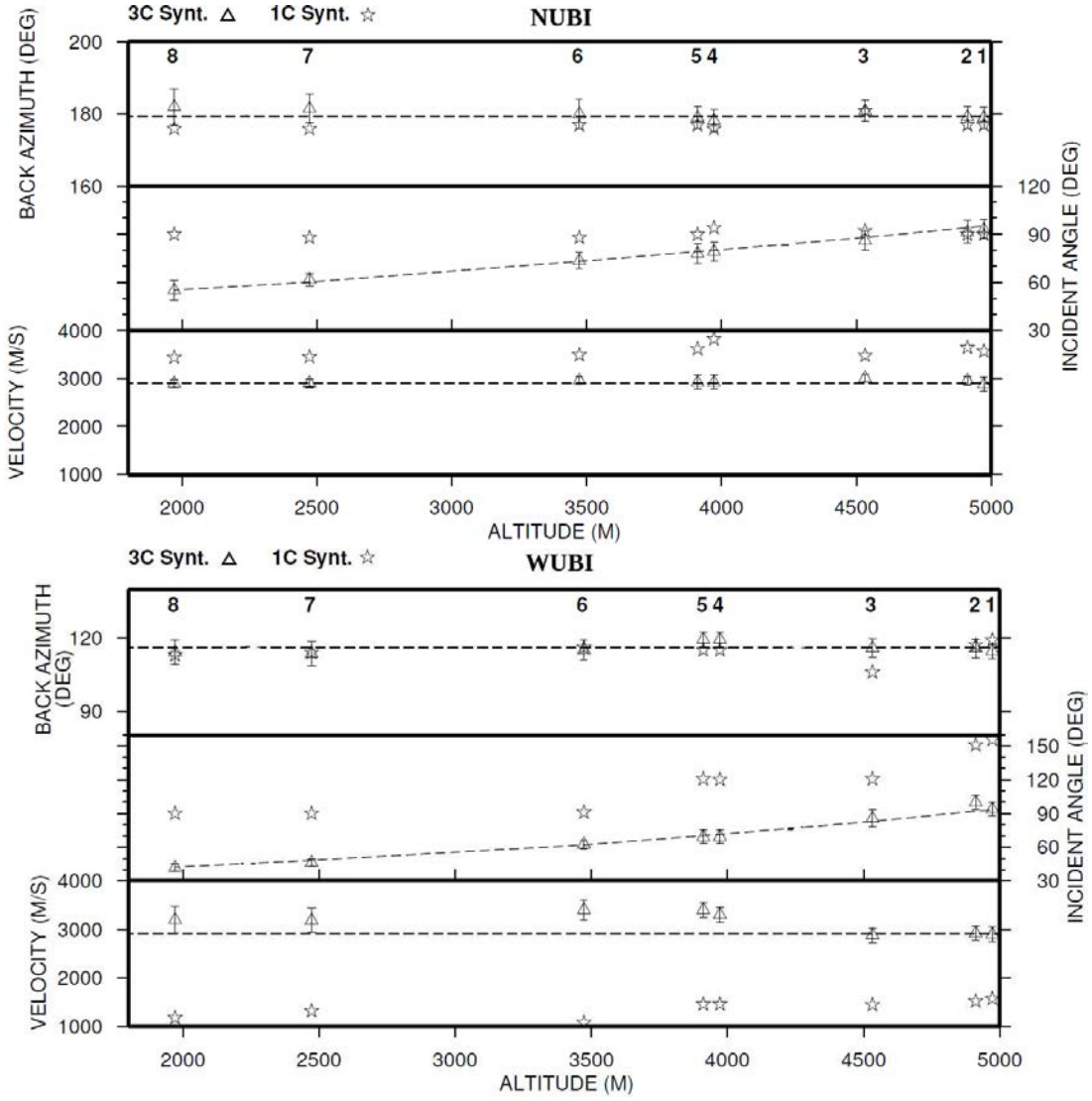


Figure 1: Les résultats obtenus pour les données de synthèse calculées pour les huit sources. Triangles vides et les étoiles représentent les résultats obtenus avec le MUSIC-3C et MUSIC-1C, respectivement. Sources sont numérotées comme dans la figure 1b. a) Back-azimut, angle d'incidence et la vitesse apparente pour NUBI antenne. b) Back-azimut, angle d'incidence et la vitesse apparente de Wubi antenne. Traits pointillés représentent les valeurs. Les cercles pleins représentent le modèle des résultats des données réelles

une à 1,3 km profond (altitude 3890 m +/-390) et l'autre moins profond à 0,5 km (4810 m +/-390 d'altitude). Nous interprétons ainsi la position de ces sources ainsi que les limites du conduit éruptif impliqué dans le processus de fragmentation. Iguchi et al. (2008) ont analysés des observations sismiques de déformations de terrain de trois stratovolcans (Sakurajima, au Japon; Suwanosejima, Japon; Semeru, Indonésie). Une séquence commune des phénomènes associés aux éruptions volcaniques a été proposé se décompose en cinq étapes (figure 2):

1. La montée du magma et l'accumulation de gaz volcanique dans le conduit en dessous d'un plafond de confinement, résulte de la pression et du volume croissant observé comme une inflation dans les inclinomètres.

2. La libération de gaz, car la pression du gaz est supérieure à la force du bouchon. La contraction mineure résultante est détectée par l'inclinaison de la déflation et les déplacements vers le bas.

3. La diminution de la pression dans le conduit au-dessous du capuchon, induit un brusque dégazage du magma saturé en eau profonde dans le conduit. L'expansion est mesurée par l'onde P premier mouvement du tremblement de terre d'explosion à la hausse.

4. Le processus d'expansion détruit le bouchon au sommet du conduit, il peut être lié à la deuxième source.

5. Face à l'écrasement des roches qui bloquant de fluide au sommet de la conduite, la poche de gaz au sommet s'effondre, provoquant une source de déformation contraction dans la partie peu profonde enregistrée par inclinomètres. Aussi dans certain cas, les explosions ont été suivi des cendres et des émissions de gaz, ces phénomènes à été liés comme une déflation vu par les inclinomètres.

Ruiz et al. (2005) ont analysé les temps d'arrivée des signaux d'explosion enregistrées dans le Mt. Tunguragua par une station équipée d'instruments à la fois sismiques et infrasons. L'observations des séries temporelles (sismiques et infrasons) ont montré que le début des explosions ont produit 2 sources, une plus profonde que les autres. Selon Ruiz et al. (2005) le moins de profondeur est liée à la fragmentation (explosion), enregistrée par les deux instruments (sismique et infrasons), et la deuxième source (le plus profonde) pourrait être liée à des troubles du magma et des gaz pour la dépressurisation brusque de conduit magmatique. En conclusion, ses résultats ont mis en évidence que les mécanismes des explosions vulcanienne se produises à deux sources, à différentes profondeurs de la conduite dans un intervalle de 1 s.

Conclusion

La figure 3 illustre la localisation de ces événements qui compile les explosions vulcaniennes et séismes de longue période (LP) situés entre le 24 mai et 03 Juin 2009 sur le terrain à Ubinas en 2009. Ces localisations nous ont permis de suivre la voie de magma avec une erreur inférieure à +/- 350

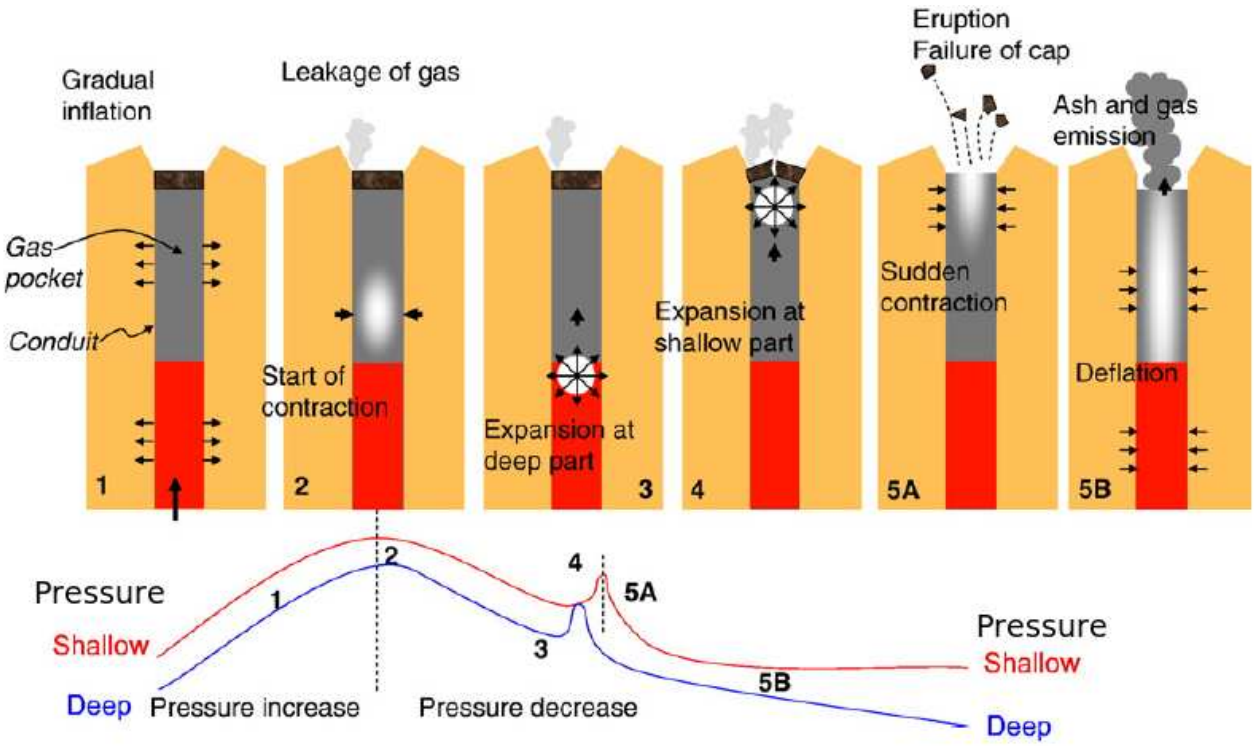


Figure 2: Modèle vulcanienne par Iguchi et al 2008

m dans la croûte supérieure sous Ubinas. Nous avons également mis en evidence, les deux sources localisées pour les explosions vulcanienne (des points rouges dans la Figure 3). Ceci a permis de suggérer l'hypothèse suivante: lorsque le magma monte la croûte supérieure, il semble y avoir une perturbation de l'écoulement situé à 1,2 km en dessous qui peut être associé à la zone de fragmentation du magma profondeur. La deuxième source de perturbation est située entre 200 et 300 m de la partie peu profonde de Ubinas cratère et peut être reliée à la zone de blocage dans le système de conduit de Ubinas. D'autre part, la localisation des LP, (points jaune dans la Figure 3) montre également une vue schématique de la voie de magma le long d'environ 5 km sous Ubinas cratère, qui a une tendance vers le sud et un peu à l'ouest. Pour conclure, la principale contribution de cette thèse est le développement d'une nouvelle approche pour la localisation des sources sismo-volcanique.

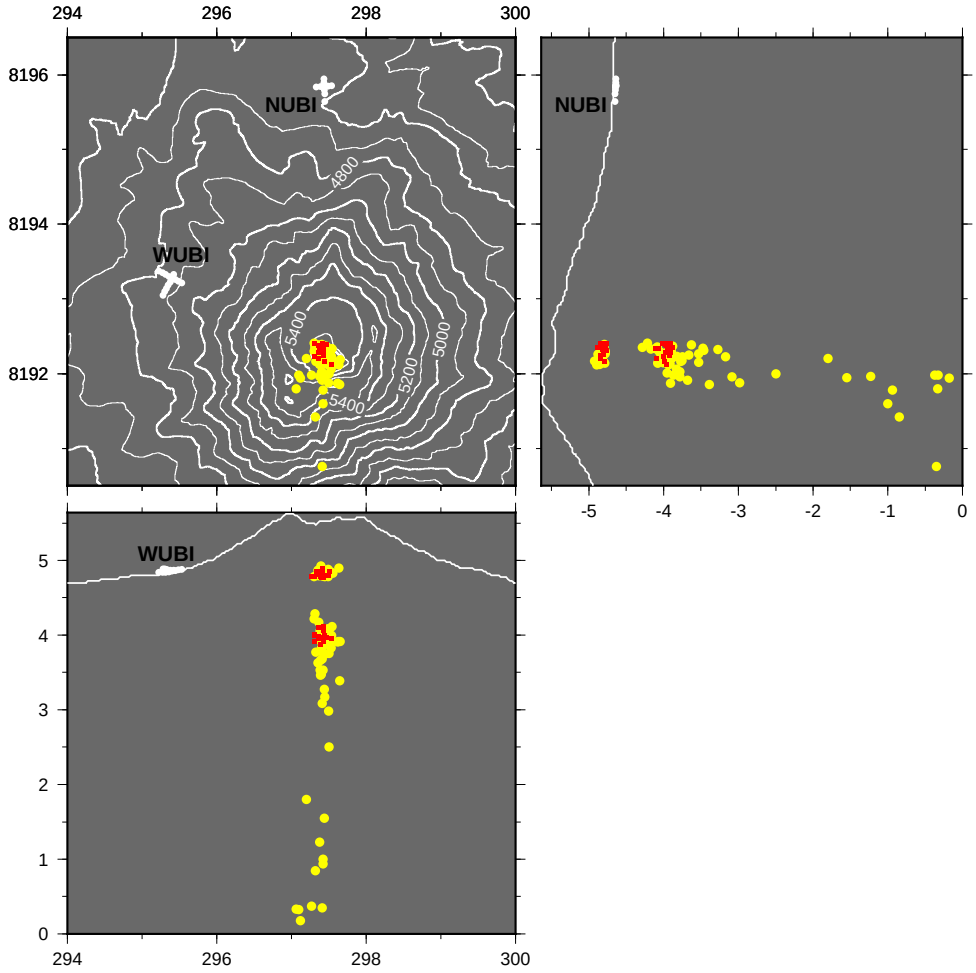


Figure 3: Carte de la topographique avec des localisation des sources à Ubinas 2009, rouge: des explosions vulcanienne et jaune: des longue période

Comprensión de los procesos magmáticos y localización de la fuente sismo-volcánica con antenas sísmicas multicomponentes

Resumén

Esta tesis, tanto metodológica y aplicada fue financiado por el IRD (l'Institute de Recherche pour le Développpment), se aplica en el contexto de localización de señales sismo-volcánicas. Esta tarea es clave para comprender el mecanismo de las erupciones volcánicas. El desarrollo emergente de los sismómetros de trés componentes (3C), nos han permitido desarrollar una aplicación moderna de localización, en particular para sismos de periodos largo (LP - Long Period), los cuales estan asociados con el transporte del magma hacia la superficie del volcán. Esta disertación se enfoca en la determinación de la localización de fuentes sismo-volcánicas registradas por arreglos de sensores. La investigación científica en este dominio y la mitigación de riesgos eruptivos, coinciden en el mismo objetivo, comprender los procesos físicos de la erupción. Desde esta perspectiva, los arreglo de sensores sísmicos de corta abertura (antena sísmica) se han convertido una herramienta fundamental y moderno para monitorear la actividad volcánica en los observatorios.

Nos concentramos en la actividad sísmica del volcán Ubinas, uno de los más activos del Perú (a unos 5400 m de altitud, con una caldera de 1,4 km). Esta tesis se ocupa del problema de la localización de las fuentes sísmicas basado en el análisis de datos registrados por arreglos de sismómetros 3C, desplegados en dos flancos del volcán. Las erupciones históricas y recientes muestran que Ubinas es caracterizado por explosiones de estilo vulcaniano que son de corta duración y muy violentas.

En el Capítulo 2, secciones 2.2 al 2.4, se especifica la geometría de dos antenas sísmicas. En este marco, el bien conocido algoritmo MUSIC (MUltiple SIgnal Classification) (Bienvenu and Kopp, 1983; Schmidt, 1986), es un método clásico para procesar señales captadas por un arreglo de sensores. La principal innovación de esta tesis es el desarrollo de un método MUSIC-3C, basado en este algoritmo MUSIC, aplicado en el contexto de ondas planas y múltiples componentes para localizar sísmos asociados con la actividad volcánica. El desarrollo consiste en reformular el problema a la luz de estos nuevos datos registrados por arreglos de sismómetros 3C.

Para validar MUSIC-3C, en el Capítulo 2, sección 2.5, se usan señales sintéticas a partir de fuentes situadas a diferentes profundidades debajo del cráter de Ubinas. Con el fin de examinar el algoritmo MUSIC-3C, se estimam los vectores lentitud (back-acimut, ángulo de incidencia y velocidad aparente) del frente de onda registrada por al menos 2 antenas sísmicas. La localización se estima mediante la interpretación de dichos vectores, a partir de un enfoque probabilístico (con funciones de densidad de probabilidad, Capítulo 2, sección 2.5.2) para cruzar espacialmente los vectores lentitud, dentro del volcan Ubinas. Los resultados demuestran que MUSIC-3C presenta ventajas significativas respecto con los métodos convencionales.

Después del análisis con datos sintéticos, en el Capítulo 3, nos ocupamos de los datos reales registrados por 2 antenas sísmicas NUBI y WUBI (Figure 3, arriba), durante Mayo a Julio 2009, en el volcán Ubinas (Perú). Dicho experimento fue llevado a cabo por los equipos de investigación del

IRD, proyecto VOLUME UCD (University College Dublin Irlanda) y el IGP (Instituto Geofísico del Perú). Mas de 400 eventos LP, 16 explosiones vulcanianas y varias horas de tremor fueron registrados, descrito en el Capítulo 1, sección 1.4. Con el fin de conocer los procesos físicos del mecanismo de los eventos explosivos, se analizan la actividad vulcaniana registrada mediante el método MUSIC-3C (Capítulo 3, sección 3.2).

Adicionalmente, se propuso un experimento en el volcán Misti en Noviembre y Diciembre 2011, con dos antenas sísmicas de 5 elementos cada uno, para examinar MUSIC-3C dentro de una transmisión continua de datos sísmicos para la vigilancia volcánica en tiempo real, descrito en el Capítulo 1, sección 1.5, de igual forma, el experimento fue administrado por los equipos de investigación del IRD, UCD e IGP.

Localización de fuentes sismicas

El conjuntos de datos sintéticos se generaron utilizando un método 3D de malla elástica numérica para señales sísmicas (O'Brien and Bean, 2004), acoplado con la topografía del volcan Ubinas y considerando un medio homogéneo. La simulacion consistió en ocho fuentes sintéticas por debajo del edificio volcanico entre 1972 m, y 4950 m de altitud. El análisis de estos datos sintéticos han demostrado que el método MUSIC-3C proporciona tres elementos básicos que son: el back-acimut, el ángulo de incidencia y la velocidad aparente, mediante el cual se define la dirección de las ondas planas. Además los datos sintéticos fueron generados para la misma posición de las dos antenas sísmicas propuestas al norte (NUBI) y el oeste (WUBI), en los flancos del volcán Ubinas (Figura 3). La Figura 1 muestra los resultados de back-acimut, el ángulo de incidencia y la velocidad aparente, calculado a partir de antenas 3C y 1C (componente vertical solamente). Sólo el método MUSIC-3C proporciona una solución correcta mediante la estimación de los 3 parámetros importantes. Donde el back-acimut, el ángulo de incidencia y la velocidad aparente son recuperados (triangulos en Figura 1) para las diferentes profundidades. Por el contrario, MUSIC-1C (antena con sensores verticales) representado por estrellas en Figura 1, sólo estima bien el back-acimut pero con mayor error. Para representar esta localizaón en el mapa de Ubinas, se usa un enfoque probabilistico (Métaxian et al., 2002; Tarantola and Valette, 1982), tanto el back-acimut y ángulo de incidencia son representados bajo la forma de funciones de densidad de probabilidad (FDP) en respecto a la posición geográfica (X,Y,Z). El resultado de la localización fué satisfactorio con una resolución en profundidad de unos 500 m para la antenna NUBI y 400 m para WUBI. Se concluye que las estimaciones obtenidas por MUSIC-3C son congruentes y de acuerdo con la simulación, donde los hipocentros fueron recuperados tanto en epicentro y profundidad.

Actividad vulcaniano de Ubinas

Con el fin de conocer la física del volcán, se estudia la actividad explosiva tipo vulcaniana en Ubinas. Se identificaron más de 16 explosiones en el experimento Ubinas 2009. La localización de dichas explosiones con MUSIC-3C, se obtienen dos fuentes sísmicas ocurridas al inicio de la explosión, uno

a 1,3 km de profundidad (3890 m de altitud + / -390) y otra más superficial a 0,5 km (4810 m +/- 390 altitud). Este resultado puede ser interpretado como los límites de la erupción que se ven involucrados en el proceso de fragmentación. Iguchi et al. (2008) se centra en las observaciones de deformaciones del suelo volcanico registrados por los inclinómetros, en tres estratovolcanes (Sakurajima, Suwanosejima en Japón y Semeru en Indonesia). Un modelo que explica las erupciones vulcanianas es propuesto que lo describe en cinco etapas (ver Figura 2 arriba):

1. La presión y la acumulación de gas volcánico aumentan gradualmente dentro del conducto cerrado (taponeado) por debajo del crater. Este fenomeno observado con el aumento de la deformación, como una inflación en los inclinómetros.

2. El tapón es vencido por la fuerza interna dentro del conducto, produciendo liberación de gas debido a la fractura de la roca en la tapa, Este fenomeno observado por el inclinometro como una deflación.

3. La disminución abrupta de la presión en el conducto interno causado por la fractura del tapón, en consecuencia, una perturbación súbita en el magma saturado, con burbujas en la parte interna (Figura 2 arriba) fue observado. Esto se registró como un pico en la deformación que corresponde a la expansión del volumen interno, por lo que se mide por la primera liberacion de energia que corresponde a la primera onda (P) del event. Puede estar relacionado a la fuente mas profunda, localizada en las erupciones en Ubinas.

4. Este proceso de expansión se traslada a la parte superior, el cual destruye la tapa en la parte superior del conducto, que puede estar relacionado con la segunda fuente en Ubinas.

5. Finalmente, la tapa que bloquaba la salida de fluido en la parte superior es destruido completamente con la explosión, causando una contracción en la parte poco profunda, registrada por inclinómetros. El conducto es liberado de manera que las explosiones son seguidos de emisiones de gases y fumarolas.

Ruiz et al. (2005) realizó observaciones de las señales de explosiones vulcanianas registradas en Mt Tungurahua, con estaciones sísmicos e infrasonidos. Los resultados han demostrado que los mecanismos del incio de las explosiones, alrededor del primer segundo, se produjeron dos fuentes de liberación de energía, uno más profunda que las otra. Según Ruiz et al. (2005) la menos profunda se relaciona a la explosión o liberación del conducto, registrada tanto sísmica y infrasonido, y la segunda fuente (el más profundo) puede estar relacionado con la actividad del magma, burbujas y gases registrado solo por los sismómetros.

Conclusión

La figura 3 muestra la ubicación de los eventos localizados durante este estudio, las explosiones de tipo vulcaniana y los eventos LP. Respecto a los eventos LP analizados, corresponden entre 24 de

mayo y 3 de junio de 2009. Estas localizaciones nos permitieron también establecer el camino del magma con un error inferior a +/-350 m en la corteza superior debajo de Ubinas. También nos permitió sugerir una hipótesis sobre la actividad del magma cerca de superficie, se observa una perturbación a una profundidad de 1,2 km, el cual puede estar asociado con la zona de la fragmentación del magma. El segundo punto de perturbación se situa entre 200 y 300 m en la parte poco profunda del cráter de Ubinas, aszociado a la destrucción del tapon que bloquea el conducto de ventilación en Ubinas. Por otro lado, la Figura 7 también muestra el recorrido del magma a lo largo de alrededor de 5 km por debajo de Ubinas cráter, que tiene una tendencia hacia el sur y un poco al oeste. Indicando que el suministro de magma viene del suroeste del crater.

Contents

Acknowledgements **5**

Summary **7**

Résumé **9**

Resumén **18**

List of figures **27**

List of tables **37**

1 Introduction **39**

1.1 Problem statement and motivation 39

1.2 Background 42

1.2.1 Introduction to volcanology 42

1.2.2 Vulcanian eruptions 44

1.2.3 Instrumentation for seismic volcano monitoring 47

Classical seismometers 48

Broadband 3C seismometers 49

1.2.4 Seismic signal processing in volcano monitoring 51

Seismic monitoring of volcanoes 51

Deconvolution - Instrument correction 54

1.2.5 New methodologies for seismo-volcano monitoring 58

Seismic wave propagation 60
Importance of coherent data 60
1.3 Ubinas and Misti volcanoes 63
1.3.1 Characteristics and eruption history of Ubinas volcano 64
1.3.2 Characteristics and eruption history of Misti volcano 66
1.3.3 Instrumentation on Misti and Ubinas 66
1.4 Ubinas field experiment in 2009 71
1.4.1 Seismic antenna configuration 71
1.4.2 Pre-processing and quality control of data set 74
1.4.3 Data processing and Presentation 74
1.4.4 Seismicity during the experiment 78
1.4.5 Time-frequency method 78
Empirical Mode Decomposition 80
Intrinsic Mode Function 80
Time frequency representation of Ubinas signals 84
1.5 Misti volcano field experiment in 2011 88
1.5.1 Seismic antenna telemetry installation 88
1.5.2 Monitoring seismic arrays in real time by Earthworm 91
1.6 Conclusion and goals 93
1.6.1 Contribution of this thesis 95
1.6.2 Thesis structure 95

2 Source Localization **97**
2.1 Introduction 97
2.2 Processing approach 100
2.2.1 Seismic sensor array 100
2.2.2 Array Response Function 102
2.3 Methods of array processing 104
2.3.1 Second-order statistic 104
2.3.2 High resolution methods 104

Beam-forming Capon's MVDR . . . 105
Subspace-based method: MUSIC . . . 105
2.3.3 Parametric Source Localization . . . 106
Maximum Likelihood . . . 106
Deterministic Maximum Likelihood - DML . . . 106
Stochastic Maximum Likelihood . . . 107
2.3.4 Discussion and comparison of source localization methods . . . 108
2.4 MUSIC-3C algorithm . . . 111
2.5 Application of MUSIC-3C . . . 114
2.5.1 Synthetic data . . . 114
2.5.2 Synthetic data analysis . . . 114
Probabilistic approach . . . 118
2.5.3 Real Data Analysis . . . 120
2.6 Discussion . . . 126
2.6.1 Capabilities of the method . . . 126
2.6.2 Volcanological aspect . . . 129

3 Physics of volcano from source localizations 133
3.1 Introduction . . . 133
3.2 Vulcanian events at Ubinas volcano . . . 134
3.2.1 Tilt observations . . . 136
3.2.2 Processing . . . 140
Determination of the useful frequency-band . . . 140
Estimation of the slowness vector and source location . . . 140
3.2.3 Synthetic sources . . . 152
3.3 Long Period event . . . 157
3.4 Discussion . . . 160
3.4.1 Swarm of vulcanian explosions . . . 160
3.4.2 Source location . . . 161
3.4.3 Explosion mechanism . . . 163

4 Conclusions and Perspectives **165**

4.1 Conclusions 165

4.1.1 Source localization 165

4.1.2 Application on real data 166

4.1.3 Telemetry seismic array system 169

4.1.4 A global view of seismicity of Ubinas volcano 170

4.2 Perspectives 171

Bibliography **174**

Appendices

A Matlab code to instrument correction **187**

Glossary **189**

List of Figures

1 Les résultats obtenus pour les données de synthèse calculées pour les huit sources. Triangles vides et les étoiles représentent les résultats obtenus avec le MUSIC-3C et MUSIC-1C, respectivement. Sources sont numérotées comme dans la figure 1b. a) Back-azimut, angle d'incidence et la vitesse apparente pour NUBI antenne. b) Back-azimut, angle d'incidence et la vitesse apparente de Wubi antenne. Traits pointillés représentent les valeurs. Les cercles pleins représentent le modèle des résultats des données réelles 14

2 Modèle vulcanienne par Iguchi et al 2008 16

3 Carte de la topographique avec des localisation des sources à Ubinas 2009, rouge: des explosions vulcanienne et jaune: des longue période 17

1.1 The city center of Arequipa, Peru, 17 km away from the summit of Misti volcano, with almost one million residents. The gray urban area is bordered by green agricultural fields. Photo courtesy of NASA. 40

1.2 Process of explosive eruption base on observations at the Sakurajima, Semeru, and Suwanosejima volcanoes (*Iguchi et al, 2008*). 1) Pressure and volume increase are observed by inflation-related tilt/strain and upward displacement. 2) Release of gas as the gas pressure exceeds the strength of the cap. 3) Pressure decrease in the conduit starting from the gas pocket, inducing sudden outgassing, in this stage starts the explosion. 4) Expansion process destroying the cap at the top of the conduit. 5A) Failure of the cap at the top of the conduit. 5B) Ash and gas emission from the conduit. 47

1.3 Block diagrams of conventional (short-period) and feedback seismometers (broad-band). Ideally, in the feedback configuration, the mechanical suspension and the displacement transducer "don't see" the full amplitude of the ground motion, which is present only in the feedback path. 48

1.4 Short period single component seismometers designed for a 3C configuration, (one vertical Z and two horizontals X,Y). 49

1.5 Integrated 3C broadband portable seismometer. Left side, STS-2 physically installed on a level surface, the instrument shows a rod oriented to the transverse direction, typically towards east geographic. Right side, a view of the internal part, where some electronic cards and a cylindrical package containing within three orthogonally oriented identical sensors. 50

1.6 From Surono et al 2012, comparison between SO2 fluxes and RSAM data from seismic station near Merapi crater. Top, overview of SO2 degassing during the 2010 Merapi volcano eruption (UTC time). SO2 fluxes were determined from ground-based scanning DOAS measurements (mean fluxes measured over hour-long intervals) and satellite images, from IR IASI and AIRS sensors (mean fluxes calculated for 12h intervals) and the UV OMI sensor (mean fluxes calculated for 24h intervals). Bottom, RSAM computed for the Plawangan station (6 km from the summit). A clear correspondence between RSAM and SO2 flux is demonstrated, supporting our identification of four distinct phases to the eruption (indicated by Phases I to IV). E stands for explosion; L for Lahar. 53

1.7 Flow chart of seismogram trace u(t) generation by the source x(t) 55

1.8 The amplitude (top) and phase (bottom) response functions for a Guralp 6TD seismometer 56

1.9 Example of instrument correction for a volcanic earthquake (explosive event) recorded at Ubinas volcano in 2009. Top: seismic signal filtered into the band 0.1 Hz to 2.2 Hz without instrument correction. Middle: Ground motion seismogram (velocity). Bottom: Ground displacement seismogram 58

1.10 A wave plane s(t) impinging on the vertical plane and crossing the array at an angle of incidence ϕ. Black squares along x-axis correspond to seismometers. Signals with period *T* above sensors are with offset according the apparent velocity and time-delays to the slope along of the x-direction 61

1.11 Seismic signals recorded at Ubinas volcano. Left: low frequency content signal recorded by the vertical component. Right: high frequency content signal recorded by the vertical component. 62

1.12 Left side: Map of the volcanic arcs in the Andes, and subducted structures affecting volcanism. Right side: Map of volcanoes in Central Volcano Zone in Peru. (Thouret et al.2005) 63

1.13 This image shows an ash cloud column of around 2 km above the Ubinas crater after an explosive event on the 02nd June 2009, photo taken from Ubinas village 65

1.14 Top: photograph of Misti volcano crater with Mount Chahani in the background. Bottom: photograph of Mount Misti. 67

1.15 Telemetry seismic network map of Misti volcano 68

1.16 Telemetry seismic network diagram of Ubinas volcano. 69

1.17 Volcanic explosion occurred in July 2006, it is preceded by LP events. From Macedo et al. (2009) 70

1.18 Evolution of the LP event occurred at Ubinas volcano between October 21 and October 31 2006 (black line). Dashed lines indicate explosion occurrence times; gray boxes an indicate increase in LP activity. From Traversa et al. (2009) 71

1.19 Ubinas crater map, white triangles are the 3-component seismometer locations of arrays WUBI and NUBI. a) Zoom of NUBI antenna. b) Zoom of WUBI antenna. . . 72

1.20 Photo of all components used for one seismic station. The seismometer 6TD is in the right middle with a Wi-Fi antenna. The white element lying in the corner of the solar panel is a GPS antenna, the blue square table is the solar panel and the black element below the solar panel is the battery. 73

1.21 Typical unfiltered seismograms, indicating date in the upper left and minimum amplitude in $\mu m/s$ (left) and their spectra (right), recorded at Ubinas experiment in 2009. . a) LP, b) VT, c) hybrid, d) LP e) LP and f) LP. 76

1.22 Typical unfiltered seismograms, indicating date in the upper left and minimum amplitude in $\mu m/s$ (left) and their spectra (right), recorded at Ubinas experiment in 2009. a) Explosive, b) VT, c) Tornillo, d) Avalanche or rockfalls e) hybrid and f) Tremor. . 77

1.23 RSEM computation, with 5 minutes sliding time windows, during the 2009 experiment. The black inverted triangles match the sequence of 16 vulcanian explosions numbered. Horizontal dashed lines match to tremor event duration and black square dots match to quakes out of volcano. 79

1.24 Seismic signal (signal) recorded at Ubinas volcano and their decomposition representing by IMFs (intrinsic mode functions) 82

1.25 a) A volcanic seismic signal (Vertical component) recorded at Ubinas volcano, b) Hilbert-Huang transform time-frequency representation (Normalized) of the seismic signal in a), c) Wigner-Ville time frequency representation (normalized) of the seismic signal in a). 83

1.26 One-day seismic recordings (25th May 2009) on the Ubinas volcano by one station (vertical component) of WUBI antenna. 85

1.27 One-day seismic recordings (02th June 2009) on the Ubinas volcano by one station (vertical component) of WUBI antenna. The biggest wave correspond to an explosion followed by tremor event. 86

1.28 Frequency-Time representation of WUBI during the experiment Ubinas volcano 2009, black triangles are explosions, squares are external earthquakes 87

1.29 Misti volcano topography. Top: triangles labeled with MISA and MISB represent the location of the seismic antennas, and the triangle OBS is the location of the IGP-Arequipa observatory, in Cayma district in Arequipa Peru. Bottom: A zoom of the area represented by a square above, each filled triangle represents a seismometer of the array. 89

1.30 Diagram representation of the harware used in the seismic array with telemetry capability 90

1.31 A view of a seismic station used to send data to the observatory, at the top of the pole a Yagi antenna and a solar panel can be seen 90

1.32 Earthworm system functional diagram 92

1.33 Flow diagram of MUSIC-3C algorithm 93

1.34 Top: Seismic waveforms of the MISA and MISB antennas of an earthquake occurred at Misti volcano. Bottom: 3D Misti topography map, with MISA and MISB antennas and blue square is the hypocenter estimated for this earthquake 94

2.1 Examples of time delay calculation with the cross-spectral method. Two windows, including (a) the onset of an explosion and (b) a section of tremor, displayed in Figure 3, are analyzed. From top to bottom: the velocity seismograms obtained at sensors 1 (solid line) and 3 (dashed line) of array TWES; the coherency Cij of the two signals; the normalized (solid line) and smoothed (dashed line) cross-spectra Sij; the weight function Wij used for the linear fit; the cross-spectrum phase φ_{ij} (dots) and the straight line obtained by weighted linear fit. The slope of the line is proportional to the time lag between the records (from Metaxian et al. (2002)) 98

2.2 A 3-D view of the source region of LP events Kilauea (from Almendros et al. (2001b)) 99

2.3 Model of triaxial sensors array for one source. XYZ represent North, East and Vertical components, θ and ϕ are the azimuth and incidence angles 100

2.4 WUBI array response function A. 103

2.5 Spectra of 8 sensors linear array spaced at half-wavelength, with two sources in 60 and 70 degrees, SNR=20dB, a) Beam-forming method. b) Capon and MUSIC methods . 109

2.6 Top: Ubinas volcano topography, NUBI, WUBI, EUBI and SUBI indicate the positions of the seismic antennas used for the numerical sources. Bottom: East-West profile of Ubinas summit topography indicating the altitude of each synthetic sources and the WUBI and EUBI antennas 115

2.7 a) The vertical (Z), north (N) and east (E) synthetic seismogram from NUBI antenna, b) averaged energy spectrum calculated for all the receivers and all the components. The vertical dash lines in (a) indicate the time window selected for the processing. The vertical dash lines in (b) represent the frequency windows used for the cross spectral matrix calculation. 116

2.8 a) Normalized MUSIC-3C spectrum calculated with synthetic data generated at source 3 for NUBI antenna. The central frequency used for the cross spectral matrix calculation (Figure 3b) is indicated in the upper left of the spectrum. b) Normalized back-azimuth profile (cross section at apparent velocity 2900 m/s). c) Normalized apparent velocity profile (cross section at back-azimuth at 181 degrees). d) Normalized incidence angle. The vertical dotted lines represent the error 95% range. 117

2.9 Results obtained for the synthetic data calculated for the eight sources. Open triangles and open stars represent results obtained with the MUSIC-3C and MUSIC-1C, respectively. Sources are numbered as in figure 1b. a) Back-azimuth, incidence angle and apparent velocity for NUBI antenna. b) Back-azimuth, incidence angle and apparent velocity for WUBI antenna. Dash lines represent the values. The filled circles represent the real data results model 119

2.10 Probability density function of the source position ρ_2 for the 8 synthetic sources. Horizontal view represented at the source depth and vertical view oriented West-East crossing the maximum likelihood of ρ_2 for the sources at the depths of a) 4972 m, b) 4912 m, c) 4532m, d) 3972 m respectively. The PDF $\rho_1(\theta^k)$ and $\rho_1(\phi^k)$ are represented as rose diagrams with an increase of 5°. White points represent the sensor positions. 121

2.11 Probability density function of the source position ρ_2 for the 8 synthetic sources. Horizontal view represented at the source depth and vertical view oriented West-East crossing the maximum likelihood of ρ_2 for the sources at the depths of e) 3912 m, f) 3472 m, g) 2472 and h) 1972 respectively. The PDF $\rho_1(\theta^k)$ and $\rho_1(\phi^k)$ are represented as rose diagrams with an increase of 5°. White points represent the sensor positions. A different vertical scale is used for e (Altitude between 3.5 and 5.6 km) and f, g, h (Altitude between 1.5 and 5.6 km). 121

2.12 a) Z component seismogram of the LP event and explosion earthquake recorded by the central station of NUBI antenna. The time and date of the first sample is indicated in the upper left of the record. Shaded zones represent part of the signals enlarged in b) and c). d) and e) Z component of the LP event and the explosion earthquake recorded by 10 stations of NUBI antenna. Waveforms correspond to the shaded parts of the signal in b) and c), filtered between 1 and 10 Hz. The vertical dash lines in d) and e) indicate the time window selected for the processing. f) and g) Averaged energy spectrum calculated for all the receivers and all the components, where the vertical dash lines represent the frequency windows used for the cross spectral matrix calculation. 122

2.13 a) Normalized MUSIC-3C spectrum calculated with the LP event for NUBI antenna. The central frequency used for the cross spectral matrix calculation (Figure 7f) is indicated in the upper left of the spectrum. b) Normalized back-azimuth profile (cross section at velocity 1794 m/s). c) Normalized velocity profile (cross section at back-azimuth at 183 degrees). d) Normalized incidence angle. The vertical dot lines represent the error range. e) Normalized MUSIC-3C spectrum calculated with the explosion earthquake for NUBI antenna. The central frequency used for the cross spectral matrix calculation (Figure 7g) is indicated in the upper left of the spectrum. f) Normalized back-azimuth profile (cross section at velocity 3151 m/s). g) Normalized velocity profile (cross section at back-azimuth at 184.5 degrees). h) Normalized incidence angle. The vertical dotted lines represent the error range. c) and d) are apparent velocities 124

2.14 Probability density function (PDF) of the source position ρ_2, for the explosion earthquake (a-c) and the LP event (d-f). a) horizontal view at 4200 m depth, b) vertical view oriented West-East crossing the maximum likelihood of ρ_2, c) same as b) oriented North-South. d) horizontal view at 2240 m depth, e) vertical view oriented West-East crossing the maximum likelihood of ρ_2, f) same as e) oriented North-South. The PDF $\rho_1(\theta^k)$ and $\rho_1(\phi^k)$ are represented as rose diagrams with an increment of 5 degrees. . 125

2.15 Ubinas map with 8 synthetic sources localizations with 3 antennas deployment in North, West and East (white circles) 128

2.16 Ubinas map with 8 synthetic sources localizations with 4 antennas deployment in North, West, East and South (white circles) 129

3.1 RSEM computation, with 5 minutes sliding time windows, during the 2009 experiment. The black inverted triangles match the sequence of 16 vulcanian explosions numbered. Horizontal dashed lines match to tremor event duration and black square dots match to quakes out of volcano. 135

3.2 Seismic energy and tremor duration as functions of the interval between the explosions. The black squares are the explosion energies and the explosion intervals. The horizontal segments are the duration of the post-explosion tremor, (*) are explosions without tremor. The numbers are the explosions, according to Table 3.1. 137

3.3 Explosion #7 waveforms recorded at the NUBI, WUBI and UB2 stations. a. Vertical components of the displacement filtered between 0.03 Hz and 2 Hz. b. Tilt signals recorded at UB2 in μrad. c. Zoom of UB2 signals inside the selected rectangle in (a) and (b), with the high frequency (2.2-6 Hz) seismic signal waveform of UB2Z in gray. d. UB2 tilt vector evolution. The black curve corresponds to the tilt for the rectangle. 139

3.4 Filtered (0.5-6 Hz) waveforms of explosion #7. a. Time-series of seven sensors of three components recorded at the WUBI antenna. b. Smoothed spectrum of the 3C components. c. Thinnest curve: average of the smoothed spectrum over all of the traces. Thicker curve: average coherence. d. Average of the smoothed spectra over each component, with the thin line for the North components, the dashed line for the East components, and the thick line for the vertical components (Z). 141

3.5 a. The Hilbert Huang transform as applied to the vertical component of the seismic signal of explosion #7, as recorded by sensor 04 of the WUBI antenna. b. The time representation of the signal in (a), where the gray region represents the first-arrival signal. 142

3.6 a. Spectral average calculated for each component of the signals recorded by all of the WUBI sensors for the time-window defined in Figure 3.5b by the gray zone (first-arrival signal). The thick line corresponds to the vertical component, the dashed line to the East component, and the thin line to the North component. b. Averaged spectrum of the three components, where the squares indicated the bins selected for analysis. 143

3.7 Music-3C spectrum obtained for a time window positioned at the beginning of the signal of explosion #7, represented as a function of the back-azimuth and the apparent velocity, for the frequencies of 1.1 Hz (a) and 1.5 Hz (d). b., c. Horizontal and vertical sections of the spectrum following the white dashed lines crossing the maximum of the peak spectrum for the frequency of 1.1 Hz. e., f. As for (b) and (c), for the frequency of 1.5 Hz. 145

3.8 Music-3C spectrum obtained for a time window positioned at the beginning of the signal of explosion #7, represented as a function of the incidence angle and the crust velocity beneath the antenna, for the frequencies of 1.1 Hz (a) and 1.5 Hz (d). b., c. Horizontal and vertical sections of the spectrum following the white dashed lines crossing the maximum of the peak spectrum for the frequency of 1.1 Hz. e., f. As for (b) and (c), for the frequency of 1.5 Hz. 146

3.9 Time series representation for the low frequency band of explosion #7. Left, for NUBI; right, for WUBI. a., f. Waveform of the vertical component for NUBI and WUBI, respectively. b., g. STA logarithmic signature for NUBI and WUBI, respectively. c., h.; d., g.; e., j. Back-azimuth, incident angles, and velocity, for the NUBI and WUBI antennas, respectively. 148

3.10 Time series representation for the high frequency band of explosion #7. Left, for NUBI; Right, for WUBI. a., f. Waveform of the vertical component for NUBI and WUBI, respectively. b., g. STA logarithmic signature for NUBI and WUBI, respectively. c., h.; d., g. ; e., j. Back-azimuth, incident angles, and velocity, for the NUBI and WUBI antennas, respectively. 149

3.11 Map of Ubinas showing the slowness vector directions given by MUSIC-3C, and the maximum likelihood solution (red contour) that indicates the localization of the two sources for explosion #7. 151

3.12 Waveforms of the MUSIC-3C procedure over NUBI and WUBI for synthetic source 1. a., f. Seismic amplitudes. b., g. Logarithmic STA of the amplitudes. c., h. Back-azimuth, in degrees. d., g. Incidence, in degrees. 153

3.13 Waveforms of MUSIC-3C procedure over NUBI and WUBI for synthetic source 4. a., f. Seismic amplitudes. b., g. Logarithmic STA of amplitudes. c., h. Back-azimuth, in degrees. d., g. Incidence, in degrees. 154

3.14 Waveforms of MUSIC-3C procedure over NUBI and WUBI for the sum of the synthetic sources 1 and 4. a., f. Seismic amplitudes. b., g. Logarithmic STA of amplitudes. c., h. Back-azimuth, in degrees. d., g. Incidence, in degrees. 155

3.15 Topography map of Ubinas indicating synthetic source localizations. a) Synthetic 1 source located at at 4920 +/-120 m altitude Waveforms. b) Synthetic 4 source located at 3920 +/-100 m altitude and c) Synthetic 1 and 4 together sources located at altitudes of 4940 +/-160 m and 3960 +/-120 m 156

3.16 Waveforms of MUSIC-3C procedure over NUBI and WUBI for the long-period event. a., g. Seismic amplitudes. b., f. Logarithmic STA of amplitudes. c., h. Back-azimuth, in degrees. d., i. Incidence, in degrees. e., j. Crust velocity. 158

3.17 Map of Ubinas Volcano showing the slowness vector directions, and the maximum likelihood solution (red, green contour), indicating the localization sources for the long-period event. The 16 explosion localizations are shown as gray points with their errors bars. 159

3.18 Hypocenter of 50 LP events represented by yellow circles, recoreded during the field experiment at Ubinas 2009. 160

4.1 Results obtained for the synthetic data calculated for the eight sources. Open triangles and open stars represent results obtained with the MUSIC-3C and MUSIC-1C, respectively. Black circles are back-azimuth and incidence angles of LP and explosion (real data). a) Back-azimuth, incidence angle and apparent velocity for NUBI antenna. b) Back-azimuth, incidence angle and apparent velocity for WUBI antenna. Dash lines represent the values. The filled circles represent the real data results model 167

4.2 Topography map of Ubinas indicating NUBI and WUBI stations location for LP and explosion events recorded at Ubinas 2009. Rose diagrams (black) for each antenna and the source location indicating a normalized color scale for the maximum likelihood 168

4.3 Hypocenter located at Ubinas volcano, with some events recoreded during the field experiment at Ubinas in 2009. Yelow circles correspond to localization of long-period events, red circles correspond to explosion events and black star corresponds to volcano tectonic event. 170

4.4 Time-frequency representation of seismic signals detected on Ubinas between on 24th May and 3rd June 2009, black triangles accompanied by numbers correspond to explosion events, black squares correspond to regional earthquakes occurred near Ubinas and green inverted triangle correspond to volcano tectonic event 171

List of Tables

1.1 Summary table: Characteristics of magma in physics of volcanoes (*Spera, 2000*). . . 42

1.2 Specifications of 3C broadband seismometers and high resolution 24-bit digitizers used frequently in seismic volcano monitoring. 51

1.3 Calibration sheet for the vertical component of a Guralp 6TD 3C broadband seismometer. 56

1.4 Pole and zero file (PZFILE.PZ) for removing the instrument by using SAC program . 57

2.1 Comparison of the existing source localization methods based on different criterion (Prior knowledge of model order, Assumption of Signal Type and Array Geometries) 110

2.2 Source localizations of the eight synthetic sources in the Ubinas model 114

2.3 Distance between the calculated and real position of each synthetic source, mean quadratic radius and altitude of each source 120

3.1 Characteristics of the 16 Vulcanian events of May and June, 2009 at Ubinas. The date and time are in universal time (local time was 5 h more), E is the event energy in MJ, the 'Interval' is the time interval since the previous explosion, and TR is the tremor duration after the explosion. 136

3.2 Source Localization given by MUSIC-3C analysis on the 16 explosion events. 152

Chapter 1

Introduction

1.1 Problem statement and motivation

Volcanoes are awesome manifestations of magma that rises from the depths of the Earth's crust. Human activity takes place near many volcanoes, which are considered as a national monument in calm conditions (Figure 1.1), during an eruption, this volcano can produce a violent explosive eruption including ash and pyroclastic fragments, and can certainly become catastrophic impact on society at this moment. No model can show eruption intervals. However, eruptions are almost always preceded and followed by volcanic unrest, indicated by strong variations in the dynamic process caused by internal forces. Such indicators can be measured by seismometers and are usually detected before the eruption, which can be very valuable to control the threat. For that reason, volcanologists are looking for a better understanding of the seismic signals generated in dynamic interactions between magma movement, degassing and pressurized condition. Localization and analysis of these signals can lead to an improved knowledge of magma transport mechanisms which is critical to better understand the eruption process.

It is known (Dingwell, 1996; McNutt, 2005; Sparks, 2000) that the upward movement of magma towards the volcano's crater, frequently breaks rocks and hence leads to seismic wave propagate. As magma rises to the surface, its physical and chemical properties are changing and causing convection currents and gas bubbles due to the decrease in pressure. These schematic processes explain the diversity of seismic waves recorded by seismometers deployed on volcanoes. A fundamental goal of volcano seismology is a better understanding of these mechanisms.

Recent technological developments and improvements, in the seismological instrumentation of volcanoes and in the seismic signal processing, have led to better understanding the eruption mechanisms. These advances occurred mainly in the last two decades, following monitoring systems in a few tens of volcanoes such as Piton de la Fournaise (Réunion island, France), Kilauea (Hawaiian, USA), St. Helens (Washington, USA), Etna (Sicily, Italy), Sakurajima (Japan), etc. Results and analysis from these different sites show that the dynamic of a volcanic unrest is reflected in the pattern of geophys-

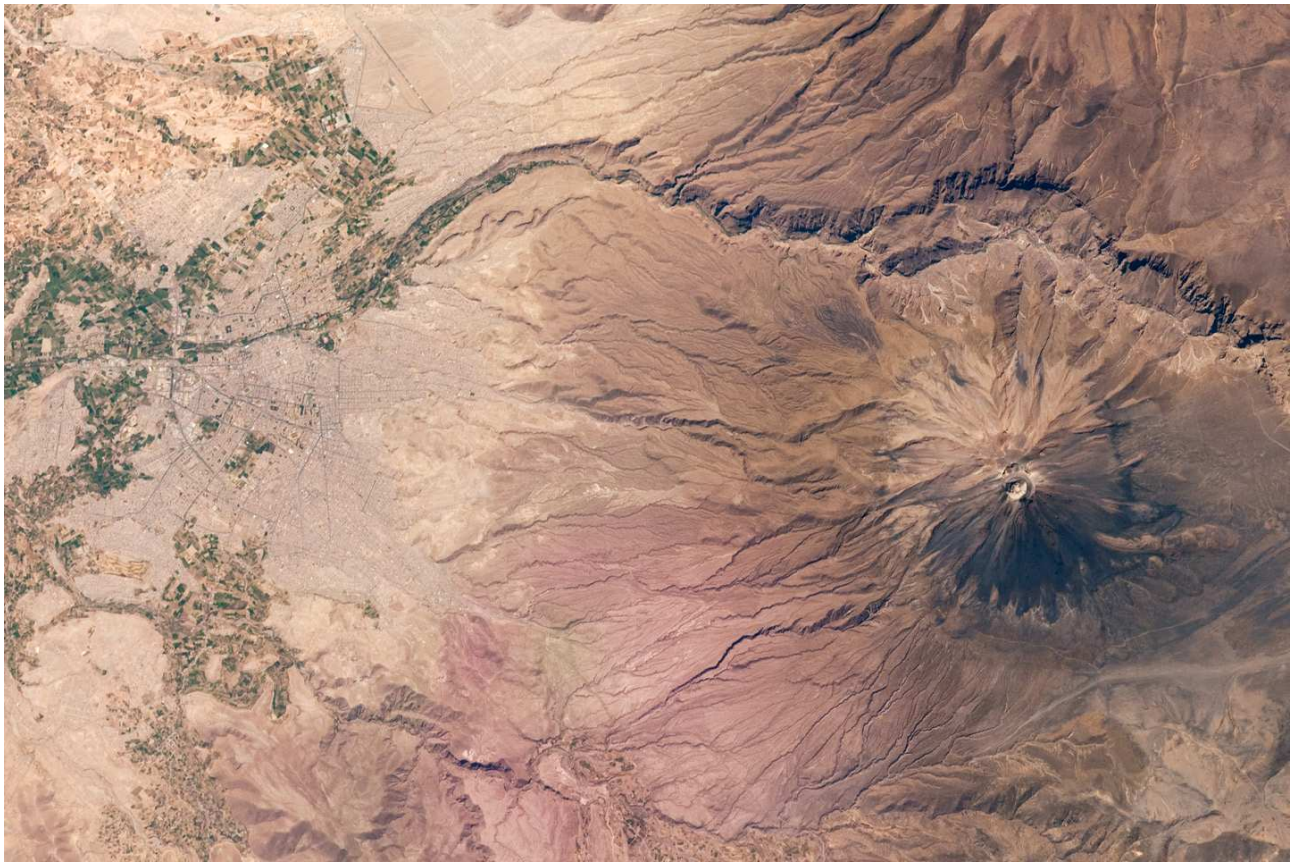


Figure 1.1: The city center of Arequipa, Peru, 17 km away from the summit of Misti volcano, with almost one million residents. The gray urban area is bordered by green agricultural fields. Photo courtesy of NASA.

ical data series, such as seismicity, ground deformation and chemical emissions. Locating sources of volcanic earthquakes in terms of azimuth, depth and magnitude, are especially important, since seismic events are frequently one of the first sign of volcanic unrest, and they can reveal how unstable is the volcano. For this reason since 10 years, hundred of volcanoes were currently seismically monitored. Recently the use of broadband 3C seismometers has significantly improved the resolution and range of signals detectable at volcanoes, and pushed new methods for the interpretation and analysis of volcanic unrest (Chouet, 2003; Wassermann, 2012).

With these new instrumentation, a great variety of seismic signals can be generally recorded on active volcanoes, it is known (Bean et al., 2008; Neuberg and Pointer, 2000) seismic waves propagation in volcanic setting are strongly influenced by topography and heterogeneity in volcanic media. Under the common sense, these signals can broadly be classified into four groups: volcano tectonic (VT) earthquakes, long-period (LP) events, tremor events and volcanic explosions. VT events are close to tectonic earthquakes in terms of signal characteristics and are thought to be caused by brittle failure on edifice faults. LP earthquakes, tremors and explosion events are generated by fluid-filled cracks or

fluid oscillation processes (Chouet, 1996; Neuberg et al., 2006; Wassermann, 2012).

Most seismo-volcanic events related to fluid movement, show emergent onset, generally ambiguous seismic P- and S-phases, and therefore can not be located precisely using classical earthquake hypocenter tools (based on phase picking and calculating their travel time residuals) (Chouet, 2003). Because seismo-volcano sources are different from those causing tectonic earthquakes, processing techniques and equipment configuration must be adapted to operate on these signals. For instance, small aperture seismic arrays have become a reliable and useful tool for tracking the sources of volcanic activity.

For this reason new methods of source localization were issued this last decade, based on estimations of back-azimuth and apparent velocity of sismo-volcanic sources. In the literature, most methods using single-component (1C) seismic sensor arrays have received considerable attention in volcano research, see for example Métaxian et al. (1997); Saccorotti et al. (2001); La Rocca et al. (2004); Almendros et al. (2004); Di Lieto et al. (2007). Unfortunately, the depth determination was poorly resolved because the incidence angle is very difficult to estimate. In signal processing community, under the same philosophy of source localization, Bienvenu and Kopp (1983) and independently Schmidt (1986) have presented a measurement model for arbitrary geometries of sensor arrays, resulting an algorithm for source detection and localization, known as MUSIC (*multiple signal classification*). Compared to a classical beamforming algorithm, this popular high-resolution algorithm is considered to be superior in estimating the direction-of-arrival of plane waves (Krim and Viberg, 1996).

Another advantage of sensor arrays is the ability to improve the signal-to-noise ratio (SNR). Consequently time-frequency analysis of these enhanced array data, can be used to explore fluctuations between different types of seismic wave from the volcanic activity, such as patterns of clustered earthquakes. Huang et al. (1998) presented a method to process nonstationary and nonlinear time-series data, called Empirical Mode Decomposition (EMD). We will show that this technique can better display and survey the Ubinas volcano activity taken during the field experiment in 2009.

Recently, two eruptions from stratovolcanoes similar to Ubinas and Misti (Peru) have been successfully predicted using the analysis of real-time seismic data. The occurrence of long-period events were used to predict in December 1989 the eruption of Mount Redoubt (Alaska, United States) (Chouet, 1996). And other, during October 2010, seismic observations around Mount Merapi located at border of Central Java (Yogyakarta, Indonesia), showed an abrupt increased of number of seismic events, statistically compared with the last two previous eruptive events, so that over tens of thousands people were evacuated from the affected area just before one-day the main explosive event (Surono et al., 2012). Despite these predictions and the development of increasingly geophysical monitoring tools, we must progress in the field of investigation on new seismic methods to improve the prediction in terms of the size and force of an eruption which remain a major challenge in volcano-seismology due to the lack of clear knowledge of volcanic mechanisms.

1.2 Background

1.2.1 Introduction to volcanology

One of the most powerful and destructive natural forces that exhibits our planet is the volcanic eruption. Every year, about 50 volcanoes throughout the planet are active above sea level, threatening millions of people living near volcanoes (Sigurdsson, 2000). To understand these phenomena, volcanology is the science that study the origin and ascent of magma through the earth's mantle and crust and its eruption at the surface. Volcanology also deals with the physical and chemical evolution of magmas, their transport and eruption, in which magma transport is fundamentally episodic as a result of inherent instability of magmatic systems at all time scales. This phenomenon is generally reflected in seismic activity, caused by dynamic interactions between gas, liquid and solid along the complex conduit (Chouet and Matoza, 2013).

Understanding how magma migrates beneath the volcano is thought to be the key factor to characterize the volcanic activity and the hazard features (Chouet, 2003), specially for andesitic and rhyolitic structures characterized by explosive episodes (Sparks et al., 1984). Recent improvements in seismic instrumentation and development of new techniques in volcano-seismology have contributed to improve the interpretation of sismo-volcanic signals and quantification their source mechanisms. Despite all the first efforts, even after a century of research, volcanic eruptions remain a major challenge for the vulcanologist community, escentially because its complex nature driven by non-linear excitations and instability conditions that are created when a magma volume rises up to the earth surface.

Magmas are defined as molten rock that consists of up to three components: liquid silicate melt, suspended crystalline solids and gas bubbles. Magmas are erupted as lava or pyroclasts when reaching the surface, and can be classified as basaltic, andesitic and rhyolitic according to typical temperature at about 1100, 900 and 700 Celsius respectively and silicate ($Si0_2$) concentration of approximately 50% , 60% and 70%, respectively (see Table 1.1) (Spera, 2000).

Magma type	Volcanic rock	Chemical composition	Temperature Celsius	Viscosity	Gas content
Mafic or Basaltic	Basalt	45-55% SiO2, high in Fe, Mg, Ca, low in K,Na	1000-1200	Low	Low
Intermediate or Andesitic	Andesite	55-65% SiO2 intermediate in Fe,Mg,Ca,Na,K	800-1000	Intermediate	Intermediate
Felsic or Rhyolitic	Rhyolite	65-75% SiO2 low in Fe,Mg,Ca, high in K, Na	650-800	High	High

Table 1.1: Summary table: Characteristics of magma in physics of volcanoes (*Spera, 2000*).

An important physical property of magmas is the viscosity that controls how fast magma flow in response to a given pressure change, as well as how fast gas bubbles and solids (e.g. crystal rock fragments) move through the magma. A magma with low viscosity (such as basaltic) can form a lava stream when it reaches the surface (like in Kilauea, Hawaii). In contrast andesitic and rhyolitic magmas are sufficiently viscous to restrict movement of bubbles, and gas bubbles become trapped in the magma due to its high viscosity. After expansion gas bubbles can generate depth explosions, frequently some hundred meters to several kilometers beneath the crater. The main parameters of the different magma types is presented in Table 1.1.

According to their physical shape, volcanoes can be divided into two principal types, merely shield and stratovolcanoes. Shield volcanoes resemble a warrior's shield, they have basaltic magma and their eruptions become almost non-explosive and show lava on the surface due to an effusive eruption (e.g. Kilauea, Hawaii and Etna, Italy). Stratovolcanoes are cone-shaped generally with steep sides (30°to 40°slopes), they have andesitic or rhyolitic magmas, and their eruptions are generally explosive.

Similar to the Richter and Mercalli scale intensity of earthquakes, a scale known as Volcanic Explosivity Index (VEI) is used to measure the intensity of volcano eruptions. This scale provides a relative measurement of volcanic eruption between 0 to 8. Zero represents a non explosive eruption and 8 a mega-colossal explosive eruption that can eject over one terameter-cubic of tephra (Newhall and Self, 1982). The Mont Visuvius, Italy (79 CE) eruption was around VEI 5 and the supervolcanic eruption of Yellowstone, USA (64000 years ago) was VEI 8.

Effusive eruptions can be divided into Icelandic and Hawaiian types, both forming shield volcanoes with lava fountain. An intermediate non-explosive eruption type with relatively high viscosity lava is the strombolian's eruption. Explosive eruptions can be vulcanian or plinian due to high viscosity lavas, such as andesitic or rhyolitic respectively. Vulcanian eruptions are characterized by short-lived and violent eruptions with ash columns rose to altitudes of 3-4 km and plinian eruptions are violent catastrophic eruptions with shoots of tephra and pyroclastic flows (super-eruptions), its eruptive column rose several tens of km high. Vulcanian and plinian are differentiated by the height and volume of the plume, and eruptive physics. For example the 2010 sub-plinian eruption of Eyjafjallajökull volcano (Iceland) developeda VEI 4 phases with ash plume rose to altitudes around 11 km causing severe disruption of European air traffic for several days.

Basaltic volcanoes are largely under the sea in mid-ocean ridges. Eruption of basaltic volcanoes on land are usually weakly, and largely produce lava, which rarely threaten life, and the endangered areas are reasonable predictable and they are usually not capable of generating large amounts of ash. At the other end of the scale, rhyolitic volcanoes are certainly the most dangerous than other eruptions and usually highly explosive. Large rhyolitic volcanoes erupt only occasionally, There were a few episodes with major impact that can be cited, such as VEI 8 Taupo (New Zeland) around 1300 CE, VEI 8 Yellowstone (Idaho, USA) 64 Ka years ago, VEI 6 Quilotoa, Ecuador 800 years ago. In fact they would be devastating events on a global scale (Sparks, 2000).

More recently, Huaynaputina volcano, Peru, developed a catastrophic eruption of VEI 6 in 1600 the only major explosive eruption in historic times in the Central Andes, which was remarkable not only for its size, but also for its impact on global climate (Thouret et al., 1999). The eruption lasted

from February 19 to March 6 in 1600, and consisted of a plinian eruption. The eruption completely destroyed the cone edifice which was described as "a low ridge in the center of a sierra". Ash from the Huaynaputina eruption was widespread and still mantles much of the surrounding countryside as far as Arequipa, 80 km away. On a global scale, the following summers were some of the coldest in the last 500 years. Sulfur aerosols erupted from Huaynaputina were pushed in the Earth's atmosphere and reflected sunlight, resulting in a global temperature drop (Adams et al., 2001; De Silva and Zielinsky, 1998).

Mont Pelée (Martinique, France) and Soufrière Hills volcano (Montserrat, Caribbian island) have illustrated that andesitic volcanoes are likely to continue to provide the greatest threat. Another problem with andesitic volcanoes is their tendency for false alarms under common monitoring system. Soufrière Hills eruption occurred on 18 July 1995, took many people by surprise, including those who lived on the island. The major dome collapses and ash fallout blanketed the capital city Plymouth (Montserrat), 6 kilometers away covered the sky almost completely.

One of the most tragic volcanic disasters in the world of the 20th century took place at Mount Pelée stratovolcano, Martinique (France), in May 1902. The eruption killed about 30 thousands people, almost all inhabitants of St Pierre city (except one prisoner in jail), most of them were caused by pyroclastic flows within minutes of the eruption (Nakada, 2000).

To come back in our study, Ramos (1999); Thouret et al. (2001, 2005); Macedo et al. (2009) show that Misti and Ubinas (Peru) stratovolcanoes have produced vulcanian eruptions. Therefore, we detail further below, about the explosive events characterized as Vulcanian.

1.2.2 Vulcanian eruptions

Andesitic volcano activity is often characterized by the source extrusion of viscous magma in a shallow conduit with violent short-lived explosions known as vulcanian eruptions. The short-duration, unsteady nature of vulcanian eruptions clearly differentiate them from plinian eruptions, as well as the height and shape of volcanic plumes. Vulcanian eruption hazards consist of sudden transitions to the explosive regime with ash plumes rising up to 4 to 5 km (Morrissey and Mastin, 2000; De Angelis and Henton, 2011).

In 1907, Mercalli introduced the term vulcanian to describe a type of eruption that took place on the island of Vulcano (Aeolian Islands) around 1888-1890. Lacroix later incorporated the term into the classification of eruption types.

Recent eruptions at Ngauruhoe 1975 (New Zeland), Irazu 1963 (Costa Rica), Sakurajima (Japan) (continuously erupting since 1955), Galeras 1989 (Colombia) volcanoes are examples of the vulcanian eruptive style (Morrissey and Mastin, 2000). More recently, eruption of Ubinas volcano (2006-2009) was mainly noted as vulcanian style (Macedo et al., 2009).

Vulcanian eruptions are generally characterized by violent explosions which are generated by an impulsive source. Often they result from a sudden decompression in a conduit containing pressurized

with vesiculated magma. Typically Vulcanian eruptions last only seconds to minutes and the volume of ejected materials are estimated less than 0.1 km^3 (Morrissey and Mastin, 2000; Self et al., 1979; Sparks, 1997; Druitt et al., 2002). Ballistic blocks commonly associated with Vulcanian eruptions were evidenced of degassed magma crystallized plug residing at the top of the conduit prior to an explosive event which sealed the system and developed high conduit overpressure (Burgisser et al., 2010, 2011)

A generally well accepted model for Vulcanian events has been described for andesitic magmas in strato volcanoes by Self et al. (1979). As magma ascend from magma chambers several kilometers underneath the crater, the confining pressure decreases below the supersaturation level, which provides favorable conditions for volatiles gradually exsolution forming gas bubbles. Bubbles nucleation requires supersaturated melt which occurs when concentration of dissolved volatiles exceeds the equilibrium solubility at a given pressure.

Bubbles grow progressively through the combination of three processes: 1) diffusion of more gas into existing bubbles, 2) decompression and expansion of the gas already in bubbles and 3) coalescence of bubbles (Parfitt and Wilson, 2008). Bubbles growth is linked to several physical parameters: diffusion rate, viscosity and decompression rate. The first step of growth is controlled by diffusion whereas it's controlled by expansion during the ascension of magma within the conduit. Bubble growth in magma decreases the bulk density by adding low density bubbles, and the specific volume of gas is much greater than dissolved gas.

A vulcanian event is supposed to be the result of magma fragmentation that transform magma from a liquid-crystal with dispersed gas bubbles to a gas with dispersed liquid-crystal drops or isolated solid particles. The fragmentation level changes its position in depth within the conduit during the eruptive process by propagating as a fragmentation wavefront (Zobin et al., 2009; Melnik and Sparks, 2002; Alidibirov and Dingwell, 1996).

Burgisser et al. (2010) focused on a series of vulcanian eruptions occurred at Soufrière Hills volcano on Monserrat Island in 1997. In which the analysis of the stratigraphic reconstruction using samples picked up from these Vulcanian episodes, demonstrated a clear relationship between lithology and the confined pressure along the conduit prior the explosion. So that, processing the porosity distribution of volcanic rock samples and crystal traces, provided a knowledge about the depth of the explosion, which is related to the pressure gradient within the conduit. The stratigraphy of the conduit provided a vision of strongly heterogeneous magma column immediately prior to its disruption. So, it is suggested that the fragmentation could not happen in a single coherent pulse but rather as stages process. A heterogeneous amounts of exsolved gas were found in the transition zone that could explain the pulsatory nature of the Vulcanian jets at the beginning of the explosion. The pre-explosive pressure of the deepest magma ejected during an explosion is around 80 MPa.

The source of vulcanian activity at Soufrière Hills volcano (Montserrat) was interpreted as processes of pressurization in the plumbing system, in which each explosion started by the rupture of a plug of dense of degassed magma (Burgisser et al., 2011). Four mechanisms of pressure gradients was thought to drive the explosive activity in Monserrat, due to stratigraphy studies (related to porosity features and crystal composition) revealed density profiles of depth-referenced of the magmatic col-

umn (Burgisser et al., 2010). Such mechanisms were attributed to 1) gas accumulation, 2) conduit elasticity, 3) microlite crystallization and 4) magma flowage. Triggered decompression caused the fragmentation and eruption of the conduit contents down to a maximum depth of about 2.5 and 3.5 km at Soufrière Hill volcano (Burgisser et al., 2011).

Ruiz et al. (2005) studied explosions of Tunguragua volcano (Ecuador), similar to Ubinas volcano (Peru). The study was based on the arrival times of seismic and infrasound measurements. Large differences in arrival times on acoustic and seismic waves observed at Tunguragua, supported a model where explosions occur at different depths inside the shallow part of the conduit. Explosions started with a first pulse exhibited only by seismic wave. After a two phase mixture rises up through the conduit and arrive at the crater floor 1 s later. Subsequently a second pulse is noted on both recordings of infrasound and seismic.

Geophysical measurements have been performed to study this phenomenon for andesitic volcanoes. Iguchi et al. (2008) focused on seismic observations and ground deformation of three andesitic volcanoes (Sakurajima, Japan; Suwanosejima, Japan; Semeru, Indonesia). Thus, a common sequence of phenomena associated with volcanic explosions was proposed and follow five steps (Figure 1.2):

1. Ascent of magma and accumulation of volcanic gas in the conduit below a confining cap, which result in pressure and volume increasing observed as an inflation in the tiltmeters and strainmeters measurements.

2. Release of gas because the gas pressure exceeds the strength of the cap. The resultant minor contraction is detected by deflation tilt and downward displacements.

3. Pressure decrease in the conduit below the cap, which induces sudden out-gassing of water-saturated magma deep in the conduit. The expansion is measured by the upward P-wave first motion of the explosion earthquake.

4. Expansion process that destroys the cap at the top of the conduit (stages 3 and 4 were not distinguishable for the Suwanosejima and Semeru volcanoes).

5. Given the failure of the cap at the top of the conduit, the gas pocket at the top collapses, inducing a contraction ground-deformation source in the shallow part recorded by tiltmeters and strainmeters. Otherwise, ash and gas emission from the conduit is observed as a deflation for the tiltmeters and downwards for the strainmeters.

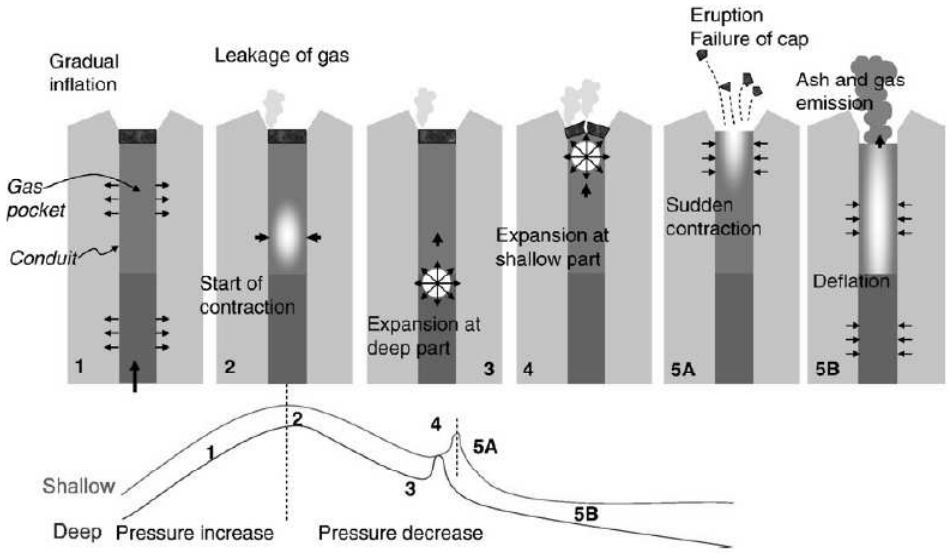


Figure 1.2: Process of explosive eruption base on observations at the Sakurajima, Semeru, and Suwanosejima volcanoes (*Iguchi et al, 2008*). 1) Pressure and volume increase are observed by inflation-related tilt/strain and upward displacement. 2) Release of gas as the gas pressure exceeds the strength of the cap. 3) Pressure decrease in the conduit starting from the gas pocket, inducing sudden outgassing, in this stage starts the explosion. 4) Expansion process destroying the cap at the top of the conduit. 5A) Failure of the cap at the top of the conduit. 5B) Ash and gas emission from the conduit.

1.2.3 Instrumentation for seismic volcano monitoring

Volcanic monitoring involves geophysical and geochemical instrumentations that tries to detect signals associated to magma transport processes (Sparks, 2003). This section discusses the instruments used in seismic monitoring allowing to study ground vibrations caused by seismic waves from volcanic unrest. Volcanic earthquakes are commonly categorized by frequency content to distinguish possible physical sources occurred in depths less than 15 km beneath the volcano. Tectonic earthquakes usually occur at depths from 15 km to over 600 km, while seismic sources at volcanoes occur at shallower depths between hundreds of meters to tens of kilometers. Volcanic seismic events also differ in their pattern of occurrence, mainly swarms that require continuous monitoring by seismic instrumentation (Lahr et al., 1994; Chouet, 2003; Neuberg, 1998; McNutt, 2005).

High-resolution seismic instrumentation has been developed in the past two decades to detect small seismic waves produced by magma processes. Since the monitoring is based on broadband seismometers, correlations could be established between the movements of magma and eruption by using seismic analysis (Sparks, 2003; Chouet, 2003). Most seismically monitored volcanic eruptions showed that they have been preceded by a phase of increased small earthquakes activity beneath the volcano, while the eruption phase is accompanied and followed by varying levels of seismicity.

Current high-resolution data-acquisition systems are also designed to insure the broadband seismometer signal. These digitizer are based on 24-bit delta-sigma ADC (analog to digital converter) to produce digital seismogram. Due to this new resolution, instruments can now be designed to record over a wide frequency range. In addition, it is able to record large volumes of data, recorded at high sample rates as 100 sps, for continuous mode, autonomous unattended long-term operation. Two main issues are addressed below:

1. The current instrumentation of seismic instrumentation for volcano monitoring.
2. Applications with the modern instrumentation for seismic volcano monitoring including new broadband three-component (3C) seismometer for sensor array models.

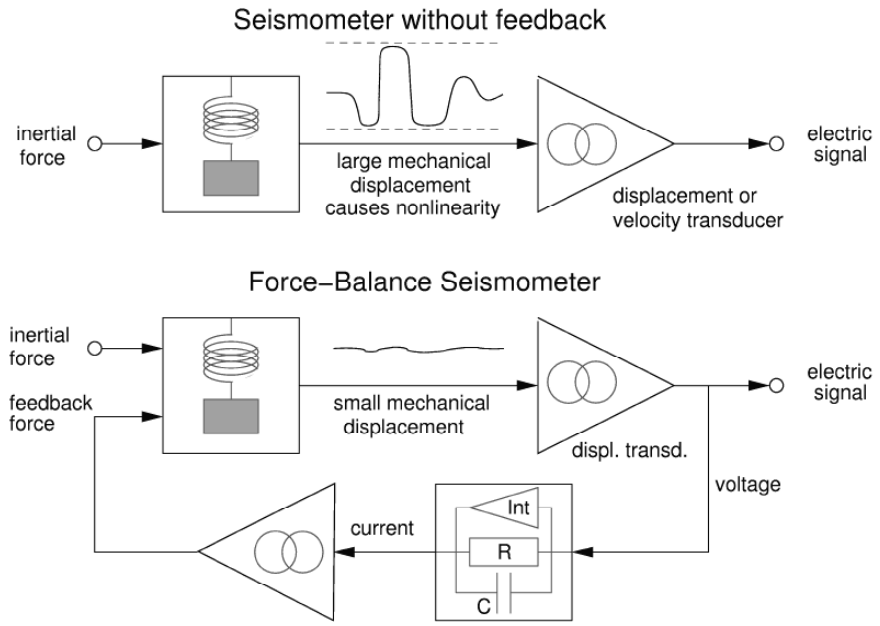


Figure 1.3: Block diagrams of conventional (short-period) and feedback seismometers (broadband). Ideally, in the feedback configuration, the mechanical suspension and the displacement transducer "don't see" the full amplitude of the ground motion, which is present only in the feedback path.

Classical seismometers

The most basic seismic transducer is the short-period seismometer, which is an inertial seismometer basically responding to ground acceleration, although the electric output signal may represent ground velocity or ground displacement over a certain bandwidth. A conventional inertial seismometer performs two subsequent conversions: ground acceleration is converted into a relative displacement

between the seismic mass and the frame; then this displacement variation is converted into an electric signal. Both conversions suffer from nonlinearity and clipping, the first one is due to imperfections of the spring and the hinges, the second for geometrical and electronic reasons. The reduction of amplitudes by making the spring stiffer is not a solution, because this destroys the ability to resolve small accelerations at low frequencies. The upper part in Figure 1.3 illustrates the concept of a conventional inertial seismometer. Seismometers supported with this technology are the *Mark-Products* L4, L22 (geophone), Kinemetrics SS-1 (ranger). Figure 1.4 shows a classical configuration of three on single-component (1C) orthogonally oriented seismometers (Kinemetrics SS-1) to yield 3C signals, such as vertical, radial and transverse components.



Figure 1.4: Short period single component seismometers designed for a 3C configuration, (one vertical Z and two horizontals X,Y).

Broadband 3C seismometers

All modern seismic broadband sensors employ a negative force feedback to keep the motion of the mass small (as illustrated in the lower half in figure 1.3). This helps greatly to avoid problems with mechanical imperfections of the sensor. The feedback loop sends a current through the force transducer (coil inductance) that keeps the mass centered with respect to the frame. The mass then follows the same acceleration as the ground, and the feedback current should be proportional to ground acceleration. Such circuit is also called a *force-balance* system because the feedback force is supposed to balance the inertial force at all times (Wielandt and Streckeisen, 1982). New 3C seismometers using this technology are for example the Streckeisen STS-2, Guralp CMG-3T, CMG-40T.

The Streckeisen STS-2 (Figure 1.5) 3C broadband seismometer is the most sensitive portable seismometer currently available on the market. It is used for permanent seismic station installation recording continuous data. The principle of the STS-2 consists to respond a single degree of freedom oscillator with free period of 120 seconds (0.008 hz), with differential feedback, and so has



Figure 1.5: Integrated 3C broadband portable seismometer. Left side, STS-2 physically installed on a level surface, the instrument shows a rod oriented to the transverse direction, typically towards east geographic. Right side, a view of the internal part, where some electronic cards and a cylindrical package containing within three orthogonally oriented identical sensors.

an output proportional to ground velocity from period of 120 s (0.008 hz) to high frequencies up to 50 Hz (period 0.02 s). Figure 1.5 shows the STS-2 seismometer containing three identical sensors with electronics and power circuits mounted in a cylindrical package (23 cm in diameter and 26cm high). The broadband seismometers usually have a preamplifier with low impedance and differential output to better control the electronic noise, known as common-mode rejection ratio (CMRR). The dynamic range of these instruments are in about 145 dB, and is defined as the ratio of the largest and the smallest voltage output resolvable by the instrument. For broadband seismometers it is usually 140 dB . Typical specifications of seismometers and digitizers frequently used in volcano monitoring are shown in Table 1.2. Each broadband seismometer has an internal calibration module in order that sensor masses can be excited by an external function signals and frequency responses (module and phase) can be tested. These instruments are generally delivered (from manufacturers) with a detailed calibration sheet showing its serial number, measured frequency response, sensor DC calibration levels, and the transfer function in poles/zeros notation. In general calibration of seismometers are often performed before an experiment since their dynamic parameters may vary during the transport and/or decay by the time of use. A practical way for calibration of seismometers is a “test table” device designed by Prof. Wielandt, which can be used to evaluate the frequency response and sensitivity of seismometers (Wielandt, 2002).

Maker	Type Seismometer	Freq-band Hz	Sensitivity volt/(m/s)	Digitizer
Streckeisen	STS-2	0.008-50	1500	Quanterra
Guralp	CMG-3T	0.008-50	1500	Reftek 130
Guralp	CMG-40T	0.033-50	800	Reftek 130
Nanometrics	Trilium 240	0.004-35	1200	Taurus
Lennarz	LE-3D/20s	0.05-50	1000	Reftek 130
Guralp	6TD	0.03-50	1200	Guralp-CD24

Table 1.2: Specifications of 3C broadband seismometers and high resolution 24-bit digitizers used frequently in seismic volcano monitoring.

1.2.4 Seismic signal processing in volcano monitoring

This section reviews some processing techniques that have led to improved seismo-volcano knowledge that resulted in a number of clear successes. As we see, a key development over the past two decades has been the design of high-resolution instrumentation such as broadband 3C seismometers and associated acquisition devices (Chouet, 2003; McNutt, 2005). Four main tasks are considered to highlight the signal processing during a seismic data acquisition: 1) acquisition, 2) storage and distribution of continuous data, 3) real-time processing and 4) reporting results. We will discuss on in the following parts.

Seismic monitoring of volcanoes

In the framework of understanding the physics of volcanoes and developing early warning system, some international institutions and projects established general protocols for volcano monitoring, e.g. IASPEI/IAVCEI manual (http://www.iavcei.org/), UNDERVOLC project, etc. In order to detect the possible unrest of a dormant volcano, one short-period seismic station with telemetry and continuous recording may be sufficient; however, at least two station are requiered to computed the cross-correlation for distinguishing between the signal produced by volcanic and non-volcanic phenomena. When an increase of the seismic activity of a volcano is detected, it is recommended to install a basic network including at least four short-period stations, preferably with broadband three components seismometers. Part of the stations should be naturally installed close to the crater (Information taken from IASPEI/IAVCEI manual).

At the time of the onset of volcanic unrest, seismic signals are taken to be indicative of magma movement but sometimes these have low signal to noise ratio (SNR). These signals are identified in a wide range of frequencies between 0.2 to 15 Hz (Chouet and Matoza, 2013; Wassermann, 1997). To create digital seismograms require another instrument known as digitizer (used for transforming the analog signal from seismic sensors into digital data streams of time series). In order to support seismometers with high dynamic range (seven orders of magnitude), a 24-bit Delta-Sigma analog-to-digital converter are required. Additionally, seismic measurements require a fairly accurate time base

to be compared with others signals, thus, it includes an accurate time stamp for each sample based on the global positioning system (GPS).

Storage and distribution of data streams generated by seismic networks are usually formatted into data packets, to keep sufficient information in the header and data fields, such as MINISEED, GCF (Guralp) and Reftek (PASSCAL) which are based on lossless data compression algorithms. Seismic instrumentation usually supports the remote exchange of data using software based on standard communication protocols. These have been developed to provide real-time data acquisition from network stations. Such protocols provides an ordered, error-free, packet-oriented transport on top of User Datagram Protocol (UDP). It may transmit packets without waiting for acknowledgment from the peer thus making efficient use of available bandwidth either radio telemetry, internet or satellite (Friberg et al., 2010).

In the communication step, radio telemetry is widely used as a means for relaying seismic data from active volcanoes to observatories. Most existing telemetry are ground based and are constrained by the topographic conditions (free line-of-sight). In order to extend the range of the telemetry, transfer stations can be installed. For instance, the radio telemetry for seismic stations deployed around Ubinas volcano (Peru) uses a repeater (transfer) station to avoid an obstacle in 40 km path. Another constraint of radio communication is the operating distance with clear line of sight up to 50 km in terms of low power consumption. Seismic real time data processing plays an important role in volcanic hazard warnings, as authorities and citizens must have enough time to take order and the appropriate precautionary measures. Therefore the observatory in charge to provide scientific information, must design the appropriate seismic network. This section briefly describes how real-time data processing is successfully carried out at volcano observatories such as IGP.

Most volcano eruptions have been an increase in earthquake activity (McNutt, 2005) and the first sign of change in volcanic unrest is seen by a clear variation in the local seismicity pattern. There are 3 techniques to observe these phenomenon.

- The first known as RSAM (real time seismic amplitude measurement developed by Endo and Murray (1991)) consists of calculating the signal amplitude continuously.

- The second technique called seismic spectral amplitude measurement (SSAM) that was developed by Stephens et al. (1994) consists in calculating time-domain and frequency-domain amplitudes in real time and producing time-series plots which must be easily to interpreted.

- A third important real time processing techniques using the STA/LTA algorithm to automatically detect events. It allows to detect different types of waveforms associated to volcanic unrest. This algorithm continuously calculates the mean values of the absolute amplitude of a seismic signal in two consecutive moving-time windows: a short-time window (STA) (sensitive to seismic event) and a the long-time window (LTA) (providing information about the temporal amplitude of seismic noise). When the ratio of both exceeds a pre-set value, an event is declared arriving (Trnkoczy, 1998; Withers et al., 1998).

After seismic events detection a difficult task is to locate their seismic sources in real time. This is still a challenge due to the complexity of the waveforms and is the subject of this thesis.

To convince readers, a real case scenario is presented here to show how important is the signal processing in real time. It is about the prediction of the eruption of Merapi (Indonesia) volcano in October-November 2010. Continuous monitoring of the seismic signal amplitudes showed an abrupt change detected by RSAM and STA/LTA, a month before the biggest eruption of Merapi. Then, other parameters were verified as well, e.g. deformation (geodetic), gas emission (chemical), and so on. Based on all information the evacuation of about tens of thousands peoples took place one-day before the catastrophic eruption that affected the entire infrastructure of many villages and cities around the volcano. The RSAM curve of this event is shown in Figure 1.6 (figure from Surono et al. (2012)).

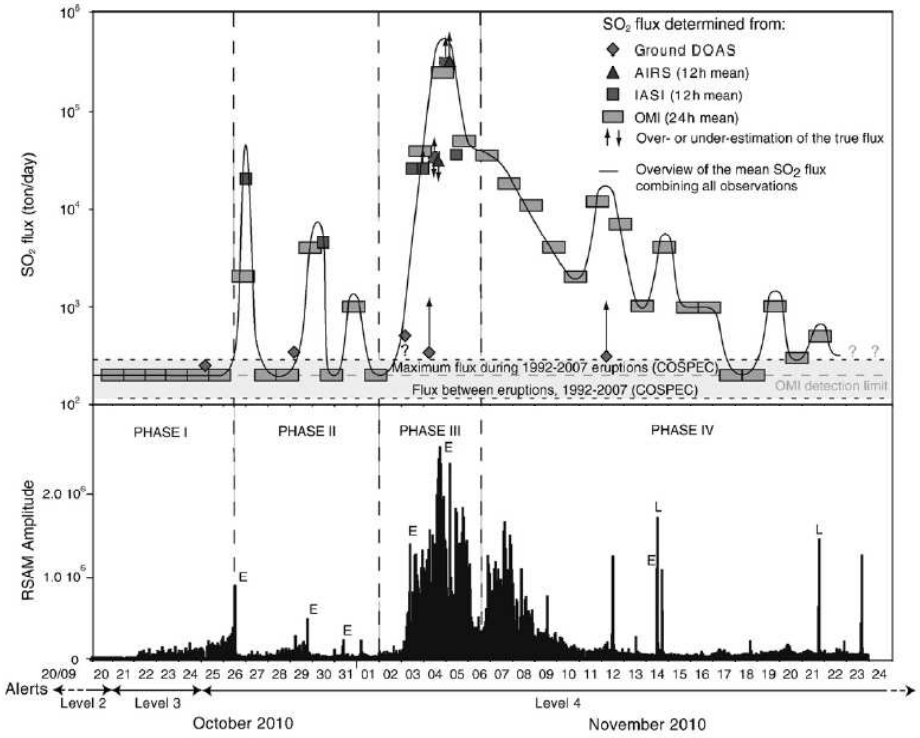


Figure 1.6: From Surono et al 2012, comparison between SO2 fluxes and RSAM data from seismic station near Merapi crater. Top, overview of SO2 degassing during the 2010 Merapi volcano eruption (UTC time). SO2 fluxes were determined from ground-based scanning DOAS measurements (mean fluxes measured over hour-long intervals) and satellite images, from IR IASI and AIRS sensors (mean fluxes calculated for 12h intervals) and the UV OMI sensor (mean fluxes calculated for 24h intervals). Bottom, RSAM computed for the Plawangan station (6 km from the summit). A clear correspondence between RSAM and SO2 flux is demonstrated, supporting our identification of four distinct phases to the eruption (indicated by Phases I to IV). E stands for explosion; L for Lahar.

Reporting scientific results are one of the most difficult tasks facing those charged with monitoring

a volcano. This task needs to combine results in order to issue an appropriate warning. One of the biggest concerns for methods to locate earthquakes properly is the knowledge of the propagation structure. Seismologists usually perform source localization by using velocity models based on layers thickness. Various techniques have been developed to determine velocity structures in the near-surface with resolutions of 0.5 km in the best case, such as, seismic tomography with the inversion of P- and S-wave arrival time data from teleseismic earthquakes (Lees, 2007). Others approaches are the spatial autocorrelation (SPAC) method, developed by Aki (1957), which is intensively used in volcano seismology (Métaxian et al., 1997; Chouet, 2003; Mora et al., 2006). An other approach to study the shallow internal structure of volcano is the frequency wave-number *f-k* method. This separates signals and computes the dispersion curve, resulting in a 1D velocity structure (Lacoss et al., 1969). Recently, Wathelet et al. (2008) has developed the *Geopsy* software package used by Perrier et al. (2012), that contains SPAC, F-K and dispersion curve processing with which an image of the shallow internal structure of volcanoes can be performed.

Deconvolution - Instrument correction

The instrument correction can be considered as the most fundamental processing step in seismology to convert the digital seismogram (raw data) to units of physical measurements as ground motion. Applying instrument corrections allows analysis of the seismogram in a proper physical context. This operation also allows to correct measurements, when instruments with different dynamic responses have in the seismic network.

The digital seismic recordings can be represented as the convolution of three terms: the source time function *x(t)*, the function of the propagation through the structures *g(t)* and the instrument response *h(t)*, as shown in Figure 1.7. The instrument response can be represented by the transfer function or impulse response (linked to the sensitivity and bandwidth of the instrumentation). Transfer function can be described by a ratio of two frequency-dependent complex polynomials in the Laplace transform domain (between the output as counts and input as ground motion). The roots of the numerator and denominator polynomials represent zeros and poles of the transfer function respectively (see Equation (1.1)).

$$H(s) = K\frac{(s-z_1)(s-z_2)...(s-z_{m-1})(s-z_m)}{(s-p_1)(s-p_2)...(s-p_{n-1})(s-p_n)} \tag{1.1}$$

where, s is the frequency variable of the Laplace transformation, m and n are the number of zeros and poles respectively and K is the sensitivity. Analyzing the block diagram (Figure 1.7), the seismogram spectrum represented with *U(f)* can be represented by Equation (1.2).

$$U(f) = X(f) \cdot G(f) \cdot H(f) \tag{1.2}$$

The ground motion is conveniently recovered by the deconvolution process represented in Equation (1.3) which performs instrument correction by manipulating seismogram spectra.

$$X(f) \cdot G(f) = \frac{U(f)}{H(f)} \tag{1.3}$$

The behavior of modern seismometers can be considered as a linear time invariant (LTI), restricted

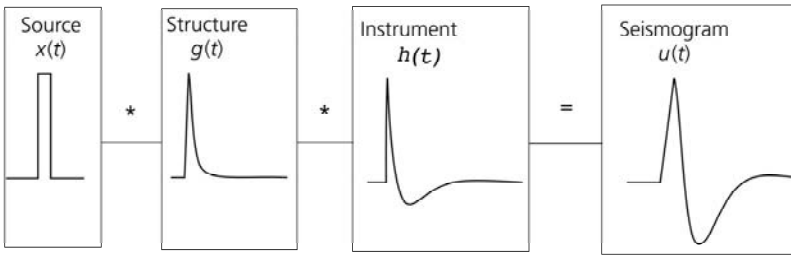


Figure 1.7: Flow chart of seismogram trace u(t) generation by the source x(t)

to its linear range. Given zeros and poles for a specific seismometer, the transfer function can be represented as output/input Laplace transforms. Considering signals are causal, then the transfer functions of velocity $H_{vel}(iw)$ (derivative of the displacement) and displacement $H_{disp}(iw)$ units can be written as Equation (1.4) in terms of Fourier transforms, where $i = \sqrt{-1}$ and $w = 2\pi f$.

$$H_{vel}(iw) = \frac{Output(iw)}{Input_{vel}(iw)} \qquad or \qquad H_{disp}(iw) = iwH_{vel}(iw) \tag{1.4}$$

The transform function of the instrument can be represented by Equation (1.5) as a general linear system (Aki and Richards, 2002), where, SEN is the sensitivity of the instrument, z_i, p_i are the complex zeros and poles of $H(s)$, $s = jw$ is the Laplace transform variable ($w = 2\pi f$ and $j = \sqrt{-1}$) and nz , np are the number of zeros and poles respectively. NF and BW are constants, namely the normalizing factor (NF) and the bit-weight (BW), which is the analog to digital conversion factor of the digitizer. The amplitude of digital seismograms is usually in units of "count" (1 bit = 1 count).

Field experiments at Ubinas in 2009 and Misti 2011 used the state of the art of broad-band of 3C seismometers based on Guralp 6TD. We noted that poles and zeros values in datasheet parameters of Guralp 6TD are in Hz units rather than the more common radians/sec. The transfer function for digital seismometer are usually given in unit of $ms^{-1}/count$ (for ground velocity measurements), to preserve this units in the transfer function, the factor $(2\pi)^{np-nz}$ is considered in Equation (1.5).

$$H(s) = \left(\frac{SEN \times NF \times (2\pi)^{np-nz}}{BW}\right) \frac{\prod_{i=1}^{i=nz}(s-z_i)}{\prod_{i=1}^{i=np}(s-p_i)} \tag{1.5}$$

Table 1.3 shows parameters for a Guralp 6TD, equipped with a Wi-Fi to continuously communicate seismic data, which is widely used in volcanology. Figure 1.8 depicts the amplitude and phase frequency responses of this Guralp 6TD seismometer with flat amplitude response between 0.03 and 50 Hz, derived from parameters listed in Table 1.3. In practice the instrument correction can be performed by standard seismic softwares, such as SAC (Seismic Analysis Code), RDSEED and Matlab code (see Appendix), all based on a frequency domain deconvolution by spectral division. The following example demonstrates how to use SAC to deconvolve the instrument response from seismic

Velocity output Volts/ m/s (SEN)	 2382
Zeros in Hz (wz=2)	0 0
Poles in Hz (np=6)	-0.02356+j0.02356 -0.02356-j0.02356 -62.3816+j135.392 -62.3816-j135.392 -350 -75
Normalizing Factor (NF)	585E+06
Bit-weight (BW) Volts/Count	0.958E-06

Table 1.3: Calibration sheet for the vertical component of a Guralp 6TD 3C broadband seismometer.

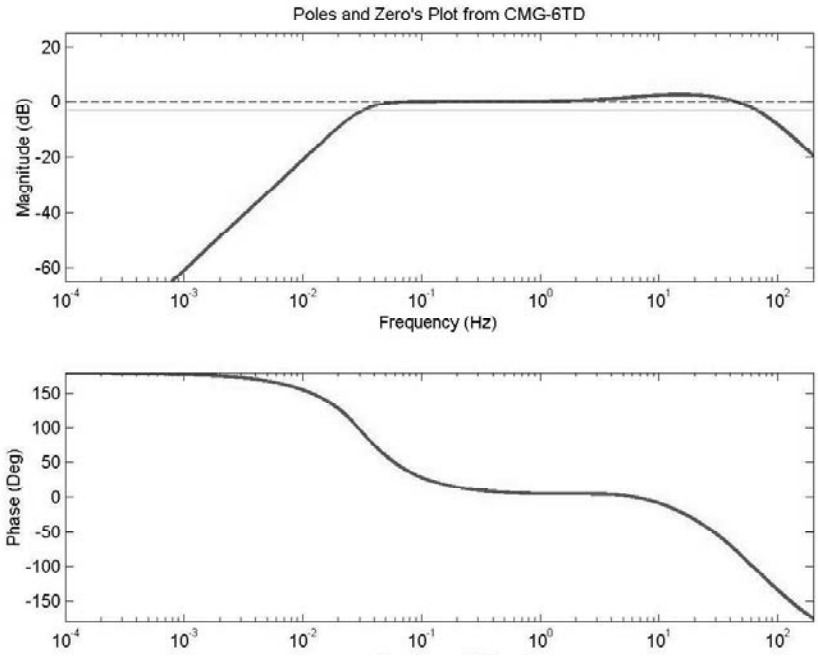


Figure 1.8: The amplitude (top) and phase (bottom) response functions for a Guralp 6TD seismometer

data recorded by a 6TD seismometer during a field experiment at Ubinas volcano in 2009. The SAC program needs a pole-zero file with a specific format as shown in Table 1.4. Note that poles and zeros in Table 1.3 are multiply by 2π.

ZEROS 2	
0.0	0.0
0.0	0.0
POLES 6	
-0.148031846	0.148031846
-0.148031846	-0.148031846
-391.95515	850.69302495
-391.95515	-850.69302495
-2199.1148571	0.0
-471.23889795	0.0
CONSTANT	2.267e+21

Table 1.4: Pole and zero file (PZFILE.PZ) for removing the instrument by using SAC program

The waveform in top of Figure 1.9 corresponds to an earthquake filtered from 0.1 Hz to 2.2 Hz without correction (amplitude in counts). To remove the instrument response, a typical way, it is useful a command line into SAC software as: "TRANSFER FROM POLEZERO SUBTYPE PZFILE.PZ TO NONE FREQLIM 0.03 0.1 2.2 2.5". The waveform in the middle of Figure 1.9 is the corrected seismic signal (ground velocity) and bottom in Figure 1.9 shows the ground displacement seismogram.

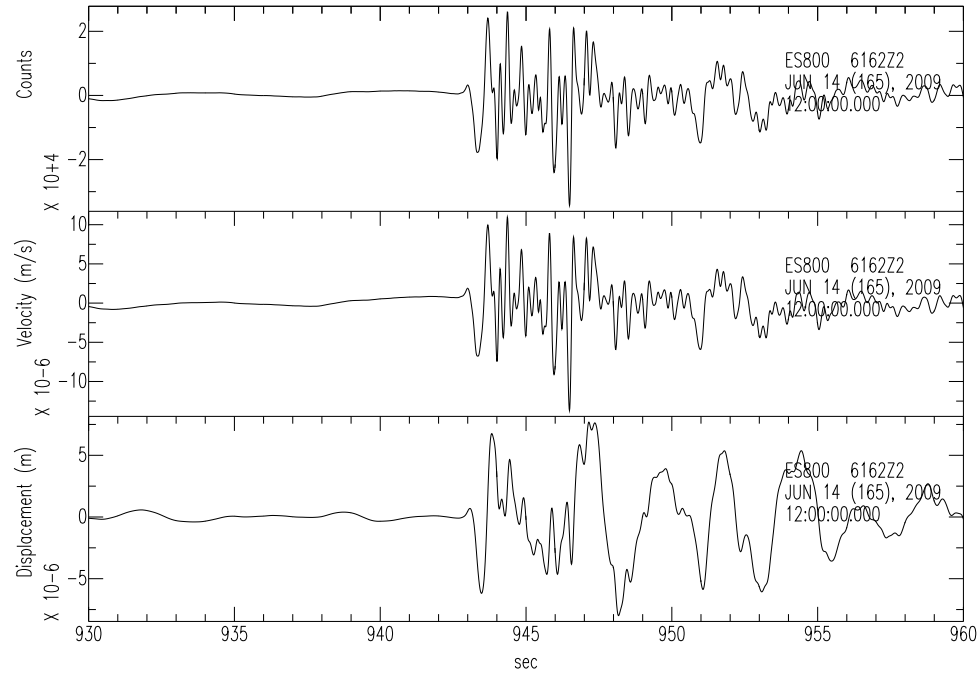


Figure 1.9: Example of instrument correction for a volcanic earthquake (explosive event) recorded at Ubinas volcano in 2009. Top: seismic signal filtered into the band 0.1 Hz to 2.2 Hz without instrument correction. Middle: Ground motion seismogram (velocity). Bottom: Ground displacement seismogram

1.2.5 New methodologies for seismo-volcano monitoring

The characteristic of ground vibrations recorded by seismometers from the volcanic unrest is quite different to those produced by subduction earthquakes or active faults. The source mechanisms of seismo-volcanic signals are induced by the magma transport rising up to the surface. Volcano seismology focus on the knowledge of seismic swarms and patterns which provide information from the magmatic activity (sources). Therefore, new techniques are required. The bibliography shows methods of source localization particularly for LP quakes and tremors events. For instance, Battaglia and Aki (2003) developed the methodology of locating LP events using seismic amplitudes instead of using arrival times. To achieve this, it was considered that the decrease of the amplitude as a function of the distance to the source which was approximated by the decay, either of surface or of body waves in a homogeneous medium. For this method, the seismic network must be sufficiently dense and well-distributed to ensure good source coverage. Almost in the same way, Kumagai et al. (2009) used amplitudes of seismic waves field, recorded by five broadband seismometers at Cotopaxi volcano (Ecuador), to track the source of lahars. Wave amplitudes were fit to a model generated from point sources positioned over the gridded surface of the volcano. The signals recorded at individual stations are corrected by site amplification factor (site effect) independently estimated from coda waves from tectonic earthquakes. The position of time windows applied to the observed signal were

corrected for the travel times of individual source and receiver pair. On the other hand, De Barros et al. (2009) used a cross-correlation technique to locate LP earthquakes at Mount Etna, with a dense seismic network around the volcano. It consisted of minimizing the mean square error of theoretical and observed time delays in order to locate the hypothetical source into a gridded volcano structure. An other application, a full waveform inversion has been carried out to not only constrain the source mechanism but to locate the LP events (Ohminato et al., 1998; Chouet, 2003; Chouet et al., 2005; Lokmer et al., 2007). More recently O'Brien et al. (2011) used a time reverse method to locate two families of LP events on Mt Etna.

The development of new portable seismic instrumentation and monitoring techniques has improved our knowledge of volcanoes and eruption forecasting, nevertheless, due to a lack of expertise and budget for instrument deployments only few volcanoes are currently monitored properly (Wassermann, 2012). A number of different physical approaches needs to be used to monitor changes in the physical processes that may indicate increased volcanic activity, such as seismicity, ground deformation and gases measurements. The experience of volcano monitoring suggests (McNutt, 2000), first, seismic measurements must be continuously done (before, during and after the eruption). So recording several years of background seismicity is important to establish a base line for evaluation of possible precursor. One of the modern approaches for volcano seismology are based on deploying seismic arrays instead of single sensors at active volcanic areas. The main advantage of such antennas and the application of array techniques is the improvement in evaluating: the radiated wavefield properties, velocity structure and the source location (Chouet and Matoza, 2013; Wassermann, 2012). Most estimations of source localization used in volcanology are based on the cross-correlation techniques and used for their ability to estimate the slowness vector. They are usually based on the assumption of a wave plane according the long distance between sensors and sources.

Small-aperture seismic arrays also known as seismic antennas, composed of single vertical component seismometers have been used intensively in volcano-seismology this last decade. Waveforms of LP earthquakes and tremor events are characterized by emergent onset. Traditionally earthquake hypocentre are determined based on the minimization of travel-time residuals determined from phases picks. This procedure is reliable for events that are characterized by clear and sharp phases that were recorded by a well-distributed geometrically station networks. Nevertheless, it is not well suited for events which are characterized by emergent onset or by absence of clear pulses (Rost and Thomas, 2002; Chouet, 2003). The relative time-delays observed at the array stations yield the direction to the source and the apparent velocity of the wave-field. La Rocca et al. (2008) used multiple arrays deployed in the far-field of a volcano crater to demonstrate that arrays of one-component seismometers can be used to locate seismic sources. The optimal design of a seismic antenna is function of seismic wavelengths of interest which are reflected in the geometry of the antenna as inter-sensor distances, number of elements, in order to ensure coherent signals are spatially sampled. The measurements sites selection are always a compromise between noise considerations, accessibility and target distance. The array must be installed at the distance of the source, almost five or more times the array aperture away from the source area in order to consider plane wave hypothesis. Each sensor should be set in a borehole of one or one and a half meters deep, in a soil with similar characteristics. If any sensor in the array is set in a different rock different than others, the array data could lose coherence

due to site effect. Boreholes provide a low noise level, temperature insulation and protection to the instrument, according the IASPEI manual (http://www.iaspei.org). In all applications of sensor arrays, wave fields are sampled both in space and in time and the propagation medium is considered as homogeneous by the sensor array.

Seismic wave propagation

Let's go to give some starting element for sensor arrays analysis. The propagation of a plane wave $s(\overrightarrow{r},t)$ in a homogeneous elastic medium is described by the solution of the wave equation (1.6) as a function of both time and space.

$$\frac{1}{v^2}\cdot\frac{\partial^2 s(\overrightarrow{r},t)}{\partial t^2} = \triangle s(\overrightarrow{r},t) \tag{1.6}$$

where $\overrightarrow{r} = (x,y,z)^T$ indicate the coordinates of a point in three-dimensional space (the symbol $(.)^T$ denotes transpose), t is time, v the wavefront velocity and $\triangle = \frac{\partial^2}{\partial x^2} + \frac{\partial^2}{\partial y^2} + \frac{\partial^2}{\partial z^2}$ the Laplace operator. The physics of wave propagation will now explained in Figure 1.10 by showing the oscillations of a harmonic wave measured by seismometers located along the x-direction, with its parameters. The solution of equation (1.6) is usually assumed to be a complex exponential and it can be written using vector notation and inner product, see equation (1.7). Note that S is the amplitude of the wavelet source, which is constant in a homogeneous medium.

$$s(\overrightarrow{r},t) = S\cdot e^{i2\pi(f_0\cdot t - \overrightarrow{k}\cdot\overrightarrow{r})} = S\cdot e^{i\cdot 2\pi\cdot f_0\cdot(t-\overrightarrow{u}(\phi)\cdot\overrightarrow{r})} \tag{1.7}$$

where $\overrightarrow{k} = (k_x,k_y,k_z)$ is the wavenumber vector, f_0 the frequency of the wavefront and $\overrightarrow{u}(\phi)$ is the slowness vector driven by $\frac{\overrightarrow{k}}{f_0} = \overrightarrow{u}(\phi)$, where ϕ is the incidence angle. The slowness vector $\overrightarrow{u}(\phi)$ is perpendicular to the wavefront with a magnitude inverse to the velocity, $|\overrightarrow{u}| = \frac{1}{v}$.

Importance of coherent data

Seismic waves propagating from the source to receivers are certainly influenced by the medium (site effect). The amplitude decay itself is also a strong function of the heterogeneity. Seismologists propose the coherence (*Coh(f)*) as a measure of the degree of relationship between two seismic signals. It is a function in frequency domain given by Equation 1.8.

$$Coh(f) = \frac{\gamma_{xy}}{\sqrt{\gamma_{xx}\cdot\gamma_{yy}}} \tag{1.8}$$

where γ_{xy} is the cross-spectral density between traces x and y, meanwhile γ_{xx} and γ_{yy} are autospectral density of x and y respectively. In seismology, the signal coherence of wave field recorded by a seismic array can be degraded with increased inter-sensor distance. High coherence $Coh(f) > 0.8$ indicates

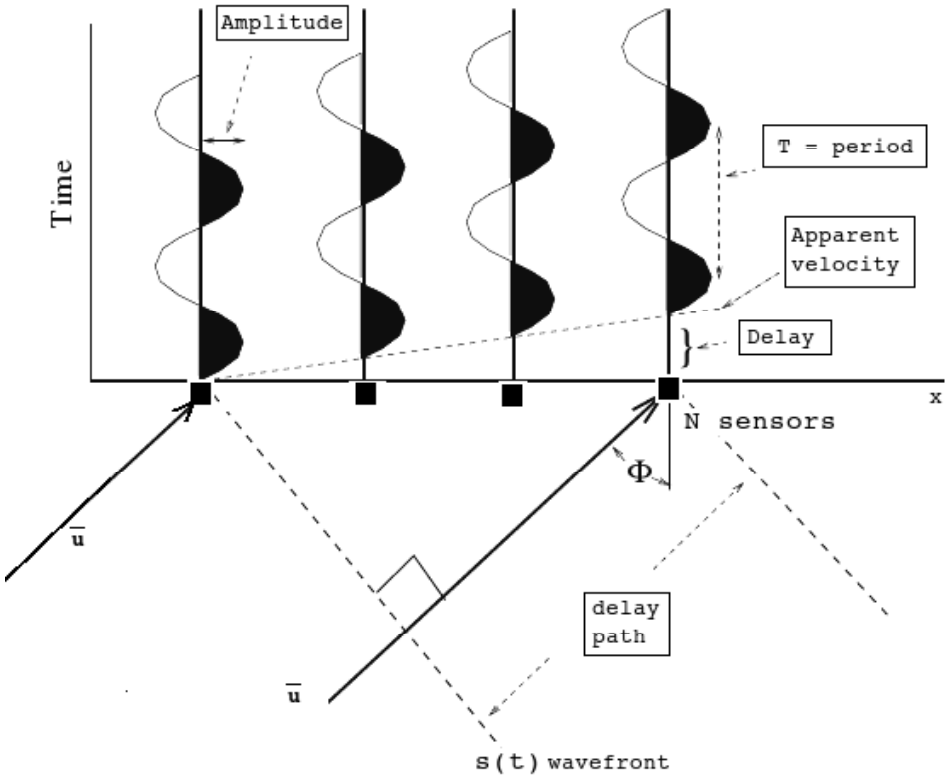


Figure 1.10: A wave plane s(t) impinging on the vertical plane and crossing the array at an angle of incidence ϕ. Black squares along x-axis correspond to seismometers. Signals with period T above sensors are with offset according the apparent velocity and time-delays to the slope along of the x-direction

that the wave field received by the array is undergoing negligible interference or distortion. The inter-sensor coherence of a seismic wave field is frequency dependent and the cross-correlation estimation have to be analyzed in different frequency bands. In a scenario of seismic array, wave-field features that are coherent across the array are identified through a measure of similarity (semblance) (Mari et al., 1997). Calculations of the coherence between the different elements of a seismic array limits the optimal bandwidth for array processing. At progressively higher frequencies the coherency becomes increasingly chaotic due to ground instability. Small aperture seismic array provide significant coherence at higher frequencies as the inter-sensors distance are closer, but at the widest inter-sensors spacing, coherence falls off for low frequency signals. Figure 1.11 shows seismic signals corresponding to the same time window recorded by a seismic antenna with an inter-sensor distance around 50 m deployed at Ubinas volcano in 2009. The signals with high coherency correspond to the band of frequencies between 1 and 4 Hz (left side in Figure 1.11). In contrast, on the right side of Figure 1.11, the same wave field filtered between 7 and 12 Hz showed low coherence affected by scattering. Stations in an array should be spaced close enough to sample a wavefield several times in a wavelength, often requiring a spacing of about between 50 m to 100 m. A more elaborate discussion of seismic

source localization of active volcanoes can be found in Chapter 2.

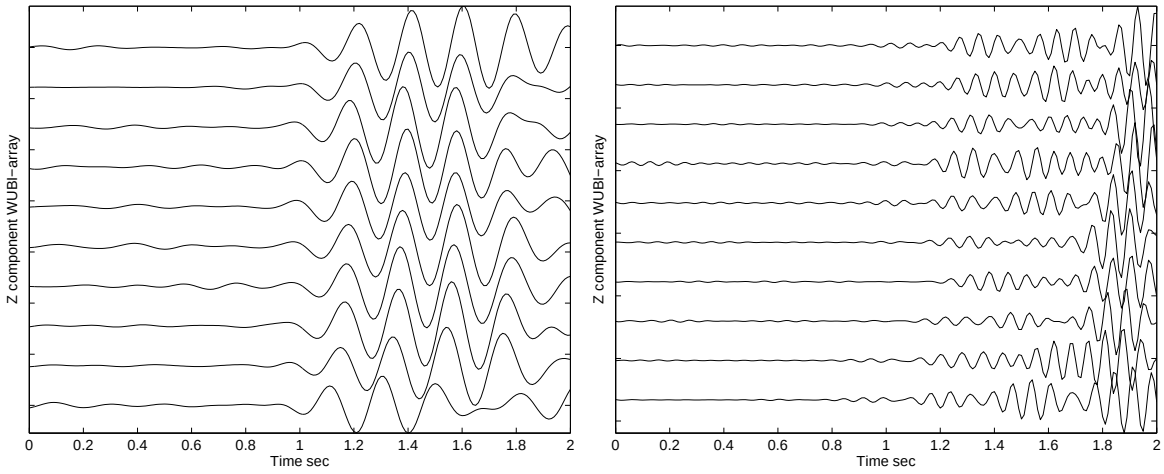


Figure 1.11: Seismic signals recorded at Ubinas volcano. Left: low frequency content signal recorded by the vertical component. Right: high frequency content signal recorded by the vertical component.

1.3 Ubinas and Misti volcanoes

This study focuses on Ubinas and Misti volcanoes in which our field seismic experiments were carried out. The Andes mountain chain extends 9000 km along the western edge of the South American region, see left side in Figure 1.12. The second highest (at an altitude nearly 7000 m) orogenic belts are located at the convergence between South America and Nazca plates (Ramos, 1999). Volcanism in this area has present together Paleozoic and Mesozoic. Four segments are associated with active stratovolcano edifices due to steeply (25-30 degrees) dipping subduction, namely the Northern (NVZ), Central (CVZ), Southern (SVZ) and Austral (AVZ) Volcanic Zones (De Silva and Francis, 1991), see left side in Figure 1.12. Stratigraphic studies have identified most of the volcanoes along the Andes to be of andesitic type (De Silva and Francis, 1991). These stratovolcanoes are usually located on continental crust above a subduction zones. The magma feeding the volcanoes of the Andes Mountains, including Misti and Ubinas, is associated with ongoing subduction of the Nazca Plate beneath the South American Plate. Several major cities in the Andean volcanic arc have grown up on the flanks of active volcanoes such as Misti (Peru), Pichincha (Ecuador), Galeras, Nevado del Ruiz (Colombia) and the famous Popocatepetl (Mexico). Some of them are eye watched as they can be dangerous. For example the eruption of Nevado del Ruiz in 1985 shows a catastrophic scenario in action, a small eruption produced an enormous lahar that killed 25,000 lives (Voight, 1990).

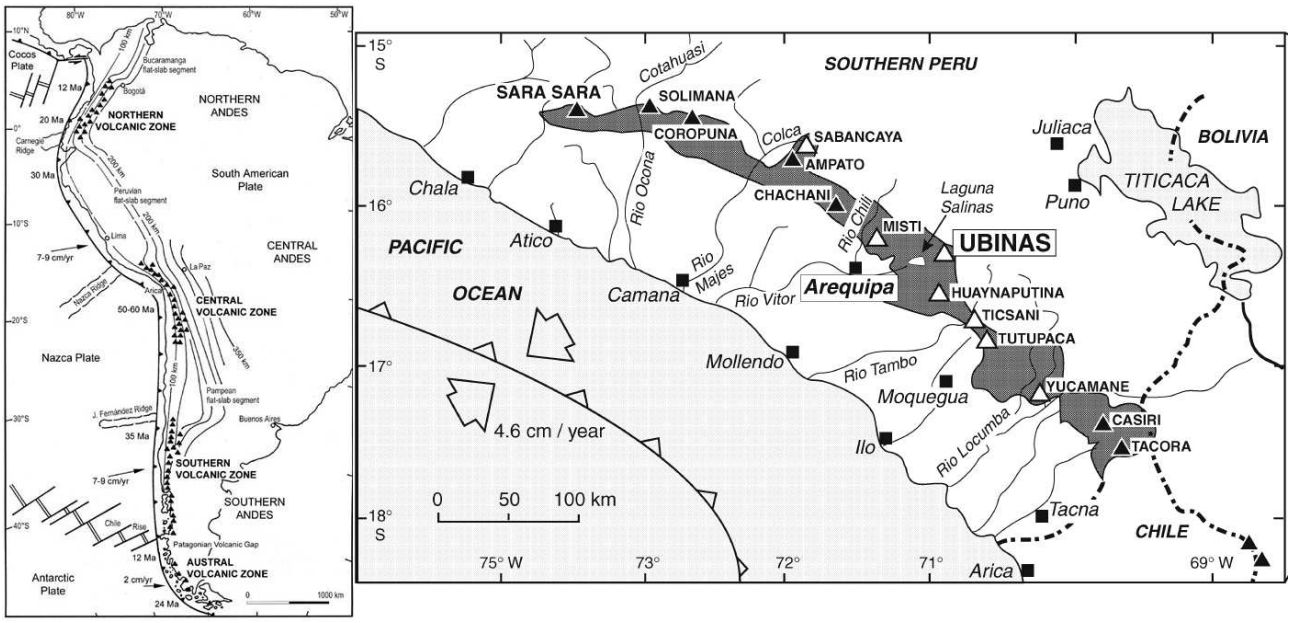


Figure 1.12: Left side: Map of the volcanic arcs in the Andes, and subducted structures affecting volcanism. Right side: Map of volcanoes in Central Volcano Zone in Peru. (Thouret et al.2005)

One group of the chain of volcanoes along the Andes is hosted southern Peru, including seven active volcanoes as part of Central Andean Volcanic Belt (CVZ) (De Silva and Francis, 1991). Five of them are considered potentially dangerous threatening southern Peru, such as Misti, Ubinas, Ticsani,

Savancaya and Huaynaputina (see right in Figure 1.12). In this work, attention has been focused on the Misti and Ubinas, located near big cities as Arequipa (see left in Figure 1.12) (Thouret et al., 2005; Rivera et al., 2010). These volcanoes are concerned by volcanologist because more and more people are living near the side of the volcano. Over one and a half million inhabitants of the cities of Arequipa, Moquegua and the valleys (Colca, Ubinas, etc) are threatened by activities of the volcanoes. Unfortunately, these volcanoes have been instrumented with few seismic sensors.

1.3.1 Characteristics and eruption history of Ubinas volcano

Ubinas (latitude 16.37S, longitude 70.9W) is the most active volcano in Peru (Thouret et al., 2005). It is a typical, steep-sided stratovolcano comprised primarily of layers of silica-rich lava flows and has a summit elevation of 5,672 meters. At 1.4 kilometers across, the volcano's caldera gives it a truncated profile. Hardened lava flows from past eruptions lay on the volcano's flanks. This andesitic volcano is located in the quaternary volcanic range in the CVZ (De Silva and Francis, 1991; Thouret et al., 2005). Thouret et al. (2005) has presented detailed studies about Ubinas volcano. Analysis of detailed stratigraphic records coupled with new chronological data with geophysical, mineralogical, geochemical and isotopic data allowed to link the volcano evolution to its present hazard. These results shown that Ubinas is the most active volcano in Peruvian historical times. Ubinas volcano evolution showed two main periods between growth and destruction. Firstly, the bottom of the edifice was built 370 ky ago by relatively monotonous andesite lavas. Then, it collapsed and a subsequent avalanche deposit of 2.8 km^3 of debris, was drained in rivers and valleys around the Ubinas area. The second stage comprises andesite to dacitic (rocks in composition between andesite and rhyolite) lava flows that built the summit cone between 370 and 140 ky ago. The summit caldera of 1.2 km diameter was formed between 25 and 10 ky and has been associated with large plinian eruptions. The last plinian eruption occurred around 1000-1160 AD, since then and up to the present day, Ubinas displays persistent fumarolic and vulcanian activity. Evidence of deposits has confirmed that during last 450 years as Ubinas erupted many times with VEI 3 (Thouret et al., 2005). Studies revealed 23 eruptions since 1550 with VEI scales between 2 and 3, and one VEI 3 eruption in 1667. Ten eruptions have been followed between 1906-1994 (VEI 2). All those activities allowed to establish the frequency of eruptions around six to seven per century (Thouret et al., 2005; Simkin and Siebert, 1994).

So, after nearly 40 years of quiescence there was a vulcanian event on 25 of March 2006 (VEI 2) (Macedo et al., 2009). A loud volcanic explosion was heard by residents at Ubinas village, located 7 km south-east of the crater. Subsequently gas plumes reached a height of about 2 and 3 km above the summit Ubinas crater and gas plume paths were according the wind direction with accompanied ashfall for 2 or 3 days (Macedo et al., 2009; Rivera et al., 2010). At that time Ubinas volcano was not permanently monitored. A temporary experiment before the crisis showed no significant geophysical activities. Then, four seismic stations network was installed by volcanologists teams of IGP and IRD composed by Kinemetrics (SS-1) short period seismometers with data transmitted to the central recording station in IGP Arequipa. Due to the complexity of waveforms as LP events, tremors and volcanic explosion events could not be localized at that time (internal reports of IGP). On April 20th



Figure 1.13: This image shows an ash cloud column of around 2 km above the Ubinas crater after an explosive event on the 02nd June 2009, photo taken from Ubinas village

2006, three consecutive volcanic explosions rumbled the Ubinas area. Authorities and civil aviation staff confirmed a volcanic ashfall on Arequipa city, located 75 km west of the crater (Figure 1.12), and this was reported by the civil defense of Peru (http://www.indeci.gob.pe as *Contingencia Ubinas 2006*). A field inspection by IGP and IRD teams revealed a huge quantity of volcanic rocks that were found in the caldera area, e.g. 40cm blocks that were ejected over distances of up to 2km (Rivera et al., 2010). This eruption was followed by several months of sustained seismicity punctuated by vigorous long periods, tremors and gases emissions and volcanic explosions (Macedo et al., 2009). An ash cloud column of around 2 km height above the Ubinas crater was observed after an explosive event in June 2009 (see Figure 1.13). By early 2010 declining seismicity probably showed the start of a more restful period. However, due to ongoing seismic activity Ubinas was still considered to be under unrest during this period (IGP monthly reports).

1.3.2 Characteristics and eruption history of Misti volcano

Misti is one of seven active volcanoes in the Central Volcanic Zone (CVZ) along the Andean Cordillera in southern Peru (Sébrier and Soler, 1991). The symmetric conical shape of Misti is typical of a stratovolcano (see Figure 1.14), a type of volcano characterized by alternating layers of lava and debris from explosive eruptions, ash and pyroclastic flows. Misti is located at latitude 16.3S, longitude 71.4W and the summit elevation is 5822 m above sea level and about 3500 m above the Arequipa town. Misti summit is located 17 km northeast of the city of Arequipa the second largest city of Peru. A large eruption of Misti is the most hazardous scenario for the about one million inhabitants as the last big eruption occurred two thousand years ago (Thouret et al., 2001), However despite the apparent peaceful rest, fumarolic activity suggests that the magmatic system is potentially still active. Thouret et al. (2001) presented a detailed description of Misti. A stratigraphic framework and an overview of the age and composition of erupted material was given. The volcanic edifice has been formed in four periods since 833 ky ago. Eight groups of lava flows and pyroclastic deposits describe the evolution of the volcano. Tens of pyroclastic flows and at least 20 tephra falls were produced by Vulcanian and sub-Plinian eruptions since 50 ky. Recent eruptive activity were consisted of vulcanian events in the period AD 1440-1470 and phreatic events were reported in 1677, 1784 and 1785. The Misti edifice is the most recently active of a group of Pleistocene volcanoes, which includes the dormant volcano Chachani and the extinct volcano Pichu-Pichu (Figure 1.12). Traditional buildings of the city of Arequipa are build with white volcanic rock known as Sillar, described by Thouret et al. (2001) as crystallized volcanic tuff.

1.3.3 Instrumentation on Misti and Ubinas

Permanent seismic monitoring has been established for Misti and Ubinas since 2006 by the governmental institution IGP with the collaboration of the IRD. There are two telemetry seismic networks consisting out of five and four stations on Misti and Ubinas volcanoes respectively, that transmit continuous seismic data to the IGP observatory in the city of Arequipa. The seismicity catalogs produced



Figure 1.14: Top: photograph of Misti volcano crater with Mount Chahani in the background. Bottom: photograph of Mount Misti.

by IGP researches show that Ubinas is currently more active than Misti. During the year 2012 there were on average around 200 LP events per month on Ubinas against 20 LP events on Misti. Whereas during the year 2011, Ubinas volcano recorded an average of 300 volcanic events per month, and Misti an average of 25 volcanic events per month. Figure 1.15 shows the telemetry seismic network

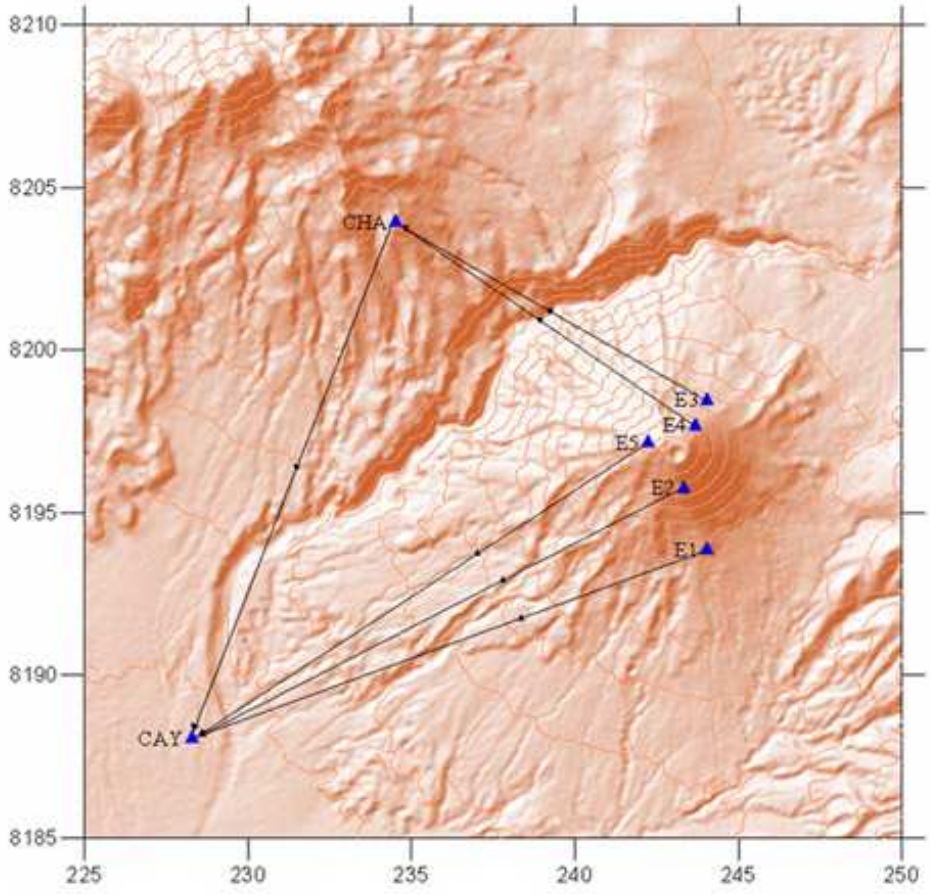


Figure 1.15: Telemetry seismic network map of Misti volcano

deployed around Misti. It consists of five short-period seismometers (E1 and E3 with triaxial L4-3C (Mark Products) seismometers, E2, E4 and E5 with vertical component L22 seismometers Mark Products). Three of them (E2, E4 and E5) located over an altitude of 5000 m, around the crater. Radio telemetry requires a clear line-of-sight between stations. Since stations E3 and E4 are located behind the volcano, with no clear line of sight to the observatory a repeater point (transfer station) in CHA location is used to retransmit seismic information in real time. In contrast, E1, E2 and E5 are directly linked to the observatory, called CAY (Figure 1.15).

The Ubinas seismic network is composed of four seismic stations (with codes UB1, UB2, UB3 and UB4) distributed on the flanks of the volcano, see Figure 1.16. From 2006 to 2007, stations were equipped with 1 hz short period seismometers with telemetry system to transmit data to the observa-

tory (IGP Arequipa). From 2008 to present, UB2 is equipped with a broadband vertical component sensor, the other three stations have short period vertical component sensors. In addition, UB2 and UB4 are equipped with a bi-axial tiltmeter with a 0.1 micro-radian resolution. The seismometer and tiltmeter at UB2, located approximately 1 km north of the Ubinas crater (Figure 1.16), have been installed 50 cm deep on a concrete base under solid volcanic rock. Seismic and tilt data are recorded by the same digitizer (a Reftek 130 with a sampling rate of 50 Hz). The tilt instrument is a bubble-type two axis sensors. The orientation of the Y-axis component is parallel the North, almost radial to the active crater. The X-axis component is oriented to the East, orthogonally to Y-axis. A positive tilt on the North component indicates an inflation of the crater area. A positive tilt on the East component indicates a tilt down toward the West (Ferro et al., 2011). Seismicity has been the most common

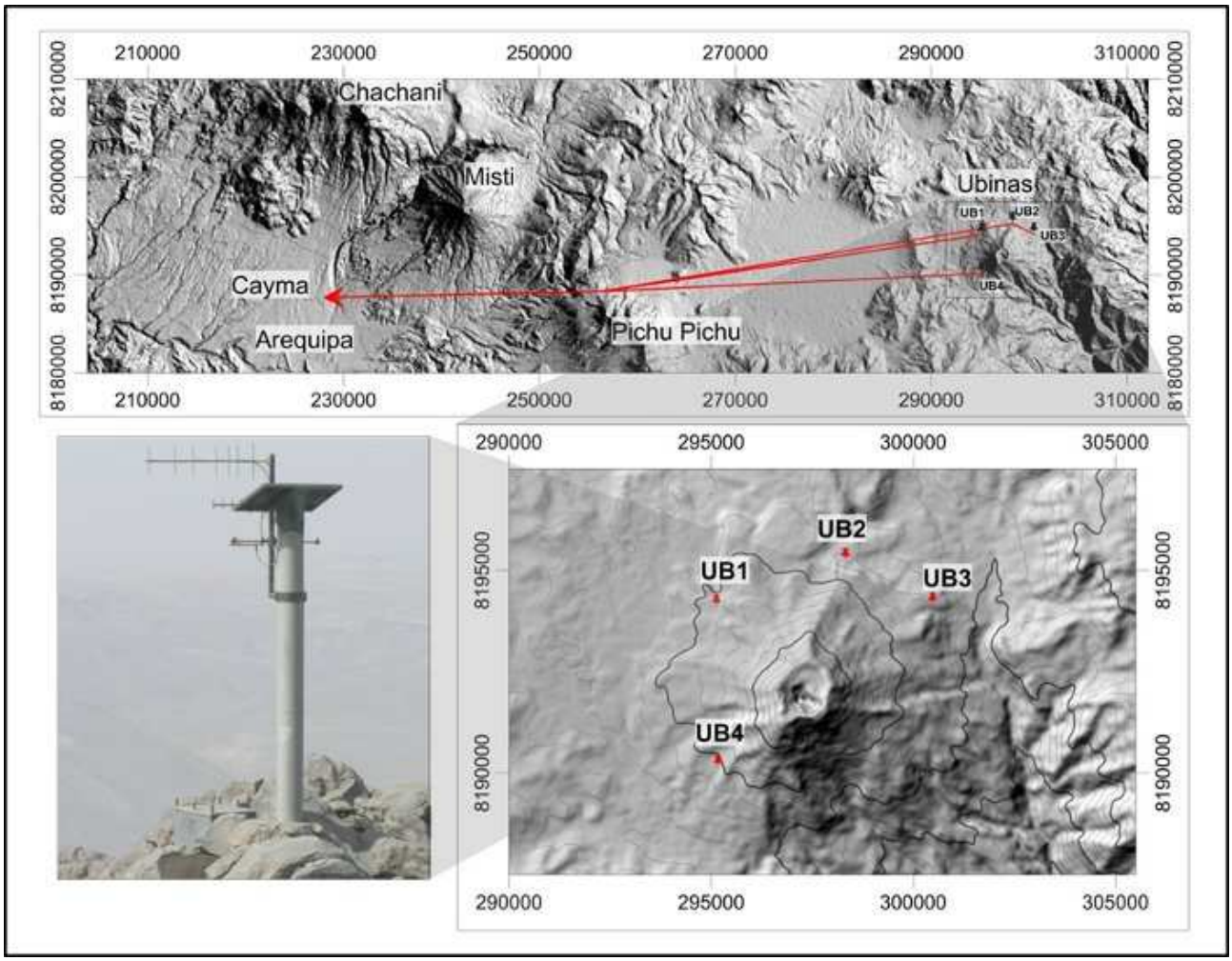


Figure 1.16: Telemetry seismic network diagram of Ubinas volcano.

disturbance in response to stress changes caused by magma movement beneath the crater. Figure 1.17 shows a long-period (LP) swarm increasing in activity from 90 minutes prior to a vulcanian explosion.

Since the eruption in 2006 more than forty thousand LP earthquakes and tremors events of moderate intensity have been recorded until July 2009. The 2006 Ubinas eruption was mainly referenced as

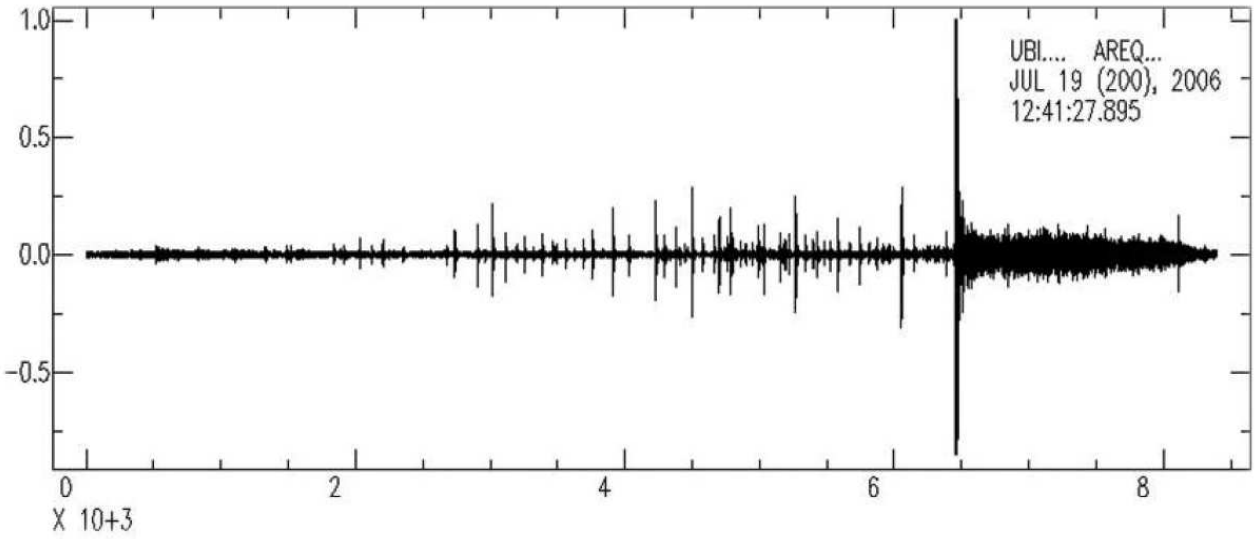


Figure 1.17: Volcanic explosion occurred in July 2006, it is preceded by LP events. From Macedo et al. (2009)

vulcanian activity (Macedo et al., 2009). Traversa et al. (2011) studied 143 explosive events with vulcanian activity that occurred between 2006-2008 at Ubinas. Swarms of LP earthquakes with increasing energy some hours prior to explosions were observed, such explained in Figure 1.18, where two explosions occurred around days 23 and 28, October 2006. The first explosion is preceded by a 6-hour long nonlinear increase in LP activity, while the second one is characterized by a continuously accelerating rate of LP earthquakes starting approximately 3 hours before the explosion. A forecasting algorithm was built based on pattern recognition which used LP event rate prior to higher energy explosions as the precursor Traversa et al. (2011).

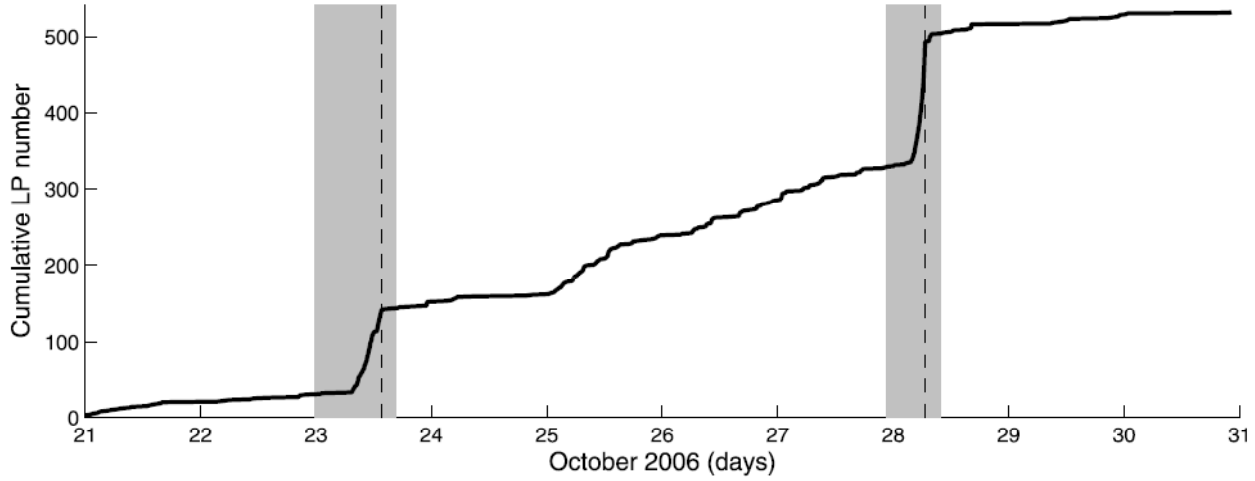


Figure 1.18: Evolution of the LP event occurred at Ubinas volcano between October 21 and October 31 2006 (black line). Dashed lines indicate explosion occurrence times; gray boxes an indicate increase in LP activity. From Traversa et al. (2009)

1.4 Ubinas field experiment in 2009

In this section, we describe seismic measurements carried out with two seismic antennas at Ubinas between May and July 2009, where an intense seismic activity was recorded during this period. Thos experiment was supported by group of researchers from IRD-France (l'Institute de Recherche pour le Développement), Geophysics group-Ireland (University College Dublin) and IGP-Peru (Geophysical Institute of Peru). One of the first targets of this experiment (Ubinas 2009) is to locate seismic sources of the seismic activity at volcano by using seismic antennas composed of broadband 3C seismometers which is discussed in more detail in Chapters 2 and 3, in this section, we here show the first analysis of the experiment.

1.4.1 Seismic antenna configuration

From May to July 2009, two small-aperture seismic arrays were deployed at Ubinas Volcano: on the north part (the NUBI antenna) and the west part (the WUBI antenna) (Figure 1.19). The NUBI (North volcano crater) antenna was composed of 10 instruments: eight Guralp-6TD and two Guralp-3ESP seismometers (see Figure 1.19a), while the WUBI antenna consisted of six Guralp-6TD seismometers and six Titan-Neomax Agecodagis instruments (see 1.19b). Each station included a seismic three-component sensor and a GPS receiver, and was set up to continuously record at 100 samples/s. The two cross-shaped antennas were installed on slightly sloping surfaces, according to the topography. The slope between the farthest sensors on each antenna were 7% and 30% for NUBI and WUBI, respectively. The distances between seismometers was approximately 50 m and the array aperture

300 m for each antenna. The centers of the NUBI antenna (altitude 4632 vm) and WUBI antenna (altitude 4732 m) were 3750 m and 2567 m away, respectively, from the northern border of the crater (Figure 1.19). The horizontal components of all seismometers were aligned to geographical North for the X-components and to East for the Y-components respectively. Distances between the seismometers were set to approximately 50 meters. Each seismometer location was surveyed with Trimble GPS (GeoXH, accuracy 0.3 m). All these seismic stations recorded data on internal disks

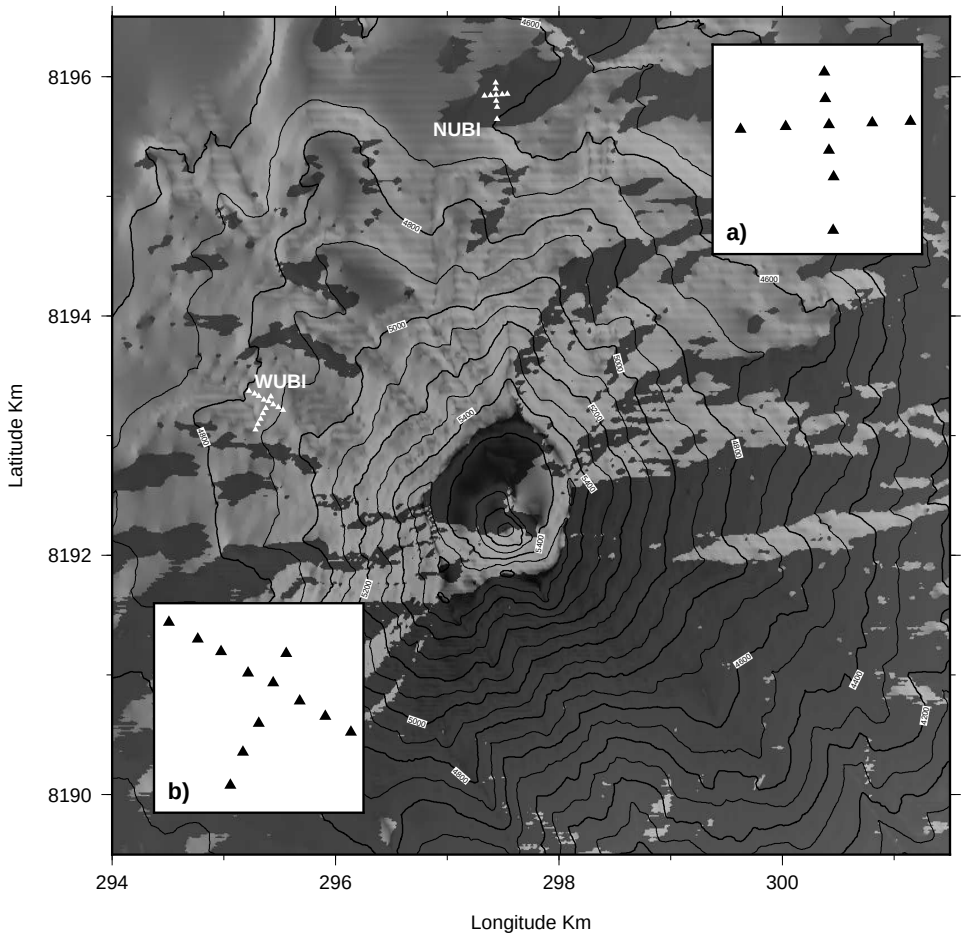


Figure 1.19: Ubinas crater map, white triangles are the 3-component seismometer locations of arrays WUBI and NUBI. a) Zoom of NUBI antenna. b) Zoom of WUBI antenna.

with 4 Gbyte storage capacity, producing reliable continuous data during almost three months after installation. The power supply for each station consisted of a small 14 amp-hour battery connected to a 30W solar panel such as shown in Figure 1.20.



Figure 1.20: Photo of all components used for one seismic station. The seismometer 6TD is in the right middle with a Wi-Fi antenna. The white element lying in the corner of the solar panel is a GPS antenna, the blue square table is the solar panel and the black element below the solar panel is the battery.

1.4.2 Pre-processing and quality control of data set

Two preprocessing controls were carried out on the raw data that were recorded in this field study, one to deconvolve the instrument response, and an other to monitor the accuracy of the time-stamp on the seismograms (as each sensor was synchronized from its own GPS clock). Time synchronization was crucial for correlating the events for post array dataset analysis. For this purpose, we examined low frequency waves (0.2-0.4 Hz) generated by ocean waves near the coast and propagated to long distances (Berger et al., 2004; Longuet-Higging, 1950). Here, the microseism was recorded 150 km away from the coast. To check the quality of the time synchronization, we computed the correlation coefficients $c(\tau)$ for each pair of sensors. $c(\tau)$ is expressed by:

$$c(\tau) = \frac{\sum_t f(t)h(t+\tau)}{\sqrt{\sum_t f^2(t)}\sqrt{\sum_t h^2(t)}} \tag{1.9}$$

where f(t) and h(t) are 1-min time windows. Good synchronization was characterized by $c(\tau)$ close to 1.0 for a time lag close to zero. Using this classical method, we ensured the good quality of the time synchronization for each array.

1.4.3 Data processing and Presentation

During the experimentation Ubinas 2009, the seismograms recorded by NUBI and WUBI broadband seismic arrays, show a spectacular diversity of signals. Figures 1.21 and 1.22 depict waveforms and their spectra of some samples of the seismicity recorded at Ubinas during the field experiment. It is generally assumed that volcano seismic waveforms contain rich information on the geometry of fluid migration, resonance effects, and transient and sustained pressure oscillations resulting from unsteady flow through subsurface cracks, fissures and conduits. Volcano seismic signals are usually classified into four groups (Wassermann, 2012; McNutt, 2005), all of which have been observed during the experiment.

1. **Volcano tectonic (VT)** events at Ubinas 2009, are characterized by high frequency signals greater than 5 hz. They often exhibit emergent P-wave onsets and S-wave arrivals which is impossible to detect due to seismic scattering (Wassermann, 2012). In Figures 1.21b and 1.22b. It shows a main frequency content between 4 and 10 hz. In contrast, VT events originating deeper, show impulsiveness of the P- and S- arrivals phases in seismograms, often observed at MISTI.

2. **Long-period (LP)** events are the most frequently seismo volcano event seen during the experiment. They show very emergent onset (no seismic phases), limited spectral bandwidth and low frequency content between 0.5 and 5 Hz. Generally a single peak dominate the event spectrum. Sometimes the spectrum includes few smaller well defined peaks. On average, they have longer duration than VT events. LP sources have been often located in the shallow part of the volcano (less than 2 km). They are associated to opening and resonating crack when magma

is ascending towards the surface (Chouet and Matoza, 2013). Figure 1.21a, 1.21d, 1.21e and 1.21f depicts some LP events.

3. **Tremor** signals observed at Ubinas during the field experiment in 2009 have a frequency content between 1 and 7 Hz. These lasted between minutes to days, consisting of degassing events correlated after a vulcanian explosion. Almost all vulcanian explosions in Ubinas were linked by tremor, probably caused by pressure fluctuation of degassing magma or molten rocks. Figure 1.22f shows a small time window of a tremors event that existed during 15 h, its spectrum present a broad frequency contents between 1 and 10 Hz. Examining volcanic tremor activity is interesting as some of them have just started after an explosion.

4. **Explosive events** recorded during the field experiment at Ubinas correspond to the vulcanian explosions. There were 16 explosions identified in our study. The most part of them were accompanied by tremor, with eruption columns reached 1-2 km altitude above the crater. These observations led to an interpretation of cyclic magma pressurization in the upper conduit, with a surge of dome growth and release of pressurized gas at the peak of a cycle and during deflation (Sparks, 2003). The waveform depicted in Figure 1.22a corresponds to an explosion. The frequency content is characterized in the band of 0.5 and 7 Hz. A detailed analysis of vulcanian events is carried out in Chapter 3.

A sample of hybrid is shown in Figures 1.21c and 1.22e. Some seismo-volcano signals recorded in Ubinas, share the signal and frequency characteristics of both LP and VT events. These signals known as hybrid events are characterized by broad frequency content between 0.7 and 10 Hz such are depicted in right side of Figures 1.21c and 1.22e, and their signal onsets are emergent. Another type of volcanic signals is shown in Figure 1.22c known as “tornillo” (screw) event considered as part of LP, for the characteristic coda like to screws, its spectrum shows an harmonic frequency contents with narrow band peaks (around 10 picks), which is ranged from 1.5 Hz to 21 Hz depicted in the right side of Figure 1.22c. The waveform in Figure 1.22d shows emergent onsets that had frequencies of 2.5 and 12 Hz according its spectrum (right of Figure 1.22d), it did not contain energy in frequencies lower than 2.5 Hz, this signal can be associated with rockfall or avalanche event that causes high frequencies (Neuberg, 1998).

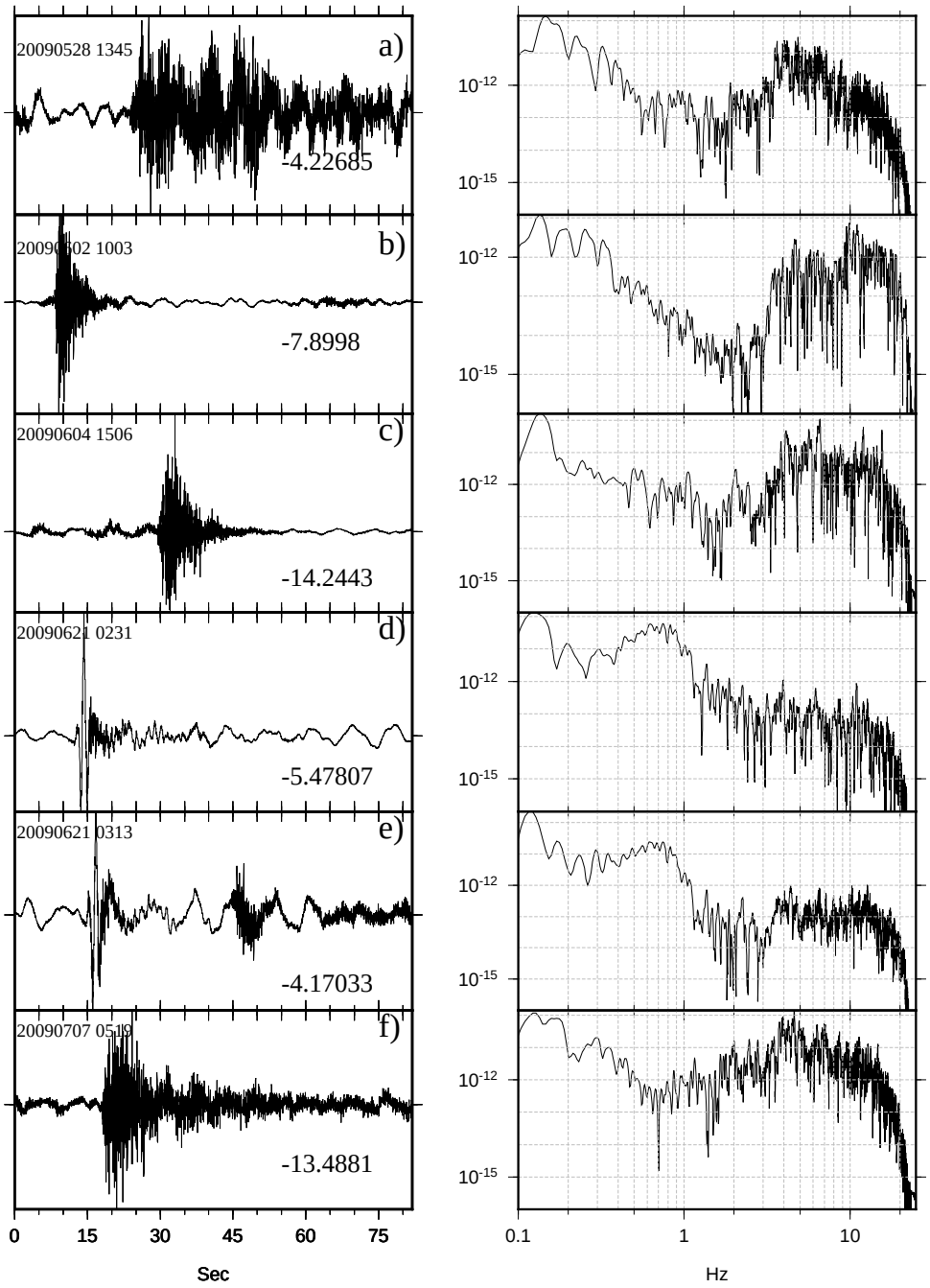


Figure 1.21: Typical unfiltered seismograms, indicating date in the upper left and minimum amplitude in $\mu m/s$ (left) and their spectra (right), recorded at Ubinas experiment in 2009. . a) LP, b) VT, c) hybrid, d) LP e) LP and f) LP.

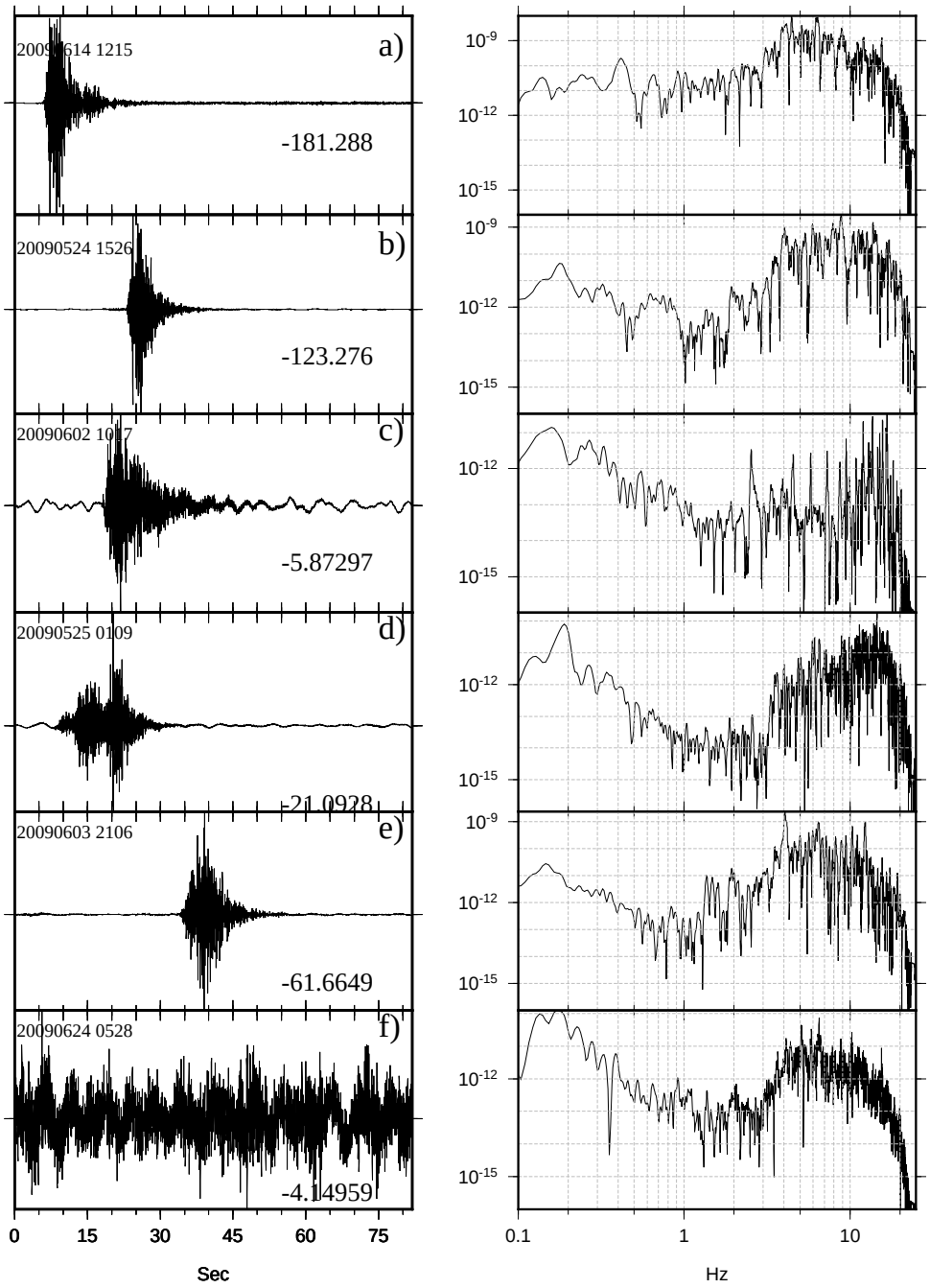


Figure 1.22: Typical unfiltered seismograms, indicating date in the upper left and minimum amplitude in $\mu m/s$ (left) and their spectra (right), recorded at Ubinas experiment in 2009. a) Explosive, b) VT, c) Tornillo, d) Avalanche or rockfalls e) hybrid and f) Tremor.

1.4.4 Seismicity during the experiment

Sixteen Vulcanian explosions, hundreds of long-period events, and several hours of tremors were identified during the period of our study, and these were classified in the catalog of the Instituto Geofisico del Peru (IGP) Volcano Observatory. The Vulcanian explosions were small to moderate-sized and lasting from seconds to minutes. Most of them (11 of 16) were followed by tremor episodes that lasted from 20 min to 2 days. A practical way to estimate the seismic intensity is to compute the energy of the time-series data, as proposed De la Cruz-Reyna and Reyes-Davila (2001). A RMS average squared amplitude of the seismic signal was performed for a fixed time window (T) on a gliding process, as in Equation (1.10), and it was then depicted as an energy function over time.

$$RSEM(iT) = (\frac{1}{T}\sum_{t=iT-\frac{T}{2}}^{t=iT+\frac{T}{2}} y^2(t))^{\frac{1}{2}} \tag{1.10}$$

where y(t) is the amplitude vector of the seismic signal, and i represents the sliding window position. Starting from the initial seismic data, the real-time seismic energy measurement function was performed with T = 5 min on the total duration of observation, as shown in Figure 1.23. In this Figure 1.23, we expose some significant events occurring from 24 May to 14 July 2009 during the experience. The inverted triangle markers correspond to the 16 Vulcanian explosions, identified by numbers, the dashed horizontal lines specify the duration of the tremor events, and the square markers correspond to tectonic earthquakes (outside the volcano edifice).

1.4.5 Time-frequency method

In this section, we develop a time-frequency analysis on seismic array data based on Empirical Mode Decomposition (EMD) (Huang et al., 1998), with the goal to graphically represent the volcanic activity and displaying temporal variation of amplitude and frequency patterns for data recorded during the field experiment in Ubinas 2009. Continuous time-frequency analysis of volcanic sismicity can exhibit the evolution of seismic patterns, which is an important contribution to monitor volcanic unrest. It can lead to better survey and help the monitoring of the volcanic activity for long-terms (hour, days or weeks). The classic real-time monitoring the volcanic activity is based on either the RSEM (real-time seismic energy measurement) method (Figure 1.23), or the RSAM (real-time seismic amplitude measurement). Another tool Seismic Spectral Amplitude Measurement (SSAM) (Rogers, 1995) for real time monitoring can be used. It computes in real time the average amplitude of the seismic signals in different frequency bands. This permits seismologists to evaluate the nature of seismicity at a volcano and recognize shifts in frequency that are related to changing dynamics of magma movement. The EMD method has been shown better to numerically describe temporal patterns in nonstationary and nonlinear time series, and acts essentially as a dyatic filter bank close to those involved in wavelet decompositions (Flandrin et al., 2004).

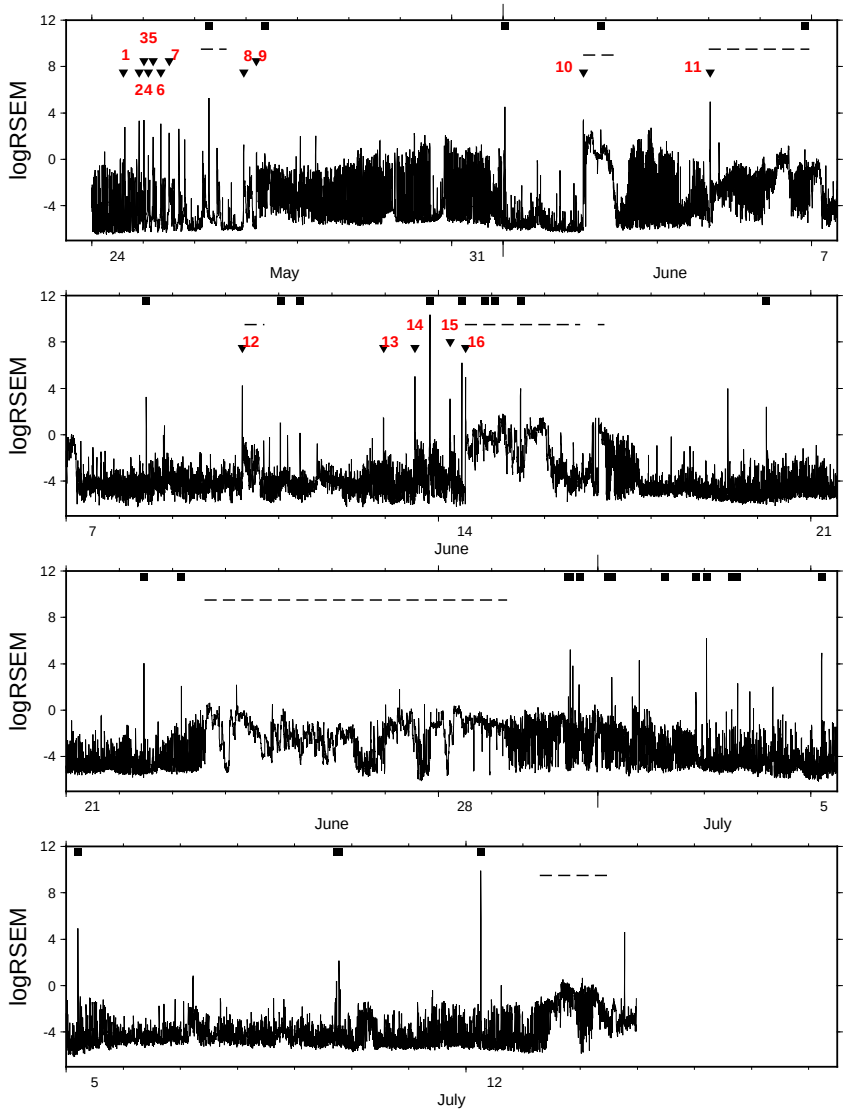


Figure 1.23: RSEM computation, with 5 minutes sliding time windows, during the 2009 experiment. The black inverted triangles match the sequence of 16 vulcanian explosions numbered. Horizontal dashed lines match to tremor event duration and black square dots match to quakes out of volcano.

Empirical Mode Decomposition

We express here the EMD principle. The EMD method is relatively new in the signal processing literature (Huang et al., 1998) and has only recently been proposed for seismic processing (Battista et al., 2007).It can be compared to other analysis methods like Fourier Transforms and wavelet decomposition since the EMD method can decompose time-series signal into different time-frequency modes known as intrinsic mode functions (IMF). The sum of these IMF reproduces quite well the original signal. The EMD method is a proven method to highlight nonstationary of a signal. The goal of EMD in this study is to use it as nonstationary filter to express instantaneous frequency of each event.

Intrinsic Mode Function

The EMD approach attempts to decompose any signal into a superposition of oscillatory terms called intrinsic mode function (IMF), Equation (1.11). The IMF signals contain frequencies ranging from the highest to the lowest ones presented as amplitude and frequency oscillatory terms calculated using a sifting process, which successively subtracts the local mean from a signal. The sifting process is described as follows (Flandrin et al., 2004):

1. Determine the local extrema (maxima, minima) of the signal.
2. Connect the maxima, with an interpolation function, creating an upper envelope for the signal.
3. Connect the minima, with an interpolation function, creating a lower envelope for the signal.
4. Calculate the local mean as half the difference between the upper and lower envelopes.
5. Subtract the local mean from the signal.
6. Iterate until reaching the IMF definition that has only one extreme between zero crossings, and has a mean value of zero (residual).
7. Exhibition of a IMF from the signal. We separate it from the rest of the data. The procedure is repeated on 1 again. The last extracted IMF is the lowest frequency component of the signal (the trend).

The sifting process is computed iteratively until the signal meets the definition of an IMF, which satisfy conditions, namely observing the number of zero crossing versus extrema must be one. Then, the IMF is subtracted from the original signal before starting a new sifting process on the remainder signal until the residual constrains no more oscillation. IMFs are considered mono-component functions which do not contain riding waves (Huang et al., 1998). For a given signal $s(t)$, the EMD processing is given by the following equation (1.11)

$$s(t) = \left[\sum_{i=1}^{n} IMF_i(t)\right] + r_n(t) \tag{1.11}$$

where $IMF_i(t)$ is the IMF sub-signal ranging from 1 to N representing the oscillations from the shortest to the longest period respectively, and $r_n(t)$ is the residual. For practical purposes, the consecutive IMF sub-signals can be considered to be locally orthogonal to each other (Huang et al., 1998; Flandrin et al., 2004).

To illustrate the sifting process, a seismic signal is processed by the EMD algorithm and their IMFs are depicted in Figure 1.24. A total of 9 IMFs. Subtracting the signal and the sum of all this IMFs give us the error is reflected to the residue which is in the order of 8E-3. To express the instantaneous frequency, the Hilbert transform is classically used. The Hilbert transform $\widehat{s}(t)$ for any function $s(t)$ is denoted in the frequency domain by :

$$\left[\widehat{S}(f) = S(f)(-i \cdot sgn(f))\right]$$

where $i = \sqrt{-1}$. The analytic signal $z(t)$ becomes:

$$z(t) = [s(t) + i \cdot \widehat{s}(t)]$$

and it can be decomposed into $a(t) \cdot e^{\theta(t)}$, where $a(t)$ and $\theta(t)$ are instantaneous amplitudes and phase function respectively. The wanted instantaneous frequency is the time derivative of the phase. Then, the instantaneous frequency becomes a time-series function of an IMF and all of them can be expressed as a time-frequency function of the seismic signal known as Hilbert Huang transform (HHT). Figure 1.25a shows the same seismic signal used in Figure 1.24, then Figure 1.25b is its HHT represented as a time-frequency image, built with all instantaneous frequency functions obtained of each IMF, the power intensity on the spectrum is obtained from RMS amplitudes of each IMF respectively. In Figure 1.25b frequencies are well defined between 0.5 and 2.5 Hz, and 3 and 6 Hz. Figure 1.25c is Wigner-Ville representation shows that frequencies are between 1 and 4 Hz.

We processed several seismic signals recorded at Ubinas 2009 with the EMD algorithm to investigate their IMFs. This analysis was first to sort high to low IMFs regarding the amplitude because EMD algorithm usually sorted respect to frequencies. Secondly we assessed the energy of each IMF, resulting that the first IMF signal generally contained around 75% of the input signal, other test with 2 IMFs showed all seismic signal represented within of 95% in terms of energy. Taking into account that the seismic noise is 5%, Hence, the 2 IMFs with highest amplitude can represent globally the seismic event. Then, we use the IMF representation to get a time-frequency representation. (Flandrin et al., 2004) assume that the sum of the Fourier transform of each IMF yields the signal in frequency domain (Equation 1.12). In our case, we can consider EMD as a dyadic filter banks expressed by:

$$\widehat{S}(f) = \frac{1}{2}\sum_{i=1}^{2}[FFT\{IMF_M\}] \tag{1.12}$$

The aforementioned time-frequency technique is applied to continuous seismic events where time and date information is given by STA/LTA algorithm. So, time-frequency analysis can be written as:

$$H(t,f) = \sum_{t=t_0}\widehat{S}(t_0,f) \tag{1.13}$$

where, $\widehat{S}(t_0,f)$ is the spectrum resulted of the sum of IMF in frequency domain and t_0 is the initial time of each seismic event found by STA/LTA algorithm.

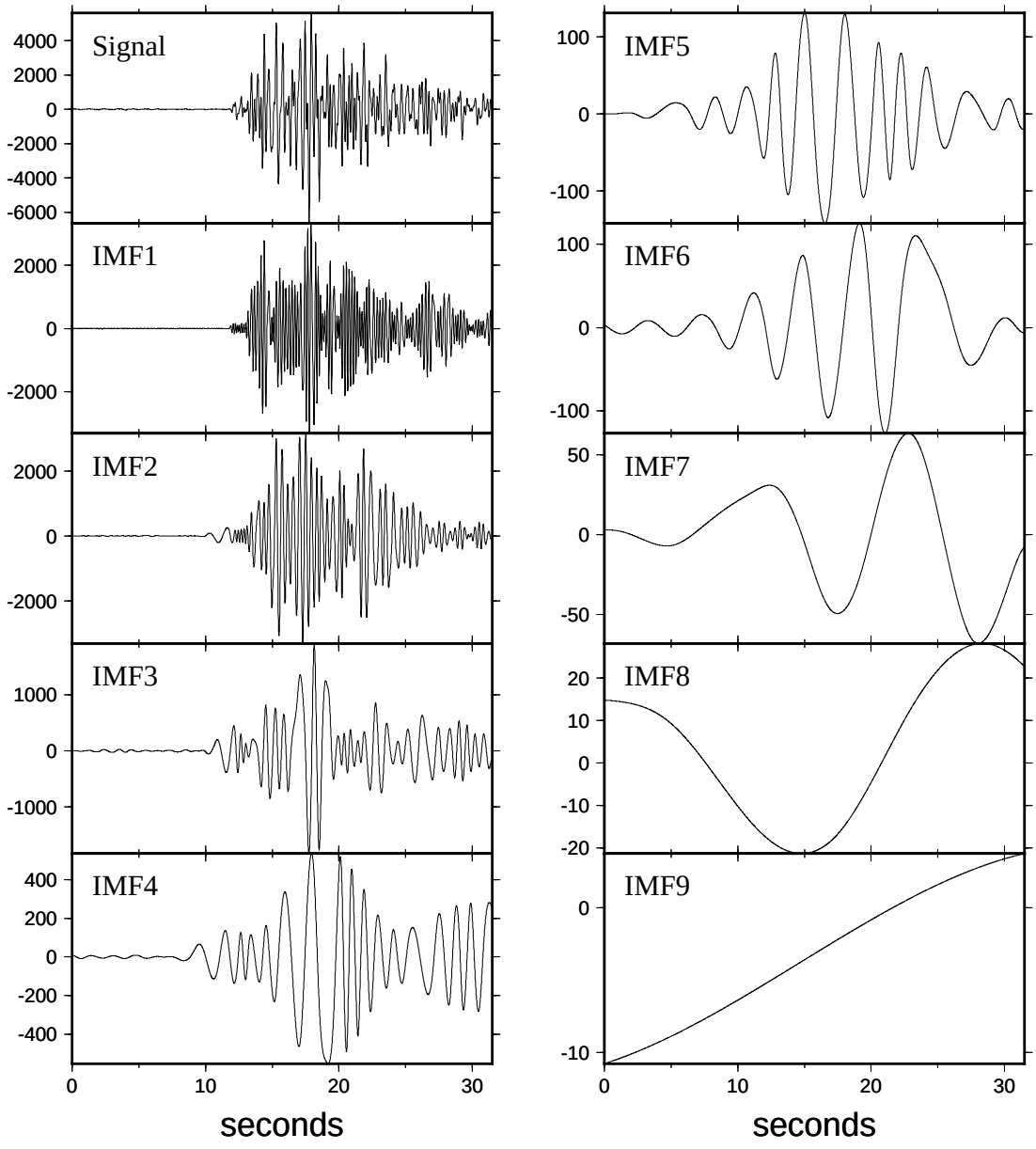


Figure 1.24: Seismic signal (signal) recorded at Ubinas volcano and their decomposition representing by IMFs (intrinsic mode functions)

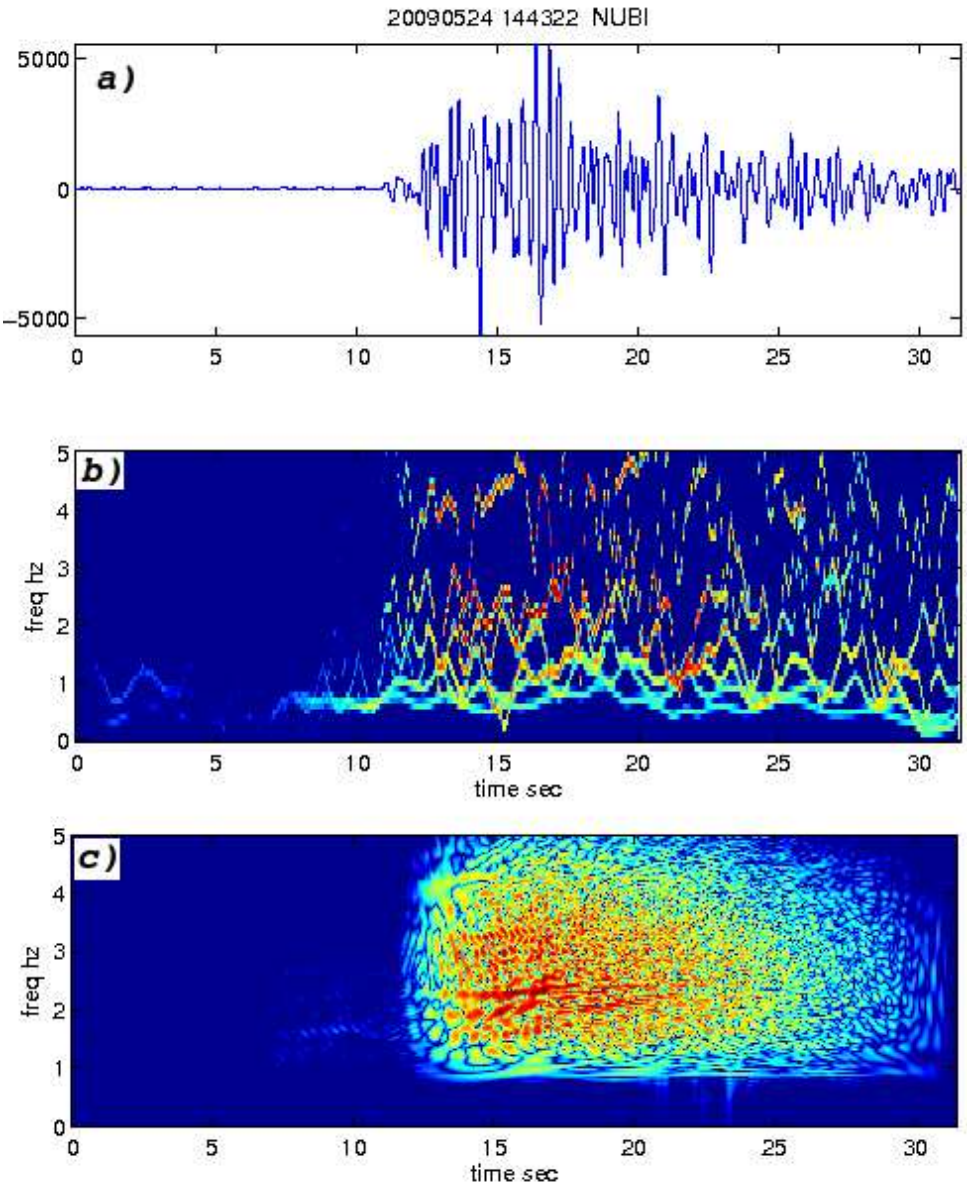


Figure 1.25: a) A volcanic seismic signal (Vertical component) recorded at Ubinas volcano, b) Hilbert-Huang transform time-frequency representation (Normalized) of the seismic signal in a), c) Wigner-Ville time frequency representation (normalized) of the seismic signal in a).

Time frequency representation of Ubinas signals

The seismic activity recorded on the Ubinas volcano in 2009 shows a high density of seismic events between explosions, long period, tremors and so on. Figure 1.26 shows one-day of continuous recording, each line is 60 min (1 hour), a large activity between several explosions occurred this day (the highest peaks), several small peaks presented allmost every hour like to the hour 11h. Figure 1.26 shows a less small peaks before the large explosion followed by 20 hours of continuous tremor activity. These activities show an inherent instability of the magmatic system. To better characterize this complex activity from seismic signals, we try to use the IMFs analysis. We set up our analysis to earthquakes with SNR upper than 12dB (based on the small peaks) which can be performed by STA/LTA algorithm under this condition. In order to better represent the frequencies we fix a threshold to 50% of the maximum peak, to plot only peaks more important of the spectrum of each seismic event represented in Equation Equation 1.12. The power intensity spectrum is related to the energy of the seismic event represented as Db and is reflected in a colors scale, such as shown in Figure 1.28 which is computed from all the events found in the analysis. The basic idea of this analysis represents the seismic event in a vertical sequence of points that are their more important frequencies (Equation 1.13). This type of representation allow us to correlate occurrences of seismic patterns or clusters. However, such activity usually exhibits some structure in time linked to the mechanisms of the volcano system. Time-frequency analysis with this new approach has highlighted the Ubinas activity from data recorded during the field experiment. Figure 1.28 shows the frequency the activity of Ubinas during the field experiment between 24th May and 14th July 2009. The black inverted triangles correspond to the 16 explosions (listed by numbers), black dashed lines specify the duration of tremor events, and the square markers correspond to regional earthquakes.

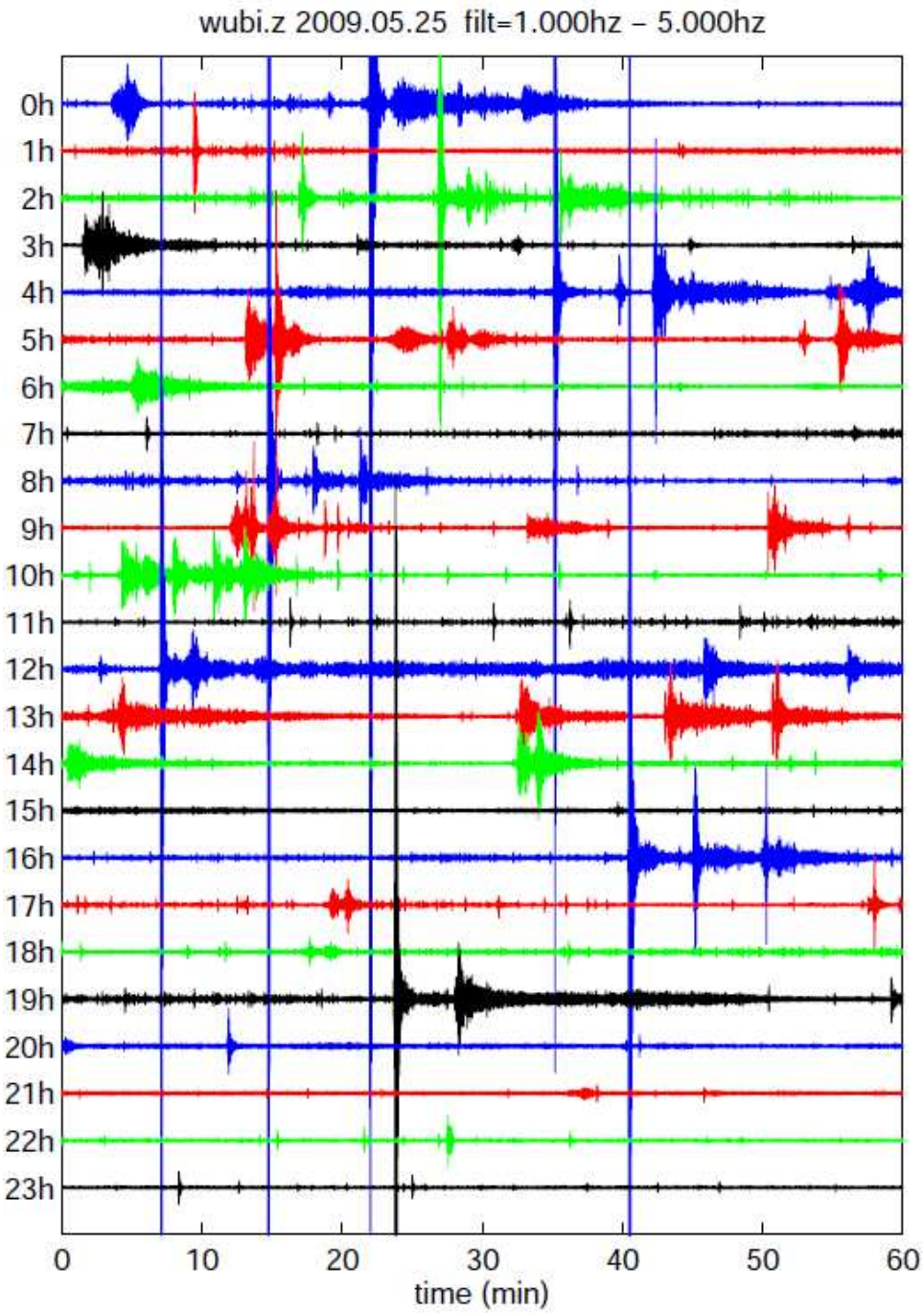


Figure 1.26: One-day seismic recordings (25th May 2009) on the Ubinas volcano by one station (vertical component) of WUBI antenna.

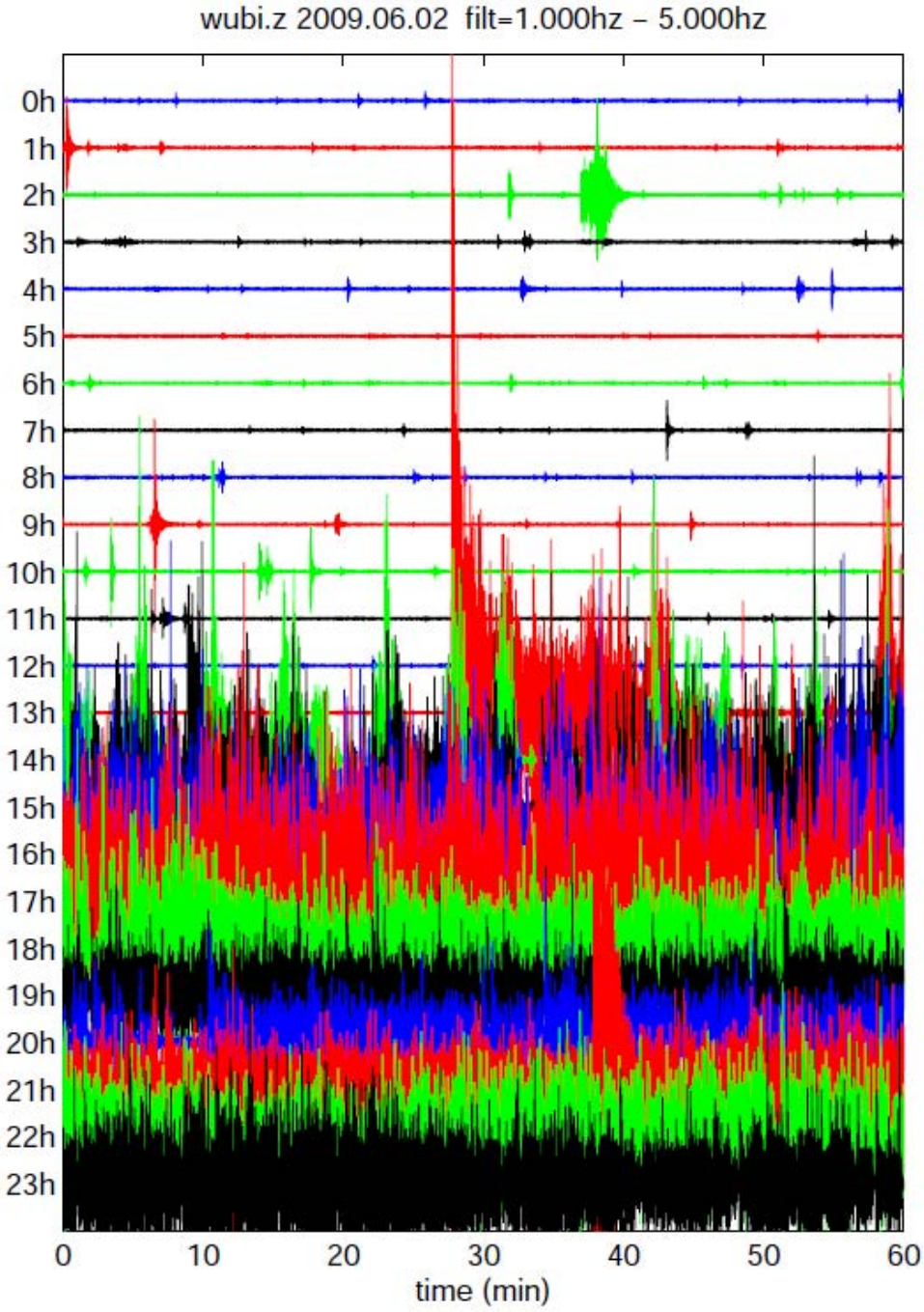


Figure 1.27: One-day seismic recordings (02th June 2009) on the Ubinas volcano by one station (vertical component) of WUBI antenna. The biggest wave correspond to an explosion followed by tremor event.

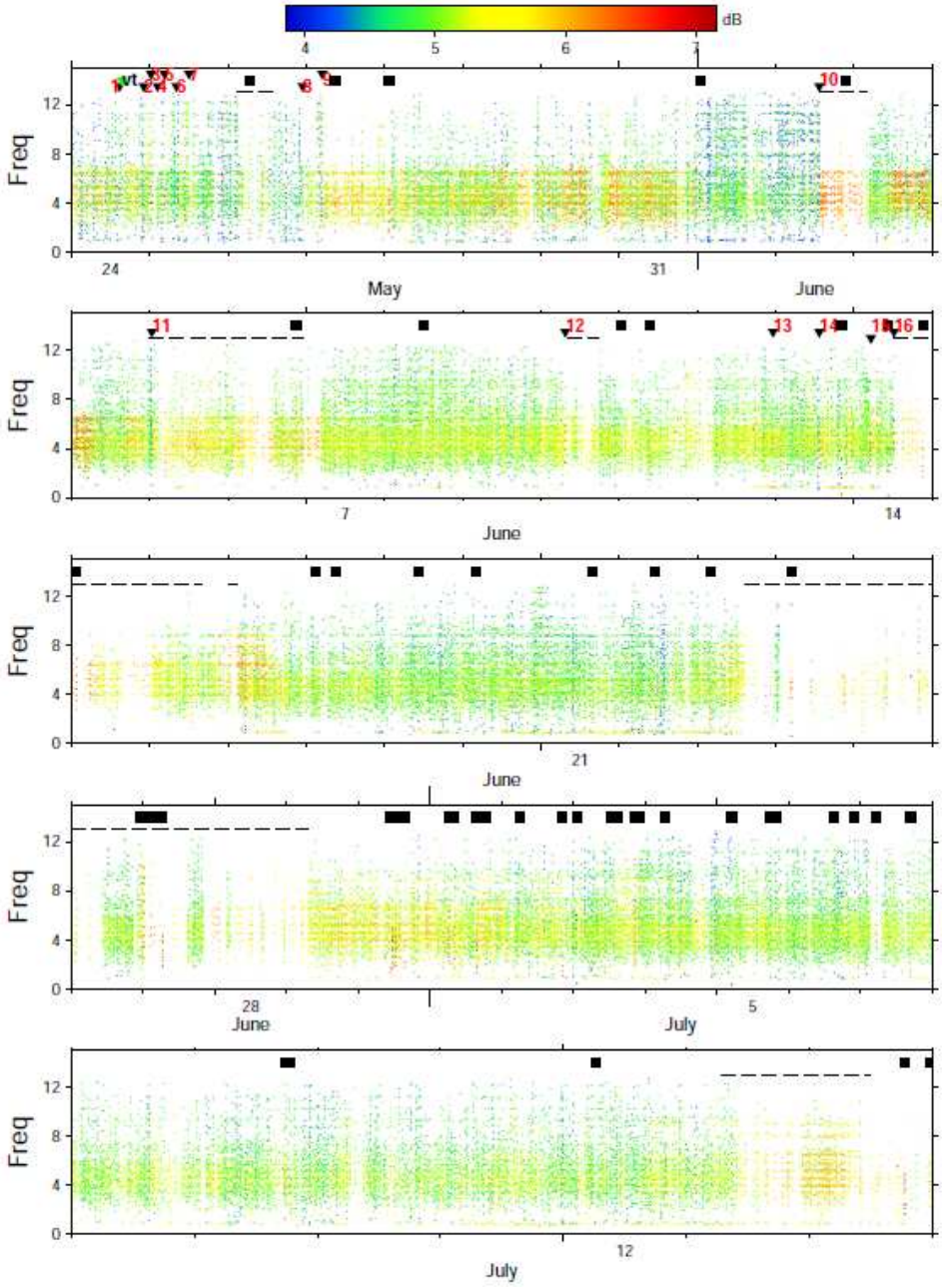


Figure 1.28: Frequency-Time representation of WUBI during the experiment Ubinas volcano 2009, black triangles are explosions, squares are external earthquakes

1.5 Misti volcano field experiment in 2011

From November to December 2011, a test experiment was carried out with two seismic antennas deployed at the flanks of Misti volcano to transmit seismic data 15 km away from the observatory (Arequipa Peru) and process them in real-time. This seismic measurement took place under the experimental framework of this thesis and the cooperation of a group of researchers from IRD-France (l'Institute de Recherche pour le Développement), Geophysics group-Ireland (University College Dublin) and IGP-Peru (Geophysical Institute of Peru). The aim of this survey was to test a seismic source localization method which was developed in this thesis on a real-time monitoring system.

1.5.1 Seismic antenna telemetry installation

Figure 1.29a shows the Misti volcano topography and locations of the MISA and MISB seismic antennas deployed at 4200 m and 4300 m altitudes respectively. The location of the observatory OBS (Arequipa Peru) is at an altitude of 2450 m (all positions were resolved by using a GPS device). Five seismometers per antenna were installed at the flanks for a period of 45 days in November 2011. MISA and MISB are 12 km and 15 km away from OBS respectively. Each array was composed of five broadband Guralp 6TD seismometers. In Figure 1.29b the area limited by the square in Figure 1.29a is shown. The two arrays geometries are almost linear with distances between individual seismometers around 50 - 60 m.

Seismometers featured as portable instruments that integrate into the same device: triaxial seismometers, digitizer and wireless communication capabilities. The main technical specifications characterized as: three-component, broad-band 0.033Hz and 50Hz, dynamic range of 120 dB, 24-bit digitizer, Wi-Fi capabilities. We took advantage of the Wi-Fi (reaching up to 500 m) to keep connected all elements of the array with the reception module CMG-DCM (Guralp), such as shown in Figure 1.30, an external high-gain 12 dBi (2.4 GHz) omni directional antennas were used to enhanced and ensure each Wi-Fi communication. A reception module CMG-DCM with a wireless capability (Figure) was located in the middle of the array in order to minimizing distance constraints. The purpose of this module has been to collect data of all seismometers and retransmit them to the observatory by using digital radios (state of art of Freewave). All instruments were used with small 14 Ah batteries and 30 W solar panels. Spread spectrum radios were configured in point to multi-point operation. This made it possible to connect remote stations by using only one radio in the observatory. Each seismometer with 3 channels (one vertical and two horizontals) produced data with 100 samples/sec/channel. The CMG-DCM received continuous data from instruments, which were controlled with an interface called SCREAM provided by Guralp. Scream is a multiplatform application for Guralp seismometers configuration, real time acquisition and monitoring. Scream includes extensive support for TCP/IP and UDP/IP data communication. It is designed to be effectively network-transparent, so users can contact and configure digitizers at remote sites as easily as those directly connected to the computer. The distant communication with the observatory was achieved with spread spectrum radio Freewave (model HTPlus) and 12 dBi directional antennas (Yagi). The "data center" receiver system located at IGP Observatory at Arequipa, Peru, was equipped with one FreeWave radio (spread spectrum)

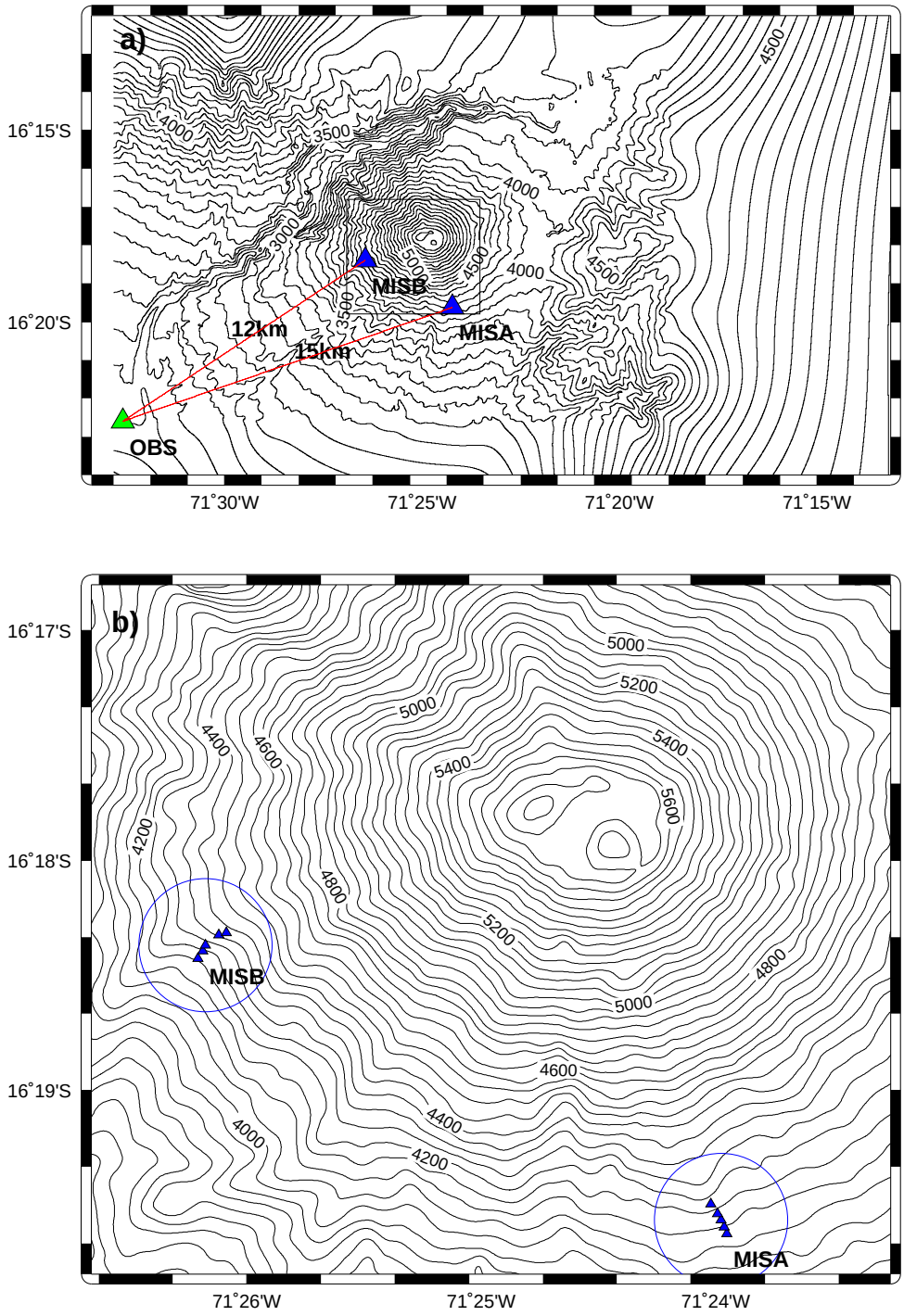


Figure 1.29: Misti volcano topography. Top: triangles labeled with MISA and MISB represent the location of the seismic antennas, and the triangle OBS is the location of the IGP-Arequipa observatory, in Cayma district in Arequipa Peru. Bottom: A zoom of the area represented by a square above, each filled triangle represents a seismometer of the array.

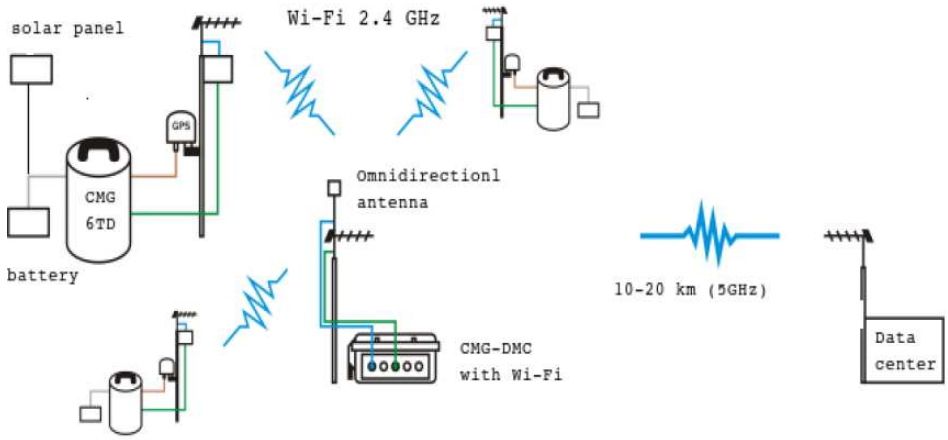


Figure 1.30: Diagram representation of the harware used in the seismic array with telemetry capability

and one computer for data reception and others computational tanks (processing, display, storage and Internet distribution of data).



Figure 1.31: A view of a seismic station used to send data to the observatory, at the top of the pole a Yagi antenna and a solar panel can be seen

1.5.2 Monitoring seismic arrays in real time by Earthworm

Earthworm system is an open source automatic earthquake processing software package written primarily in the C language. Originally developed by the United States Geological Survey (USGS), Earthworm now has many modules that are contributed by users all over the world. Earthworm has been an active open source project for over 15 years (Friberg et al., 2010). Seismometers and digitizers from different hardware manufacturers can export their data into shared memory rings. Various open source processing modules can operate in conjunction with shared memory data. Earthworm provides a common protocol for seismo-volcano networks to share waveforms, picks, etc. The EW software package controls the acquisition and processing of data efficiently and is widely used for volcano monitoring at observatories (Friberg et al., 2010). The EW data acquisition system is currently being used at the IGP Arequipa observatory. The telemetry system fed the data center with continuous digital seismic signal, these incoming data was then decompressed and made available by the SCREAM software developed by Guralp to handle data for their seismometers. Figure 1.32 graphically describes the test experiment. Data was introduced to the Earthworm (EW) system by the "SREAM to EW module" which data was converted from Guralp GCF format to EW format. EW system here handled the seismic data incoming from remote stations, in which the WAVE RING module is a data memory driven as a FIFO model (circular buffer) (Figure 1.32). The maximum volume of the virtual data was dependent on computer store capacity. We observed the data consumption of 500 MB/day for 30 channels.

The circles in Figure 1.32 represent shared dynamic-memory sectors, where data and messages flow through them to control all processing modules. WAVE-RING, PICK-RING and HYPO-RING modules work as servers in order that can be accessed by clients modules (represented by rectangles). The rectangles represent the processing modules. For instance, the WAVE SERVER is a data feed module that manages seismic data which can be requested by processing modules. The CARLSTATRIG and CARLSUBTRIG automatically perform seismic detections which is based on a STA/LTA algorithm. Earthquake detection procedure examines data in real-time from the WAVE SERVER module, if an earthquake is declared, detection results are reported on the HYPO-RING module. The MUSIC-3C block in Figure 1.32 corresponds to the method for source localization of seismo-volcano events that we implemented for this test experiment and is discussed in more detail in Chapter 2. The MUSIC-3C block is an algorithm that receives seismic array data incoming form the EW system and output information with their back-azimuth and incidence angle in realtime. The MUSIC-3C block was implemented for this experiment to process data from two ways. First, the MUSIC-3C continuously processed time window data provided by *WAVE-RING*. Second, the MUSIC-3C processed data from seismic event detected by the STA/LTA algorithm (see more of this algorithm in section 1.2.4) .

The core of the MUSIC-3C algorithm is written in C++ code, and graphical interface of waveforms in Labview 6.0. The flow chart in Figure 1.33 describes the first part of the MUSIC-3C algorithm. During the field experiment the MUSIC-3C estimated the slowness vectors from each array in real time. There were two scenarios to test array processing in real time: The first test consisted to continuously record time-series back-azimuth and incidence angle, basically, as soon as the EW system had

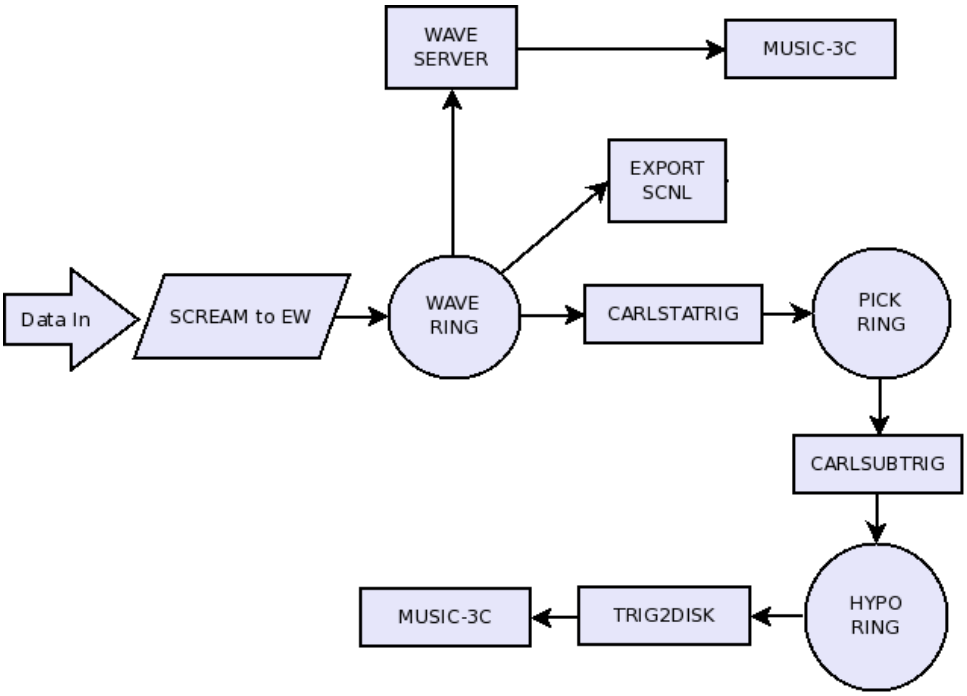


Figure 1.32: Earthworm system functional diagram

available new data into the "WAVE RING" module (circle block in Figure 1.32), the MUSIC-3C algorithm was alerted to get a time window of full array data to be processed and write their results on log files. Secondly, the EW system automatically detected seismic events using the STA/LTA algorithm, this detection method needs 2 modules such as shown in Figure 1.32: CARLSTATRIG and CARLSUBTRIG modules. The CARLSTATRIG module checks the incoming data using the STA/LTA algorithm, if an event is declared a message is sent to the "PICK RING" module, this "ring" shares messages about the seismic signal detected, so that 'CARLSUBTRIG and TRIG2DISK modules (Figure 1.33) can transfer all the event waveforms to be used by the MUSIC-3C algorithm. These two tests correctly performed estimations in realtime, we consider that the second test is usually advisable for volcano monitoring. Figure 1.33 shows in a flow diagram how the MUSIC-3C algorithm was configured to perform in this field experiment. At the beginning, data is recovered from all stations of the MISA and MISB array. Then all time series are identified by comparing information between data header and parameter tables and then fed to the next module with all relevant information. A sliding window processing is initialized to analyze multicomponent data. The source localization procedure is discussed in chapter 2, however top of Figure 1.34 depicts seismic waveforms corresponding to MISA and MISB antennas, detected by the EW system, and bottom of Figure 1.34 is the MISTI topography map, indicating the MISA and MISB antennas and the blue square is the localization for this earthquake located at the north-west of the MISTI crater. At this stage it is worth mentioning that the ISTI (Instrument software technogies inc.) supported the attending of a course on the Earthworm seismic monitoring software, in June 2011 (Saratoga Springs, New York).

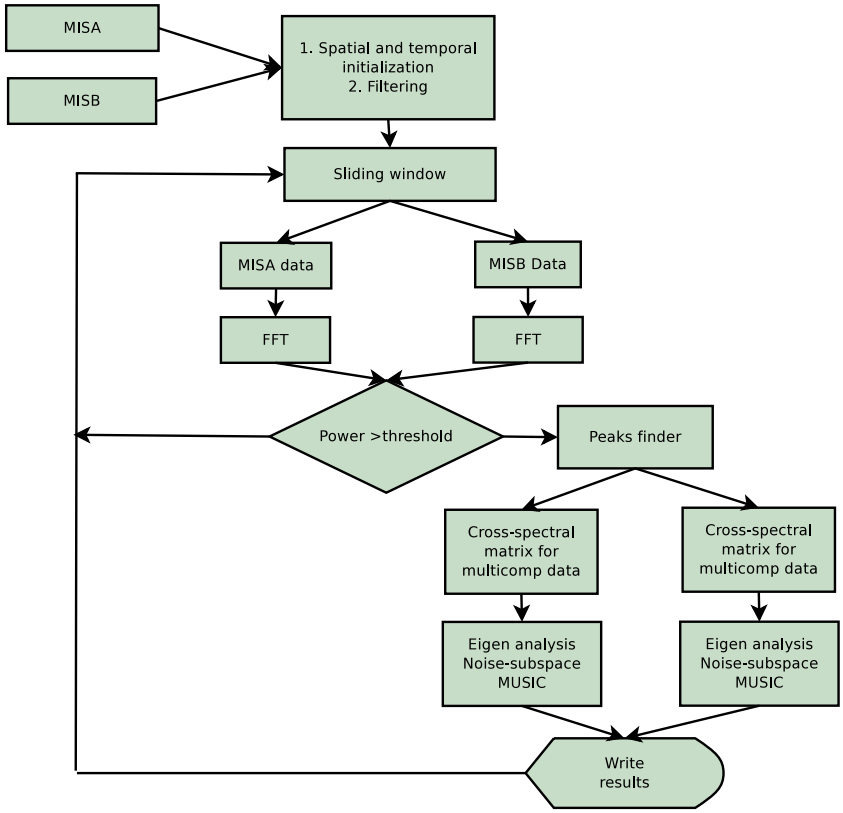


Figure 1.33: Flow diagram of MUSIC-3C algorithm

1.6 Conclusion and goals

After this first paper, the purpose of this thesis is to better understand the phenomenon of magmatic activity at Ubinas volcano, which is reflected in seismic activity by the instability of magma trying to reach the surface. The focus of this thesis is to propose a source localization algorithm based on three-component (3C) seismometer arrays and then their application on volcano monitoring. To achieve this objective, both real and synthetic datasets are available from a field experiment Ubinas 2009 and numerical simulations respectively.

Ubinas is the most active of seven volcanoes in southern Peru, also considered hazardous for the surrounding population and society. Historical eruptions was described as a predominantly vulcanian style (Thouret et al., 2005; Macedo et al., 2009). The Geophysical Institute of Peru (IGP) is responsible to research and monitoring all volcanoes in the country. The IGP operates a network of four seismic stations around Ubinas, in which seismic activities are broadly characterized by signals associated to vulcanian style explosive events, long period earthquakes and tremors. The source localization becomes a major challenge since this type of seismicity cannot be located by conventional means because the lack of impulsive phases in seismograms (Chouet, 2003).

This study focuses on the problem of finding the seismic source location in the multi-dimensional

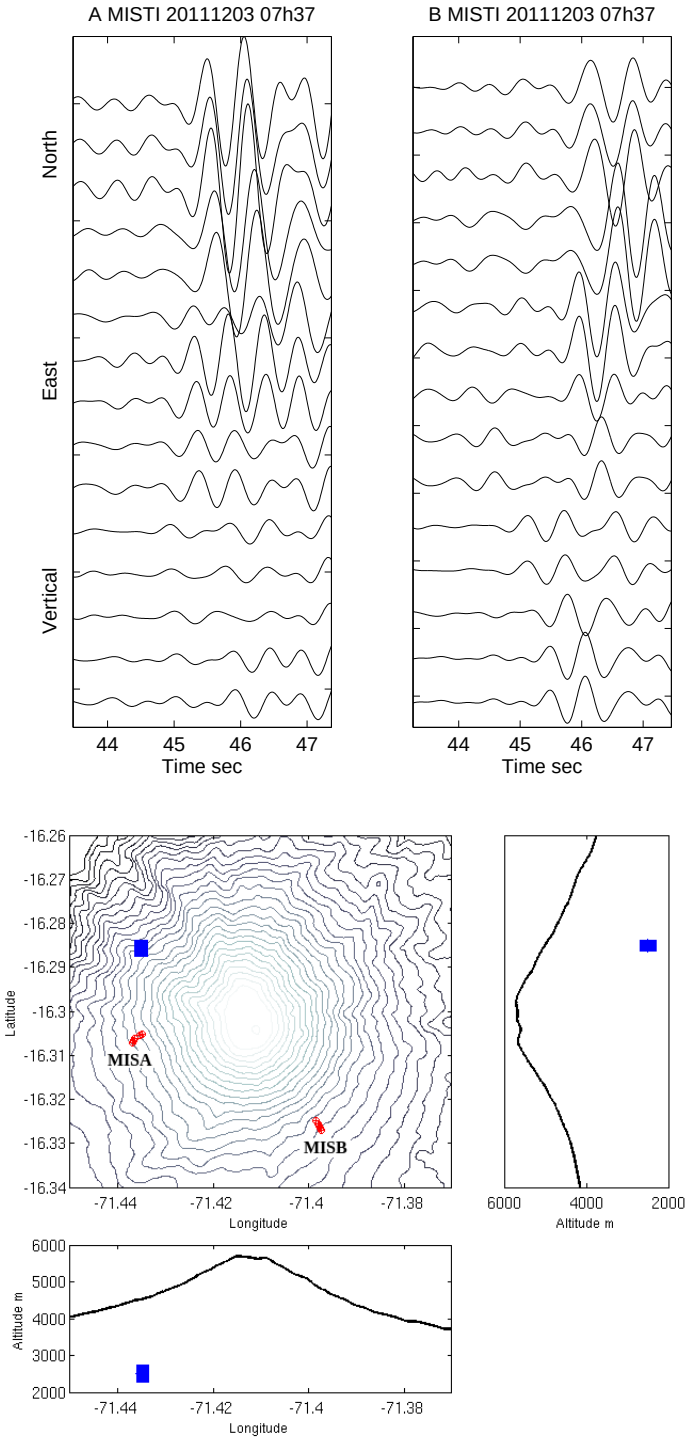


Figure 1.34: Top: Seismic waveforms of the MISA and MISB antennas of an earthquake occurred at Misti volcano. Bottom: 3D Misti topography map, with MISA and MISB antennas and blue square is the hypocenter estimated for this earthquake

space in which is contained within the data recorded by multidimensional seismic arrays. Three component (3C) seismic array provides data associated with a multidimensional spatially and temporally sampling of the seismic wavefield.
Another objective of this study is to apply the source localization method on seismic events and investigate their magmatic processes. A great variety of sustained seismic signals were identified during the field experiment on the Ubinas volcano in 2009, such signals classified as explosive, long period (LP) and tremor events. Most of these recordings are thought to be caused by the inherent instability of magmatic system at all time scales.

1.6.1 Contribution of this thesis

Before describing the structure of the second part of this dissertation, we briefly summarize our main contributions. The first contribution is the development of a new approach (MUSIC-3C) to locate sources from seismo-volcano signals. In this framework, we formulate an extension of the well-known high-resolution multiple signal classification (MUSIC) method, to be applied on data recorded by 3C seismic arrays. The performance of the MUSIC-3C method is then tested using a synthetic dataset created for Ubinas topography. We establish a set of conditions to accurately locate volcanic sources, focusing on the first arrival of the signal since this is the first sign received from the source (P-wave). For instance, STA/LTA algorithm (short-term-average over long-term-average) is used to identify the first arrival wave. Then, the MUSIC-3C method completes estimates of components of the slowness vector of the wave (a back-azimuth and an incidence angle). Finally, the source localization is computed with a probabilistic approach to constrain the source. A detail discussion of this issue is presented in Chapter 2.
The application of the MUSIC-3C method is the second contribution in this thesis. To explain the possible origin of vulcanian eruptions, we apply the MUSIC-3C method to signal associated to vulcanian events occurred during the field experiment at Ubinas in 2009. Vulcanian analysis is presented in Chapter 3.

1.6.2 Thesis structure

As a methodological and an applicative responses to these goals the thesis is organized in four chapters including the conclusion chapter.

- Chapter 1: Introduction (above, this section) is made up of 5 sections that deal of theoretical and practical definitions of a formalism about the nature of volcanoes and its monitoring; to provide a link the physical and methodological aspects. In section 1.1 is a general view of volcano seismology that presents the problematic and the motivation. In section 1.2 we describe the background about volcanoes in terms of the physic and volcano seismology; also we discuss components of seismic station and seismic data processing for volcano monitoring. In section 1.3 we describe volcanoes in south-america, specially Misti and Ubinas volcanoes in Peru. In

section 1.4 we report the seismic field experiment carried out at Ubinas volcano in 2009 with 3C seismic sensor arrays. we present seismic recordings in which preprocessings are done in order to put data ready to be processed. Continuous data is presented in the form of energy. A new approach is developed to perform time-frequency representation of continuous seismic data. Finally in section 1.5 we report the seismic field experiment carried out at Misti in 2011 with telemetry system for 3C seismic array and real time seismic data processing. we describe the hardware and the software used during this test experiment.

- From this stage forward, Chapter 2 (based on an article Inza et al. (2011)) contains the more extensive component of the framework that focuses upon the source localization from sismo-volcanic signals. This part of the framework shares 5 sections. In section 2.1, we first explore the state of the art of sismo-volcanic source localizations because they provide useful insights into the nature and dynamics of seismic sensor arrays on the volcanic unrest, and partly because this thesis reflects back upon their results. In section 2.2 we deal with the seismic sensor array in which data model is assumed throughout this study, introducing some statistical assumptions and review basic geometrical properties as the array response function. In section 2.3 we briefly review of different methods of source localization, such as high resolution and parametric algorithms in order to highlight the benefits and drawbacks in terms of resolution. In section 2.4, we conduct of the development of a source localization method (MUSIC-3C) for data recorded by multicomponent seismic arrays. This development is driven by the inter-spectral matrix formed from 3C-seismic sensor array data, in order that can be applied MUSIC algorithm. In section 2.5, synthetic sources are presented to be used with MUSIC-3C method in order to test slowness vector estimations. We then delve deeper into the locating synthetic dataset and compare with single component seismic arrays results. Finally, we present two examples of source localization with an long-period earthquake and an explosion event, recorded in the field experiment at Ubinas in 2009. In section 2.6 is dedicated to the discussion of the results and associated them to volcanic dynamics, highlighting the methodological and the interpretation about source localization.

- Chapter 3 (based on a recently submitted article to JVGR, Inza et al. (2013)) discusses the MUSIC-3C method on real data, we focus on vulcanian style eruptions at Ubinas volcano, performing the MUSIC-3C method to signals associated to vulcanian activity, recorded in the field experiment at Ubinas volcano in 2009. To complement our analysis about vulcanian eruptions, we consider tiltmeter data to analyze an explosive event in order to constrain more precisely the mechanism of vulcanian phenomena. Then we present the source localization of an explosion event. As usual to test the MUSIC-3C method, two synthetic sources are used to retrieve multiples sources. On the other hand, we analyze the source localization of a long-period (LP) earthquake recorder during the experiment. We discuss our results focusing on methodological and interpretative aspects about vulcanian activity on Ubinas.

- Chapter 4 presents the overall conclusions and perspectives on soruce localization of sismo-volcanic earthquakes and earthquake volcano interaction.

Chapter 2

Source Localization

2.1 Introduction

The sensor array signal processing addresses the problem of source localization of the collection of data recorded from sensors distributed in space. Multiple 3C sensor arrays with small aperture distributed over around the volcano provide the means for locating the position of seismic sources by crossing their slowness vectors. We begin by reviewing the state of the art in small aperture seismic arrays model which have provided great progress in seismology research (Goldstein and Archuleta, 1987; Rost and Thomas, 2002). The first seismic array with real time processing was deployed to monitor the seismicity from nuclear weapons testing, by the CTBTO (The Preparatory Commission for the Comprehensive Nuclear-Test-Ban Treaty Organization) group, which has deployed multiple-parameter sensor arrays, based on seismic, infrasound and hydrophone arrays around the world. Seismic antennas model for locating sources of seismic sources caused by volcanic activity has been formulated during the past two decades, in order to track the magmatic processes beneath volcanoes. Such as (Métaxian et al., 1997; Saccorotti et al., 2001; La Rocca et al., 2004; Almendros et al., 2004; Di Lieto et al., 2007) propose different approaches to identify volcanic sources. The processing is mainly based on time delays, giving an estimation of the slowness vector of the wavefront propagating across the array. Such studies have been constrained to seismic antennas composed by one-component (1C) seismometers. For example Saccorotti and Del Pezzo (2000); La Rocca et al. (2004) apply dense one-component array techniques to locate explosive activity at Stromboli. Di Lieto et al. (2007) use two dense one-component arrays of short period seismometers to track volcanic tremor at Mt. Etna. La Rocca et al. (2004); Del Pezzo et al. (1997) used a cross-correlation in time domain known as zero-lag cross-correlation. Furumoto et al. (1990) use the coherence of the signals to characterize the source of tremors recorded by a seismic antenna near the caldera of Izu-Ochima volcano, Japan. They observed post eruption activities by a 24 seismometers seismic array. The semblance analysis of the recorded data revealed some characteristics of the source, such as high frequency more than 5 Hz.
Rost and Thomas (2002) proposed a description of the theory and application of seismic antenna techniques, including the beamforming. One of the first applications of sensor array approach us-

ing a time-delay beamforming method to locate sources in volcanology was presented by Métaxian et al. (2002). This method is based on cross-spectral analysis for coherent wavefront recorded by the seismic antenna. As time delay between two similar signals corresponds the maximum of their cross-correlation function, as the cross spectrum is the Fourier transform of the cross-correlation function, the time delay is proportional to the slope of the cross-spectrum phase. So, the slowness vector has been estimated by a linear inversion as standard least squares, of delay times. Figure 2.1 shows examples of calculations of delay for a volcanic eruption and an earthquake, and shows the functions in time and in frequency involved in the calculation. Almendros et al. (2001a,b) presented a source

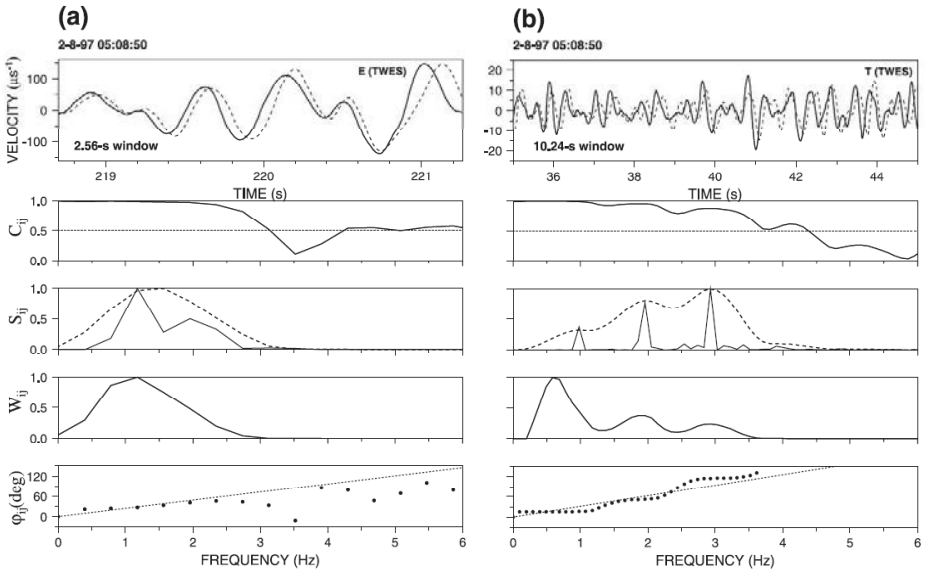


Figure 2.1: Examples of time delay calculation with the cross-spectral method. Two windows, including (a) the onset of an explosion and (b) a section of tremor, displayed in Figure 3, are analyzed. From top to bottom: the velocity seismograms obtained at sensors 1 (solid line) and 3 (dashed line) of array TWES; the coherency Cij of the two signals; the normalized (solid line) and smoothed (dashed line) cross-spectra Sij; the weight function Wij used for the linear fit; the cross-spectrum phase φ_{ij} (dots) and the straight line obtained by weighted linear fit. The slope of the line is proportional to the time lag between the records (from Metaxian et al. (2002))

localization method for volcanic sources, based on the high resolution method MUSIC. They located source areas of the long period (LP) seismicity and tremor observed at Kilauea, Hawaii (USA). This seismicity was recorded in 1997 during a campaign which three seismic antennas composed of one-component (1C) seismometers, were installed (each comprising 41, 22 and 12 sensors). The analysis was based on the estimation of back-azimuths and apparent slowness vetors of 1129 LP and 147 tremors. Depth is estimated from a velocity model. They used a probabilistic approach on a grid of the volcanic edifice. Figure 2.2 (extracted from Almendros et al. (2001b)) shows source localization for LP events on three regions, two superficial zones A and C located around 200 m north-east and 200 m south-east respectively from the cratere; and a third zone B located around 400 m depth.

In almost all studies using 1C seismic sensor arrays (vertical component), the depth estimation is

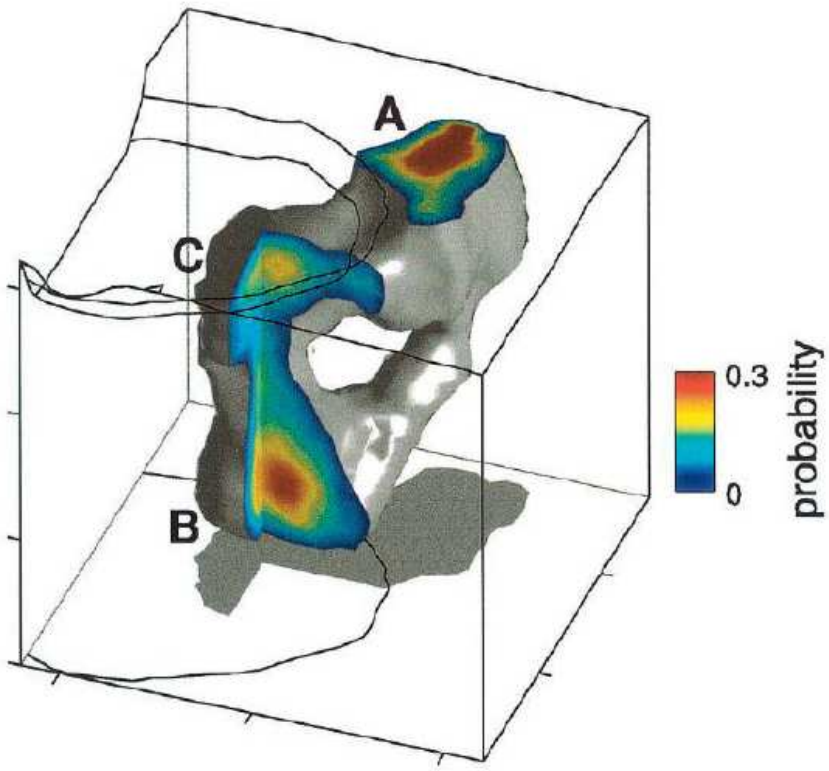


Figure 2.2: A 3-D view of the source region of LP events Kilauea (from Almendros et al. (2001b))

poorly resolved because the incidence angle is very difficult to determine. To overcome this problem we use arrays formed by triaxial sensors (3C). In this work, we focus on high resolution method to improve estimations of back-azimuth and incidence angle (related to the source depth) from array data recorded by three-component seismometers rather than one-component. The MUSIC (MUltiple SIgnal Classification) developed by Bienvenu and Kopp (1983); Schmidt (1986), is extended for 3C array data. This Chapter is part of an article published in GJI (Geophysical Journal International) as Seismo-volcano source localization with triaxial broad-band seismic array (Inza et al., 2011).

2.2 Processing approach

2.2.1 Seismic sensor array

Three-component broadband seismic array data is suitable for multidimensional signal processing techniques, where the size, shape, aperture of seismic antenna is designed in order to avoid spatial and temporal aliasing (Mars et al., 2004). We consider the scenario of an arbitrarily spaced array of triaxial sensors identically oriented and with identical instrument responses (Figure 2.3).
In order to explain the processing, we suppose P sources traveling from different directions, and arriving at the antenna with N triaxial sensors $(P < N)$. Equation (2.1) represents $w_n(t)$ the signal recorded by one component of the the *n-th* sensor in the time-space domain.

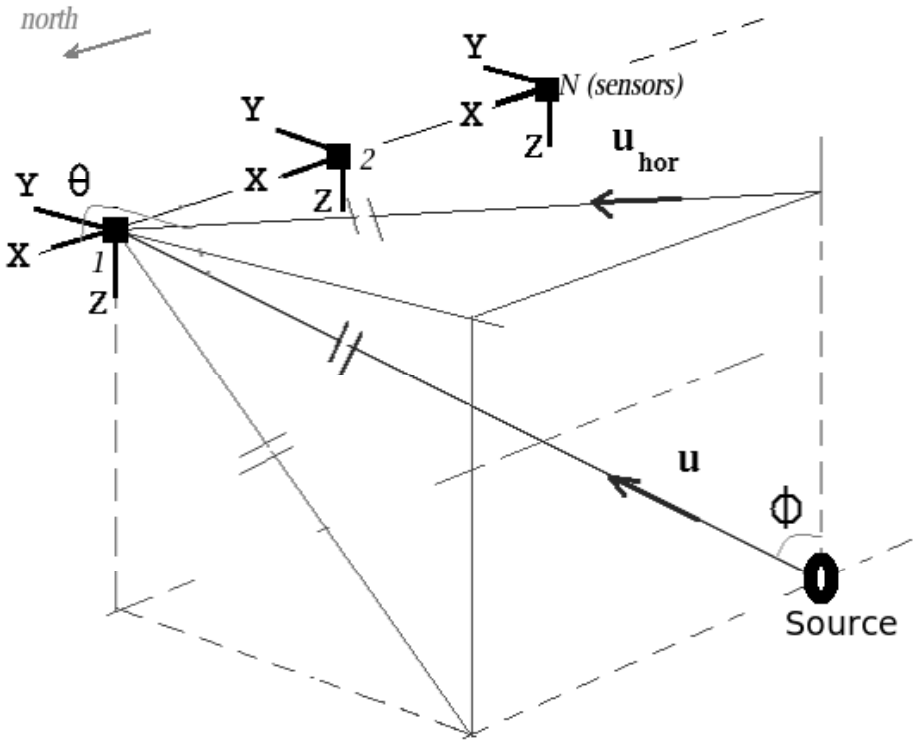


Figure 2.3: Model of triaxial sensors array for one source. XYZ represent North, East and Vertical components, θ and ϕ are the azimuth and incidence angles

$$w_n(t) = \sum_{p=1}^{P} s_p(t - \tau_{n,p}) + b_n(t); \;\; n = 0, 1, ..., N-1 \tag{2.1}$$

where, $s_p(t)$ is the $p-th$ source signal, $\tau_{n,p}$ is the relative propagation time delay of the $p-th$ source for the $n-th$ sensor and $b_n(t)$ represents the noise recorded of one component of the $n-th$ sensor. The

noise $b_n(t)$ is usually assumed to be uncorrelated with the sources and both temporally and spatially white with Gaussian variance σ_B^2. The corresponding relative propagation time delay is defined as

$$\tau_{n,p} = \mathbf{d_n} \cdot \mathbf{u}(\theta_p, \phi_p)$$

where, $\mathbf{d}_n$ is the relative position vector of sensor *n-th* with respect to the first sensor located arbitrarely at (0,0,0) and $\mathbf{u}(\theta_p, \phi_p)$ is the slowness vector indicating the direction of the *p-th* source. The slowness vector is expressed in the equation (2.2), note that its module is the reciprocal of velocity v_p of the uppermost layer beneath the array.

$$\mathbf{u}_p = \mathbf{u}(\theta_p, \phi_p) = \frac{1}{v_p} \begin{bmatrix} -\cos(\theta_p)\sin(\phi_p) \\ -\sin(\theta_p)\sin(\phi_p) \\ -\cos(\phi_p) \end{bmatrix} \tag{2.2}$$

The wave number vector is related to the slowness vector and is defined as:

$$\mathbf{k}_p = \frac{1}{\lambda_w}\frac{\mathbf{u}}{|\mathbf{u}|} = \frac{f_p}{v_p}\frac{\mathbf{u}}{|\mathbf{u}|}$$

where λ_w is the wavelength for the frequency f_p and velocity v_p of the wavefield of the *p-th* source. The frequency wave number (f-k) representation of equation (2.1) allows to express this signals as:

$$W_n(f_p) = \sum_{p=1}^{P} S_p(f_p) exp(-2\pi j(\mathbf{d}_n \cdot \mathbf{k}_p)) + B_n(f_p) \tag{2.3}$$

where, $j = \sqrt{-1}$ and $W_n(f_p)$, $S_p(f)$ and $B_n(f_p)$ are the Fourier transforms of $w_n(t)$, $s_p(t)$ and $b_n(t)$ respectively. The antenna output of the equation (2.1) for narrowband signals can be represented in matrix form as:

$$\mathbf{W}(\mathbf{f}) = \mathbf{A}(\theta, \phi)\mathbf{S}(\mathbf{f}) + \mathbf{B}(\mathbf{f}) \tag{2.4}$$

where, the $N \times P$ matrix $\mathbf{A}(\mathbf{f})$ is the "array response matrix" or "steering matrix" (Miron et al., 2006a) given in equation (2.5). The P sources are represented by a $P \times 1$ matrix as:

$$\begin{aligned} &\mathbf{S}(\mathbf{f}) = [S_1(f_1), ..., S_P(f_P)]^T \\ &\mathbf{A}(\theta, \phi) = [\mathrm{a}_1(\theta_1, \phi_1), \mathrm{a}_2(\theta_2, \phi_2), .., \mathrm{a}_P(\theta_P, \phi_P)] \\ &\mathrm{a}_p(\theta_p, \phi_p) = [1 \;\; exp(-2\pi j(\mathbf{d}_2 \cdot \mathbf{k}_p)) \;\; ..... \;\; exp(-2\pi j(\mathbf{d}_N \cdot \mathbf{k}_p))]^T \end{aligned} \tag{2.5}$$

Note that the array manifold vector $\mathrm{a}_p(\theta_p, \phi_p)$ depends on the path direction of the signal through the wave number vector $\mathbf{k}_p$ for frequency f_p from the source p. Usually, $\mathbf{A}(\mathbf{f})$ is a full rank matrix assuming that the array manifolds $\mathrm{a}_p(\theta_p, \phi_p)$ with different path directions are independent. Using the group of Equations in (2.5) on Equations (2.3) and assuming that one-source wave plane impinging

the antenna with back-azimut θ an incidence angle ϕ at frequency f_0, the antenna output for a narrow band sense can be written as:

$$W(f) = \begin{bmatrix} W_1(f) \\ W_2(f) \\ .... \\ W_N(f) \end{bmatrix} = \begin{bmatrix} 1 \\ e^{-2\cdot\pi j\cdot f_0\cdot \mathbf{u}(\theta,\phi)\cdot \mathbf{d}_2} \\ .. \\ e^{-2\cdot\pi j\cdot f_0\cdot \mathbf{u}(\theta,\phi)\cdot \mathbf{d}_n} \end{bmatrix} \cdot S(f) + B(f) = A(\theta,\phi)\cdot S(f) + B(f) \tag{2.6}$$

where, $W_n(f)$ is the Fourier transform of the signal with dominant frequency f_0 and $A(\theta,\phi)$ is *N x 1* matrix, it called manifold matrix which contains the phase delay information of the impinging signal to the array. In the same way, the final version of the model takes the following form in time domain as Equation (2.7):

$$w(t) = A(\theta,\phi)s(t) + b(t) \tag{2.7}$$

The purpose of this work is to develop and test the MUSIC-3C algorithm and show that we obtain a more robust estimation of the azimuth angle θ and a reliable incidence angle ϕ related to the source depth determination. This implies the sensors spatial position are known.

2.2.2 Array Response Function

In this section, we examine the array response function (ARF) to an external plane wavefront (far field), in sensor outputs as a time-series waveform. The seismic antenna consists of a set of three component seismometers (isotropic sensor) located along the X-axis (Figure 2.3), in order to sample the signal spatially at their relative positions. The ARF require knowledge on spatial parameters such as number of elements, inter-sensor distances in order to achieve a satisfactory performance. The purpose of the array response function was to evaluate the sensitivity and resolution of seismic antenna recording wavefronts with different wavelengths. Classically, an antenna operates as a wavenumber filter, or wavelength filter. Assuming a plane wave propagating through the antenna with a back-azimuth θ and an incidence angle ϕ, the wavenumber vector ($\mathbf{k}$) for this wave, in Cartesian coordinates, can be written as Equation (2.8) (Rost and Thomas, 2002):

$$\mathbf{u}(\theta,\phi) = \frac{1}{f}\mathbf{k}(\theta,\phi) \tag{2.8}$$

where f is the wavefront frequency. For an antenna composed by N seismometers, the wavefront $s(t)$ recorded by the n-th seismometer with the relative position of $\mathbf{r_n}$, can be expressed as Equation (2.9):

$$w_n(t) = s(t - \mathbf{d_n}\cdot\mathbf{u}) \tag{2.9}$$

Consequently, the optimal beam of the N sensors in the antenna for any slowness $\mathbf{u}$ relative to slowness $\mathbf{u_0}$ can be represented by Equation (2.10):

$$\widehat{w}(t) = \frac{1}{N}\sum_{j=1}^{N} s(t - \mathbf{d_j}\cdot(\mathbf{u} - \mathbf{u_0})) \tag{2.10}$$

The energy E of this beam can be computed by summing the square amplitude of $\widehat{w}(t)$. According to the Parseval theorem and Fourier shift properties, E can be defined as a function of waveforms **k**, using Equation 2.8, it can be written in the frequency domain as:

$$E(\mathbf{k}-\mathbf{k_0}) = \int_{-\infty}^{+\infty} |s(f))|^2 \left| \frac{1}{N} \sum_{j=1}^{N} exp(i \cdot 2\pi \left[\mathbf{k}-\mathbf{k_0}\right] \cdot \mathbf{d_n}) \right|^2 df \tag{2.11}$$

where k_0 is wevenumber related to k_0. Consequently, the array response function $A(\mathbf{k})$ is expressed as:

$$|A(\mathbf{k}-\mathbf{k_0})|^2 = \left| \frac{1}{N} \sum_{j=1}^{N} exp(i \cdot 2\pi \left[\mathbf{k}-\mathbf{k_0}\right] \cdot \mathbf{d_n}) \right|^2 \tag{2.12}$$

In the case of surveying the array response function for the horizontal plane, the wavenumber should be equal $\mathbf{k} = (k_x, k_y)$. According to the spatial Nyquist wavenumber, a minimum of two grid points per wavelength are theoretically enough for the spatial sampling of the wavefront. For the WUBI antenna, with an X-north aperture of 321 m and a Y-east aperture of 315 m, the array response function for this antenna is shown in Figure 2.4. Analyzing this results gives the smallest wavenumber around 0.5 km^{-1}, and the maximum wavenumber without aliasing around 18 km^{-1}. With these characteristics, it is possible to discriminate the wavelengths associated with Ubinas Volcano. For example, for an explosive quake recorded by the WUBI antenna, the wavenumbers were identified as 5 km^{-1} (f = 1.1 Hz; wave velocity, 1.4 km/s), or 6 km^{-1} (f = 1.5 Hz; wave velocity, 1.5 km/s), which were in good agreement with the antenna resolution.

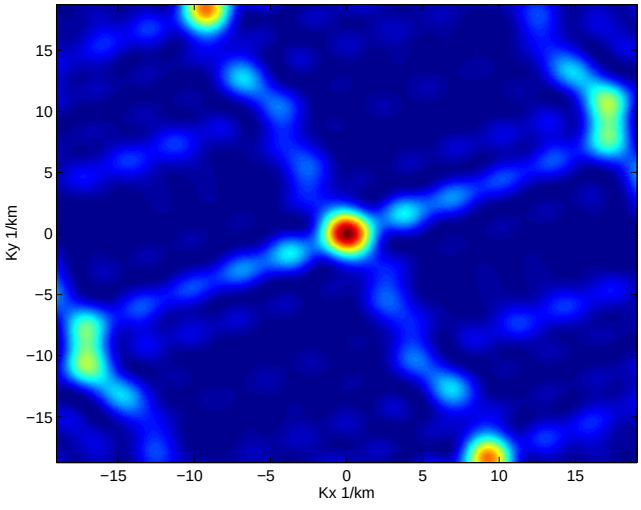


Figure 2.4: WUBI array response function A.

2.3 Methods of array processing

In this section, it is to formulate the source localization problem mathematically, providing an overview of the most notable source localization methods in order that can process seismic array data. We discuss some of their advantages and limitations.

2.3.1 Second-order statistic

Most modern source localization methods are relied on statistical characterization of the sensor outputs with second-order statistics (Krim and Viberg, 1996; Miron et al., 2006a). The statistic allows to describe the cross-spectral (or cross covariance for time domain) information among sensors. The spatial inter-spectral matrix of the outputs (Equation 2.6) is:

$$\Gamma = \xi\left[W(f)W^H(f)\right] = \mathbf{A}(\theta,\phi)\xi\left[S(f)S^H(f)\right]\mathbf{A}^H(\theta,\phi) + \xi\left[B(f)B^H(f)\right] \tag{2.13}$$

here, symbols $(.)^H$ denote complex conjugate and transpose (Hermite) and ξ the mathematical expectation operator. Assuming, they are uncorrelated sources for the case of multiple sources, temporal whiteness and symbolizing $\delta_{t,s}$ the Kronecker delta. The source matrix is defined as $\xi\left[S(f)S^H(f)\right] = \mathbf{P}\delta_{t,s}$ and the noise matrix is modeled as given by $\xi\left[B(f)B^H(f)\right] = \sigma_b^2\mathbf{I}\delta_{t,s}$. It is assumed the noise has the same level σ_b^2 in all sensors, and it is uncorrelated between sensors. The source covariance matrix $\mathbf{P}$ is often assumed non-singular. Then the spatial inter-spectral matrix can be rewritten as Equation (2.14),

$$\Gamma = \mathbf{A}(\theta,\phi)\mathbf{P}\mathbf{A}^H(\theta,\phi) + \sigma_b^2\mathbf{I} \tag{2.14}$$

with $\mathbf{I}$ the identity matrix and σ_b^2 denotes the noise power. Since the exact expectation ($\xi[.]$) is unknown, a practical estimation of the inter-spectral matrix for M samples in outputs array, is used as

$$\widehat{\Gamma} = \frac{1}{M}\sum_{1}^{M} W(f)W^H(f) \tag{2.15}$$

However, for the case of time domain $\xi\left[s(t)s^H(t)\right] = \mathbf{P}\delta_{t,s}$, sampling M points in time, it is given as:

$$\mathbf{R} = \xi\left[w(t)w^H(t)\right] = \mathbf{A}(\theta,\phi)\mathbf{P}\mathbf{A}^H(\theta,\phi) + \sigma_b^2\mathbf{I} \tag{2.16}$$

$$\widehat{\mathbf{R}} = \frac{1}{M}\sum_{1}^{M} w(t)w^H(t) \tag{2.17}$$

2.3.2 High resolution methods

Existing source localization procedures may be divided into two main categories: those spectral-based and the parametric approaches in order to estimate the direction-of-arrival signals. The high

resolution spectral-based methods are basically divided into the beamforming CAPON approaches and subspace methods. Parametric approaches are based on maximum likelihood method, which in turn divided in deterministic and stochastic Rost and Thomas (2002); Johnson and Dudgeon (1993). Most array of sensors used in volcano monitoring is typically configured in small aperture in order to record coherent wavefront, and data is processed by using spectral-based. It also assumes a plane wave arriving at the array as a far-field scenario.

Beam-forming Capon's MVDR

A well-known method was proposed by Capon (1969), also called Minimum Variance Distortionless Response (MVDR). It attempts to minimize the variance due to noise, while keeping the gain in the direction of steering equal to unity: $\mathbf{p}_{CAP}(\theta,\phi) = arg[min_p(\xi[\mathbf{p}^H ww^H \mathbf{p}])]$, subject to $Re[\mathbf{p}^H A(\theta,\phi)] = 1$. The optimal Capon weight ($\mathbf{p}_{CAP}$) can be optimized by using Lagrange multipliers (Krim and Viberg, 1996), resulting as Equation (2.18).

$$\mathbf{p}_{CAP}(\theta,\phi) = \frac{\widehat{R}^{-1}A}{A^H\widehat{R}^{-1}A} \tag{2.18}$$

The weight in Equation (2.18) in turn leads to the spatial spectrum has an analytic expression, such as in Equation (2.19).

$$P_{CAP}(\theta,\phi) = \frac{1}{A^H\widehat{R}^{-1}A} \tag{2.19}$$

The main advantage of this method is a substantial increase in resolution compared to conventional Beamforming. The beamformer uses very single degree of freedom to concentrate the received energy along one direction, namely the bearing of interest. An additional benefit is the lower amount of ripple in the side-lobes (Johnson and Dudgeon, 1993).

Subspace-based method: MUSIC

Bienvenu and Kopp (1983) and independently Schmidt (1986) presented a measurement model in the case of sensor arrays of arbitrary forms. The resulting algorithm was called MUSIC (*multiple signal classification*). MUSIC is a prominent method eigenstructure based source localization estimator. The underlying idea is to separate the eigenspace of the covariance matrix of sensor outputs into the signal and noise subspaces. The sensor output correlation matrix admits the following decomposition of $\mathbf{R}$ (Equation (2.20)), in order to ensure the positivity of this Hermitian matrix (Marcos, 1998; Stoica and Nehorai, 1991).

$$\mathbf{R} = \mathbf{A}(\theta,\phi)\mathbf{P}\mathbf{A}^H(\theta,\phi) + \sigma_b^2\mathbf{I} = \mathbf{U}\Lambda\mathbf{U}^H \tag{2.20}$$

The eigenspace decomposition of $\mathbf{R}$ can be written as Equation (2.21), by:

$$\mathbf{U}\Lambda\mathbf{U}^H = \mathbf{U}_s\Lambda_s\mathbf{U}_s^H + \mathbf{U}_n\Lambda_n\mathbf{U}_n^H = \mathbf{R} \tag{2.21}$$

Where $\mathbf{U}$ is the eigenvector (unitary vectors) matrix, $\Lambda = diag\lambda_1, \lambda_2, ..., \lambda_N$ a diagonal real matrix and positive eigen-values for the N sensor array, so such $diag\lambda_1 > \lambda_2 >, ..., > \lambda_N$. On the one hand, the largest eigenvalues represent to the signal subspace. On the other hand smallest eigenvalues and their corresponding eigenvetor represent the noise subspace. Due to the orthogonality of eigensubspaces corresponding to different eigenvalues, the noise subspace is orthogonal to the steering vectors corresponding to the direction of wave propagation ($\mathbf{U}_n\mathbf{A}(\theta,\phi)$). MUSIC is the squared norm of this term into the denominator, which leads to very sharp estimate of the position of the sources. Take into account, the orthogonal projector onto the noise subspace is estimated as $\widehat{\Pi}^{\perp} = \widehat{\mathbf{U}}_n\widehat{\mathbf{U}}_n^H$. The MUSIC spatial spectrum is then defined as Equation (2.18), by:

$$P_{MUSIC}(\theta,\phi) = \frac{1}{A^H(\theta,\phi)\widehat{\Pi}^{\perp}A(\theta,\phi)} \tag{2.22}$$

2.3.3 Parametric Source Localization

Maximum Likelihood

In contrast with spectral based methods, in parametric approaches, the model are estimated without depicts a spectrum. They are more efficient than spectral based (Krim and Viberg, 1996) for scenarios involving highly correlated signals. The price to pay for this increased efficiency is that the algorithms typically require a numerical optimization to find the estimates. A variety of methods resides under the maximum likelihood (ML) header according the signal model. When it is deterministic the method is called as Deterministic Maximum Likelihood (DML), when the signal model is Gaussian the method is referred to Stochastic Maximum Likelihood (SML). One of the key assumptions used in the formulation of both the DML and SML estimators is the so-called *spatially homogeneous white noise*.

Deterministic Maximum Likelihood - DML

The noise is modeled as a stationary Gaussian white random process whereas the signals waveforms are deterministic and unknown. Assuming spatially white and circularly noise, symmetric and identically distributed imaginary parts is given by $\xi[\mathbf{b}(t)\mathbf{b}^H(s)] = \sigma_b^2\mathbf{I}\delta_{t,s}$ and $\xi[\mathbf{b}(t)\mathbf{b}^T(s)] = 0$. Thus, the received signal defined by our data model in Equation (2.7) can also be assumed as a circularly symmetric and Gaussian white random process with mean $\mathbf{A}(\theta,\phi)\mathbf{s}(t)$ and covariance $\sigma_b^2\mathbf{I}$. The likelihood function is the probability density function (PDF) of array outputs given the unknown parameters. The PDF for single snapshot vector $\mathbf{w}(t)$ is the complex Gaussian variable, described as :

$$\frac{1}{(\pi\sigma_b^2)^N}e^{-\|\mathbf{w}(t)-\mathbf{A}\mathbf{s}(t)\|^2/{\sigma_b}^2} \tag{2.23}$$

with $\|.\|$ denotes the Euclidean norm. In addition, for M-snapshots in time, the likelihood function for all unknown parameters (the DOA θ, ϕ, $\mathbf{s}(t)$ and the noise variance σ_b^2) is obtained as :

$$L_{DML}(\theta, \phi, s(t), \sigma_b^2) = \prod_{t=1}^{M} \frac{1}{(\pi\sigma_b^2)^N} e^{-\|\mathbf{w}(t)-\mathbf{A}\mathbf{s}(t)\|^2/{\sigma_b}^2} \tag{2.24}$$

where θ, ϕ is the vector of source locations. The log-likelihood function is:

$$l_{DML}(\theta, \phi, s(t), \sigma_b^2) = -N\ log\sigma_b^2 + \frac{1}{\sigma_b^2 M} \sum_{t=1}^{M} -\|\mathbf{x}(t) - \mathbf{A}\mathbf{s}(t)\|^2 \tag{2.25}$$

furthermore, ${\hat{\sigma_b}}^2$ and $\hat{s}(t)$ in Equation (2.25) can be computed by:

$${\hat{\sigma}_b}^2 = \frac{1}{N} \mathrm{Tr}\{\Pi_{\mathbf{A}}^{\perp} \hat{\mathbf{R}}\} \tag{2.26}$$

$$\hat{s}(t) = \mathbf{A}^{\dagger} \mathbf{w}(t) \tag{2.27}$$

in addition, the estimation of sample covariance matrix is given by $\hat{\mathbf{R}} = \frac{1}{M} \sum_{t=1}^{M} \mathbf{w}(t)\mathbf{w}^H(t)$. The Moore-Penrose pseudo-inverse of $\mathbf{A}$ is obtained by $\mathbf{A}^{\dagger} = (\mathbf{A}^H\mathbf{A})^{-1}\mathbf{A}^H$. The orthogonal projector $\Pi_{\mathbf{A}}^{\perp}$ onto the null space of $\mathbf{A}^H$ is denoted by $\Pi_{\mathbf{A}}^{\perp} = \mathbf{I} - \Pi_{\mathbf{A}}$. Substituting the equations (2.26) and (2.27) into equation (2.25), the DML method finally estimates signal parameters by the following equation:

$$\hat{\theta, \phi}_{DML} = \arg\{\min_{\theta} \mathrm{Tr}\{\Pi_{\mathbf{A}}^{\perp} \hat{\mathbf{R}}\}\} \tag{2.28}$$

This process consists of projecting the received signal $\mathbf{w}(t)$ onto the subspace $\Pi_{\mathbf{A}}^{\perp}$, which is orthogonal to the anticipated signal subspace, and finding a minimum power value when the projector indeed removes all the true signal components (Johnson and Dudgeon, 1993; Krim and Viberg, 1996).

Stochastic Maximum Likelihood

Differing from the deterministic maximum likelihood (DML) method presented above, the stochastic maximum likelihood (SML) is built from modeling the signal waveforms as a Gaussian random processes. This model works well if measurements are obtained by filtering waveforms with a narrow band-pass filter. It assumes that the signals are zero-mean with second-order properties as

$$\xi\{s(t)s^H(t)\} = \mathbf{P}\delta_{t,s} \qquad\qquad \xi\{s(t)s^T(t)\} = 0$$

Thus, the observation vector $\mathbf{w}(t)$ is a white, zero-mean and circularly symmetric Gaussian random vector. Moreover, its covariance matrix is given by:

$$\mathbf{R} = \mathbf{A}(\theta, \phi)\mathbf{P}\mathbf{A}^H(\theta, \phi) + \sigma_b^2\mathbf{I}$$

In this case, the likelihood function depends on θ, ϕ, $\mathbf{P}$ and σ_b^2 and the negative log-likelihood function is proportional to:

$$\frac{1}{M}\sum_{t=1}^{M}\|\Pi_{\mathbf{A}}^{\perp}\mathbf{w}(t)\|^2 = \mathrm{Tr}\{\Pi_{\mathbf{A}}^{\perp}\hat{\mathbf{R}}\} \tag{2.29}$$

Assuming K signals impinging the sensor array of N elements, for a θ; according Johnson and Dudgeon (1993); Krim and Viberg (1996), σ_n^2 and $\mathbf{P}$ can be represented by:

$$\sigma_{SML}^2 = \frac{1}{N-K}\mathrm{Tr}\{\Pi_{\mathbf{A}}^{\perp}\} \tag{2.30}$$

$$\hat{\mathbf{P}}_{SML}(\theta) = \mathbf{A}^{\dagger}(\hat{\mathbf{R}} - \hat{\sigma}_{SML}^2(\theta,\phi)\mathbf{I})\mathbf{A}^{\dagger H} \tag{2.31}$$

Thus, substituting the estimates of parameters (σ^2 and $\mathbf{P}$) in Equation (2.30) and Equation (2.31) to the log-likelihood function shown by (2.29), the SML method estimator are achieved by finding the minimum value of the following equation:

$$\hat{\theta,\phi}_{SML} = \arg\{\min_{\theta} log|\mathbf{A}\hat{P}_{SML}(\theta)\mathbf{A}^H + \hat{\sigma}_{SML}^2(\theta)\mathbf{I}|\} \tag{2.32}$$

2.3.4 Discussion and comparison of source localization methods

Beamforming is a source localization method robust and simple, but it has a limited resolution in terms of the ability to distinguishing closely spaced signal sources. Figure 2.5 depicts the results for source localization spectra-based methods, such as Beamforming (Figure 2.5a), Capon and MUSIC (Figure 2.5b). This is a simulation with two far-field waves separated by 10 degrees (SNR=20dB) impinging on a uniform linear array with 8 identical sensors spaced at half-wavelength. Beamforming is not able to separate the two sources due to the Rayleigh resolution limit, the two picks are merged. Capon and MUSIC improve the resolution capabilities of Beamforming and are able to resolve the two sources well.

Maximum likelihood estimators are parametric, results are not a spectrum, however the results are a set of point estimates of source locations. In general they are more robust than spectra-based source localization methods, but they are heavy in terms of computer. The drawback of maximum-likelihood source localization is initialization parameters that need special attention to ensure convergence to global minimal. A drawback of the DML method is that the dimension of the parameter vector increases without bound of a number of incoming snapshots grows. On the other hand, MUSIC method yields asymptotically unbiased and efficient estimates of the DOA, equivalent to DML method (Stoica and Nehorai, 1989; Wong and Zoltowski, 2000). MUSIC in contrast of ML methods: 1) It does not require precise initialization parameters. 2) Demand less computation 3) It does not require any a priory information of the joint probability density relating to the sources. 3) Produce at moderate SNR estimation performance.

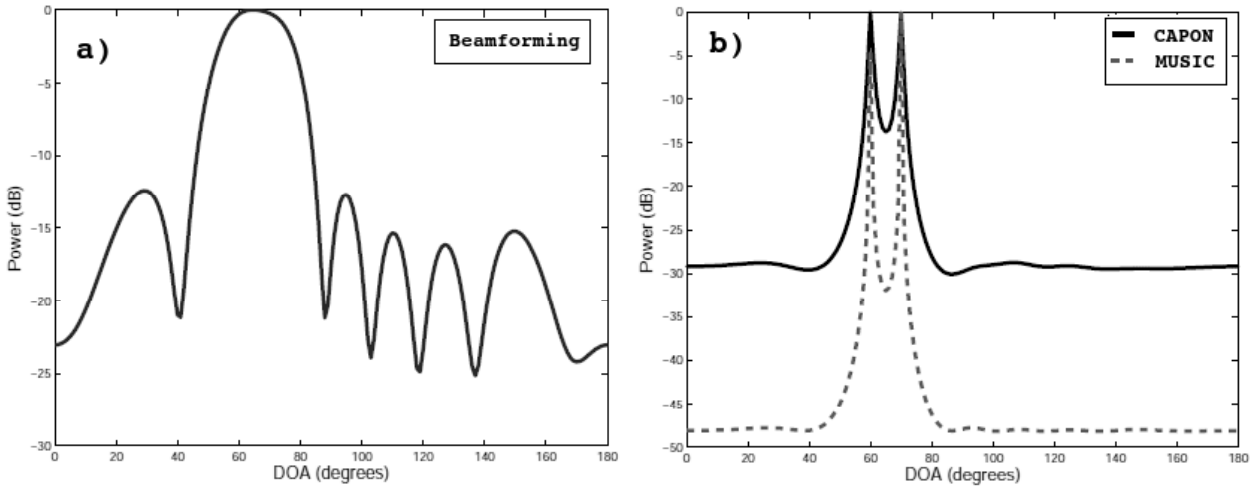


Figure 2.5: Spectra of 8 sensors linear array spaced at half-wavelength, with two sources in 60 and 70 degrees, SNR=20dB, a) Beam-forming method. b) Capon and MUSIC methods

From a brief review of source localization based on seismic array applied in volcano monitoring, number of techniques based on spectra methods have been developed by several authors (Goldstein and Chouet, 1994; Métaxian et al., 1997; Saccorotti et al., 2001; La Rocca et al., 2004; Almendros et al., 2004; Di Lieto et al., 2007). On the other hand, sensor arrays are used in a way range of applications in earth-sciences, others methods are found in order to improve resolution algorithms such as, maximum a posteriori on noise subspace fitting (MAP-NSF) method, root-MUSIC, ESPRIT, MUSIC-4 (high order), vector array method (Quaternion-MUSIC, 2D-MUSIC). Table 2.3.4 summarize the comparison of these methods (table taken from the thesis Gipsa-JIANG 2012). We note that Quaternion-MUSIC method is used to extract seismic attributes and separate seismic sources on multichannel seismic data set, in terms of polarized wavefront (Miron et al., 2006b).

Method	Prior knowledge of order	Assumption of Signal Type
Beam-forming	No	Gaussian
MUSIC	Yes	All types
DML	No	-
SML	No	-
MAP-NSF	No	-
Esprit	Yes	Gaussian
Root-MUSIC	Yes	Gaussian
MUSIC-4	Yes	No
Q-MUSIC	Yes	Gaussian
2D-MUSIC	Yes	Gaussian

Table 2.1: Comparison of the existing source localization methods based on different criterion (Prior knowledge of model order, Assumption of Signal Type and Array Geometries)

2.4 MUSIC-3C algorithm

MUltiple SIgnal Classification (MUSIC) is an eigenstructure subspace analysis method, that is widely used in geophysics, particularly to enhance the signal-to-noise ratio in order to estimate the direction of arrival of multiple waves impinging the array. The MUSIC uses the noise-subspace eigenvectors of the input cross-spectral matrix data and the steering matrix to form a null spectrum. The MUSIC method is applicable to an irregularly spaced array such as explained in (Paulus and Mars, 2010; Wong and Zoltowski, 2000).

Multidimensional seismic antenna composed by three-component seismometer provides multidimensional matrix data. Equation 2.33 described the three dimensional matrix of M samples of time-series seismic data set recorded by 3C seismic antenna composed by N sensors. However, *z(t)*, *x(t)* and *y(t)* represent each component of 3C seismometers (Figure 2.3), for vertical, north and east components respectively. Note that, the vertical *z(t)* component towards the bottom of the earth. Indeed, the standard convention for installation is to orient all 3C seismometers such that horizontal components are aligned with true north geographic and east respectively.

$$w(t) = \begin{bmatrix} x_{1,1} & x_{1,2} & \dots & x_{1,M} \\ \dots & \dots & \dots & \dots \\ x_{N,1} & x_{N,2} & \dots & x_{N,M} \\ y_{1,1} & y_{1,2} & \dots & y_{1,M} \\ \dots & \dots & \dots & \dots \\ y_{N,1} & y_{N,2} & \dots & y_{N,M} \\ z_{1,1} & z_{1,2} & \dots & z_{1,M} \\ \dots & \dots & \dots & \dots \\ z_{N,1} & z_{N,2} & \dots & z_{N,M} \end{bmatrix} = \begin{bmatrix} x_{N,M}(t) \\ y_{N,M}(t) \\ z_{N,M}(t) \end{bmatrix} \tag{2.33}$$

We focus on primary signal (P-wave), because it is the first seismic signal received by the seismometers. Therefore, a data window for all components of N triaxial sensors of the array is selected, including the first arrival waves to yield the source information. The signal processing is done in the frequency domain rather than the time domain in order to identify dominant bins. A convenient way to find the dominant frequencies f_o is to integrate the power spectral density (averaged spectrum) of a length of time window of each component enough to represent the first arrival signal. It makes use of coherent structures of the seismic signal in order to ensure real representation of the signal radiated from the seismic source.

To explain the method, we suppose that the averaged spectrum of the time window selected previously shows a peak in the frequency f_o, to be a priori knowledge of the desired signal. The sampling of this peak leads to consider M intervals around it. A frequency domain data model (Equation 2.34) is constructed by using time-series data (in frequency domain), taking into account the frequency f_0 the center of the interval, so that M is a odd number.

$$W(f_0) = \left(\begin{bmatrix} X_{1,-\frac{M-1}{2}} & .. & X_{1,0} & .. & X_{1,\frac{M-1}{2}} \\ .. & .. & .. & .. & .. \\ X_{N,-\frac{M-1}{2}} & .. & X_{N,0} & .. & X_{N,\frac{M-1}{2}} \end{bmatrix}, \begin{bmatrix} Y_{1,-\frac{M-1}{2}} & .. & Y_{1,0} & .. & Y_{1,\frac{M-1}{2}} \\ .. & .. & .. & .. & .. \\ Y_{N,-\frac{M-1}{2}} & .. & Y_{N,0} & .. & Y_{N,\frac{M-1}{2}} \end{bmatrix}, \right.$$

$$\begin{bmatrix} Z_{1,-\frac{M-1}{2}} & .. & Z_{1,0} & .. & Z_{1,\frac{M-1}{2}} \\ .. & .. & .. & .. & .. \\ Z_{N,-\frac{M-1}{2}} & .. & Z_{N,0} & .. & Z_{N,\frac{M-1}{2}} \end{bmatrix}) \tag{2.34}$$

where, $X_{1,0}$, $Y_{1,0}$ and $Z_{1,0}$ are complex numbers which represent the signal for the frequency f_0, for the time-series window. Since we consider as realization each component, the *m-th* sample can be represented as *N x 3* matrix data, then the *m-th* sample can be represented as *Nx3* matrix data (*N* is the number of triaxial sensor).

$$\mathbf{W}_m = [Xn_m \; Yn_m \; Zn_m] \qquad m = 1,2,....,M \tag{2.35}$$

where, Xn, Yn and Zn represent the data vector of each component of the sensor for the sample m. Then the cross-spectral correlation estimates over M frequencies bins is defined in the equation (2.36) (Paulus et al., 2005).

$$\widehat{\Gamma}_W = \sum_{m=1}^{M} \xi \left\{ \mathbf{W}_m \mathbf{W}_m^{\mathbf{H}} \right\} \tag{2.36}$$

ξ denote the mathematical expectation operator and $\mathbf{H}$ is the conjugate transpose. Following the assumption made for the equation (2.37), the cross-correlation $\widehat{\Gamma}_W$ can be writen as (Paulus et al., 2005; Miron et al., 2005; Paulus and Mars, 2010).

$$\begin{aligned} &\widehat{\Gamma}_W = A\,\xi\{\mathbf{S}\mathbf{S}^H\}A^H + \xi\{\mathbf{B}\mathbf{B}^H\} \\ &\widehat{\Gamma}_W(f_o) = A(f_o)\widehat{\Gamma}_s(f_o)A^H(f_o) + \sigma_B^2(f_o)\mathbf{I} \\ &\widehat{\Gamma}_s(f_o) = \xi\{\mathbf{S}\mathbf{S}^H\} \end{aligned} \tag{2.37}$$

Where, $\widehat{\Gamma}_s(f_o)$ is the cross-spectral matrix of the source, $\mathbf{I}$ is the identity matrix and σ_B^2 is the variance of the noise. The eigenstructure of $N \times N$ cross-correlation matrix $\widehat{\Gamma}_W$ solves the eigenvalues λ_n and eigenvectors $\mathbf{v_n}$ respectively (N=number of sensors), given by:

$$\widehat{\Gamma}_W = \sum_{n=1}^{N} \lambda_n \mathbf{v_n} \mathbf{v_n^H}$$

considering the eigen-values as:

$$\lambda_1 \geq ... \geq \lambda_P \geq \lambda_{P+1} > ... > \lambda_N \approx \sigma^2$$

The *P* largest eigenvalues correspond to the signal subspace, while *N-P* eigenvalues correspond to the noise subspace, usually no longer equal to σ_B^2. Considering to $\Pi^{\perp}$, the orthogonal projector onto the noise subspace, it can be written as:

$$\Pi^{\perp} = \sum_{n=p+1}^{N} \mathbf{v}_n \mathbf{v}_n^H$$

Then, MUSIC-3C estimator is given in the equation (2.38) by M_{3C} which computes the azimuth and incidence angles as well.

$$\mathbf{M}_{3C}(\theta,\phi) = \frac{1}{\mathbf{A}^H(\theta,\phi)\,\Pi^{\perp}\mathbf{A}(\theta,\phi)} \tag{2.38}$$

The following steps summarize the process of MUSIC-3C method:

1. Selection of the time window corresponding the first arrival for either an explosion or LP event.
2. Calculate the average power spectral density to determine the frequency bins f_0, we pointed out Equation (2.35) related to 3C array data, considering M intervals around the frequency peak.
3. The cross-spectral matrix defined in equation (2.36) can be estimated by equation (2.39) (Paulus et al., 2005; Miron et al., 2005). Note that, $\mathbf{W}_m$ is *N x 3* matrix, equation (2.35), therefore the $\widehat{\Gamma}_x$ is a *N x N* Hermitian matrix.

$$\widehat{\Gamma}_W = \frac{1}{M}\sum_{m=1}^{M}(\mathbf{W}_m\mathbf{W}_m^H) \tag{2.39}$$

4. Then perform the eigen structure analysis of the cross-spectral matrix. The eigenvalues and eigenvectors are permuted from large to small. Then, one way to estimate the source number is looking for the largest eigenvalues, in our case a threshold is set up to 5% the maximum for signal space. The remainder eigenvalues determine the noise sub-space with which to build the noise projector.
5. The MUSIC-3C estimator is evaluated on a grid. The steering matrix (equation (2.37)) is computed on the grid, where the azimuth angle is between $[0-2\pi]$, the incidence angles is between $[0-\pi]$ and velocity would be set up between $[10-5010]$m/s.
6. First iteration: compute MUSIC-3C estimator (equation (2.38)) by assuming the incidence angle $\phi = \pi/2$ (horizontal plane), whose the maximum value of the MUSIC-3C spectrum will be the azimuth angle θ.
7. Second iteration: Since the azimuth is estimate in the previous step, MUSIC-3C estimator estimates the incidence angle ϕ (vertical plane) and velocity. So twice iterations more, using the incidence and azimuth values in order to refine the back-azimuth, incidence and velocity.

2.5 Application of MUSIC-3C

2.5.1 Synthetic data

A full waveform synthetic data set was generated to test the accuracy of the location method. The synthetic data set was created using a digital elevation map of Ubinas topography and the 2009 experimental array locations NUBI (4640 m above sea level) and WUBI (4840 m above sea level). An additional array was considered to test the source localization. A 3D discrete numerical elastic lattice method (O'Brien and Bean, 2004) was used to propagate waves in the structure with eight broadband isotropic sources located beneath the summit, see Figure 2.6. The altitude of each source is indicated in Table 2.2. The velocity structure for the simulation was generated from a tomography study (Monteiller et al., unpublished) assuming a density of 2300 kg/m^3 and a homogeneous medium. The sample rate of the synthetic data was 100 Hz, $V_P = 3000$ and $V_P/V_S = \sqrt{3}$.

Source	1	2	3	4	5	6	7	8
Depth	4972	4912	4532	3972	3912	3472	2472	1972

Table 2.2: Source localizations of the eight synthetic sources in the Ubinas model

2.5.2 Synthetic data analysis

To investigate the performance of the MUSIC-3C technique, we applied it to our synthetic data set. For the source number #3 located underneath Ubinas crater at an altitude of 4532 m (1140 m depth) and recorded by synthetic array data set of NUBI. One time window including the first arrival was selected (Figure 2.7a). In order to find the dominant frequency, we averaged the power spectral density computed for the selected time window of each component and for each receiver. The dominant energy peak is located at 2.3 Hz (Figure 2.7b).

The cross-spectral matrix was then calculated by using a windowd around the peak frequency (32 bins). In the first stage, we determined the eigenvectors corresponding to the noise subspace, which gives the projector. In the second stage, we calculated the steering vector which consists of the slowness vector estimated between $[0-360]$ degrees with steps of 3.6 degrees and wave velocity interval between $[10-5010]$ m/s with steps of 50 m/s. Given the projector and the steering vector, we obtained the MUSIC-3C spectrum represented in Figure 2.8a.
The maximum amplitude of the spectrum gives the back-azimuth and the apparent velocity. The largest estimator point is located at 181 degrees +/-3 for the back-azimuth and 2900 m/s +/-75 for the velocity. The vertical and horizontal cross-section of the MUSIC-3C spectrum are shown in Figures 2.8b and 2.8c. The incidence angle is deduced from the back-azimuth and velocity. We found 85.5 degrees +/-6 as shown in Figure 2.8d. The errors are estimated by taking the peak width of 95% of the maximum amplitude. These values agree well with the numerical model values.

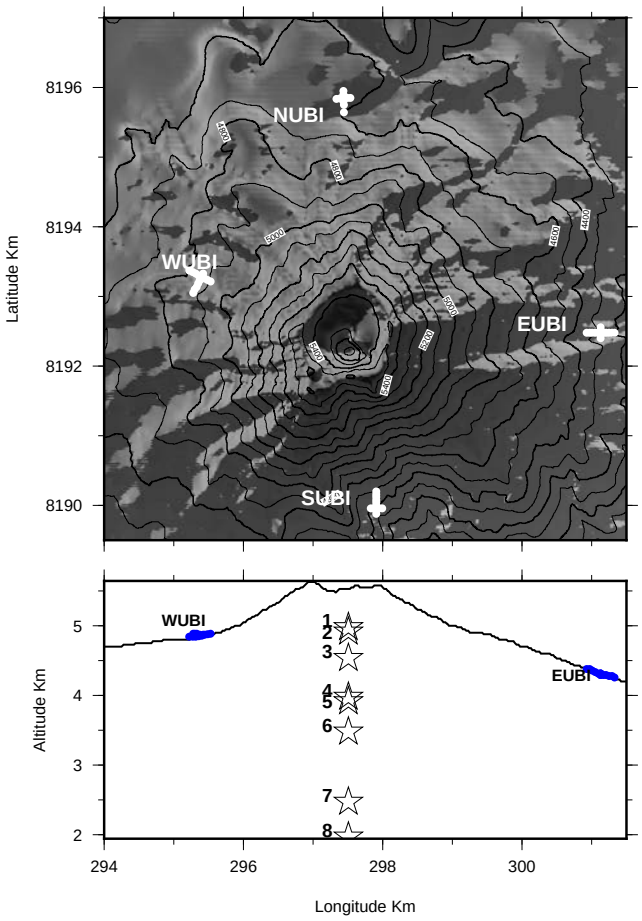


Figure 2.6: Top: Ubinas volcano topography, NUBI, WUBI, EUBI and SUBI indicate the positions of the seismic antennas used for the numerical sources. Bottom: East-West profile of Ubinas summit topography indicating the altitude of each synthetic sources and the WUBI and EUBI antennas

We applied the same analysis to the synthetic data generated for both arrays and for all eight sources. In order to compare the 3C and 1C methods, we also analyzed the same synthetic data set using only the vertical components. The results are shown in the Figures 2.9a and 2.9b for NUBI and WUBI antennas respectively. Back-azimuth results obtained both with the MUSIC-3C and the MUSIC-1C fit well with the model values for both antennas. Errors are +/-3 degrees and +/-6 degrees, with the 3C and the MUSIC-1C algorithm, respectively. However, the incidence angles are significantly different between the MUSIC-3C and the MUSIC-1C analysis.
For NUBI antenna, values vary from 55 degrees for the deepest source to 93 degrees for source #1. These incident angles are consistent with the variation of the source depths. Errors are +/-6 degrees for the MUSIC-3C analysis. These errors allow us to distinguish source depths separated by several hundreds of meters but are unable to separate close sources such as #1 and #2 or sources #4 and #5. The MUSIC-1C analysis gives depths close to the model values for the superficial sources (#1, #2 and #3) while depths for sources #4, #5, #6, #7 and #8 are far away from the model values. The

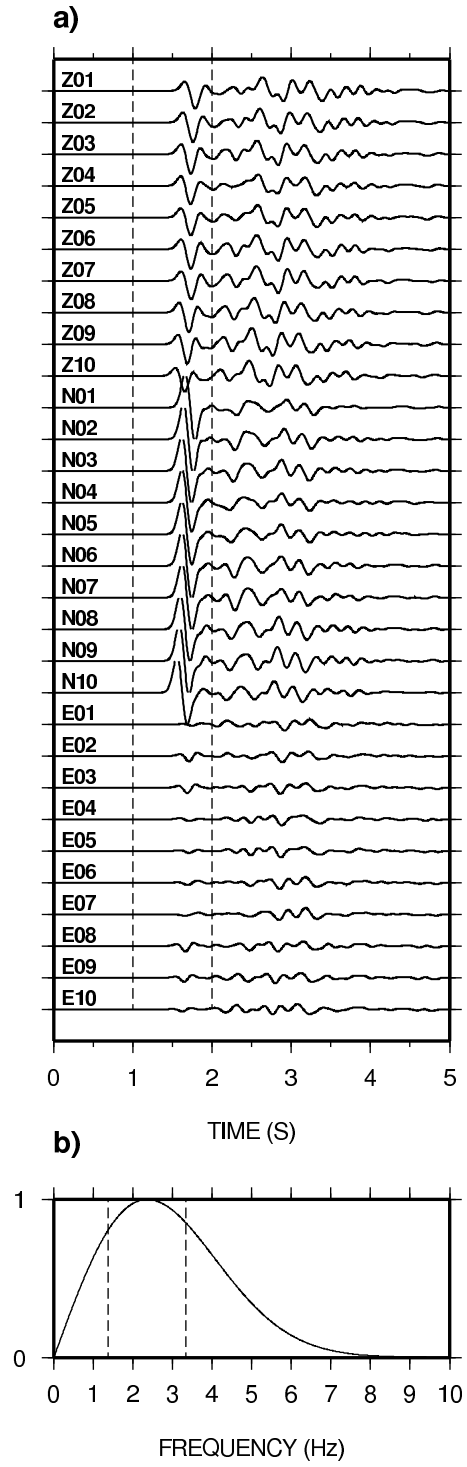


Figure 2.7: a) The vertical (Z), north (N) and east (E) synthetic seismogram from NUBI antenna, b) averaged energy spectrum calculated for all the receivers and all the components. The vertical dash lines in (a) indicate the time window selected for the processing. The vertical dash lines in (b) represent the frequency windows used for the cross spectral matrix calculation.

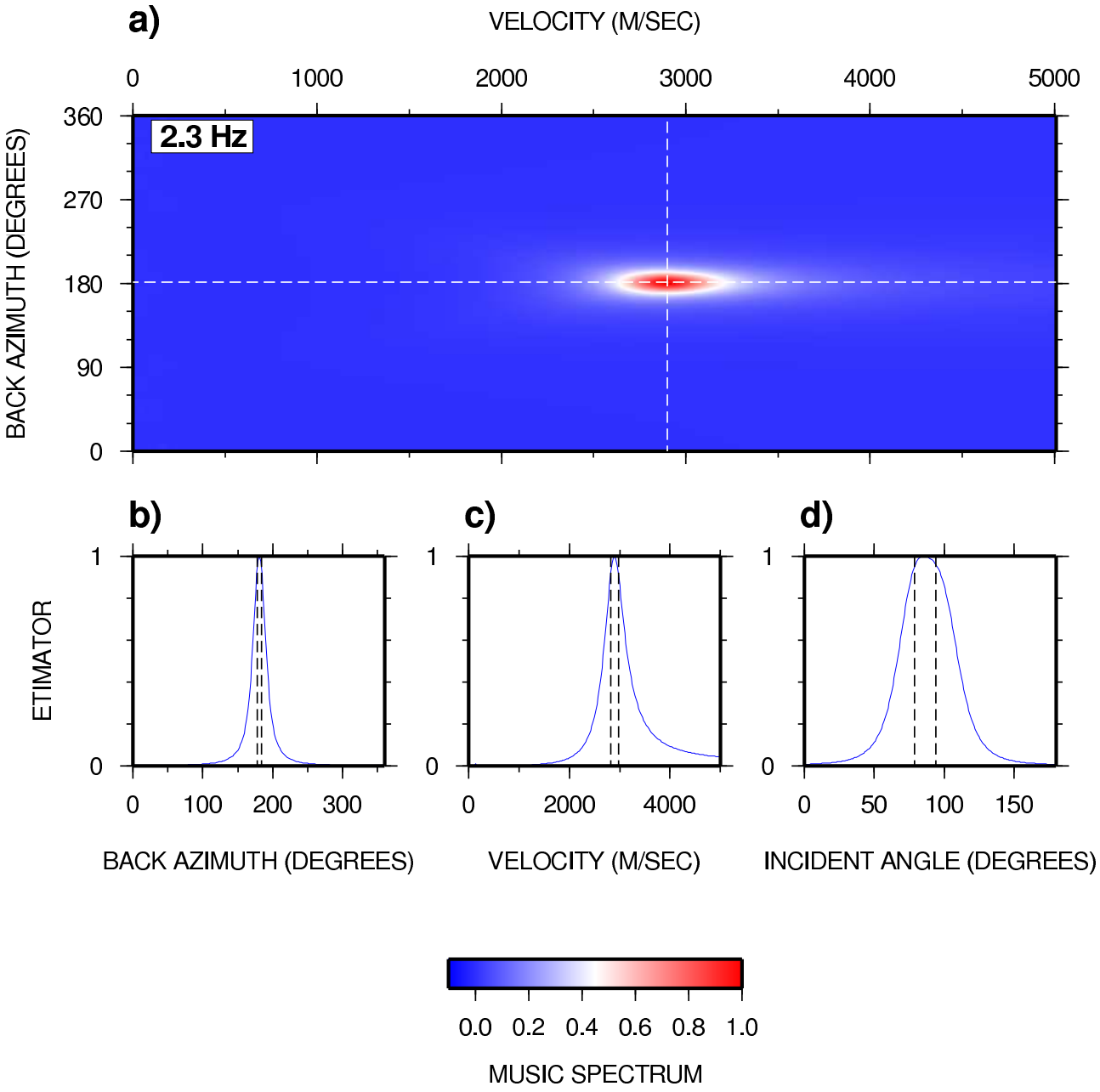


Figure 2.8: a) Normalized MUSIC-3C spectrum calculated with synthetic data generated at source 3 for NUBI antenna. The central frequency used for the cross spectral matrix calculation (Figure 3b) is indicated in the upper left of the spectrum. b) Normalized back-azimuth profile (cross section at apparent velocity 2900 m/s). c) Normalized apparent velocity profile (cross section at back-azimuth at 181 degrees). d) Normalized incidence angle. The vertical dotted lines represent the error 95% range.

incident angle remains approximately the same value, around 90 degrees. The error obtained with the MUSIC-1C processing is +/-12 degrees. None of the sources can be distinguished with the MUSIC-1C analysis.
For WUBI antenna, the MUSIC-3C analysis gives incident angles between 43 degrees for source #8 and 94 degrees for source #1 (Figure 2.9b). For WUBI, solutions follow the depth variation with errors of approximately 6 degrees. The MUSIC-1C analysis gives higher incident angles than the model values (90° for source #6 to 156 degrees for source #1). Errors are larger than the 3C algorithm at approximately +/-15 degrees. The MUSIC-1C analysis does not give reliable solutions for any of the synthetic source depths. In this case, it seems that the solutions are affected by the topography below the antenna and possibly by the inclined free surface. On the other hand, noise was also added to synthetic data to test the performance of MUSIC-3C. Localizations have retreived almost the same results for signals with signal-to-noise ratio upper than 10 dB. Similar results are observed for the velocity. In summary, incident angles obtained by the MUSIC-3C algorithm are close to the theoretical values for both antennas, whereas those obtained with the MUSIC-1C are not reliable.

Probabilistic approach

In the following, we examine how crossing the source directions obtained with both antennas to find (delimit) the source area by crossing slowness vetors. The back-azimuth (BAZ) and the incident angle (INC) can be represented as Gaussian variables with mean μ_{BAZ} ($0 \leq \theta_{BAZ} \leq 360°$) and μ_{INC} ($0 \leq \phi_{INC} \leq 120°$) and standard deviations σ_θ and σ_ϕ corresponding to the errors respectively. This allows the definition of a probability density function (PDF) $\rho(\theta^k)$ of the back-azimuth and a PDF $\rho(\phi^k)$ of the incident angle for each array k. $\rho_1(\theta^k)$ and $\rho_1(\phi^k)$ are shown in Figures 2.10 and 2.11 as rose diagrams in the horizontal plane for the back-azimuths and in the vertical planes oriented N-S and W-E for the incident angles. The last step is to locate the source by using the information obtained at each antenna. For each point with geographical coordinates (x,y,z) in the source region and each array k, the back-azimuths $\theta^k(x,y,z)$ and the corresponding value of $\rho_1(\theta^k)$, as well as the incident angle $\phi^k(x,y,z)$ and the corresponding value of $\rho_1(\phi^k)$ can be calculated. In order to represent the results the probability density function (PDF) of the source position is derived from the different PDF's of the back-azimuth and the incident angle (Métaxian et al., 2002).

$$\rho_2(x,y,z) = \prod_{k=1}^{2} \rho_1(\theta^k(x,y,z)) \cdot \rho_1(\phi^k(x,y,z)) \tag{2.40}$$

The maximum likelihood of the PDF ρ_2 yields an estimate of the source location. We define the mean quadratic radius R = $\sqrt{(\sigma_1^2+\sigma_2^2+\sigma_3^2)/3}$, where σ_1^2, σ_2^2 and σ_3^2 are the principal variances of $\rho_2(x,y,z)$. We gathered in Table 2.3 the results obtained for the mean quadratic radius and the distance between the real position and the maximum likelihood of the probability density function describing the source position. Both values have generally higher values for deeper sources, which would indicate a decrease of the resolution of the method for increasing depths. It is also noticeable that the mean quadratic radius that we consider as an estimate of the error is always much greater than

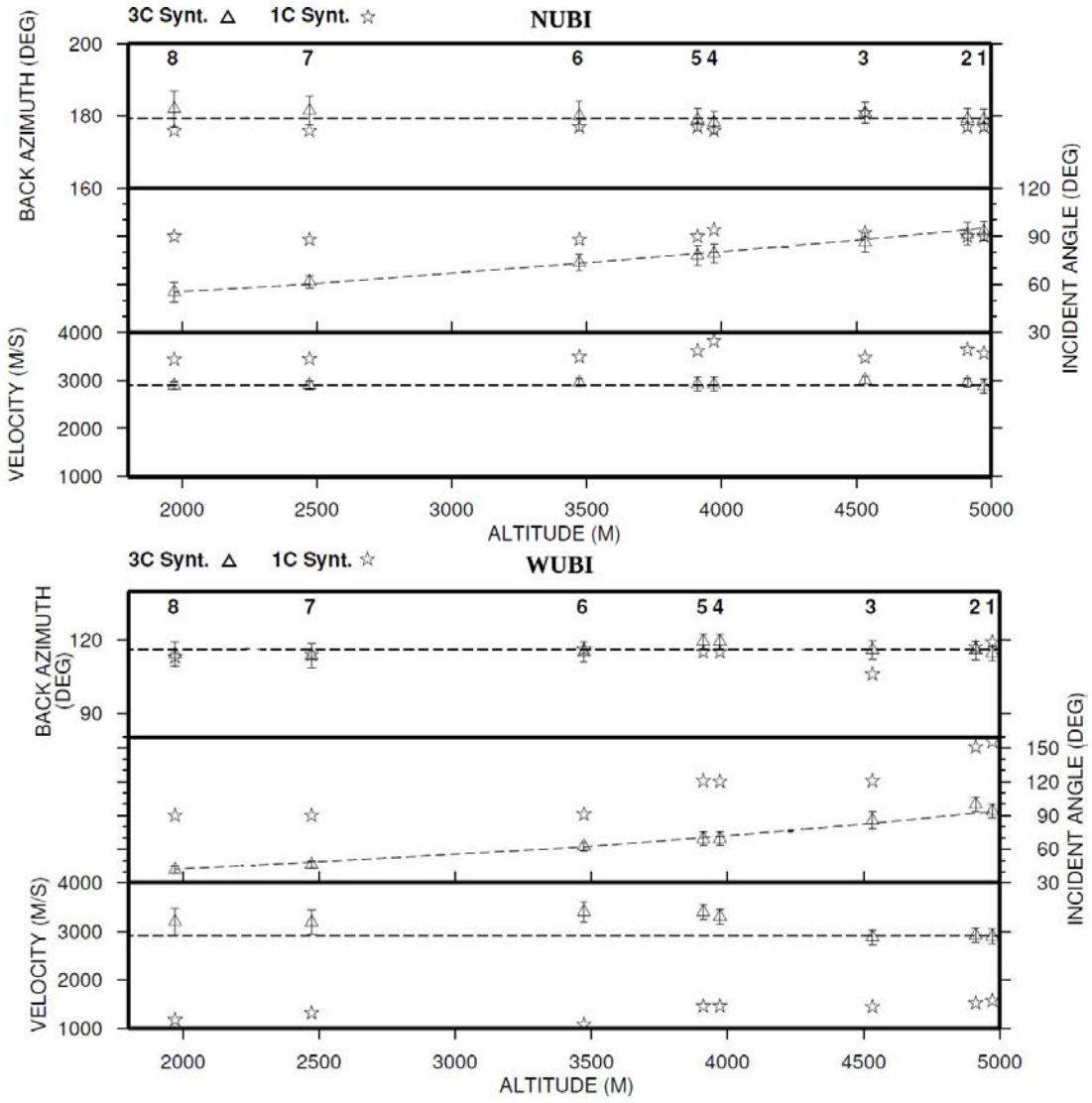


Figure 2.9: Results obtained for the synthetic data calculated for the eight sources. Open triangles and open stars represent results obtained with the MUSIC-3C and MUSIC-1C, respectively. Sources are numbered as in figure 1b. a) Back-azimuth, incidence angle and apparent velocity for NUBI antenna. b) Back-azimuth, incidence angle and apparent velocity for WUBI antenna. Dash lines represent the values. The filled circles represent the real data results model

the distance between the real and calculated source position. Hence, MUSIC-3C allows to locate the synthetic sources, in all the cases. Moreover, it is interesting to notice that our estimation of the error is probably overestimated in some cases.

Source Number	Distance to the source (m)	R (m)	Altitude (m)	Theoretical altitude (m)
1	200	450	4991	4972
2	140	500	4957	4912
3	220	570	4655	4532
4	330	630	4090	3972
5	300	630	3955	3912
6	120	750	3587	3472
7	390	800	2728	2472
8	500	820	2217	1972

Table 2.3: Distance between the calculated and real position of each synthetic source, mean quadratic radius and altitude of each source

Figures 2.10 and 2.11 show in details the results obtained for each synthetic source. The horizontal position is well determined for all sources. Looking at the vertical views, the PDF of the source position is well centered on synthetic sources for the 2 highest sources (Figure 2.10a,b). Uncertainty is larger for the source 3 positioned at the altitude of 4532 m (Figure 2.10c). This source cannot be distinguished from sources 1 and 2 positioned at 4972 m and 4912 m, respectively. The PDF of the source position gives a good solution for sources 4 and 5 (Figures 2.10d and 2.11e). These sources can be clearly differentiated from sources 1, 2 and 3. It is more complicated to differentiate source 6 from source 5, which is located 430 m above (Figures 2.11f). On the same manner, it is not clearly possible to differentiate sources 7 and 8 (Figures 2.11g,h). On the other hand, MUSIC-3C allows to easily differentiate the 2 groups of sources 5, 6 and 7, 8.
The PDF results corresponding to source 6 is situated near the the source 5, which also prevents us in this case from distinguishing sources 5 and 6. The PDF of source position would be better determined with more antennas. Nevertheless, shallow and deep sources are clearly distinguished as shown in the Figure 2.11 f,g,h.

2.5.3 Real Data Analysis

In this section, we discuss the performance of MUSIC-3C method by applying it to two examples of real seismic events recorded at Ubinas volcano. We consider an explosion earthquake signal and an LP event. These two kinds of events are representative of the seismic activity that recorded during the experiment. The selected events, recorded respectively at 00:37 for the LP event and at 01:27, June 2nd, 2009 for the explosion are shown in Figure 2.12. The data was corrected for the instrument response and bandpass filtered between 1 and 10 Hz. Figure 2.13 shows the antenna (NUBI) energy

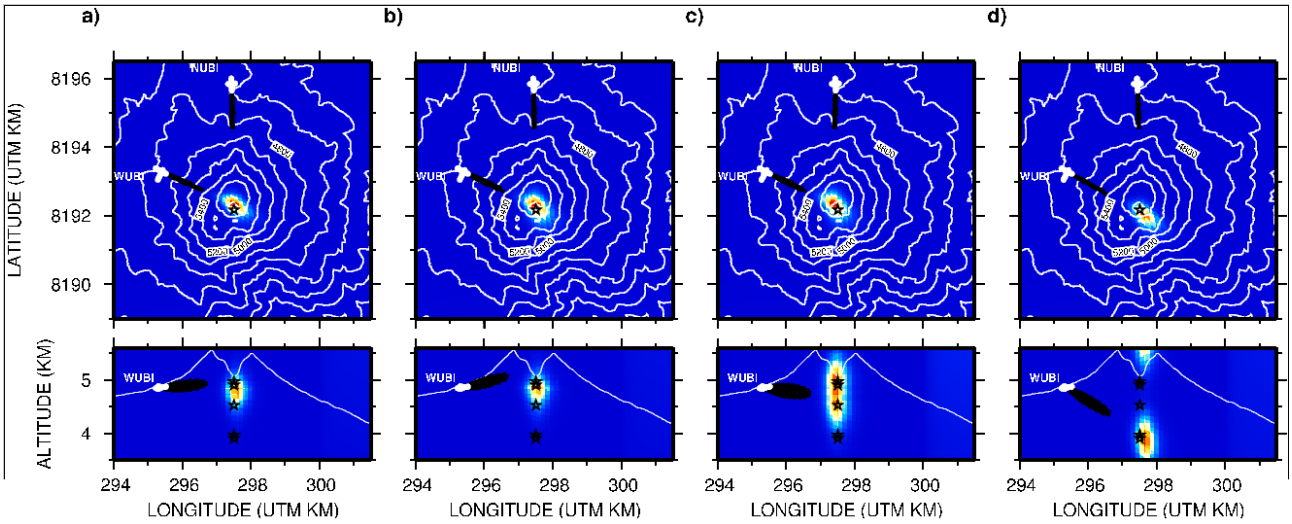


Figure 2.10: Probability density function of the source position ρ_2 for the 8 synthetic sources. Horizontal view represented at the source depth and vertical view oriented West-East crossing the maximum likelihood of ρ_2 for the sources at the depths of a) 4972 m, b) 4912 m, c) 4532m, d) 3972 m respectively. The PDF $\rho_1(\theta^k)$ and $\rho_1(\phi^k)$ are represented as rose diagrams with an increase of 5°. White points represent the sensor positions.

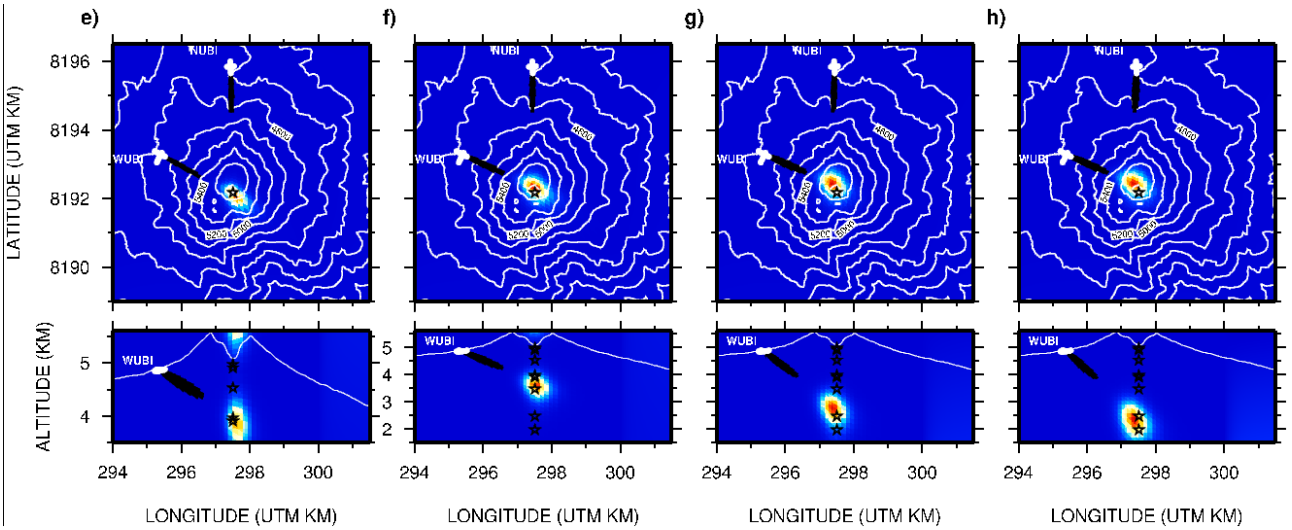


Figure 2.11: Probability density function of the source position ρ_2 for the 8 synthetic sources. Horizontal view represented at the source depth and vertical view oriented West-East crossing the maximum likelihood of ρ_2 for the sources at the depths of e) 3912 m, f) 3472 m, g) 2472 and h) 1972 respectively. The PDF $\rho_1(\theta^k)$ and $\rho_1(\phi^k)$ are represented as rose diagrams with an increase of 5°. White points represent the sensor positions. A different vertical scale is used for e (Altitude between 3.5 and 5.6 km) and f, g, h (Altitude between 1.5 and 5.6 km).

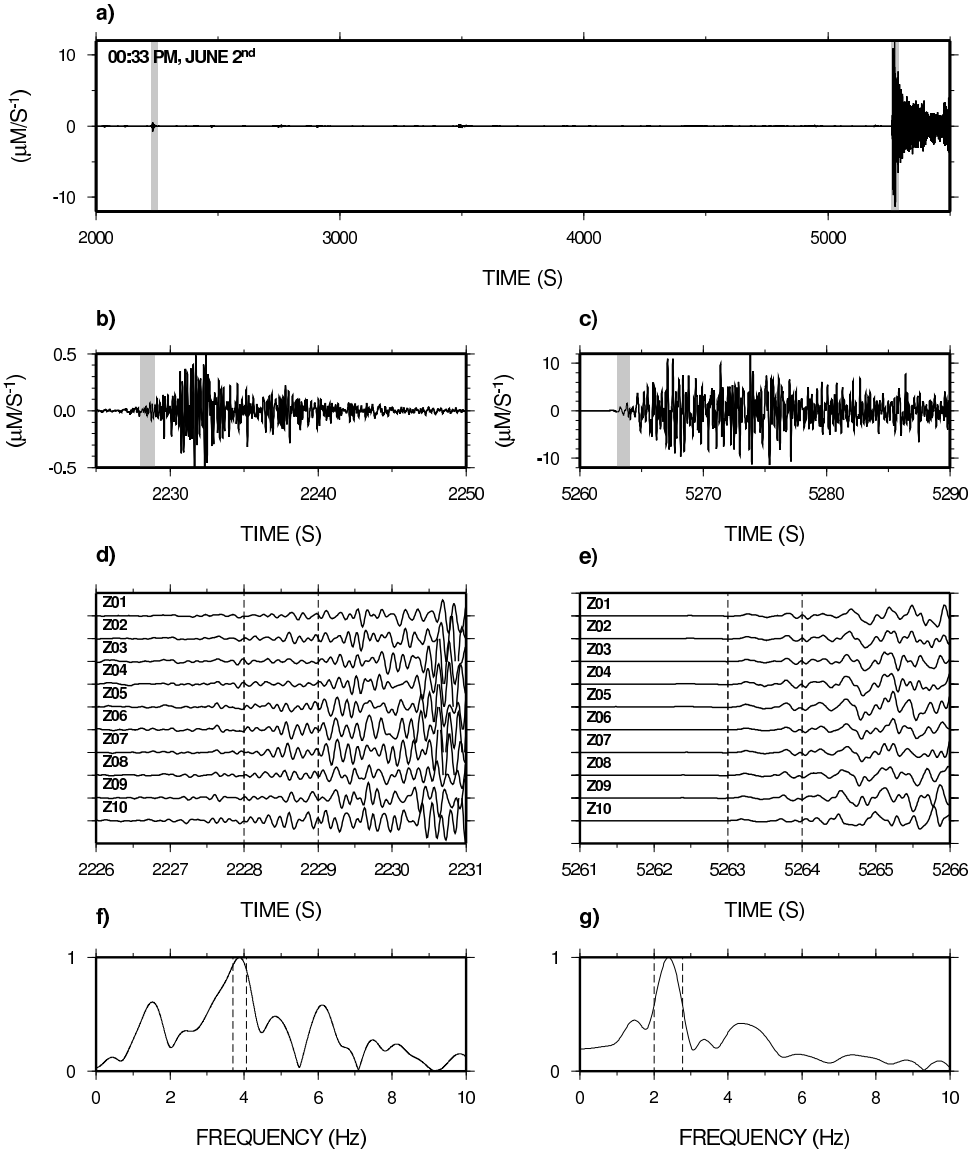


Figure 2.12: a) Z component seismogram of the LP event and explosion earthquake recorded by the central station of NUBI antenna. The time and date of the first sample is indicated in the upper left of the record. Shaded zones represent part of the signals enlarged in b) and c). d) and e) Z component of the LP event and the explosion earthquake recorded by 10 stations of NUBI antenna. Waveforms correspond to the shaded parts of the signal in b) and c), filtered between 1 and 10 Hz. The vertical dash lines in d) and e) indicate the time window selected for the processing. f) and g) Averaged energy spectrum calculated for all the receivers and all the components, where the vertical dash lines represent the frequency windows used for the cross spectral matrix calculation.

spectrum average obtained from two seconds of signal including the first arrival. The dominant peak is centered at 3.9 Hz for the LP event. The maximum of the MUSIC-3C spectrum gives a back-azimuth of 183 degrees +/-6, a velocity of 1851 +/-221 m/s and an incidence angle of 49 +/-7 degrees. For WUBI, we obtained a back-azimuth of 116 +/-7 degrees, a velocity of 1520 +/-295 m/s and an incidence angle of 47 +/-7 degrees. The dominant peak is centered at 2.4 Hz for the explosion. We find a back-azimuth of 184 +/-5 degrees, a velocity of 2975 +/-125 m/s and an incidence angle of 86 +/-7 degrees. For WUBI, we obtained a back-azimuth of 119 +/-6 degrees, a velocity of 3100 +/-120 m/s and an incidence angle of 75 +/-7 degrees. We used equation (2.40) to calculate the PDF of the source position for the LP event and the explosion earthquake. Results are shown in Figure 2.14. The maximum likelihood of the PDF is situated 3000 m below the bottom of the crater at the altitude of 2240 m. The radius R is 730 m. The source area of the explosion is situated 150 m West and 1000 m below the bottom of the crater at an altitude of 4200 m, the radius R is 660 m.

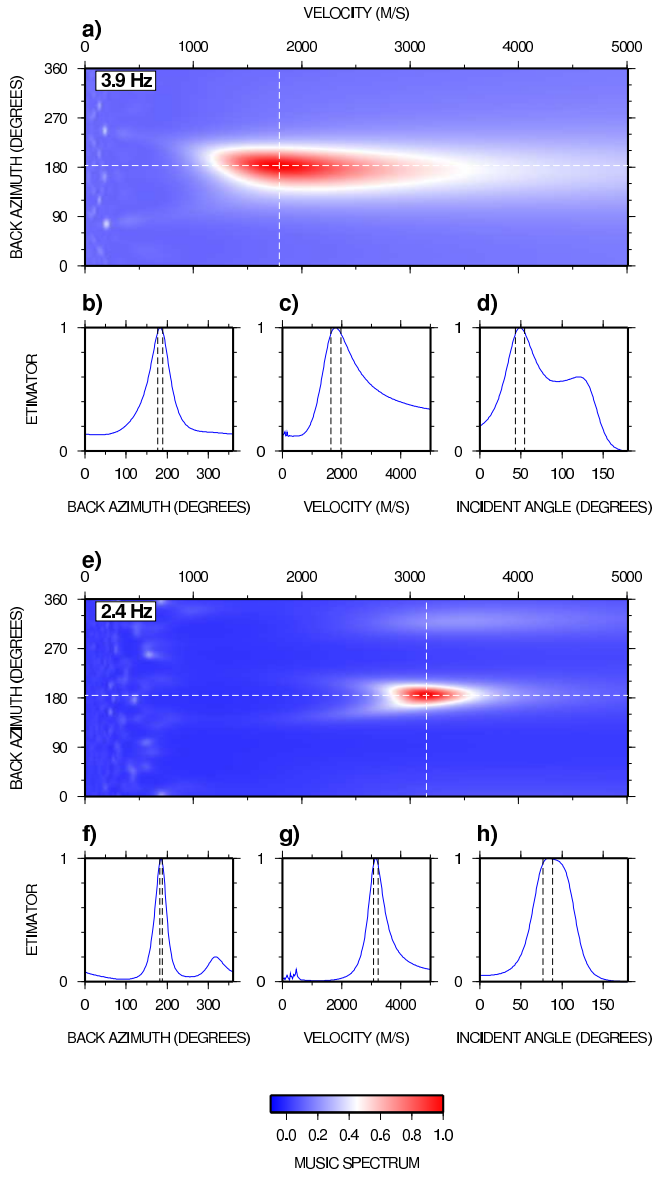


Figure 2.13: a) Normalized MUSIC-3C spectrum calculated with the LP event for NUBI antenna. The central frequency used for the cross spectral matrix calculation (Figure 7f) is indicated in the upper left of the spectrum. b) Normalized back-azimuth profile (cross section at velocity 1794 m/s). c) Normalized velocity profile (cross section at back-azimuth at 183 degrees). d) Normalized incidence angle. The vertical dot lines represent the error range. e) Normalized MUSIC-3C spectrum calculated with the explosion earthquake for NUBI antenna. The central frequency used for the cross spectral matrix calculation (Figure 7g) is indicated in the upper left of the spectrum. f) Normalized back-azimuth profile (cross section at velocity 3151 m/s). g) Normalized velocity profile (cross section at back-azimuth at 184.5 degrees). h) Normalized incidence angle. The vertical dotted lines represent the error range. c) and d) are apparent velocities

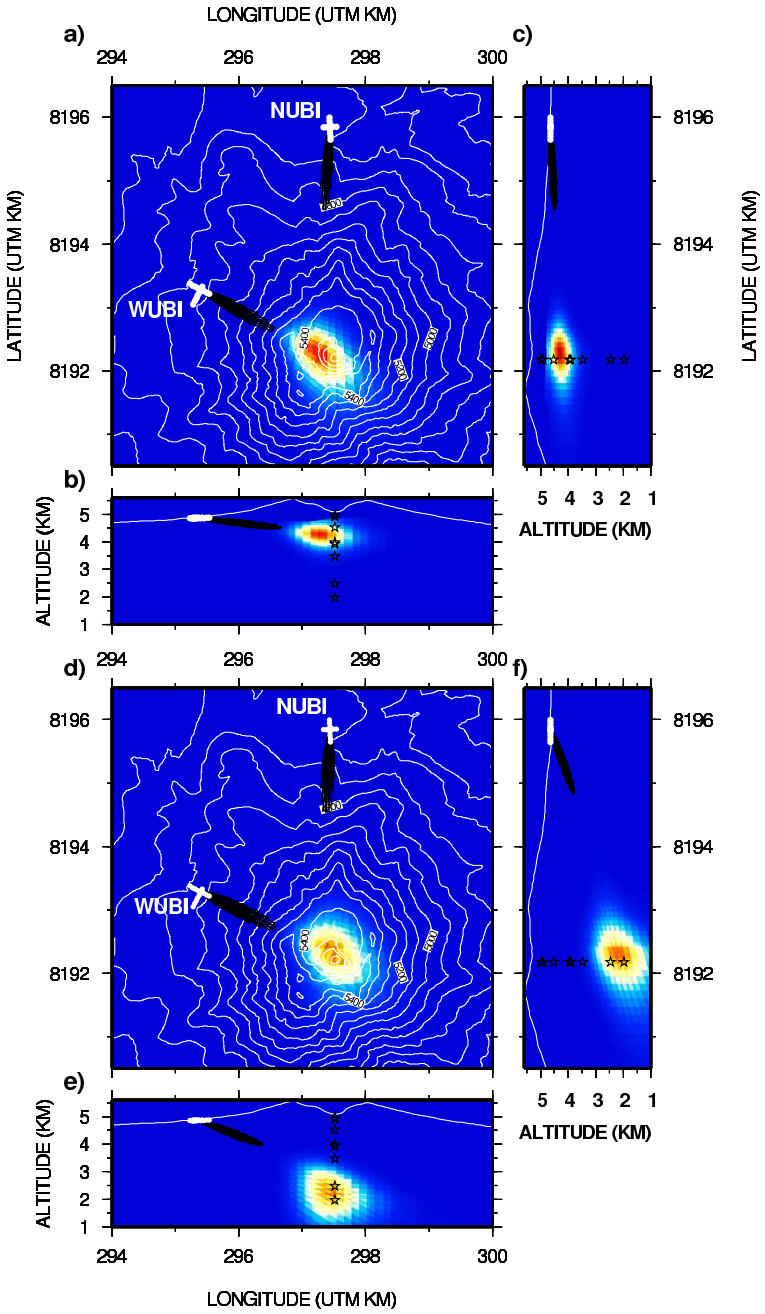


Figure 2.14: Probability density function (PDF) of the source position ρ_2, for the explosion earthquake (a-c) and the LP event (d-f). a) horizontal view at 4200 m depth, b) vertical view oriented West-East crossing the maximum likelihood of ρ_2, c) same as b) oriented North-South. d) horizontal view at 2240 m depth, e) vertical view oriented West-East crossing the maximum likelihood of ρ_2, f) same as e) oriented North-South. The PDF $\rho_1(\theta^k)$ and $\rho_1(\phi^k)$ are represented as rose diagrams with an increment of 5 degrees.

2.6 Discussion

2.6.1 Capabilities of the method

MUSIC-3C gives good results for locating seismo-volcanic sources. Results obtained with synthetic sources generated in an homogeneous medium are convincing. The main contribution of MUSIC-3C compared with MUSIC-1C is the determination of the depth. Only the three components seismic array can receive the entire wavefield in 3D, where the full energy impinging the antenna can be well determined.
The depth resolution is related to the incidence angles estimation. The incidence angle is affected by the inter-sensor level differences, in our case, the antennas have a good distribution on horizontal plane, it is the reason that azimuth angle can be well determined with MUSIC-3C and MUSIC-1C too. On the vertical plane the inter-sensor level differences is not as well as horizontal case, then the signal-noise ratio of the signal in this analysis play an important role in order to increase the resolution of the estimator. Especially our analysis is on the first arrival part of the signal, where the signal-noise ratio is still weak.
Then one-component array data is not enough to get a good resolution on the MUSIC estimator, it has presented a broad lobe in the spectrum. We observed the average signal-noise ratio for the first arrival section of LP event recorded on NUBI antenna is 6dB bigger the vertical components only.
The incident angle is determined with a weaker resolution than the back-azimuth. This can be explained by the spatial distribution of the sensors constituting the antennas. Theoretically, the incident angle can't be determined if all the sensors of the antenna are positioned in the same plane. Métaxian et al. (2009) defined an index of coplanarity ranging between 0 and 1 allowing to determine if the incident angle can be estimated or not for a given antenna geometry.
The index of coplanarity is 0.08 for NUBI and 0.4 for WUBI. NUBI was set up on a plain of ash, whereas WUBI was installed on a steep and irregular slope. Thus, the antenna geometry seems to be a reasonable explanation of the lowest resolution obtained for the incident angle. Antenna geometries with index of coplanarity closest to one would probably have improved the incidence angle resolution.
An interesting subject, but not easy to deal with is the comparison of the resolution of the various methods for locating LP seismicity. Several methods have been applied in the last decade. Different approaches are used, such as attenuation of seismic amplitudes (Battaglia and Aki, 2003), full waveform inversion (Chouet, 2003; Chouet et al., 2005; Lokmer et al., 2007; Bean et al., 2008; De Barros et al., 2011), the semblance method (Kawakatsu et al., 2000; Almendros and Chouet, 2003), cross-correlation methods (De Barros et al., 2009), time-reverse method (O'Brien et al., 2011) or array technics by slowness analysis (Saccorotti and Del Pezzo, 2000; Almendros et al., 2001a,b; Métaxian et al., 2002; La Rocca et al., 2004; Garcia Yeguas et al., 2011). Moreover, these different technics are adapted to different kinds of seismic arrays with different geometries and number of sensors. They are applied to volcanoes characterized by distinct dynamics and structures. One distinguishes two main families of techniques used for locating LP sources, techniques using: 1) arrays constituted of plain sensor stations, which are generally spatially distributed around the volcano; 2) arrays formed of

seismic antennas distributed generally on a few sites (maximum 3 or 4), because of the high number of sensors needed for each antenna.
In most of the location methods used with the arrays of the first category, the discrepancy between the model and the observations are quantified. It is the case for example for the attenuation of seismic amplitudes or for full waveform inversion methods. A grid search is performed to determine the best solution for a point source and to define an error region. The size of this region characterize the resolution of the method. For antennas techniques, parameters characterizing the wave propagation through the array (azimuth apparent, slowness, incident angle) are estimated.
These parameters are estimated on the basis of delay calculations between all the couples of sensors composing the antennas. The errors associated to delay calculation are quantified and included directly in the slowness vector estimation.
One of the main limitation of array techniques is the plane wave assumption. Saccorotti and Del Pezzo (2000) pointed out several causes inducing errors in the time delays calculations and therefore in the resolution of location with antennas methods. These causes can be local velocity heterogeneities beneath the array, near-field effects (intertwining of P and S waves), near-sites scatterers, random velocity fluctuations, multipathing and interference phenomena. Neuberg and Pointer (2000) show that the plane wave approximation remains valid if the dominant wavelength does not exceed twice the source depth, which is the case for the LP events and the explosions of Ubinas.
Almendros et al. (2001a) applied the MUSIC-1C technique to data recorded at Kilauea volcano with 3 seismic antennas. To estimate the error in the determination of the slowness vector, they took the region within which the slowness power spectrum is larger than 90% of the maximum value. They estimated individual LP event locations to have an error of 200 m. This result is obtained by comparing slownesses derived from the data analysis with a slowness vector model calculated while taking into account the 3-D velocity model of Kilauea and the topography. This process of source location can't be applied at Ubinas as the velocity model is not known. Hence, we stayed at the stage of crossing in the volcano volume the directions given by the back-azimuth and the incident angle obtained at each antenna. This assumes a rectilinear propagation in a homogeneous medium between the source and the sensors, which is of course a strong approximation. All the location methods are highly dependent of the knowledge of the structure as well as the topography. Velocity structures are not yet known for most of the volcanoes. Even when a 3-D velocity model exists, the resolution of the model, particularly in the near-surface (Bean et al., 2008), stems a strong limitation for locating LP events.
Neuberg and Pointer (2000) pointed out the importance of topography on waveforms. They show that for broad-band waveforms, the angle of incidence as well as the back-azimuth is affected by an inclined free surface. Tests performed with synthetics revealed that the inclined free surface seems to influence strongly the MUSIC-1C analysis at WUBI, but not the MUSIC-3C analysis. Other causes of errors have been put in evidence, as the influence of the near-field effects. Lokmer et al. (2010) shown that the near-field term can introduce errors to the amplitude decay location technique, since the near-field term has variable decaying properties for small distances. On the other hand, this effect is not strongly pronounced for sources with a strong isotropic component and doesn't affect source locations when using full wave techniques as the near-field is inherent in the simulations.
Finally, we used only 2 antennas for logistic reasons. Métaxian et al. (2002, 2009) studied the influence of the number of antennas and their spatial distribution on source location at Arenal volcano.

We made similar tests at Ubinas by generating synthetics for 2 additional antennas situated East and South of the volcano. Results, show that the error is significantly smaller when using 3 or 4 antennas. But, at the same time, the deepest sources are found close, but beside the real positions when using 4 antennas, which clearly indicate the limitation induced by using an homogeneous medium, such as shown in Figures 2.15 and 2.16 show in details the results obtained for each synthetic source with 3 and 4 antennas. The horizontal position is well determined for all sources. Looking at the vertical (depth) views and comparing with exact position given in Figure 2.6, the errors estimations are comparatively lower than obnained with 2 antennas. However, even with this approximation, tests made

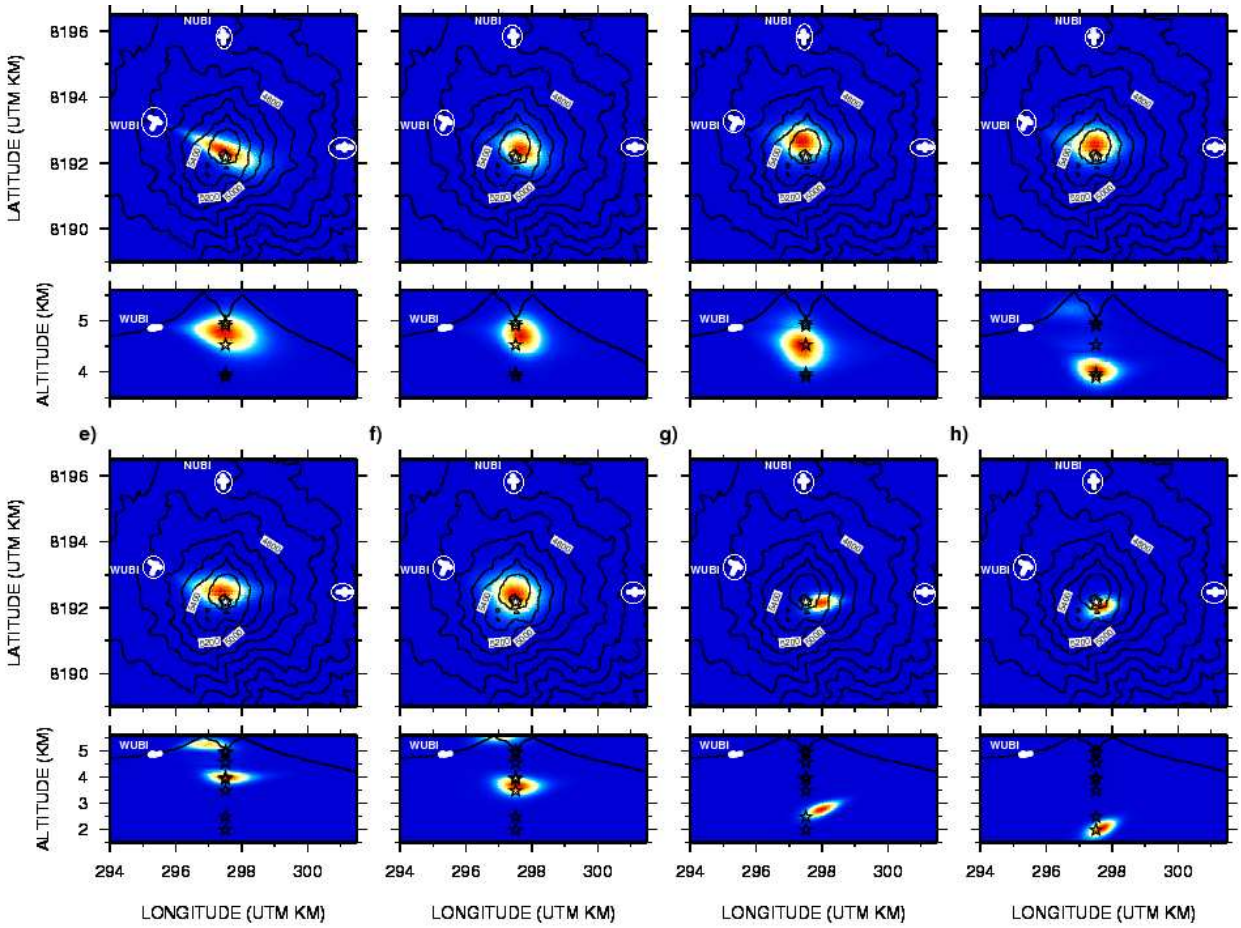


Figure 2.15: Ubinas map with 8 synthetic sources localizations with 3 antennas deployment in North, West and East (white circles)

with 2 antennas and synthetics generated at 8 different depths show that sources separated by depth of several hundreds of meters are easily differentiated by applying MUSIC-3C. Consequently, it is reasonable to think that the explosion earthquake we analyzed is not located superficially, but deep in the conduit. In the same manner, we conclude that the LP event is located deeper than the explosion.

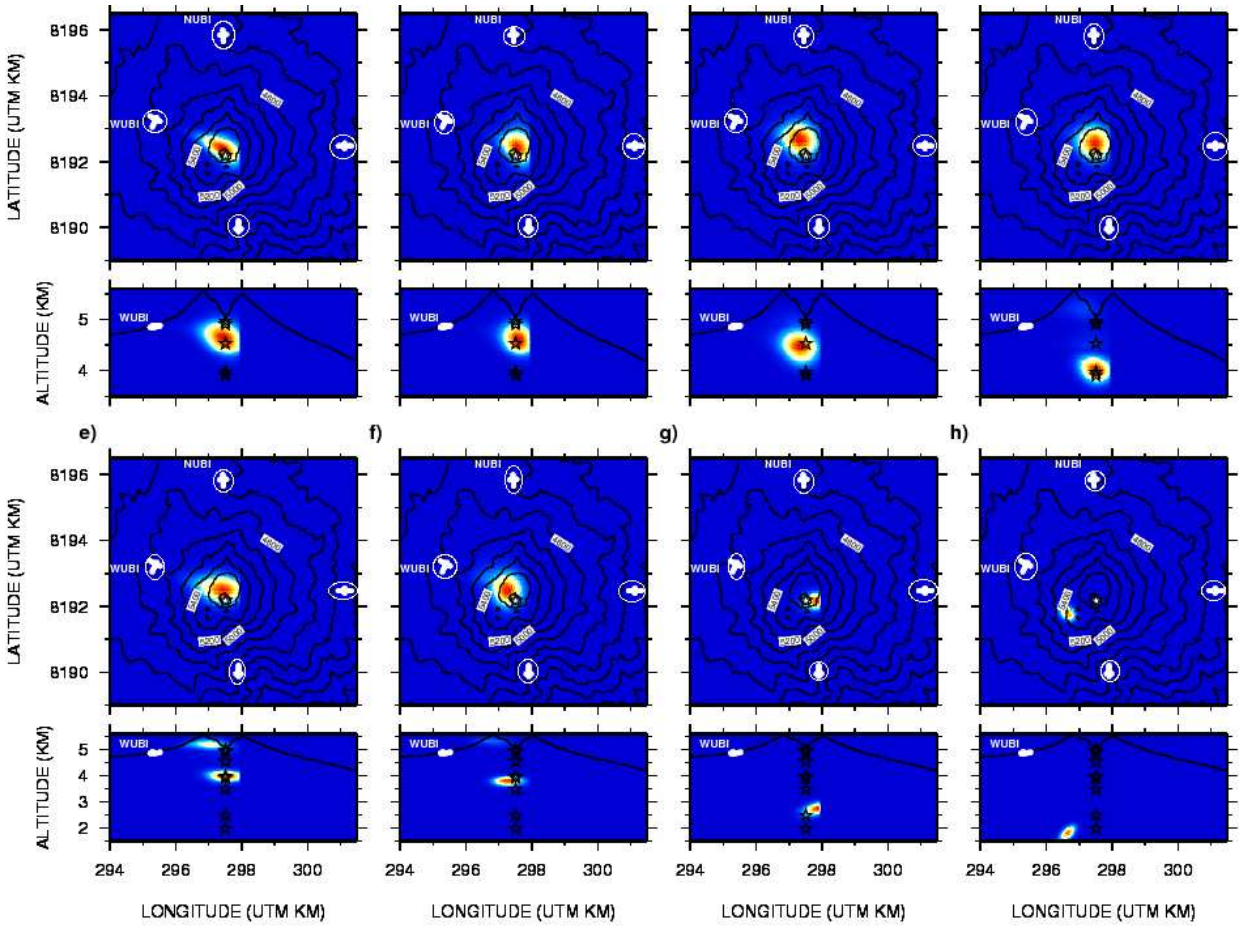


Figure 2.16: Ubinas map with 8 synthetic sources localizations with 4 antennas deployment in North, West, East and South (white circles)

2.6.2 Volcanological aspect

In the following, we discuss some of the possible mechanisms that might explain deep sources in the conduit for an explosion earthquake or an LP event. Fragmentation of viscous magma by brittle failure is thought to be responsible of explosions in silicic volcanoes (Alidibirov and Dingwell, 2000). Melnik and Sparks (2002) have modeled unsteady conduit flow in explosive eruptions after unloading through dome collapse. These models have been applied to the episodes of explosive activity occurred shortly after dome collapse at Soufrière Hills volcano. The unloading triggers gas exsolution and magma rising in the conduit, increasing its internal pressure. An explosion is triggered when the internal pressure equals the tensile strength of the magma. Over pressure is responsible of magma fragmentation generating gas-particle dispersion, which propagates to the exit of the conduit to form a volcanic column in the atmosphere (Melnik and Sparks, 2002). Other studies also suggest that fragmentation occurs when a critical overpressure or critical elongation strain rate of magma is

reached (Alidibirov and Dingwell, 1996, 2000; Papale, 1999).
Studying tuffisites veins in the dissected vent of rhyolite conduits at Torfakökull, Iceland, (Tuffen et al., 2003) and Tuffen and Dingwell (2005) interpreted fault textures as resulting from shallow seismogenic faulting within rising magma during the emplacement of highly viscous lava flows. They suggest that the faulting process recorded in these conduits is consistent with many characteristics of LP and hybrid events during lava dome eruptions.
Neuberg et al. (2006) proposed a seismic trigger model to explain source mechanism of LP events on Soufrière Hills, which are characterized by non-destructive, repetitive and stationary source location. This model is based on brittle failure of magma, the source location is proposed to mark the transition from ductile conduit flow to friction controlled magma ascent, approximately 1500+/-100m below the active dome.
Given the above works proposed for modeling explosions and LP events at Soufrière Hills volcano, identical source models are envisaged for Ubinas. Indeed, as for Soufrière Hills, Ubinas explosions are characterized by short duration events (tens of seconds to one minute), fountain collapse consistent with abrupt halt of fragmentation, followed by slower degassing and patterns of repetitive explosions. Moreover, Vulcanian activity at Ubinas is also characterized by pulsations of explosions, with time intervals of a few hours to tens of hours between each event. During the 2 months of experiment, 17 vulcanian explosions were observed between the 15th of May and the 14th of June 2009, among which 6 occurred the 25th of May.
No dome was observed at Ubinas, but a magmatic plug positioned at the bottom of the active vent (Macedo et al., 2009). Visual observations of ash pulses rising from hundreds of meters to several km correlate with seismically recorded explosions. Slow degassing accompanied with pulses of ash emissions was almost continuous at Ubinas during the experiment. These pulses can be interpreted as releases of pressure resulting from fracturing or a sufficient permeability of the superficial solid cap of the plug. Such a process indicates pressure increases in the magma conduit probably induced by bubble growth. The occurrence of some LP events was also correlated visually with pulses of ash. The pulses can't all be associated to an LP event. Variability in the intensity of the pulses could be observed and their number is much higher compared to the number of detectable LP.
Ash emission associated with explosions and LP events could be clearly differentiated by the altitude reached by the column, but also by the intensity and the velocity of the ejection of ashes in the atmosphere. Unfortunately, particle velocities couldn't be measured and this assumption is based only on visual observations.
According to Neuberg et al. (2006), the LP event can be interpreted as resulting from shear-fracturing of magma at the conduit walls. The fracturation level, which is considered by Neuberg et al. (2006) as the ductile to brittle transition zone where cracks open, is considered to correspond to the source position of the LP event in the conduit. We found the source located at 2240 +/-730 m a.s.l., which is approximately 3000 m below the bottom of the crater. The explosion, which occurs 50 minutes after the LP event is located at 4200 +/-660 m a.s.l, thus 2000 m above the LP source.
There is no necessarily relation between the two events. A lot of LP events occur without being followed by an explosion earthquake in the next hours or days. On the other hand, Traversa et al. (2011) who studied the time evolution of the LP seismicity rate prior to 143 explosion earthquakes recorded over a 2 years period (2006-2008) at Ubinas, observed an acceleration of the LP rate above

the background level during 2-3 hours preceding the explosion onset. These results do not allow to establish any direct relation between the two events we are studying, but show that, in average, LP activity increases statistically before explosions, which implies necessarily an increase of gas ascent in the conduit. If the solidified cap keeps a sufficient level of permeability, the gas can escape through the fractures formed at the conduit walls. Hence, the internal pressure stays below the tensile strength of the magma. No explosion occurs in this case. Should the opposite occur, the gas accumulates in the conduit and the overpressure can generate fragmentation. The gas escaped following the fracturing of solidified magma at the conduit walls that produced the LP event may have been responsible of an increase of the internal pressure in the conduit and an overpressure state that may have initiate fragmentation.

Considering the mechanism of explosion and the onset of fragmentation, Traversa et al. (2011) found that the rate of LP events preceding another LP event shows similar pattern to the rate of LP events preceding explosions. The slope of the LP rate acceleration is smaller prior to an LP event and appears to be related to the energy of the explosions, stronger for higher energy explosions (Traversa et al., 2011). This is a strong argument for a common mechanism for the generation of LP events and explosions at Ubinas. Analysis of the whole catalog of data recorded during the experiment, including 17 explosions and 450 LP events has to be achieved to study more in details the relation between LP events and explosions.

Depth values found for the LP event and the explosion earthquake are consistent with results found on other silicic volcanoes. Druitt et al. (2002) estimated the drawdown depths of Vulcanian explosions at a few hundred meters to 2 km for Soufrière Hills volcano. On this same volcano, applying a classical method of arrival times to families of multiplets of LP events, Neuberg et al. (2006) located sources approximately 1500+/-100m below the active dome. Chouet et al. (2005) located sources of VLP signals generated by explosions at Popocatepetl from waveform inversion, 1500 m below the western crater wall. Using a similar inversion technique, Kumagai et al. (2011) located an explosion event at Tungurahua volcano 6 km below the crater. Analyzing deposits at Katmai Volcano, Alaska, Hildreth (1987) found evidences that fragmentation occurred at depths of less than 1.5 km.

More data has to be processed to confirm or to invalidate these results and to try to find a model that could explain the occurrence of LP events and explosions at different levels into the conduit. The determination of depth of LP events and explosion earthquakes should make it possible to carry constraints to the determination of eruptive dynamics.

Chapter 3

Physics of volcano from source localizations

3.1 Introduction

The physical mechanisms behind Vulcanian events remain a challenge in our community, with andesitic volcanoes characterized by violent and unpredictable eruptions. It is known that the Vulcanian phenomenon is controlled by the physical and chemical properties of the magma. Vulcanian episodes can be generated by magma with intermediate properties between basaltic and rhyolitic, which comes from the deepest parts of the Earth, and which is less dense than the surrounding rock (Sparks, 2000). Dingwell (1996) carried out experimental studies of physical and chemical processes of magma, and described explosive eruptions that involved viscous bubbles (nucleation, growth, acceleration), brittle failure, and post-fragmentation. The fragmentation can occur by brittle failure of magma as the tensile strength is overcome by the stress.
Geophysical measurements have been performed to study this phenomenon for andesitic volcanoes. Iguchi et al. (2008) focused on seismic observations and ground deformation of three andesitic volcanoes (Sakurajima, Japan; Suwanosejima, Japan; Semeru, Indonesia). Thus, a common sequence of phenomena associated with volcanic explosions was proposed to follow five steps: 1. Ascent of magma and accumulation of volcanic gas in the conduit below a confining cap, which result in pressure and volume increases that are observed as an inflation in the tiltmeters and strainmeters. 2. Release of gas because the gas pressure exceeds the strength of the cap. The resultant minor contraction is detected by deflation tilt and downward displacement. 3. Pressure decrease in the conduit below the cap, which induces sudden out-gassing of water-saturated magma deep in the conduit. The expansion is measured by the upward P-wave first motion of the explosion earthquake. 4. Expansion process that destroys the cap at the top of the conduit (stages 3 and 4 were not distinguishable for the Suwanosejima and Semeru volcanoes). 5. Given the failure of the cap at the top of the conduit, the gas pocket at the top collapses, inducing a contraction ground-deformation source in the shallow part. Tiltmeters and strainmeters revealed this step. Otherwise, ash and gas emission from the conduit is observed as a deflation for the tiltmeters and downwards for the strainmeter.
Another approach was analyzed by Yakoo et al. (2009), who used both an infrasound network and

video image time-series observations of the Vulcanian eruption that occurred at Sakurajima Volcano (Japan) in January 2002. These observations suggested that the volumetric increase of the gas pocket caused a swelling of the surface of the crater bottom, and its subsequent failure. When the expansion velocity exceeded a threshold level, the main impulsive compression phase radiated with a high velocity through the sudden release of the pressurized gases. This volume change indicated that the vertical displacement of the swelling ground was of the order of one meter, assuming the radius of the lava plug was approximately 10 m.
Druitt et al. (2002) surveyed the eruption of the Soufriere Hills Volcano on Monserrat in 1998, and reporting 88 Vulcanian episodes that revealed the Vulcanian mechanism. This mechanism can be broken down into the following scenario. The explosion starts when the pressure in the conduit goes over a threshold trigger of the cap of degassed crystal-rich magma. A fragmentation wave goes down the conduit into a region of pressurized magma with an approximate velocity of 50 m/s, which results in an upward speed of around 140 m/s.
On the other hand, small-aperture seismic arrays have been useful to locate seismic sources in volcanic unrest, as seismic waveforms have a lack of clear body-wave phase arrivals. Emergent onset in long-period and tremor seismic waves make it extremely difficult to solve a source localization from classical hypocenter methods based on phase picking and calculated travel-times. Therefore, different methods of source localization have been applied to array data recorded from volcanic unrest (Métaxian et al., 2002; O'Brien et al., 2011; Saccorotti and Del Pezzo, 2000; La Rocca et al., 2004; Di Lieto et al., 2007; Inza et al., 2011). Also, high resolution techniques for multicomponent array data have been developed that can be applied to the locating of seismic sources (Paulus and Mars, 2006; Miron et al., 2005). This chapter is based on an article submitted to JVGR (Journal of Volcanology and Geothermal Research) in April 2013.

3.2 Vulcanian events at Ubinas volcano

A field experiment was carried out from May to July 2009 at Ubinas Volcano (Peru) that was carried out with two small-aperture seismic arrays that were composed of three-component seismometers deployed on two flanks of the Ubinas Volcano, see section 1.4 in Chapter 1.
Sixteen Vulcanian explosions, hundreds of long-period events, and several hours of tremors were identified during the period of our study, and these were classified in the catalog of the Instituto Geofisico del Peru Volcano Observatory. The Vulcanian explosions were small to moderate-sized and lasting from seconds to minutes. Most of them (11 of 16) were followed by tremor episodes that lasted from 20 min to 2 days. In Figure 3.1 shows the RSEM (real time seismic energy measurement) (De la Cruz-Reyna and Reyes-Davila, 2001) of continuous data (time window = 5 min, see Equation (1.10) in chapter 1) corresponding to the vertical component of the sensor located in the middle of the WUBI antenna, including explosions during the campaign in UBinas 2009. The inverted triangle markers correspond to the 16 Vulcanian explosions, identified by numbers, the dashed horizontal lines specify the duration of the tremor events, and the square markers correspond to tectonic earthquakes (outside the volcano edifice). The 16 Vulcanian events are listed in Table 3.1, which summarizes

the date of occurrence of each event, the maximum amplitudes of explosion waveform, the seismic energy, the intervals between the events, and the durations of the post-explosion tremor. The energy E was computed according to Equation (3.1) (Johnson and Aster (2005)), by integrating the square amplitudes of the velocities between the full wave of the explosion confined to a window of 1 min, where ρ is the volcano density (2600 kg/m^3, r is the source-station distance (2567 m), v_P is the body-wave velocity, $A = 1$ is the attenuation correction, and $S = 1$ is the site-effect constant.

$$E = \frac{2\pi r^2 \rho v_P S^2}{A} \int_0^T y^2(t) d(t) \tag{3.1}$$

The event energy of the explosions varied between 3 MJ and 383 MJ (Table 3.1). During this period

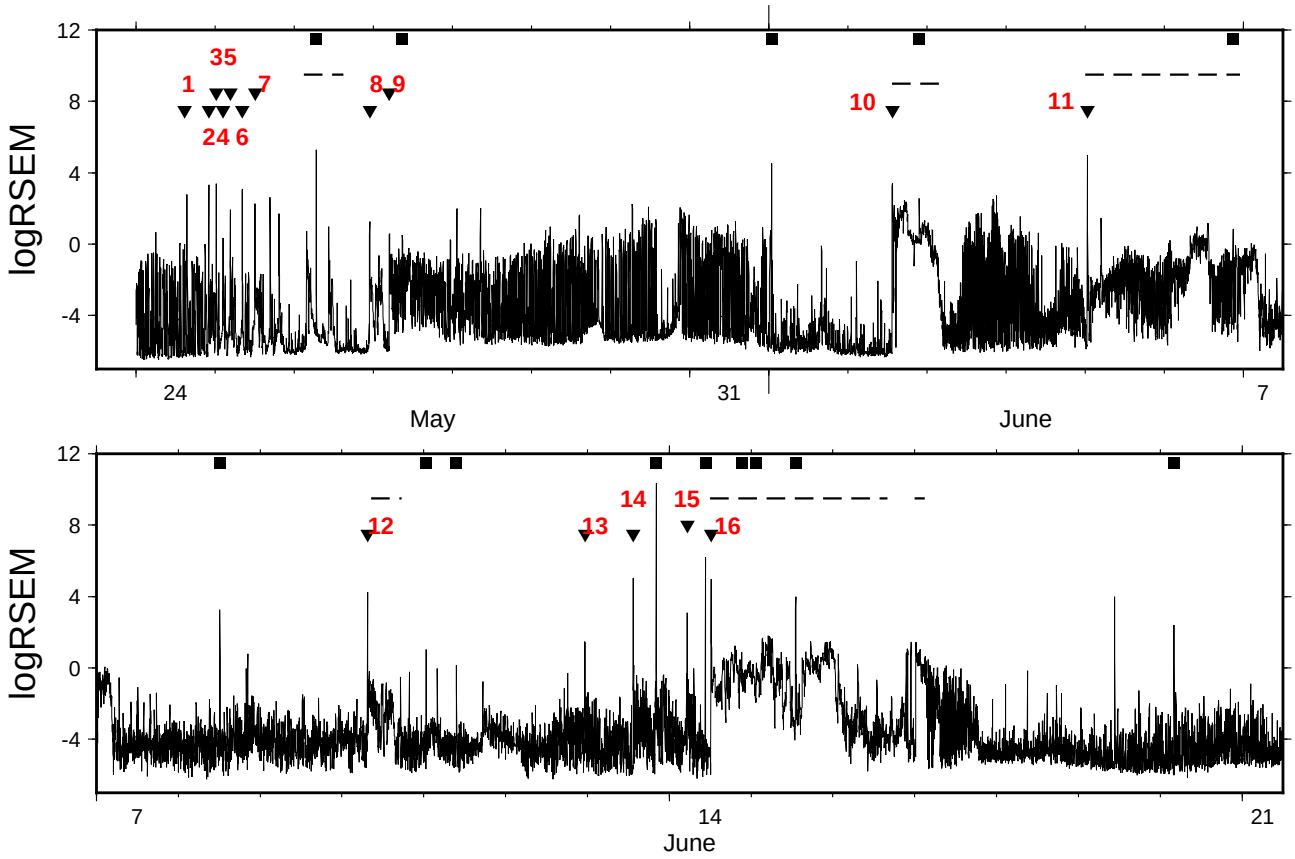


Figure 3.1: RSEM computation, with 5 minutes sliding time windows, during the 2009 experiment. The black inverted triangles match the sequence of 16 vulcanian explosions numbered. Horizontal dashed lines match to tremor event duration and black square dots match to quakes out of volcano.

of explosive activity that lasted 22 days, the interval between two successive explosions varied from 2.1 h to $> 6 days$. The tremors that followed most of the explosions lasted from 0.4 days to > 2 days. There were no tremors following four of the explosions. The means of the seismic energy, time interval and tremor duration were 89 MJ, 33.5 h and 7.7 h, respectively.

Item	Date Time	E (MJ)	Interval	TR
1	2009/05/24 14:43:33	3	0	0
2	2009/05/24 22:05:23	60	7.4 h	0
3	2009/05/25 00:21:56	56	2.3 h	0.5 h
4	2009/05/25 02:26:47	3	2.1 h	0
5	2009/05/25 04:35:05	13	2.1 h	1.6 h
6	2009/05/25 08:14:40	48	3.6 h	0.5 h
7	2009/05/25 12:06:59	22	3.9 h	1.5 h
8	2009/05/26 22:54:33	14	1 d 10.8 h	4 h
9	2009/05/27 04:52:53	9	6 h	1.1 h
10	2009/06/02 01:27:42	48	6 d 8.6 h	16 h
11	2009/06/05 00:39:37	314	2 d 11.2 h	2 d 3 h
12	2009/06/10 07:31:35	145	5 d 7.8 h	9 h
13	2009/06/12 23:16:03	5	2 d 15.3 h	0
14	2009/06/13 13:26:02	218	14 h	20 min
15	2009/06/14 05:15:24	85	16 h	0.5 h
16	2009/06/14 12:15:42	383	7 h	1 d 13 h

Table 3.1: Characteristics of the 16 Vulcanian events of May and June, 2009 at Ubinas. The date and time are in universal time (local time was 5 h more), E is the event energy in MJ, the 'Interval' is the time interval since the previous explosion, and TR is the tremor duration after the explosion.

We did not see any clear relationship between the interval duration and the energy. For example, on May 25, five explosions occurred with very short and relatively similar intervals, of between 2.1 h and 3.9 h, while the energy fluctuated considerably, between 3 MJ and 56 MJ. In the same manner, explosion #6 occurred 3.6 h after explosion #5 with an energy of 48 MJ, while explosion #10 occurred 6d 8.6 h after explosion #9 with an equivalent energy, of 48 MJ. Figure 3.2 shows the seismic energy and the tremor duration as functions of the intervals between the explosions. Except for explosion #16, the explosions that occurred with relatively small time intervals compared to the mean (< 8 h) were of low energy (< 60 MJ). On the other hand, the explosions with greater time intervals were of either low or high energy. Therefore, it does not appear that the time interval is related to the intensity of the explosions. For the tremor duration following the explosions, it appears that in most cases the following apply: 1. The tremor lasted a short time after low-energy explosions and for short time intervals; 2. The tremor lasted longer for high-energy explosions (#11 & #16) and for long time intervals.

3.2.1 Tilt observations

We compared the tilt and seismic data of explosion event #7 (Table 3.1), occurred on 25 May 2009 at about 12:07 universal time in Ubinas. The seismic waveforms were filtered with band-pass filters between 0.03 Hz and 2 Hz, and converted to displacement (Figure 3.3). In Figure 3.3a, NUBIZ and

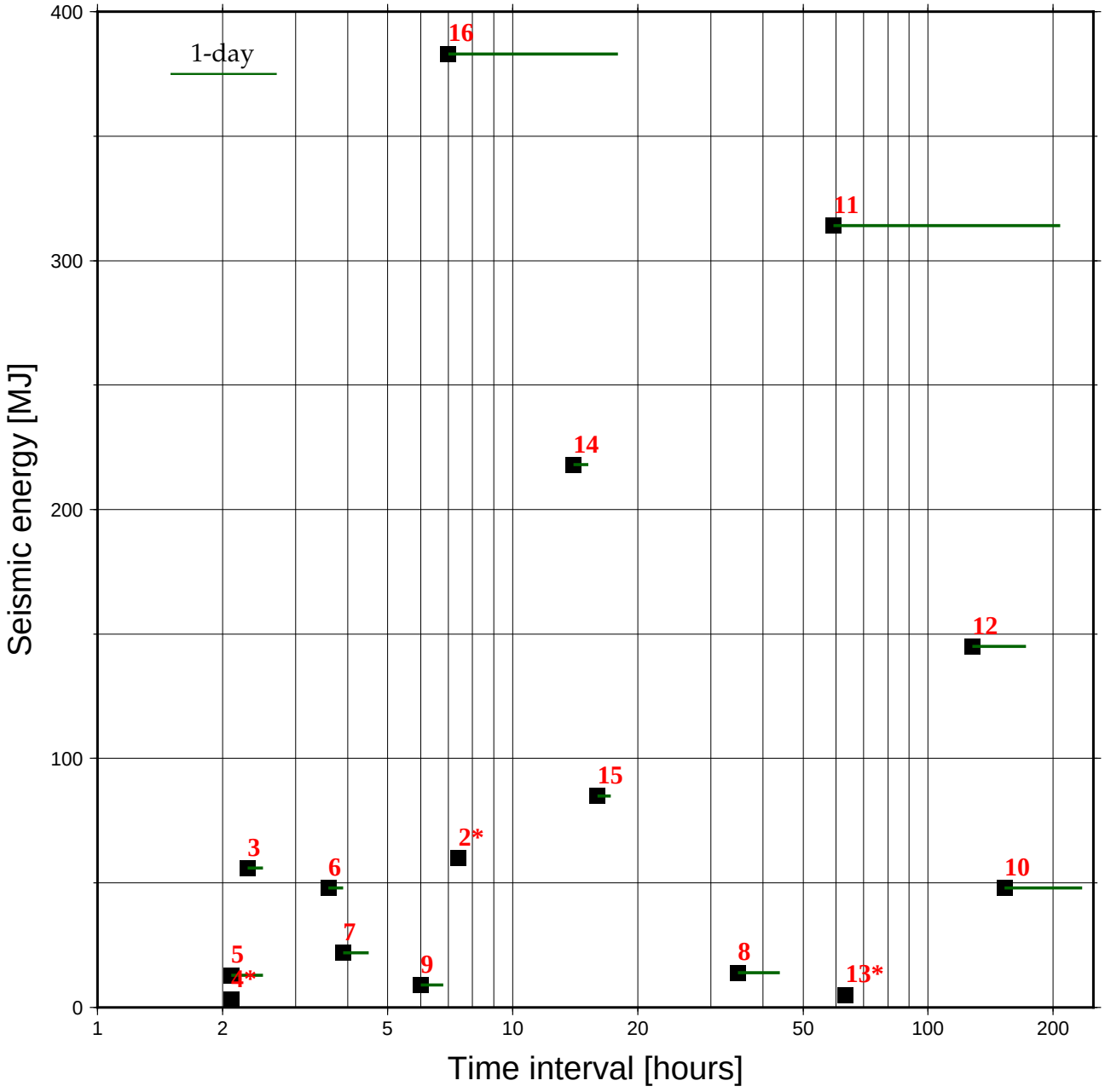


Figure 3.2: Seismic energy and tremor duration as functions of the interval between the explosions. The black squares are the explosion energies and the explosion intervals. The horizontal segments are the duration of the post-explosion tremor, (*) are explosions without tremor. The numbers are the explosions, according to Table 3.1.

WUBIZ correspond to the vertical components of one seismometer located in the middle of each antenna, and UBI2Z is the vertical component at UB2. The tilt data were converted to micro-radians (Figure 3.3b). An expansion of the UB2 first-arrival waveforms in the time window of 415 s to 422 s is shown in Figure 3.3c. It is worth recalling that UB2Y was oriented to the north, almost radial to the volcano crater, and UB2X was oriented to east. The gray curve of UB2-HF in Figure 3.3c is the vertical seismic signal (UB2Z) filtered into the band of 2.2 Hz to 6 Hz.
The vector sum of the tilt channels (UB2Y and UB2X) yield the direction and magnitude of rotation with respect to the vertical gravity vector (Applied-Geomechanic Tiltmeter manual). The black curve in Figure 3.3d is the UB2 tilt vector for the time window of 418 s to 420.5 s (Figure 3.3c, red dashed rectangle). This time window corresponds to the signal prior to the seismic broadband first arrival (UB2). The gray curve in Figure 3.3d corresponds to the UB2 tilt vector given by the signals UB2X and UB2Y for the whole time window (Figure 3.3c). The radial trend can be described as a slight upward tilt [418-419], followed by a minor downward tilt [419-420.5], and a clear upward tilt to the maximum [≈ 421] that coincides with the upward displacement recorded by the broadband seismometer at UB2. The tilt pattern observed on the radial component of UB2 can be described as a slight inflation followed by a deflation, such that a contraction of the crater area started at 419 s. This was followed by a strong inflation (expansion), which can be seen as the onset of the explosion between 420.5 s and 421 s. The beginning of the vertical seismic movement that coincided with the maximum of the radial tilt was also observed at WUBI. This was less clear at NUBI, which was at a greater distance from the crater. In addition, an emergent high-frequency signal (Figure 3.3c, UB2Z-HF) started almost simultaneously with the UB2Y downward movement, at around 419 s.

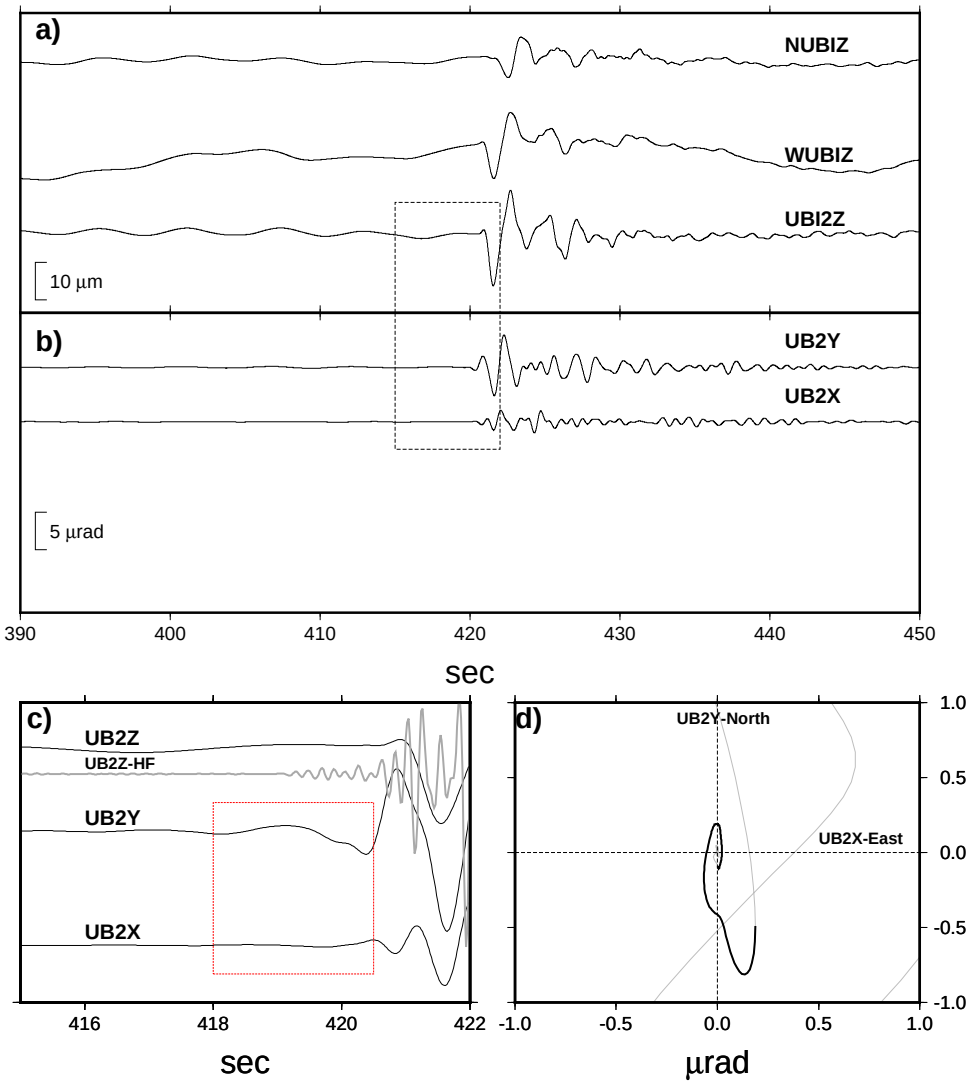


Figure 3.3: Explosion #7 waveforms recorded at the NUBI, WUBI and UB2 stations. a. Vertical components of the displacement filtered between 0.03 Hz and 2 Hz. b. Tilt signals recorded at UB2 in µrad. c. Zoom of UB2 signals inside the selected rectangle in (a) and (b), with the high frequency (2.2-6 Hz) seismic signal waveform of UB2Z in gray. d. UB2 tilt vector evolution. The black curve corresponds to the tilt for the rectangle.

3.2.2 Processing

A primary objective of this study was the location of the sources of the 16 Vulcanian events that were identified, as in Table 3.1, to try to better understand the explosive dynamics at Ubinas. With this aim, we applied the MUSIC-3C method, as proposed by (Inza et al., 2011). Given the lack of a velocity model for the Ubinas Volcano, the propagation medium was assumed to be homogeneous. This next section is divided in several parts. We begin by identifying the frequency bands where the energy of the explosions was concentrated. We then describe the different steps of the slowness vector estimation, with its application to one of the explosions. Synthetic data are also used to validate our results. Finally, we present the results obtained for the whole set of explosions, an example of long-period events, and we discuss how our data have improved our understanding of the explosive dynamics.

Determination of the useful frequency-band

In this part, we focus on the analysis of explosion #7. We consider the most relevant waveforms within the band of 0.5 Hz to 6 Hz, as shown in Figure 3.4. From the top to the bottom of Figure 3.4 there are the time-series waveforms of each 3C component clustered as north (NS), east (EW) and vertical (Z), with the power spectral density for each component, computed by the smoothed periodogram method. The coherences were calculated between the waveforms using the data of each clustered components shown in Figure 3.4a. The thicker curve in Figure 3.4c shows the average coherence, where high coherence occurs at frequencies between 0.5 Hz and 2.2 Hz, whereas less significant coherence is seen between 2.2 Hz and 6 Hz. The arithmetic average of the spectrum of each component depicts the global spectrum of the antenna (Figure 3.4b), which illustrates the frequency bins contributing to the seismic body. Moreover, the average of these three spectra shown in Figure 3.4c reveals two frequency bands, 0.5 Hz to 2.2 Hz and 2.2 Hz to 6 Hz; they will be analyzed separately. Our interest is focused on the early arrivals of the signals that express the most direct waves from the source. A time-frequency distribution is performed to identify the frequency ranges that correspond to the first arrivals. We used time-frequency representation to analyze the nonstationary behavior of the signal that composes the explosion quake. The Hilbert-Huang transform (Huang et al., 1998; Flandrin et al., 2004) provides a clear time-frequency representation of the body waves. The vertical component waveform of explosion #7 was analyzed using the Hilbert-Huang transform. The time-frequency representation (Figure 3.5a) shows the dominant frequencies between 0.5 Hz and 2.2 Hz, and lower intensity for frequencies between 2.2 Hz and 6 Hz, in the time window between 3.8 s and 5.8 s, which are depicted in the gray region in Figure 3.5b, and which are the first-arrival seismic waves.

Estimation of the slowness vector and source location

To estimate the slowness vector and to describe its variability with time, we applied a sliding window technique over the entire waveforms. The sliding window was set to a length of 2 s, with 85% overlap.

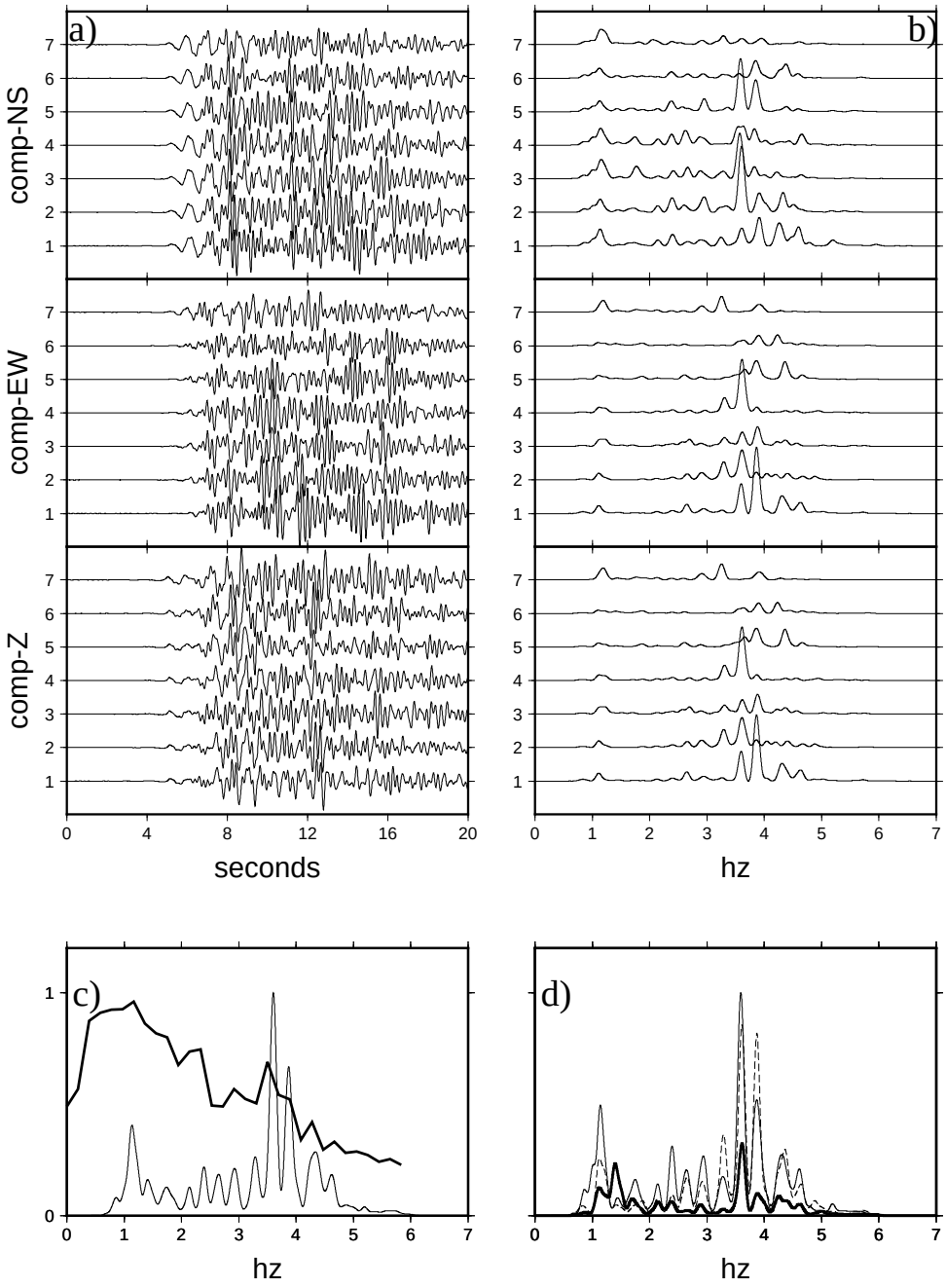


Figure 3.4: Filtered (0.5-6 Hz) waveforms of explosion #7. a. Time-series of seven sensors of three components recorded at the WUBI antenna. b. Smoothed spectrum of the 3C components. c. Thinnest curve: average of the smoothed spectrum over all of the traces. Thicker curve: average coherence. d. Average of the smoothed spectra over each component, with the thin line for the North components, the dashed line for the East components, and the thick line for the vertical components (Z).

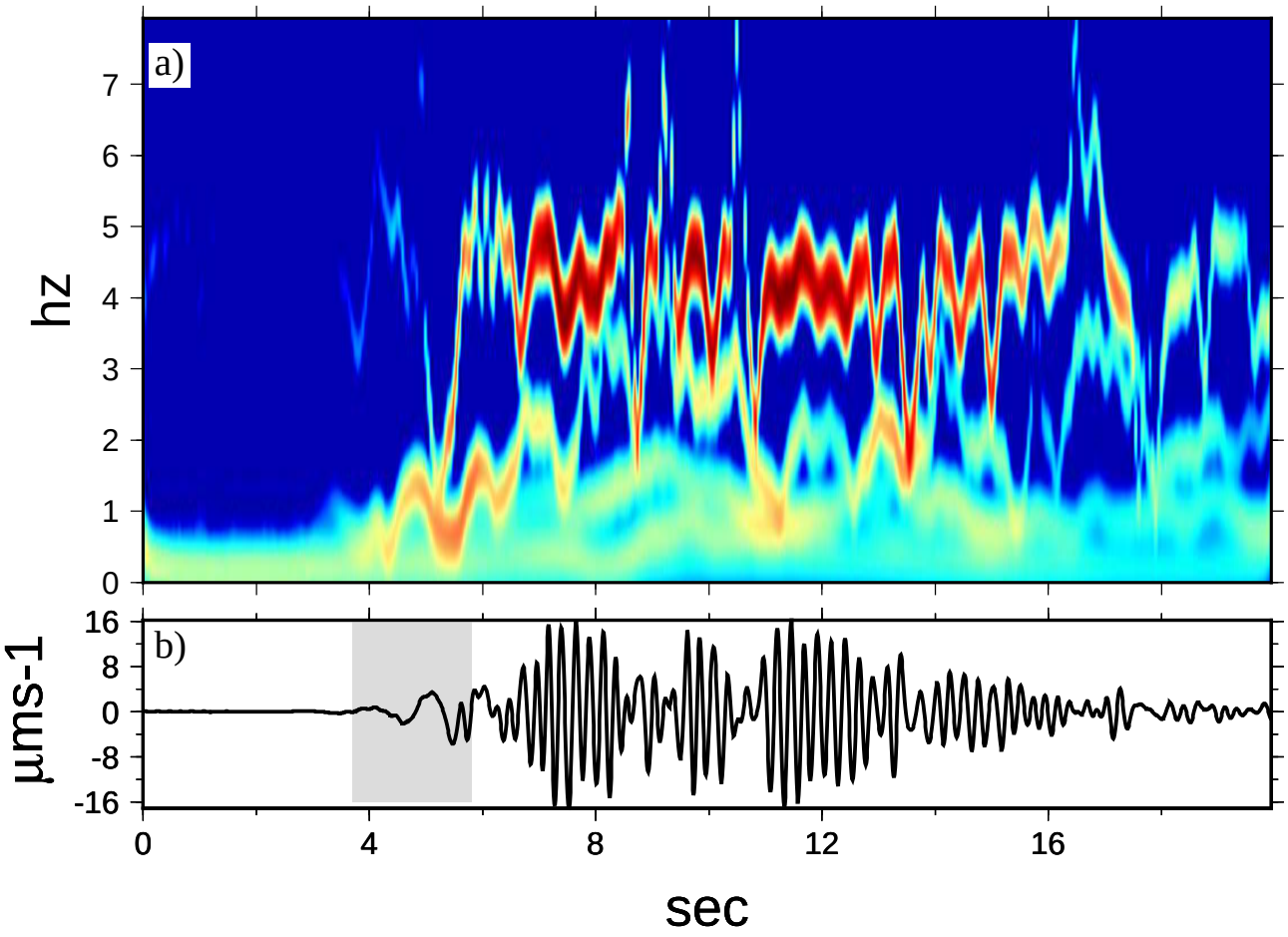


Figure 3.5: a. The Hilbert Huang transform as applied to the vertical component of the seismic signal of explosion #7, as recorded by sensor 04 of the WUBI antenna. b. The time representation of the signal in (a), where the gray region represents the first-arrival signal.

This allowed certain inconsistencies of the sliding window process to be managed correctly, such as some waveforms cannot be completely inside the sliding window for some iterations, due to the lag time. Following the time-frequency analysis, the two frequency bands had to be analyzed separately, as 0.5 Hz to 2.2 Hz, and 2.2 HZ to 6 Hz (Figure 3.5). We first processed the data for the low frequency band (0.5-2.2 Hz). To explain the processing for each sliding window, one time window was taken from the sequence. We are mainly interested in the beginning of the seismic traces of the explosion, as our objective was to study the initiation of the physical process of the explosions. Then, we computed the average spectrum for one time window positioned at the beginning of the explosion quake. We first have to identify the bins where the seismic energy is concentrated (Figure 3.6a and 3.6b). The bins were selected by taking the spectral peaks above the threshold of 70% of the maximum. There were two frequencies bins at f1 = 1.1 Hz, and f2 = 1.5 Hz (Figure 3.6b).
The MUSIC-3C analysis was performed by processing each frequency bin (f1, f2) separately. Fol-

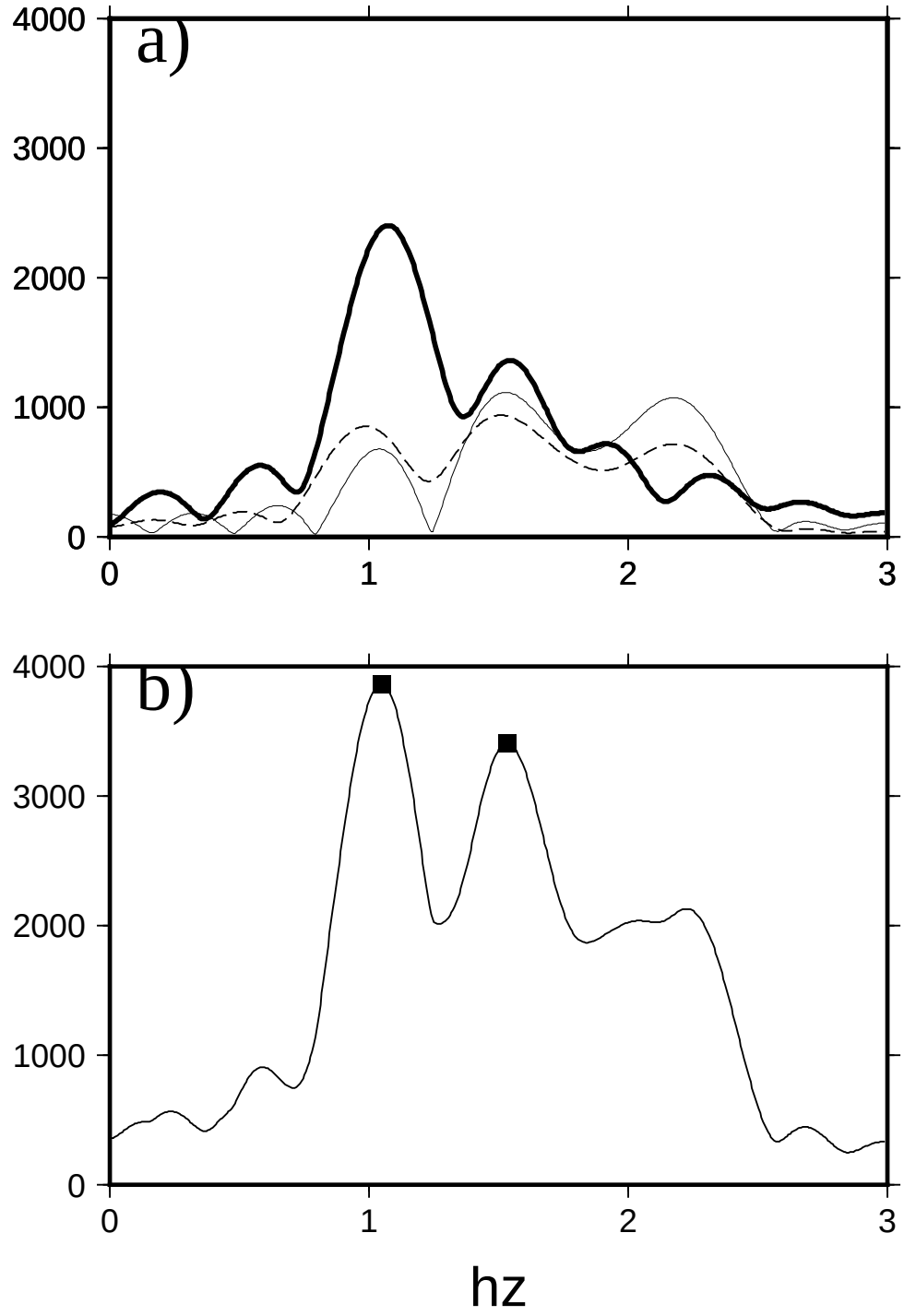


Figure 3.6: a. Spectral average calculated for each component of the signals recorded by all of the WUBI sensors for the time-window defined in Figure 3.5b by the gray zone (first-arrival signal). The thick line corresponds to the vertical component, the dashed line to the East component, and the thin line to the North component. b. Averaged spectrum of the three components, where the squares indicated the bins selected for analysis.

lowing this method, a cross-spectral matrix was assembled using the three components. Then the eigendecomposition of the data cross-spectral matrix was split into two subspaces (signal, noise). The MUSIC-3C spectrum is the inverse of the projection of the steering vector onto the noise space. Ideally, the steering vector of a frequency bin is orthogonal to the noise subspace. At this stage, the MUSIC-3C results were expressed in terms of the back-azimuth and the apparent velocity spectrum (see Inza et al. (2011) for details). The back-azimuth is the angle of the wavefront that arrives at the antenna, measured clockwise between North and the direction towards the epicenter in the horizontal plane. Figure 3.7a and 3.7b show the MUSIC-3C spectrum as it was applied to each frequency bin (1.1 Hz, 1.5 Hz, respectively). These Figures show the vertical sections of the azimuth and the apparent velocity passing through the maximum of the peak of the spectrum. We deduced from these curves the values of the back-azimuth, the apparent velocity, and the associated errors. We obtained the back-azimuths of 123° +/-4° and 119° +/-5° for f1 and f2, respectively. The apparent velocities were 1356 +/-188 m/s and 1507 +/-250 m/s, respectively. The errors were estimated by taking the peak width of 90% of the peak maximum of the MUSIC-3C spectrum. Fixing the back-azimuth and the apparent velocity found previously, the MUSIC-3C algorithm allows an estimation of the incident angle. The MUSIC-3C spectrum is represented in Figure 3.8a and 3.8d as a function of the incidence angle and the crustal velocity below the antenna, for each frequency bin, f1 and f2. The incidence is the angle measured between the direction of the wavefront moving towards the antenna and the vertical (in the vertical plane). The incident angles and the velocities were estimated by taking the maximum of the MUSIC-3C spectra (Figure 3.8b, 3.8c, 3.8e and 3.8f). This gave 75° +/-10° (f1 = 1.1 Hz) and 89.5° +/-15° (f2 = 1.5 Hz) for the incident angle, and 1367 +/-140 m/s (f = 1.1 Hz) and 1391 +/-150 m/s (f = 1.5 Hz) for the velocity. These values of the velocity are representative of the most superficial layer.

This analysis was then performed iteratively to each sliding window over the explosion signal. Figure 3.9 shows the results obtained by the processing of several successive sliding time windows, starting from before the beginning of the explosion, and including the first 10 s of the signal. The left part of Figure 3.9 shows NUBI, and the right part shows WUBI. Figure 3.9a and 3.9f show the waveforms for the vertical components of one element of each antenna. Figure 3.9b and 3.9g show the logarithm of the short-term average (STA) expressed by Equation (3.2) for a time-window of 1 second, as applied to the waveforms represented in Figure 3.9a and 3.9f. Here, we have used the recursive algorithm of STA presented by Withers et al. (1998):

$$STA_i = \frac{y_i}{f_s t_{sta}} + (1 - \frac{1}{f_s t_{sta}}) STA_{i-1} \tag{3.2}$$

where y_i is the amplitude of the time-series signal, f_s is the sample frequency, t_{sta} is the STA length of the time window, and i is the position of the time window.

The STA algorithm is widely used for real-time seismic detection, most of the time using the formulation of the STA/LTA ratio (Trnkoczy, 1998; Withers et al., 1998), where the LTA is the long-term average. Here, we have used STA analysis because it is more appropriate for short time windows. To obtain the first arrival zone, it is enough to evaluate only the STA, as it surveys the signal variation for a short time window. When the signal is noise, the STA represents the energy noise for a time window. The negative slope at the beginning of the curves in Figure 3.9b and 3.9g are due to the

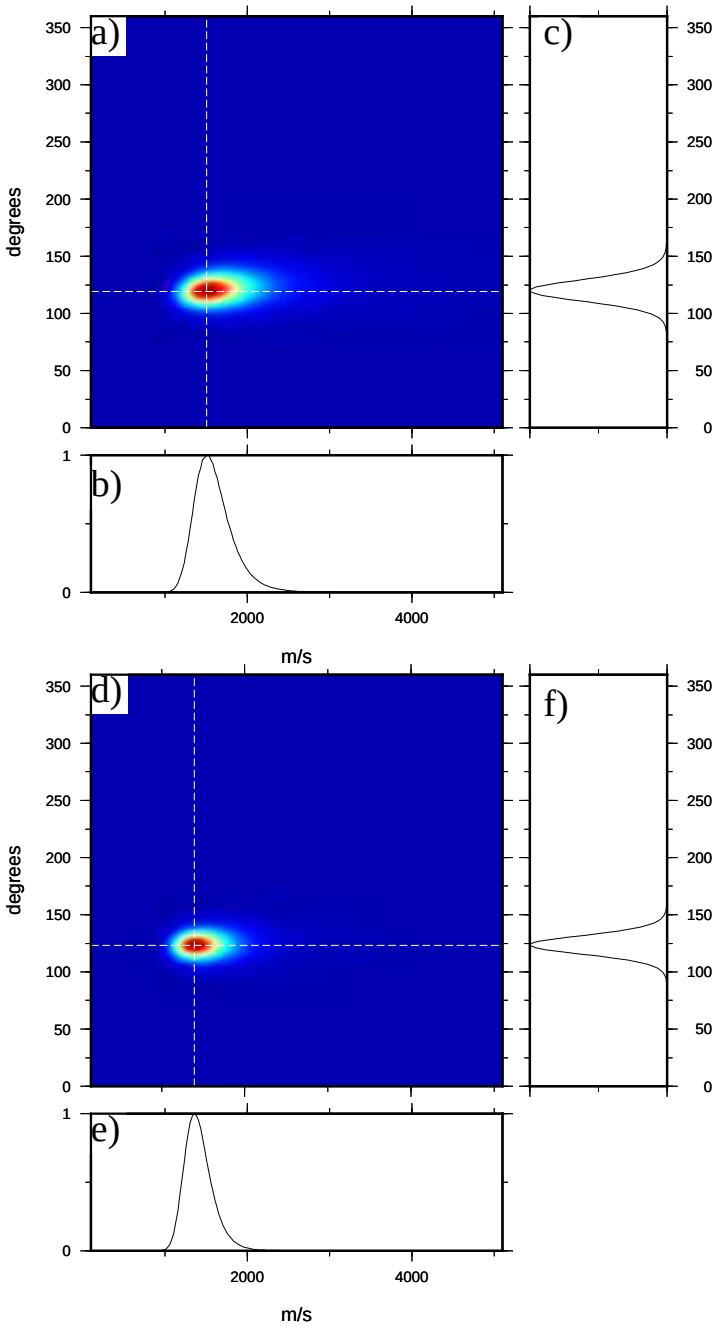


Figure 3.7: Music-3C spectrum obtained for a time window positioned at the beginning of the signal of explosion #7, represented as a function of the back-azimuth and the apparent velocity, for the frequencies of 1.1 Hz (a) and 1.5 Hz (d). b., c. Horizontal and vertical sections of the spectrum following the white dashed lines crossing the maximum of the peak spectrum for the frequency of 1.1 Hz. e., f. As for (b) and (c), for the frequency of 1.5 Hz.

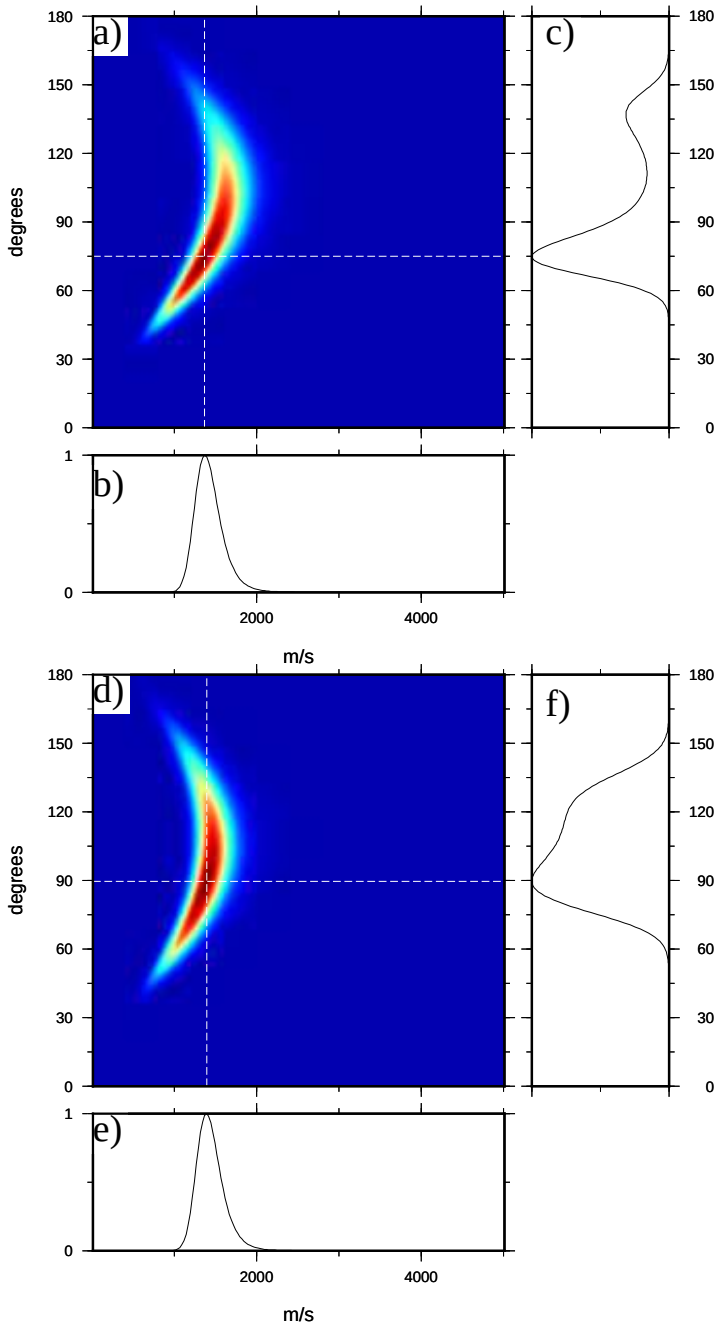


Figure 3.8: Music-3C spectrum obtained for a time window positioned at the beginning of the signal of explosion #7, represented as a function of the incidence angle and the crust velocity beneath the antenna, for the frequencies of 1.1 Hz (a) and 1.5 Hz (d). b., c. Horizontal and vertical sections of the spectrum following the white dashed lines crossing the maximum of the peak spectrum for the frequency of 1.1 Hz. e., f. As for (b) and (c), for the frequency of 1.5 Hz.

initial values of STA being bigger than the noise energy. The inflection point indicates the first arrival waves. This is around 418 s for NUBI and 417 s for WUBI. The STA curve indicates well-defined arrivals at both antennas, and shows that the wavefield arrives first at WUBI, which is consequently closer to the source. The curves in Figure 3.9c, h and 3.9d, i show the back-azimuth and incident angles, respectively. The time series of back-azimuth depicted in Figure 3.9c and 3.9h, remained extremely stable for the first arrivals, with values around 180° for NUBI and 116° for WUBI. After 424 s for NUBI and 422 s for WUBI, the back-azimuth was more unstable, probably due to the mixing of several waves. The evolution of incidence angles shown in Figure 3.9d and 3.9i express two branches. Focusing on the first arrival times, one set of incidence angles was delimited between 75° for NUBI and 79° for WUBI, with the second source in the range of 90° for NUBI and 92° for WUBI. These two sets of incident angles corresponded to the distinct frequency bins, of 1.1 Hz and 1.5 Hz, respectively. If these two frequencies correspond to distinct sources, this result indicates that they have different positions. Another piece of information given by the slowness analysis is that the position of the sources were separated in depth but not in the horizontal plane, as the back-azimuth remains constant whatever the frequency. Finally, Figure 3.9e and 3.9j indicate the crust velocities in the most superficial layer for the NUBI and WUBI antennas, respectively. For both of the antennas, the velocities were about 1450 +/-125 m/s. A similar analysis was applied to the same explosion #7 for higher frequencies. Figure 3.10 summarizes the data from the MUSIC-3C processing applied to the NUBI and WUBI array data, with filtering at the high frequency band between 2.2 Hz and 6 Hz. The first arrivals were identified between 421 s and 422 s (Figure 3.10a, f and 3.10b, g) with dominant frequencies around two bins of 3.6 Hz and 3.8 Hz. The back-azimuth estimations are shown in Figure 3.10c and 3.10h. These data are relatively similar to those obtained in the lower frequency band, at about 180° to 185° for NUBI, and 115° and 120° for WUBI. The incident angles are shown in Figure 3.10d and 3.10i. The incident angles were extremely scattered in this frequency band, so that no representative value could be deduced. Given these data, we focused our analysis only on the frequency band from 0.5 Hz to 2.2 Hz.

Returning to the results obtained previously in the frequency band of 0.5 Hz to 2.2 Hz, we estimated the source positions by crossing the source directions obtained with both of the antennas. To do this, we first fix the values of the back-azimuth and the incident angle for both of the antennas, with their respective errors. These angles were taken for the selected time windows corresponding to the first arrivals, which were defined by the two inflection points of the STA curves (Figure 3.9b and 3.9g). Hence, the average back-azimuth angles and the corresponding errors were estimated by taking the average values for the selected time windows (gray section in Figure 3.9c and 3.9h). This give 181.5° +/-4° for NUBI, and 117.8° +/-3° for WUBI. Two distinct values of incident angles were found for both antennas (green and orange sections in Figures 3.9d and 3.9i). These corresponded to 74.2° +/-7° and 93.1° +/-8° for NUBI, and 74.95° +/-8° and 90.3° +/-7.6° for WUBI. To delimit the source location, we used a probability approach, as presented by (Inza et al., 2011). We defined a probability density function (PDF) of the back-azimuth and the incident angle by representing these two parameters as Gaussian variables with the mean between (0°-360°) for the back-azimuth, and (0°-120°) for the incident angle, with standard deviations corresponding to the errors estimated in the processing. The PDF of the back-azimuth and the incident angle is presented as a rose diagram in Figure 3.11. Moreover, a conditional probability function was created from the product of the individual PDF of

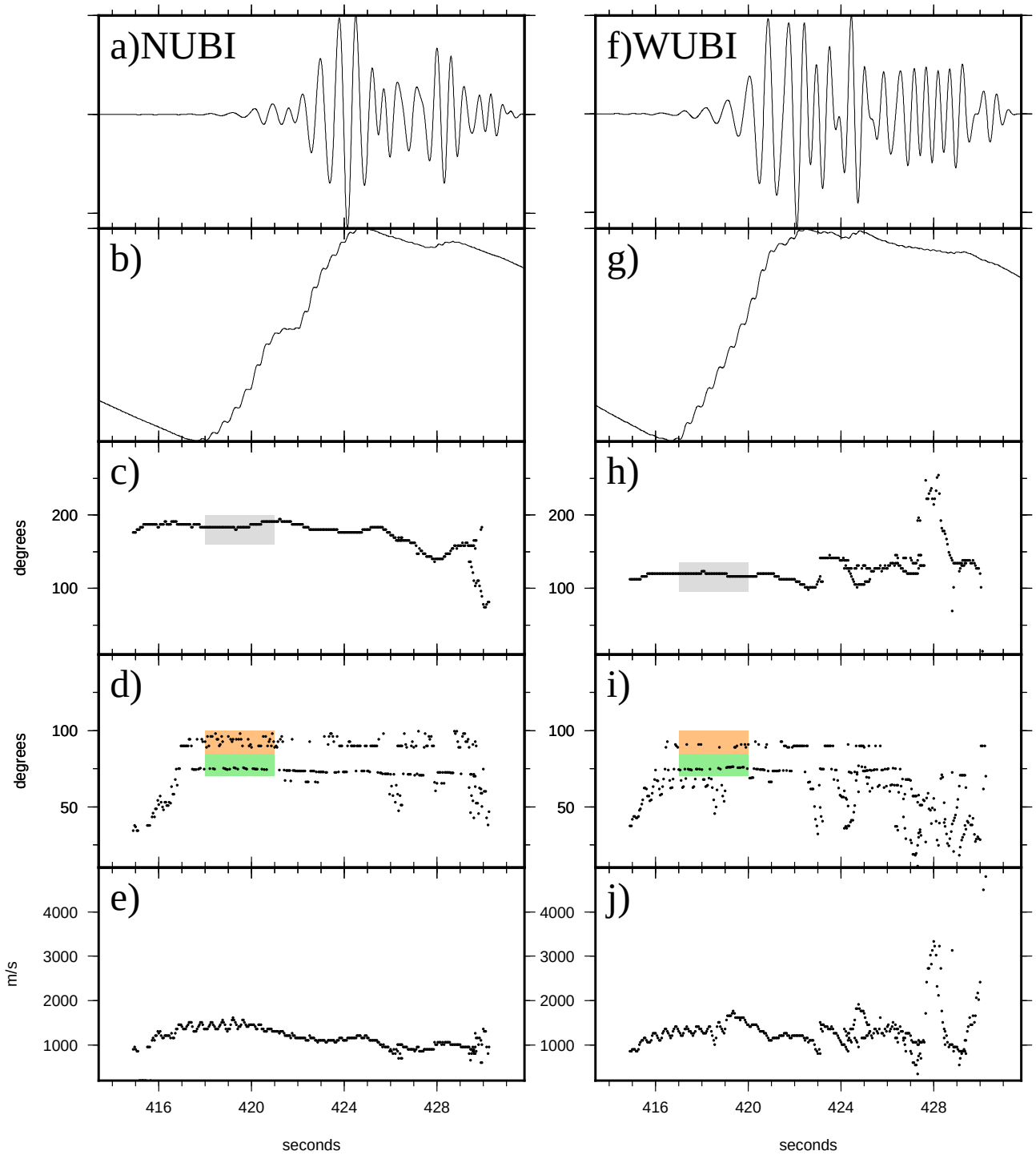


Figure 3.9: Time series representation for the low frequency band of explosion #7. Left, for NUBI; right, for WUBI. a., f. Waveform of the vertical component for NUBI and WUBI, respectively. b., g. STA logarithmic signature for NUBI and WUBI, respectively. c., h.; d., g.; e., j. Back-azimuth, incident angles, and velocity, for the NUBI and WUBI antennas, respectively.

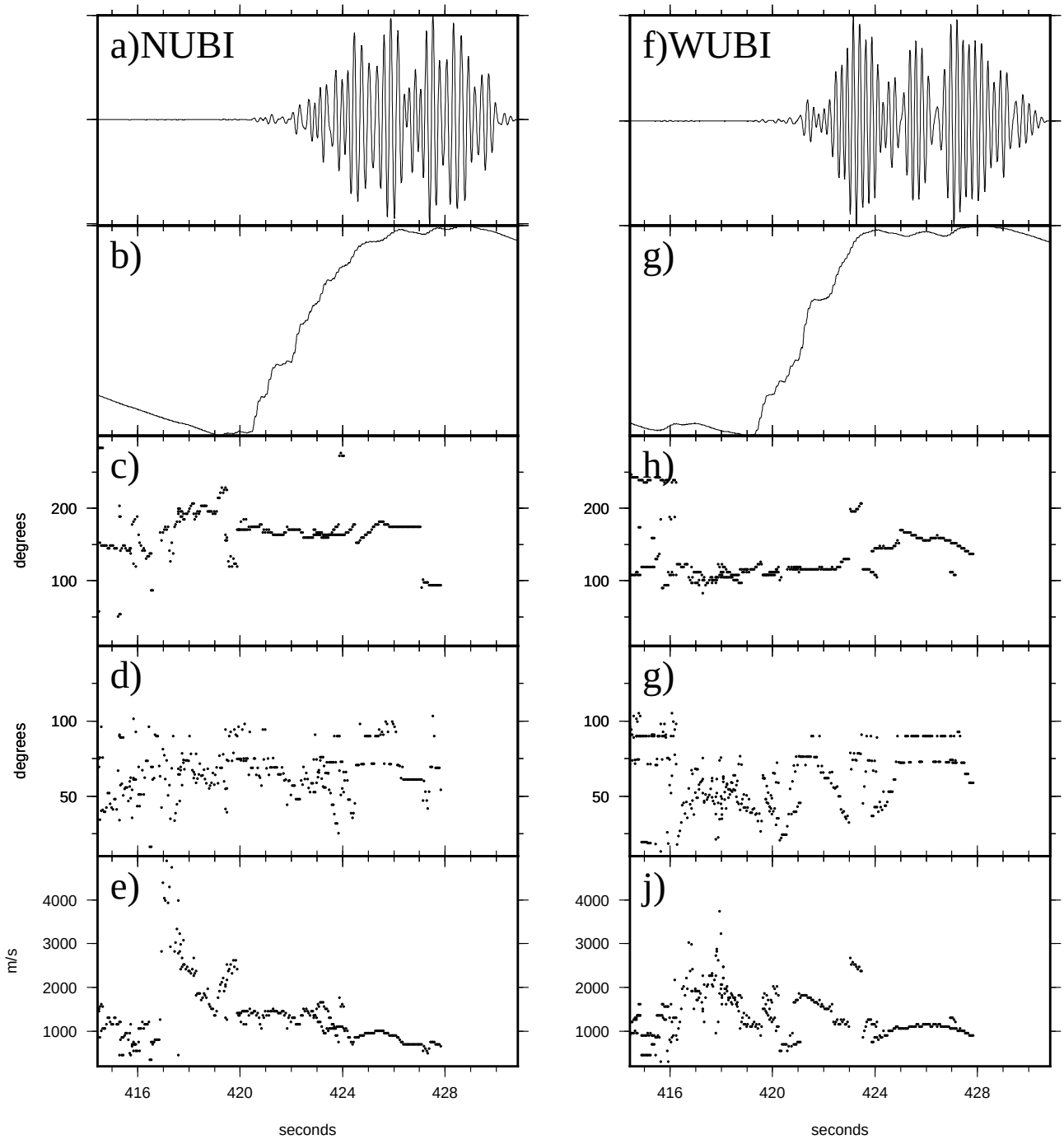


Figure 3.10: Time series representation for the high frequency band of explosion #7. Left, for NUBI; Right, for WUBI. a., f. Waveform of the vertical component for NUBI and WUBI, respectively. b., g. STA logarithmic signature for NUBI and WUBI, respectively. c., h.; d., g. ; e., j. Back-azimuth, incident angles, and velocity, for the NUBI and WUBI antennas, respectively.

the back-azimuth and the incident angle for both of the antennas. The resulting PDF, which includes information given by the two angles of both of the antennas, was represented inside the digital grid of the Ubinas map as a function of the Universal Transverse Mercator coordinates, as presented by Inza et al. (2011). The maximum likelihood of the PDF yielded an estimate of the source location. The error is defined by the mean quadratic radius R of the PDF of the source position, and is defined as

$$R = \sqrt{\sigma_1^2 + \sigma_2^2 + \sigma_3^2}$$

where $\sigma_1, \sigma_2, \sigma_3$ are the principal variances. The two sources lie below the crater, at 4.1 km and 4.85 km in altitude, +/-250 m, as shown in Figure 3.11. These data clearly showed two source areas for explosion #7. At this point, the sliding-window average spectrum of the antenna data (around the first arrival wave) were shown with either one or two frequency bins that exceeded the trigger level of 70%, at about 1 Hz and 1.5 Hz. The multiple signal classification (MUSIC) algorithm (Schmidt, 1986; Bienvenu and Kopp, 1983) identified (N-1) sources (constrained by the array response function) simultaneously (in its spectrum), and uncorrelated sources arriving at the antenna from different locations, where N is the number of sensors. Here, MUSIC-3C based on MUSIC identified two sources arriving at the antenna.

Looking at Figure 3.9, we observe that two different values of the incidence angle appear simultaneously. These angles correspond to two different waves (frequencies) in our analysis, where the process is controlled by a sliding window of 2-s width for the waveforms between 0.5 Hz and 2.2 Hz. This would thus mean that the two waves were generated almost simultaneously, or at least over a time lapse of 2 s.

Sixteen explosions (Table 3.1) were performed following the same above procedure, and each one showed two sources that were located almost in the same regions where explosion #7 was located. Table 3.2 shows the details of the locations for each of the 16 explosions, these are then transformed into a rose diagram which an average of them is depicted in Figure 3.17 (gray color) and as well as the location including their error bars. To ensure that our processing analysis could identify two waves that were emitted at the same time, and with two locations that were separated by 800 m, we used synthetic data.

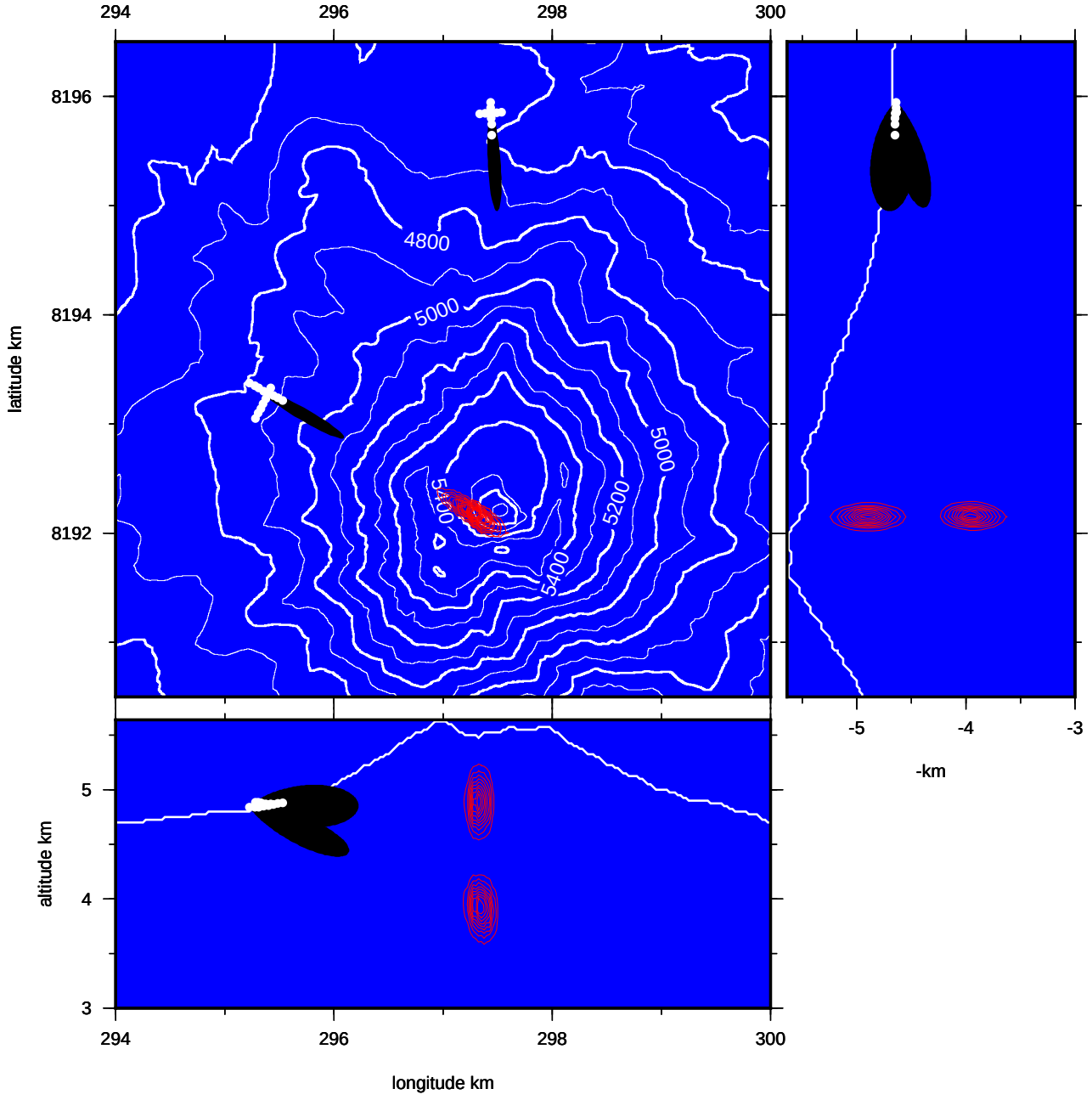


Figure 3.11: Map of Ubinas showing the slowness vector directions given by MUSIC-3C, and the maximum likelihood solution (red contour) that indicates the localization of the two sources for explosion #7.

Item	Date	Xlon	Ylat	Alt1	Alt2	Error
1	2009/05/24 14:43:22	297.53	8192.12	3.96	4.79	0.42
2	2009/05/24 22:05:13	297.43	8192.34	4.06	4.85	0.24
3	2009/05/25 00:21:50	297.41	8192.41	3.97	4.81	0.27
4	2009/05/25 02:26:39	297.30	8192.41	4.01	4.81	0.20
5	2009/05/25 04:34:58	297.32	8192.41	3.92	4.78	0.31
6	2009/05/25 08:14:32	297.37	8192.34	3.95	4.85	0.28
7	2009/05/25 12:06:53	297.37	8192.20	4.10	4.85	0.25
8	2009/05/26 22:54:26	297.36	8192.28	3.98	4.82	0.27
9	2009/05/27 04:52:49	297.44	8192.17	3.99	4.85	0.42
10	2009/06/02 01:27:34	297.43	8192.24	3.92	4.77	0.35
11	2009/06/05 00:39:31	297.43	8192.34	4.11	4.89	0.26
12	2009/06/10 07:31:25	297.37	8192.38	3.97	4.79	0.27
13	2009/06/12 23:15:52	297.47	8192.39	3.97	4.77	0.22
14	2009/06/13 13:25:55	297.39	8192.35	3.88	4.81	0.28
15	2009/06/14 05:15:15	297.43	8192.28	3.91	4.80	0.32
16	2009/06/14 12:15:35	297.32	8192.23	4.00	4.78	0.29

Table 3.2: Source Localization given by MUSIC-3C analysis on the 16 explosion events.

3.2.3 Synthetic sources

With the purpose of examining the robustness of the MUSIC-3C algorithm for multiple sources, a full waveform synthetic dataset was generated for eight sources beneath the crater, at different altitudes. Starting from a digital elevation map of the Ubinas topography, the three-dimensional discrete numerical elastic lattice method (homogeneous media) (O'Brien and Bean, 2004) was performed to propagate waves in the structure, with the eight broadband isotropic sources listed in Table 2.2, and located beneath the summit with the Universal Transverse Mercator (UTM) coordinates of longitude 297.5 km and latitude 819.2 km. In this case, the dataset was calculated for the same array location as that used in the field study in 2009. These synthetic data were analyzed in detail in a previous Chapter 2, to test the MUSIC-3C algorithm and to compare it with MUSIC-1C and MUSIC-3C.
In the present study, we used only two synthetic sources, as sources 1 and 4 of Table 2.2, which corresponded more or less to the depths obtained by the locating of explosion #7. The back-azimuth and incidence angles are depicted in Figures 3.12 and 3.13.
The data show that the source positions are recovered efficiently, as 4920 +/-120 m for source 1 and 3920 +/-100 m for source 4. To test the efficiency of separating two distinct sources, we mixed the two signals together and applied MUSIC-3C processing to the resulting signal. The data showing the back-azimuth and incidence angles are shown in the Figure 3.14.

Results of the source position for the sources 1 and 4 (listed in Table 2.2) are showed in Figure 3.15a,b, and for the mixed sources (1 and 4) is shown in Figure 3.15c. We observed two incident angles. Two depths were recovered in good agreement at altitudes of 4940 +/-160 m for source 1, and 3960 +/-120 m for source 4.

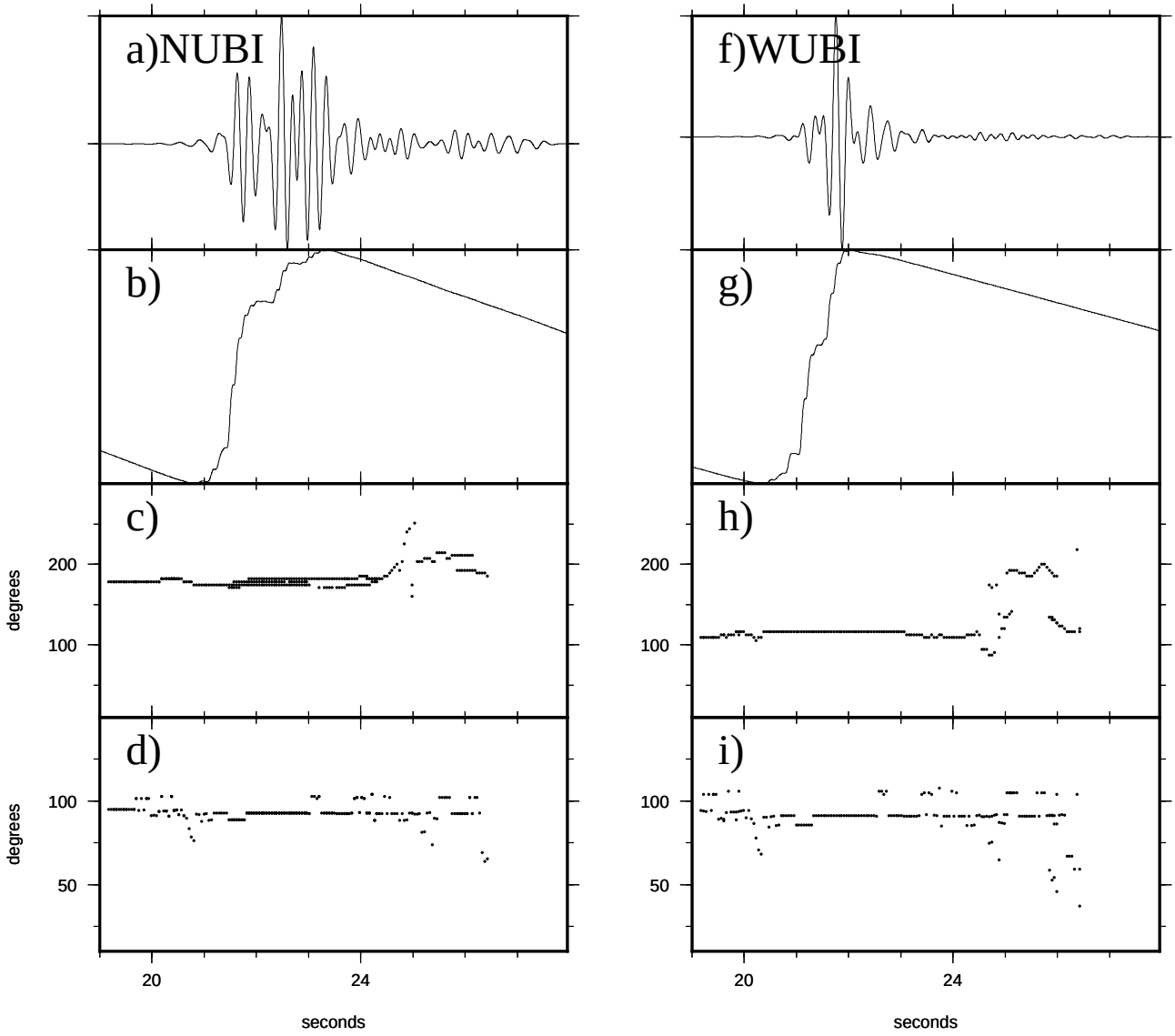


Figure 3.12: Waveforms of the MUSIC-3C procedure over NUBI and WUBI for synthetic source 1. a., f. Seismic amplitudes. b., g. Logarithmic STA of the amplitudes. c., h. Back-azimuth, in degrees. d., g. Incidence, in degrees.

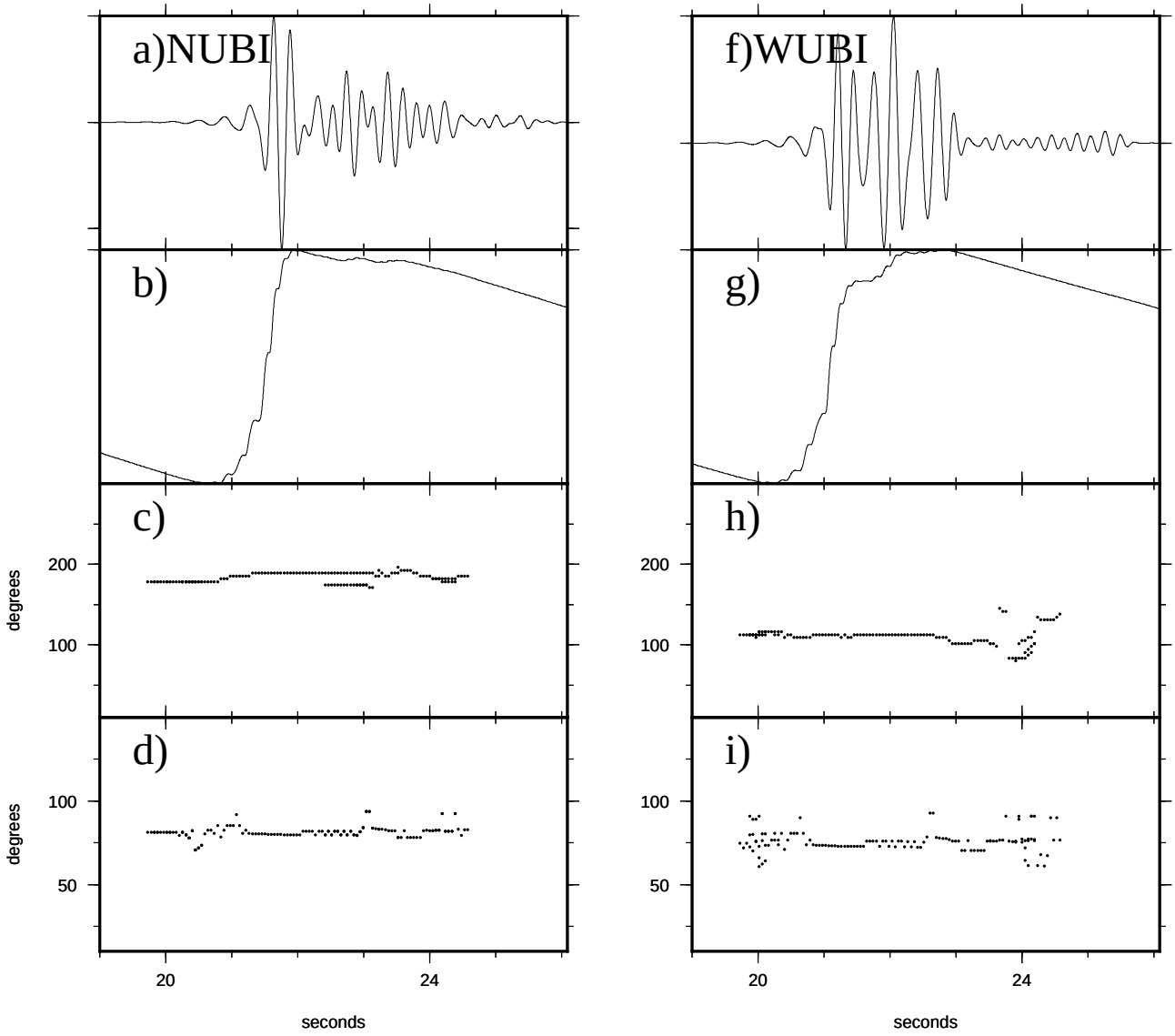


Figure 3.13: Waveforms of MUSIC-3C procedure over NUBI and WUBI for synthetic source 4. a., f. Seismic amplitudes. b., g. Logarithmic STA of amplitudes. c., h. Back-azimuth, in degrees. d., g. Incidence, in degrees.

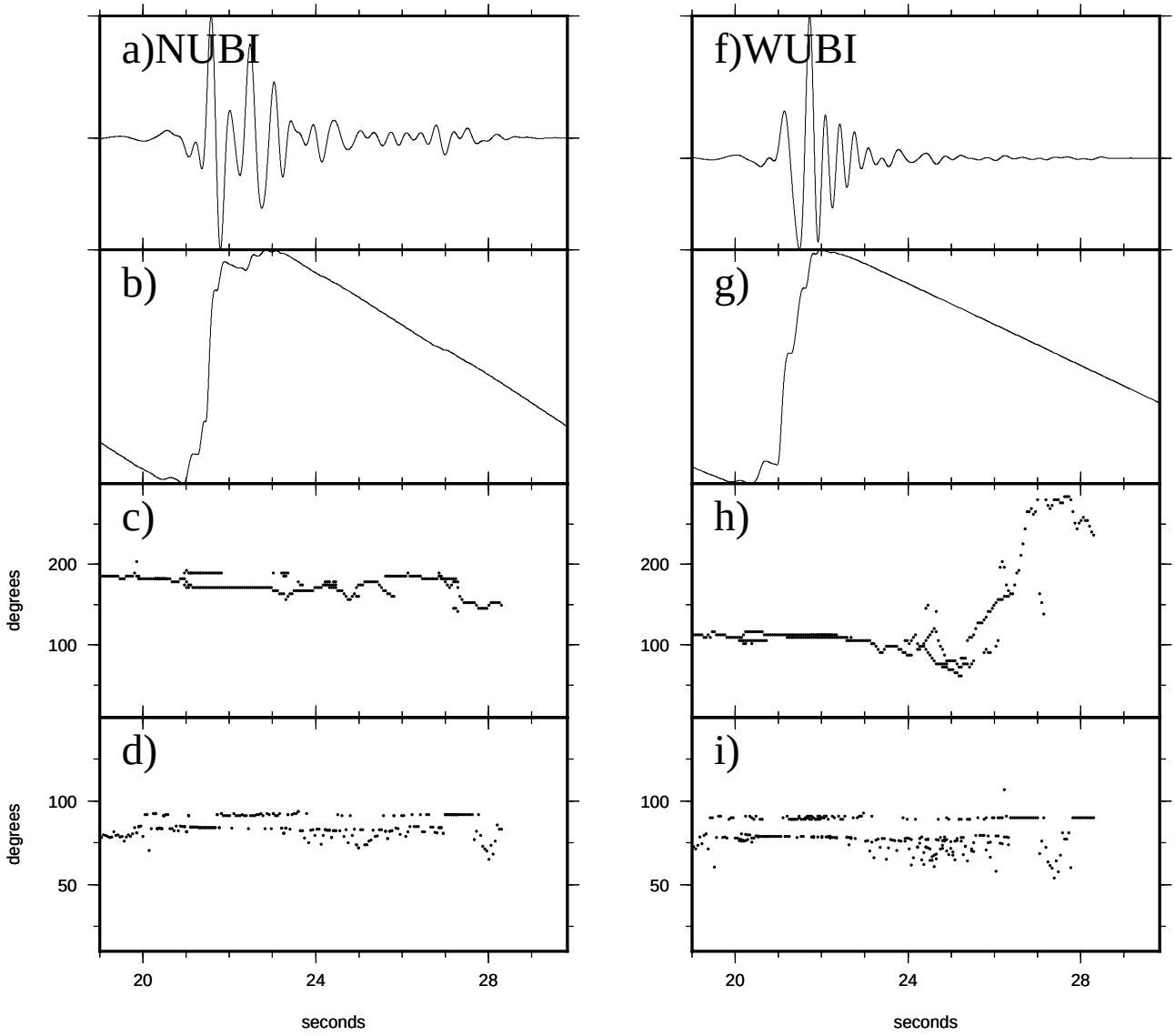


Figure 3.14: Waveforms of MUSIC-3C procedure over NUBI and WUBI for the sum of the synthetic sources 1 and 4. a., f. Seismic amplitudes. b., g. Logarithmic STA of amplitudes. c., h. Back-azimuth, in degrees. d., g. Incidence, in degrees.

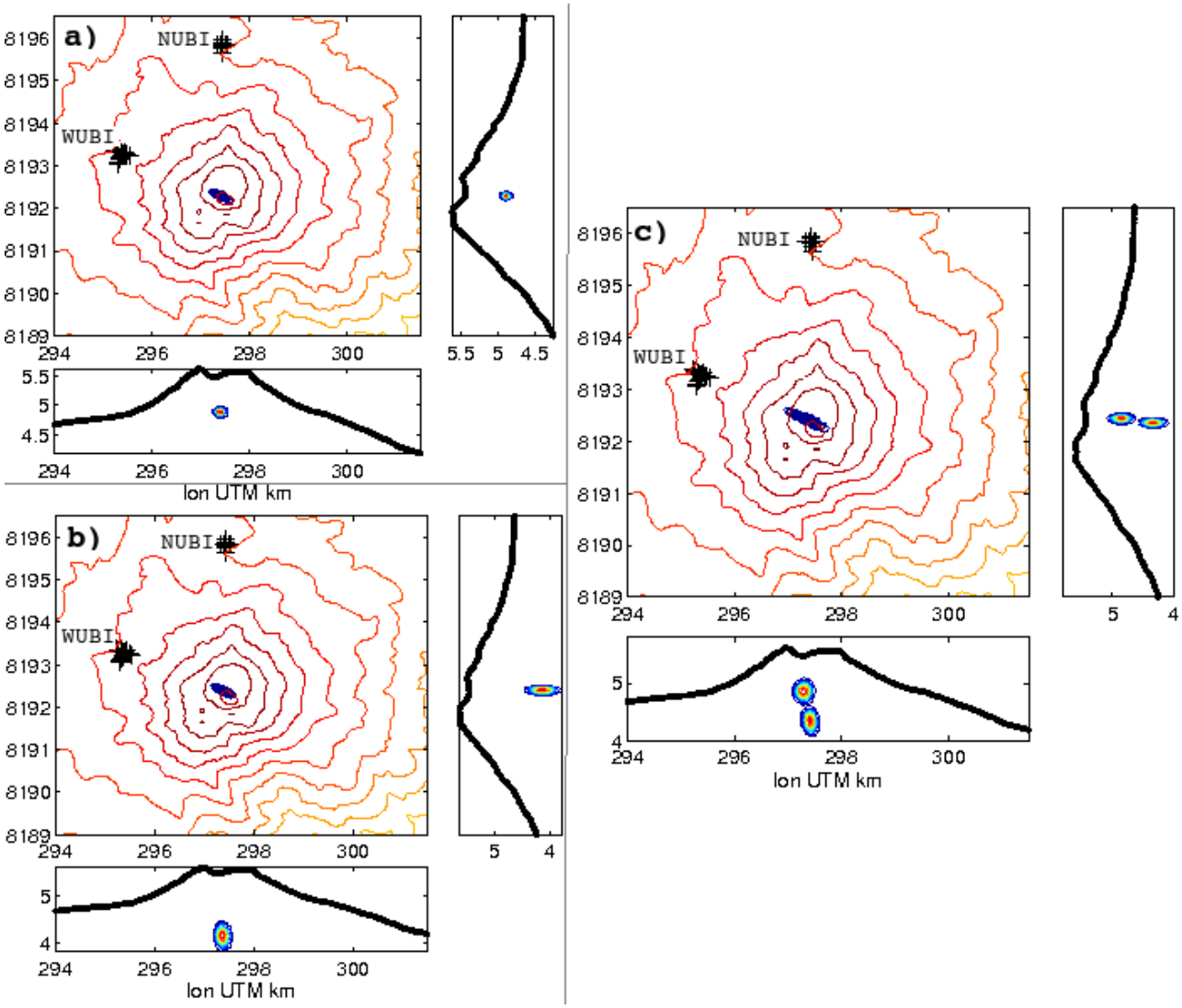


Figure 3.15: Topography map of Ubinas indicating synthetic source localizations. a) Synthetic 1 source located at at 4920 +/-120 m altitude Waveforms. b) Synthetic 4 source located at 3920 +/-100 m altitude and c) Synthetic 1 and 4 together sources located at altitudes of 4940 +/-160 m and 3960 +/-120 m

3.3 Long Period event

A similar analysis was applied to a long-period (LP) event, with the different dominant frequencies compared to the explosion quakes to check the nature of the sources of these events and to compare this with the explosions. We took as an example a long-period event recorded on June 13, 2009, around 19:58:59. The waveforms were filtered into the same band as for the explosions, as 0.5 Hz to 2.2 Hz. Figure 3.16 shows the results from the MUSIC-3C analysis. Starting from the first inflection point, there were temporal variations of the back-azimuth for the NUBI, while it was relatively stable for the WUBI (Figure 3.16c and 3.16h). The incident angle curves shown in Figure 3.16d and 3.16i show two sections that indicate a displacement of the source with time, or eventually of two sources, one more superficial than the other, but not at the same time, as was observed for the explosion quakes. There were two dominant bins for each section, at about 0.55 Hz and 0.7 Hz. The first section can be distinguished nearby at 3537-3539 s ($f_1 = 0.55$ Hz), for both antennas. An average back-azimuth appeared at 187° +/-8° for NUBI and 119° +/-4° for WUBI.
The average incidence angle was 49.9° +/-5.9° for NUBI and 37.8° +/-3.9° for WUBI. For the second section, (Figure 3.16d and 3.16i) between 3541-3544 seconds, the average of the back-azimuths and the errors were 181° +/-6° for NUBI and 119° +/-4° for WUBI, with incidence angles of 60° +/-9° for NUBI and 49° +/-3° for WUBI. The maximum likelihood of the PDF of the source positions is shown in Figure 3.17. The deeper source (Figure 3.17, red contours) was located at longitude 297.2 km and latitude 8192.2 km, with a 1.8 km altitude with a mean quadratic radius error of 490 m. The second source (Figure 3.17, green contours) was located at longitude 297.5 km and latitude 8192 km, with a 2.5 km altitude with a mean quadratic radius error of 339 m.

We have analyzed the first seconds of the low frequencies of a LP events by filtering the signal. A deep source is not contradictory with the short duration of the signal and the lack of coda at low frequencies. In fact, a coda exists and is composed of highest frequencies (2 Hz). The total duration of this event is 26 seconds. Several events, identical to this one have been recorded during the experiment. The LP event we analyzed is not a unique case. This type of LP events seems to be characteristic of a non destructive source. LP events will be studied in details in a future work.
Finally, around 50 events of hundreds of recordings in the field experiment at Ubinas 2009, were located by using MUSIC-3C along this study. Figure 3.18 illustrates the localization of these long-period (LP) events. LP events located correspond to those with highest energies between 24 May and 03 June 2009. These localizations allowed us to track the magma pathway with an error less than +/-350 m in the upper crust underneath Ubinas. It also allowed us to suggest a hypothesis that when magma rise up to the upper crust, it seems to be a high flow disturbance located around 1.2 km underneath which can be associated to the depth magma fragmentation zone (Dingwell, 1996). Another zone of disturbance was located between 200 and 300 m at the shallow part of Ubinas crater which can be related to degassing on the open conduit sytem of Ubinas. As you will recall, these two zones were characterized by the localization of the vulcanias explosions. On the other hand, Figure 3.18 show also a schematic view of the magma pathway along around 5 km beneath Ubinas crater, which has a trend to the south and a little bit to the west. It seems that magma supply to Ubinas come from suth-west.

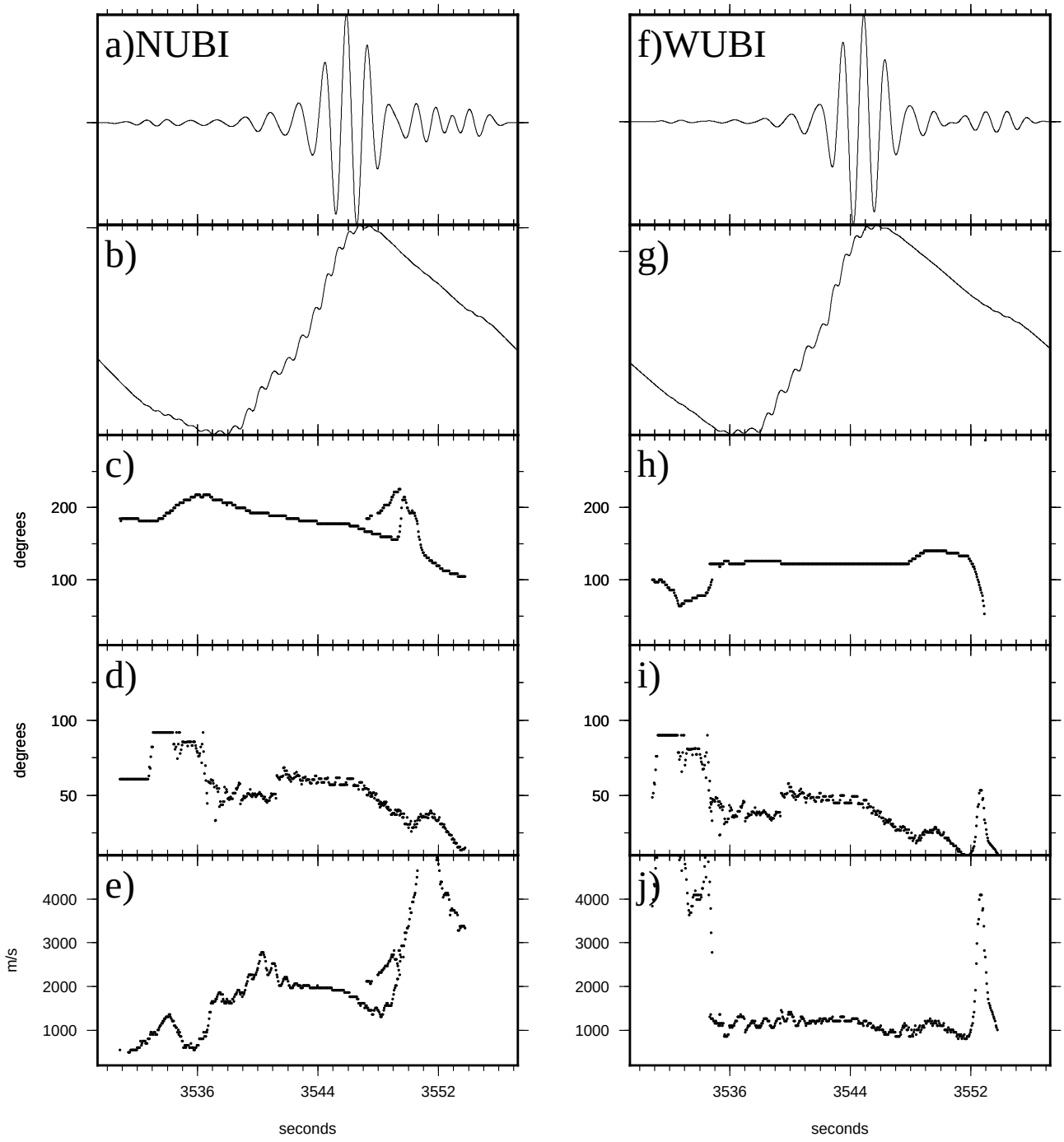


Figure 3.16: Waveforms of MUSIC-3C procedure over NUBI and WUBI for the long-period event. a., g. Seismic amplitudes. b., f. Logarithmic STA of amplitudes. c., h. Back-azimuth, in degrees. d., i. Incidence, in degrees. e., j. Crust velocity.

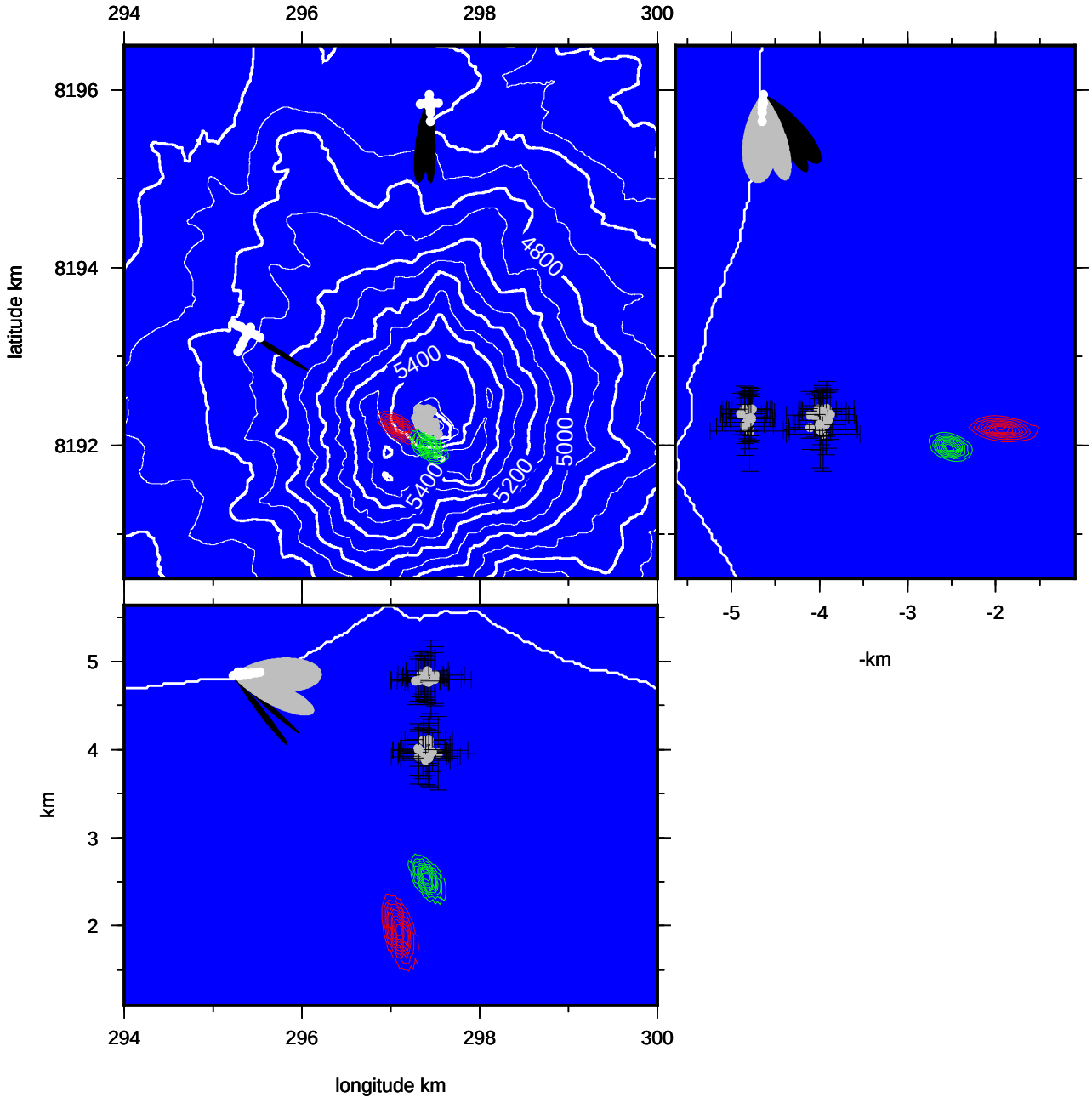


Figure 3.17: Map of Ubinas Volcano showing the slowness vector directions, and the maximum likelihood solution (red, green contour), indicating the localization sources for the long-period event. The 16 explosion localizations are shown as gray points with their errors bars.

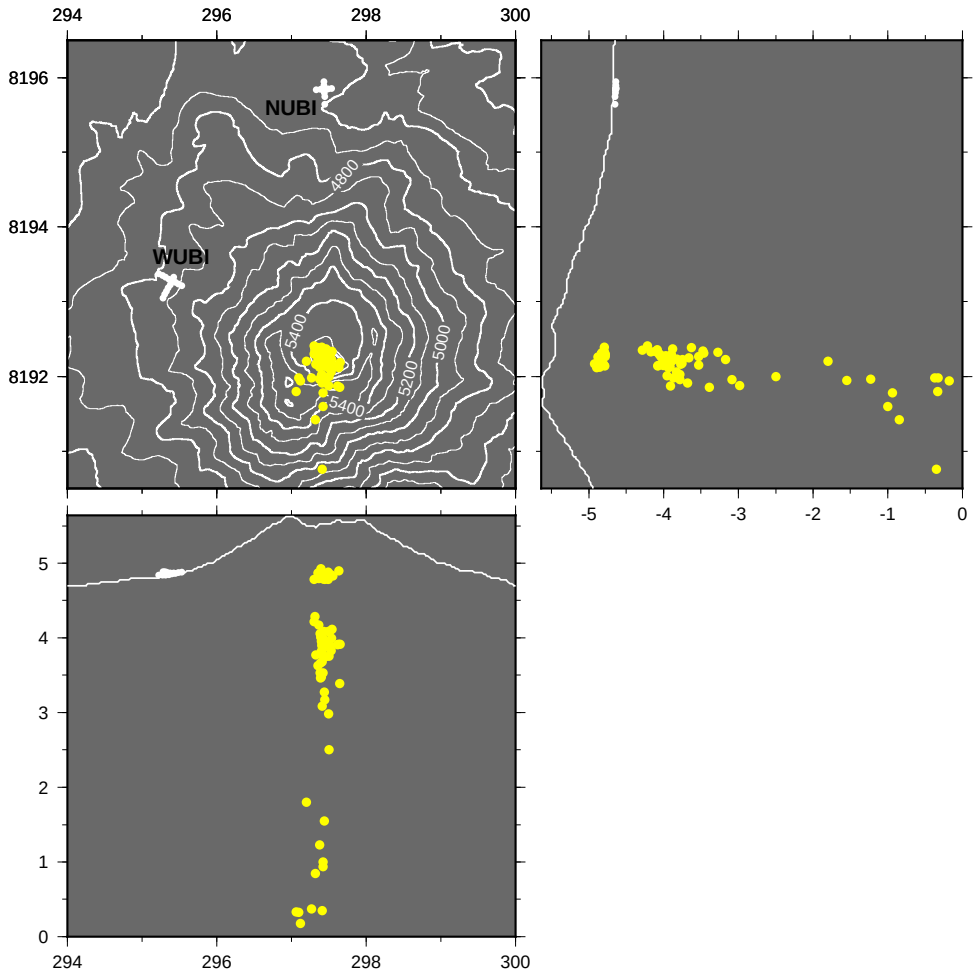


Figure 3.18: Hypocenter of 50 LP events represented by yellow circles, recoreded during the field experiment at Ubinas 2009.

3.4 Discussion

3.4.1 Swarm of vulcanian explosions

Ubinas Volcano produced 16 Vulcanian explosive events from May 24 to June 14, 2009. The time intervals between these explosions varied from 2.1 h to 6 days, 8.6 h. The mean interval was 33 h, although considering only the first nine explosions, which occurred from May 24 to May 27, the average time interval was 7.8 h. For the whole period, 67% of the intervals were lower than 24 h, and 53% were lower than 8 h, the mean time interval for the first nine explosions. In comparison, when considering the catalog of 162 Vulcanian explosions that occurred between May 2006 and June 2009, the time intervals were less than 24 h in 41% of cases, and less than 8 h in 33% of cases. This shows that Ubinas Volcano produces swarms of explosions. Even if most of the explosions were

'timely isolated', the maximum interval during these 3 years of eruptions was 3 months, with several periods of concentrated series of explosions. This suggests a regime of cyclic explosive behavior with processes of successive filling and drawdown in the conduit. This observation has important consequences for the monitoring of Ubinas Volcano. Series of Vulcanian explosions have also been observed for other volcanoes. Soufriere Hills Volcano produced 13 explosions between August 4 and 12, 1997, and 75 explosions between September 22 and October 21, 1997 (Druitt et al., 2002). Each episode was preceded by a large dome collapse, while at Ubinas Volcano, there was no dome formation during the eruptions, but there were plugs at the bottom of the crater. The explosions at Soufriere Hills Volcano occurred at intervals of 2.5 h to 63 h, with a mean of 10 h. Interestingly, the minimum refilling time is quite similar for both of these volcanoes, at 2.1 h for Ubinas Volcano and 2.5 h for Soufriere Hills Volcano.
We examined the possible relationships between the time interval and the energy of the explosions and the duration of the tremor after the explosions. A statistical study cannot be performed with a series of 16 explosions. However, two main observations can be noted. First, except for in one case (explosion #16), all of the explosions that occurred after a short time interval ($< 8h$) had low energy. This suggests that the refilling time was not sufficient to allow large accumulation of gas. Looking at the longer time intervals, it appears that some of the explosions were of higher energy, which would be consistent with previous observations. Nevertheless, some of the explosions that occurred after a long period of time were of low energy. The small number of observations does not allow us to define any hypothesis relating to the relationship between the refilling time and the volume of emitted gas in the conduit. However, this does highlight the importance of measuring the gas flow in this type of system. Secondly, the duration of the tremors following the explosions was longer for the two highest energy explosions (explosions #11 & #16). There were no tremors in only four cases. These tremors coincided with pulses of ash emission. Such ash discharge was also observed for 1 h to 3 h after explosions at Montserrat (Druitt et al., 2002). However, potentially this tremor represents a process of discharge of fragmented magma that remained in the conduit, which itself remained open after the explosion. Alternatively, the tremor might be the seismic signature of the phenomenon of refilling of the conduit. Jellinek and Bercovici (2011) proposed a model of such tremors that consisted of a column of magma surrounded in its conduit by an annulus of gas bubbles. The column oscillates or 'wags' in the conduit, with the gas bubbles acting as springs. This model proposed an explanation for the longevity of the tremors. They reported that oscillations persisted longer for taller columns.

3.4.2 Source location

The main result of this study is the identification of two distinct sources for each explosion, which were located at different depths in the conduit. The seismic signal was composed of an initial low-frequency part [0.5-2.2 Hz] and a second high frequency part [2.2-6 Hz]. The low frequencies were dominant at the beginning of the explosion. This initial part of the signal was generally composed of two distinct peaks, at 1.1 Hz and 1.5 Hz, which we have analyzed separately. We used MUSIC-3C, based on the use of three components of the sensors to estimate the slowness vectors for the antennas (Inza et al., 2011). Compared to other methods of estimation of slowness vectors (Saccorotti and

Del Pezzo, 2000; Almendros et al., 2001a; Métaxian et al., 2002; La Rocca et al., 2004), Music-3C uses seismic information in three dimensions, which allows the estimation of the angle of incidence of the wave field. This is an apparent incident angle that corresponds to the propagation of rays in the underlying layer to the array. The angle of incidence was determined, however, with a lower resolution than the back-azimuth, due to the geometry of the network. Indeed, the inter-sensor distance was greater in the horizontal than in the vertical plane.
The analysis of the initial part of the explosive events at the two frequencies 1.1 Hz and 1.5 Hz gave a single back-azimuth value for the antennas, but two incident angles. We interpreted this result as the presence of two distinct sources. The back-azimuths and incident angles estimated at both of the antennas were spatially crossed to define the source location. We used the approximation of a homogeneous medium, which can be justified by the position of the antennas in the near-field. According to Lokmer et al. (2007), the distortion of waveforms is minimized when they are recorded at close distances from the sources. However, this approximation leads to an additional uncertainty in the resolution of the location along the vertical axis. The analysis of all of the 16 explosions gave similar results. We found two sources in each case. The two sources have the same positions in the horizontal plane. They were located just beneath the crater. Along the vertical axis, they were separated by about 800 m. The average altitudes of these sources were 3890 m and 4810 m, with an average error of 390 m. Since the altitude of the bottom of the caldera was 5200 m, and the bottom of the crater was about 200 m to 300 m below, the most superficial source was about 100 m to 200 m below the superficial part of the conduit. These two sources were produced simultaneously, or in any case, as our method of analysis used a sliding time window set to a width of 2 s, these two sources cannot be distinguished temporally. To check the validity of these data, we tested the ability of our algorithm to separate two sources that were generated simultaneously using synthetic sources separated by 800 m in the vertical plane. The positions of the two synthetic sources were correctly found by analyzing the signals separately, and also by stacking the waveforms. This reinforces the idea of the physical origin of these two sources. In our previous study (Inza et al., 2011), we tested the MUSIC-3C approach through the analysis of a single explosion, which corresponded to event #10 on the present list. We found only one source at a depth of 4200 m +/-600 m. In this new study, we found two sources at altitudes of 3920 m +/-350 m and 4770 m +/-350 m, respectively. In the first study, we analyzed the dominant peak of the unfiltered signal, which was set to 2.4 Hz. In the present study, we filtered the signal between 0.5 Hz and 2.2 Hz, to keep the part of the signal that had the maximum coherency (Figure 3.4c). So, we chose to analyze only the dominant peaks of the portion of the signal that had more coherency. Otherwise, this allowed us to obtain a gain of resolution in the localization error, as the value obtained in this study is two-times lower. This explains the differences in the data. The 2.4 Hz peak still exists (Figure 3.4c), but with less energy, because of the filtering. That said, the single source found in the first study was positioned between the two source positions defined in the current study. Hence, the two results do not contradiction one another. It also shows that there might be several seismogenic zones in the conduit that correspond to different frequencies of the signal. The location of several seismic sources in a conduit was demonstrated by Thomas and Neuberg (2012) in the case of low-frequency activity at Montserrat. In our case, we found two sources, with perhaps the more important result being that the sources were simultaneous, or were almost simultaneous. We discuss in the next section the possible interpretations based on models of Vulcanian explosions

proposed in the literature.

3.4.3 Explosion mechanism

Kanamori et al. (1984), and more recently Iguchi et al. (2008), proposed a macroscopic model of a dynamic explosion process in which overpressure triggered Vulcanian explosions are generated by gas accumulation below a plug positioned at the top of the conduit. Iguchi et al. (2008) examined processes of inflation and deflation that were associated with explosions recorded at three different volcanoes: Sakurajima and Suwanosejima in Japan, and Semeru in Indonesia. The authors interpreted the seismic and ground-deformation observations as inflation before the explosions that was associated with gas accumulation at the top of the conduit, and then deflation that began at the start of the explosion, which was interpreted as the ejection of the magma and draining of the conduit. They also observed a slight and short contraction just before the explosion (4-6 s before in the case of Semeru). This was interpreted as the response to gas leakage at the cap as a result of the pressure exerted by the gas pocket at the top of the conduit. We examined this model on the basis of our data.
The formation of a gas pocket in the conduit is a very credible hypothesis, as it has been shown by Traversa et al. (2011) that the number of earthquakes increased the long period before an explosion at Ubinas. This study with 143 explosions recorded during the period of 2006 to 2008 showed an accelerated rate of the long period for 2-3 h before the explosion. The acceleration of seismicity was consistent with overpressure in the conduit. We examined the seismic data from three sites, one of which (UB2) also had a tiltmeter. The seismic signal represented as displacement (filtered between 0.03 Hz and 2 Hz) indicated the initiation of an explosion by a slight movement up (inflation), which was followed by a strong downward movement that corresponded to the decompression. The movement of decompression was not as marked as for the case analyzed by Iguchi et al. (2008). This can be explained by a greater station-to-crater distance at Ubinas ($\approx 2km$) compared to, for example, Semeru (< 0.5 km). For the same reason, we did not see slow inflation several minutes before the explosion for the tilt data, or the seismic data, as observed by Semeru and Suwanosejima. However, the recordings made in 2006 in the caldera with a CMG-40T seismometer (30 s) 500 m from the crater showed significant slow vertical movement that started 40 s before the explosion. However, we clearly saw a slight movement of deflation with the tilt component normal to the crater. This movement was consistent with a decompression of the superficial part of the conduit. It started 2 s before the explosion, and it lasted little more than 1 s. This moderate deflation was quite similar to that observed by Iguchi et al. (2008) for Semeru, where it was interpreted as the failure of the cap at the top of the conduit. The duration of this moderate deflation was variable on the other volcanoes, as 1 min to 2 min for Sakurajima, 0.2 s to 0.3 s for Suwanosejima, and 2 s to 3 s for Semeru.
The observations made at Ubinas are consistent with these data. The assumption of the cap rupture just before the start of the explosion can be strengthened by the observation of the higher frequency seismic signal (2.2-6 Hz). Indeed, this signal appeared 2 s before the explosion, and a few tenths of a second before the decompression movement observed on the tilt (Figure 3.4c). We saw two peaks at 1.1 Hz and 1.5 Hz that dominated the first few seconds of the seismic signal of the explosion, and these signals corresponded to sources located at depths in the conduit that were separated by 800

m. How should these two sources be interpreted? Iguchi et al. (2008) also referred to two sources. The first corresponded to a decreasing pressure source that started from the gas pocket, and the second was associated with increasing pressure, which corresponded to outgassing of water-saturated magma deep in the conduit. The second source was deeper, and it was positioned at 2 km in depth at Sakurajima, and 500 m in depth for Semeru. The two sources of explosions at Ubinas might be associated with these two processes; the distance between the two sources was consistent with the results from other volcanoes. For Montserrat, Druitt et al. (2002) proposed conduit depths of between 500 m and more than 2 km.

Other mechanisms have been proposed to explain how the pressurization exerted by a cap on a column of magma can generate Vulcanian explosions. Burgisser et al. (2011) tested four mechanisms by combining data of pressure and porosity of a pre-explosive magma column into a physical model that reconstructed a depth-reference density profile of the column. This study was performed from samples produced by Vulcanian explosions at Montserrat between August and October 1997 (Burgisser et al., 2010). The mechanisms tested corresponded to: (1) gas accumulation, which is similar as the mechanism proposed by Iguchi et al. (2008); (2) conduit wall elasticity; (3) microlite crystallization; and (4) magma flow.

Depending on these mechanisms, Burgisser et al. (2011) provided vertical layering of the conduit prior to an explosion, composed of: (1) a dense and strongly degassed plug from a meter to a few tens of meters in thickness; (2) a shallow transition zone that is characterized by complex mingling between vesicular and dense magma, with a thickness varying from 200 m to 500 m, or from 400 m to 700 m; and (3) at greater depth, a more homogeneous, low-porosity zone that takes the total column length from 2.5 km to $\approx$ 3.5 km.

If we compare our data to these models, the two sources that we have defined might correspond to the boundaries of the transition proposed by Burgisser et al. (2011). Assuming a cylindrical conduit with a radius of 25 m to 30 m, as estimated at Montserrat (Druitt et al., 2002), the volume of the transition zone was of the order of $5x10^5$ to $5.5x10^5$ m^3. This volume corresponds to the maximum volume emitted, assuming all of the conduit empties during an explosion. The locations were extremely stable over time. The errors in the determinations of the positions of the sources were on average 35% of the distance between the two sources. This might explain why variations in the height of the zone of fragmentation of this order were not detectable. It is also possible that the geometry of the conduit constrained the eruptive dynamics. At depth, it is possible that the shape of the conduit did not allow an extension of the transition zone. We analyzed only a few long-period events from the whole catalog, which includes hundreds of events during the period of the explosive phase. These events with the dominant frequencies of 0.55 Hz and 0.7 Hz were located 1.5 km to 2 km deeper than the explosions. The sources for these two frequency peaks were located at different depths, but contrary to the explosions, the two sources were not simultaneous. The deepest one (0.55 Hz) corresponded to the beginning of the signal, or preceded it slightly, while the more superficial source (0.7 Hz) was generated a few seconds later. At this level, we cannot make further interpretations about the origins of these signals. A larger number of signals must be analyzed in future work. The temporal relationships with the explosions should also be analyzed in detail.

Chapter 4

Conclusions and Perspectives

4.1 Conclusions

4.1.1 Source localization

Ubinas is the most active volcano in southern Peru. Historical and recent eruptions presented a predominantly vulcanian style characterized by short-duration and violent explosions. The source localization has became the main challenge to study this volcano, since the seismic waves radiated by Ubinas cannot be located by conventional means because the lack of impulsive phases in seismograms (Chouet, 2003). In this work, three component (3C) seismic array datasets (synthetic and real) were used to develop and apply a method of sismo-volcanic source localization. Two measurements campaigns were carried out, one at Ubinas volcano in 2009 and the other one at Misti volcano in 2011 (Peru). These two active volcanoes have been chosen because their hazard impacts are considered catastrophic for society.

In chapter 2, we have presented a source localization method (MUSIC-3C), based on 3C seismic array, and compared with the single-component (1C) seismic array used in previous studies on volcanoes (Almendros et al., 2001a; Saccorotti et al., 2004). The MUSIC-3C method proposed and then developed is an extension of the well-known multiple signal classification (MUSIC) algorithm, in order that can process data recorded by three-component (3C) seismic arrays deployed at volcano flanks. The rough topography of Ubinas stratovolcano allowed us to deploy seismic sensors with an irregular spacing between sensing elements (around 50 m), on a geometry of 3D array, that totally eliminates the ambiguity of direction of arrival of the incoming signal found on 1D or 2D array geometries (Manikas et al., 2001). The geometry form of cross-shape became useful to make sure the optimal localization from different directions since seismic source locations of Ubinas were unknown. This method (MUSIC-3C) provided spectra estimations from eigenanalysis of the 3C seismic data cross-spectral matrix and a noise subspace information. The maximum peak on spectra gave us, back-azimuth and incidence angle (components of the slowness vector). Datasets from two (3C)

seismic arrays (known as NUBI and WUBI antennas in our experiments) were used in this study to estimate slowness vectors, in order to constrain a region of the source. Estimation errors were associated to the finite grid spacing and the width of the estimator spectra peaks.

Synthetic data sets were available which were generated using a 3D numerical elastic lattice method (O'Brien and Bean, 2004) coupled with digital elevation Ubinas topography (in homogenous media). It consisted on 8 synthetics sources numerically simulated with elevations from altitudes between 1972 m and 4950 m which were successfully retrieved from synthetic datasets by MUSIC-3C. We compared estimations of slowness vectors for different depths computed from 3C-arrays and 1C-arrays (vertical component), (Figure 4.1) in which only 3C-array allowed the recovery of both back-azimuth with a resolution of +/- 3 degrees and incidence angle with an error of +/-6 degrees. Whereas MUSIC-1C recovered only back-azimuth with higher errors (+/- 6 degrees). To represent the localization on maps, a probability density function (PDF) of the source position was derived from PDF's of slowness vectors estimated for each antenna (Métaxian et al., 2002; Tarantola and Valette, 1982). The depth resolution was around 500 m for NUBI antenna and 400 m for WUBI antenna. On the other hand, the MUSIC-1C analysis does not allow the depth to be determined. We conclude that MUSIC-3C provided realistic estimates of sismo-volcanic hypocenters (epicenter and depth).

4.1.2 Application on real data

Given the performance of the MUSIC-3C method, we applied it to real datasets recorded at Ubinas 2009. First, a LP and an explosion earthquakes were processed, as usual, we considered in each analysis, a time window corresponding to the signal onset (P-waves). The back-azimuth and incidence angle for both LP and explosion are respectively represented by black circles in Figure 4.1. We found sources located beneath the Ubinas crater at an altitude of 2240 +/-730 m for the LP event and 4200 +/-660 m for the explosion. Consequently, Figure 4.2 shows the source localization of LP and explosion events, were around 3000 m and 1000 m depth underneath the crater level.

In chapter 3, we also focused on the 16 explosive events recorded during the experiment at Ubinas 2009. The explosions occurred at intervals of 2.1 h to 6 days 8.6 h, with a mean interval of 33 h. All of the explosions, except four, were followed by a tremor episode that coincided with pulses of ash emission. The duration of the tremor following the explosion was longer for the two highest energy explosions. We analyzed the seismic signals associated to explosions in order to find out some statistical trend related to the physical constraints. But the occurrence interval and the energy between explosions did not show any relationship in time evolution. We processed all explosion waves with the MUSIC-3C algorithm. Source localization for vulcanian style explosions recorded during Ubinas 2009, allowed us to identify two separated sources located at 4810 m and 3890 m +/-390 altitude, respectively. The position of these two sources was the same for the full 16 explosions. This implies the reproduction of similar mechanisms in the conduit. Based on the eruptive mechanisms proposed for other volcanoes of the same type, we interpreted the position of these two sources as the limits of the conduit portion that was involved in the fragmentation process.

Observations to the signals induced by vulcanian phenomena recorded by a tiltmeter near the Ubinas

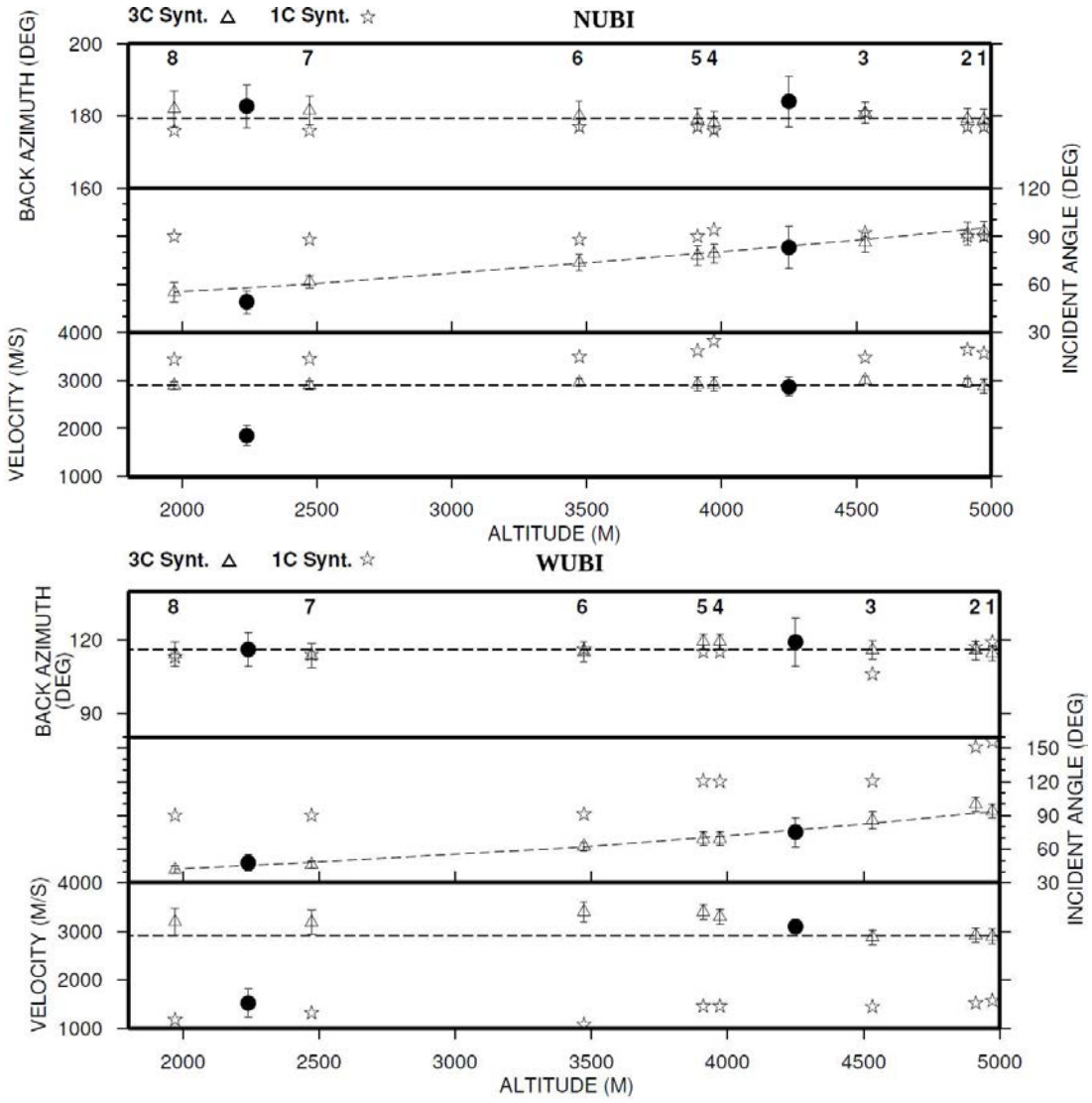


Figure 4.1: Results obtained for the synthetic data calculated for the eight sources. Open triangles and open stars represent results obtained with the MUSIC-3C and MUSIC-1C, respectively. Black circles are back-azimuth and incidence angles of LP and explosion (real data). a) Back-azimuth, incidence angle and apparent velocity for NUBI antenna. b) Back-azimuth, incidence angle and apparent velocity for WUBI antenna. Dash lines represent the values. The filled circles represent the real data results model

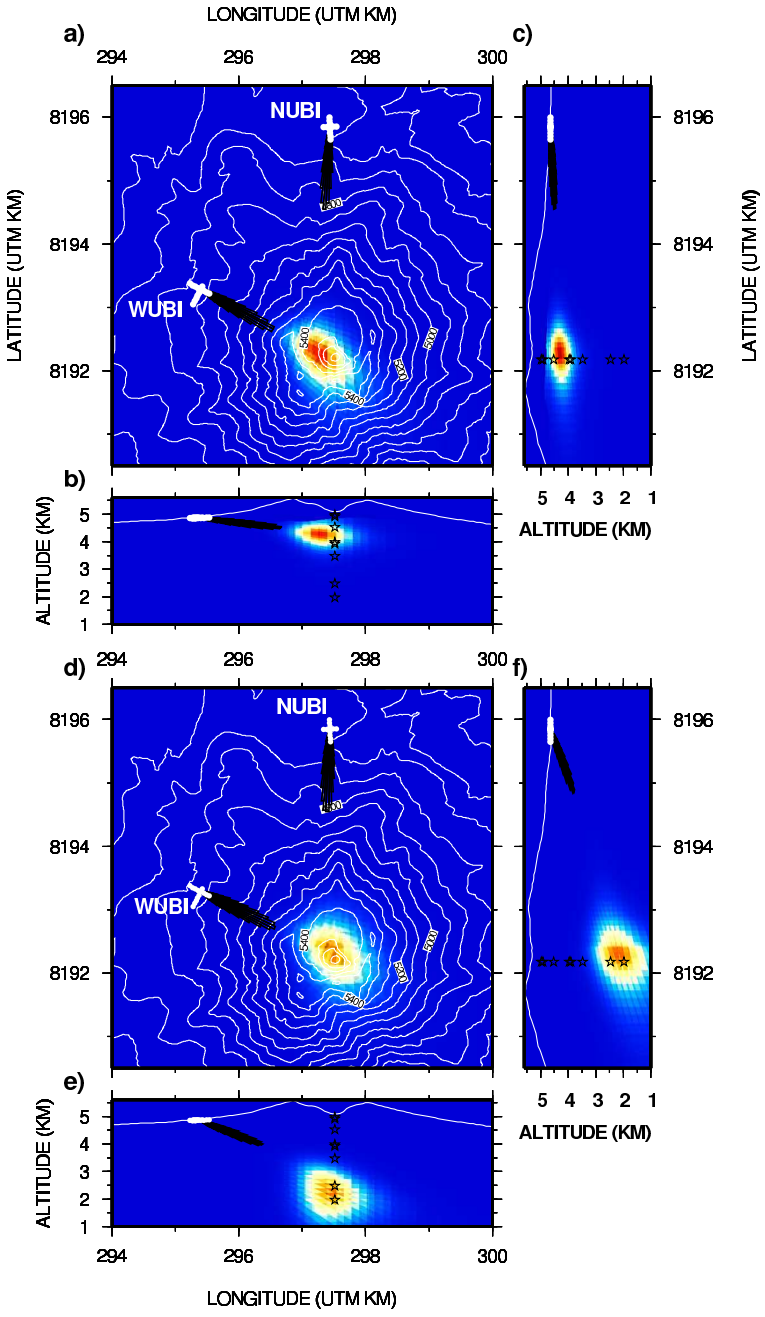


Figure 4.2: Topography map of Ubinas indicating NUBI and WUBI stations location for LP and explosion events recorded at Ubinas 2009. Rose diagrams (black) for each antenna and the source location indicating a normalized color scale for the maximum likelihood

crater, shown inflation and deflation patterns prior the explosion onset. This movement can be interpreted as gas leakage at the level of the cap before its destruction. The pressure drop generated in the conduit could be the cause of the fragmentation process that propagated deeper. Based on these observations, we interpret the position of the highest source as the part of the conduit under the cap, and the deeper source as the limit of the fragmentation zone.

We consider consistent to the fact that two seismic sources found during the explosion onset compared with others studies of the vulcanian activity on stratovolcanoes, also have referred to two seismic sources in their observations. For instance, Mt Sakurajima (Japan) and Mt Tunguragua (Ecuador). Yakoo et al. (2009) focused on seismic, infrasound and video data of vulcanian events recorded at Mt Sakurajima in 2007, two shock waves were observed in an interval of 1 s at different height during the explosion onset. On the other hand, Ruiz et al. (2005) analyzed arrival times of explosion signals recorded in Mt Tunguragua by an station equipped with both seismic and infrasound instruments, and results evidenced that explosions occurred at different depths inside of the shallow part of the conduit into an interval of 1 s.

Along this study, one part of all seismic events recorded in the field experiment Ubinas 2009 were processed by the MUSIC-3C algorithm. Figure 4.3 illustrates the localization of these events which compile both explosion, long-period (LP) events and volcano tectonic (VT) earthquake. LP events located correspond to those with highest energies between 24 May and 03 June 2009. These localizations allowed us to track the magma pathway with an error less than +/-350 m in the upper crust underneath Ubinas. It also allowed us to suggest a hypothesis that when magma rise up to the upper crust, it seems to be a high flow disturbance located around 1.2 km underneath which can be associated to the depth magma fragmentation zone (Dingwell, 1996). Another zone of disturbance was located between 200 and 300 m at the shallow part of Ubinas crater which can be related to degassing on the open conduit system of Ubinas. As you will recall, these two zones were characterized by the localization of the vulcanian explosions. On the other hand, Figure 4.3 show also a schematic view of the magma pathway along around 5 km beneath Ubinas crater, which has a trend to the south and a little bit to the west. It seems that magma supply to Ubinas come from South-West.

4.1.3 Telemetry seismic array system

We described and presented results of a test experiment using two 3C seismic arrays deployed at two flanks of Misti volcano (Peru) during November and December 2011. Recent technologies development in the seismological instrumentation of volcanoes allowed to install five 3C-seismometers (equipped with Wi-Fi technology) per array and data were transmitted to the reception center (IGP observatory) located 15 km away. The central reception continuously received 30 channels in real-time. A well-know Earthworm (EW) system (Friberg et al., 2010) was used as the acquisition system in the observatory. We developed an interface to process seismic array data in real-time with the MUSIC-3C method as a data client of the EW system. This application was successfully tested with source localization estimations of continuous data, where results were into a file sequences of back-azimuth and incidence angle. We also tested the localization on seismic events triggered by the EW system

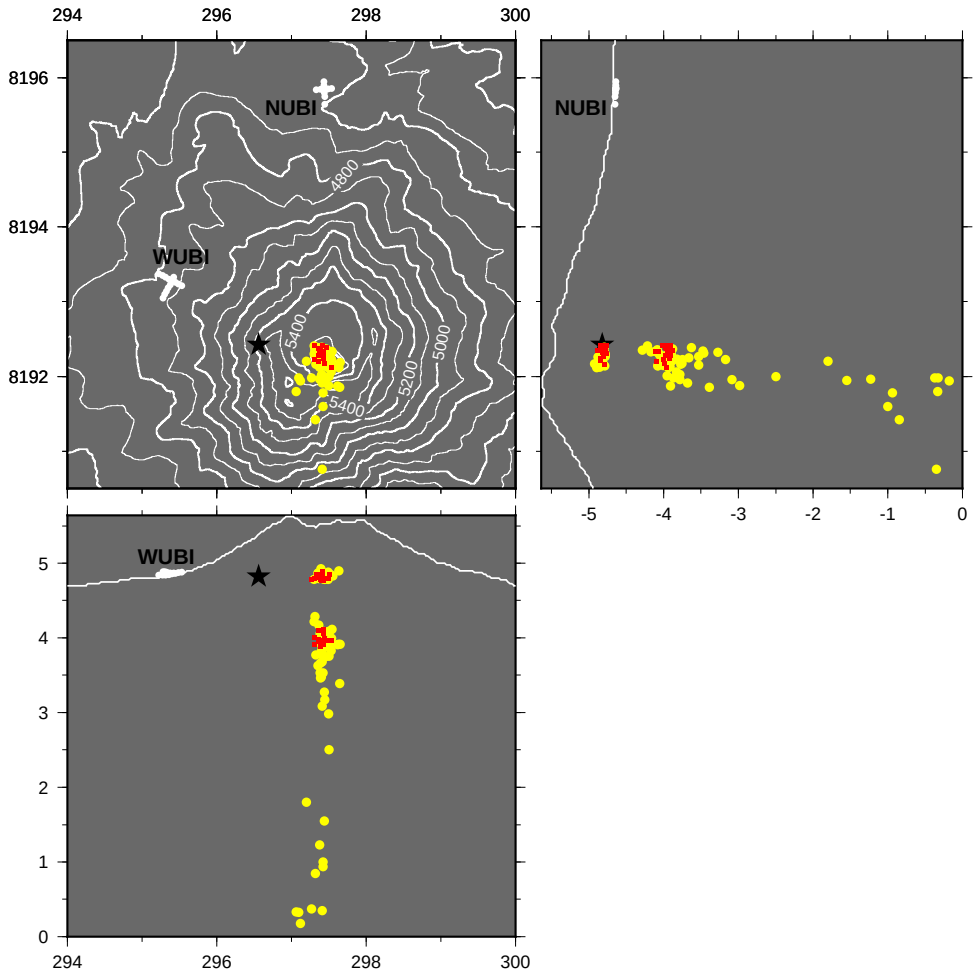


Figure 4.3: Hypocenter located at Ubinas volcano, with some events recoreded during the field experiment at Ubinas in 2009. Yelow circles correspond to localization of long-period events, red circles correspond to explosion events and black star corresponds to volcano tectonic event.

(events detected by STA/LTA algorithm). However in real scenarios, the source localization normally process on seismic events triggered by the system.

4.1.4 A global view of seismicity of Ubinas volcano

After focused our attention to source localization, we cannot ignore some highlights observed during this study. A global view of the magmatic activity in Ubinas was described in section 1.4, Chapter 1. Both volcanic activity and regional earthquakes were identified from seismic recordings. Figure 4.4 shows a time series array data obtained from time-frequency analysis. We identified two episodes where magmatic activity was affected by external earthquakes. First, a volcano tectonic VT earthquake (green inverted triangle in Figure 4.4) on 24th May 2007 15:27 with important amplitude and

high frequency content between 4 and 12 hz, and located on the shallow part of the volcano edifice (black star in Figure 4.3), 7 h later there were a swarms of explosions with an average interval of 3.6 h between days 24 and 25 May in Figure 4.4 (explosions #2 to #7 in Table 3.1).

Secondly, a subduction earthquake (Mw 4, 1st June 2009 00:53 UT) occurred on the South-West 60 km away from Ubinas volcano, was identified on Ubinas seismic recordings (square mark in Figure 4.4). It can be observed that magmatic activity has changed abruptly until the explosion #10 occurred on 2dn June 2009. We are aware that not enough witness data to even give an hypothesis but it would be an inquiry activity of monitoring in order that can establish a earthquake volcano interaction.

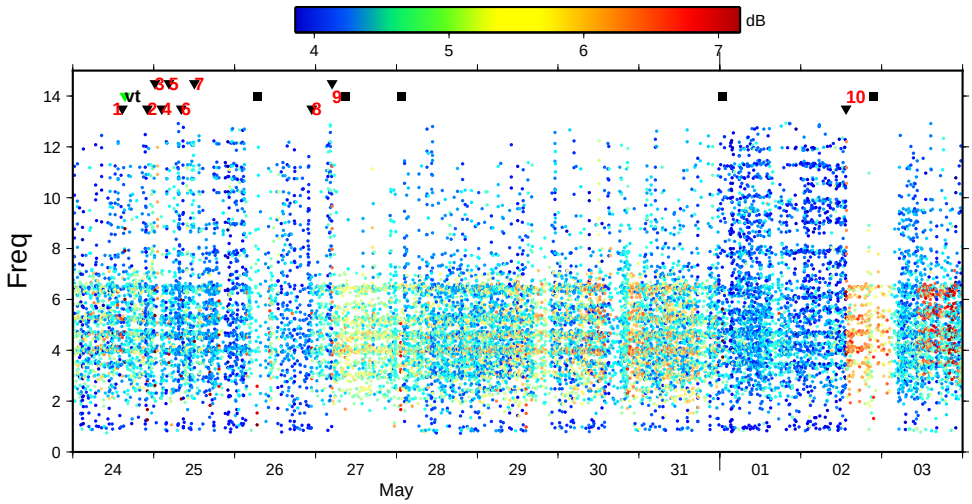


Figure 4.4: Time-frequency representation of seismic signals detected on Ubinas between on 24th May and 3rd June 2009, black triangles accompanied by numbers correspond to explosion events, black squares correspond to regional earthquakes occurred near Ubinas and green inverted triangle correspond to volcano tectonic event

4.2 Perspectives

We summarize the general open challenges to go deeper into the research of seismic source localization to better understand the physic of volcanoes. Given the performance of the MUSIC-3C method, we will apply it to other seismo-volcanic events recorded at Ubinas during the experiment to better characterize the eruptive dynamics of this volcano. In addition, the MUSIC-3C method will be integrated with the IGP monitoring system to try to locate the seismic activity of volcanoes in real time. This algorithm is not restricted to volcanic sources but can be used to locate other types of non-volcanic signals. Then, the MUSIC-3C method needs to be implemented for easy use in volcanology community. On the other hand, the MUSIC-3C method was developed based on MUSIC algorithm, however there are other approaches from MUSIC, e.g. broadband MUSIC and the MUSIQUE algorithm for multicomponent data based on a combination of the original MUSIC algorithm and the

quaternion-MUSIC algorithm Miron et al. (2006b), which Love and Rayleigh waves are distinguished and their respective properties retrieved from multicomponent seismic array data.

The estimation errors can be induced by the heterogeneous structure of the volcano, hence a study of the internal structure of Ubinas is necessary. This could be done using the noise processing method, similar to Perrier et al. (2012) which used SPAC (Aki, 1957) and F-K (Capon, 1969) approaches to determine properties of the shallow structure (200 m) of the Yasur-Yenkahe volcanic complex, Vanuatu.

To complete source localizations application, both long-period earthquakes and tremor events need to be processed with MUSIC-3C, these events were generally accompanied to vulcanian eruptions. Hence, to better understand and correlate physical mechanisms: it is necessary process events corresponding to before, during and after explosions, in order that can answer some typical questions in volcanology, e.g. where are located LP earthquakes before and after a explosion episode?. What is the relationship between the LP events prior the eruption and tremors duration post-explosion?.

The test experiment carried out at Misti volcano in 2011, consisting of a telemetry seismic array system and real-time array data processing were demonstrated that 30 channels were remotely retrieved and continuously processed with the MUSIC-3C method. Results were constrained to estimate slowness vectors. To complete these results, several modules need to be built in order that source localization can be run automatically and computed the source localization from estimations of back-azimuth and incidence angle. We are aware that the main real limitation may be the budget to implement the hardware of seismic arrays in terms of instruments, however a solution to reduce costs by implementing part of these instrumentation as homemade designs. For example, digitizers and radio communication for geophysics application were already designed and built in the IGP.

During an internship in the Geophysical Institute of Peru - Arequipa (September - December 2011) on the framework of this thesis, the IGP installed a permanent broadband seismic station in between Misti and Ubinas (50 km away of these volcanoes). The goal of this station is to study the impact of subduction earthquakes on volcanoes, using spectral ratios and nonlinear filter. Combining the source location of seismo-volcanic activity and an analysis on spectral ratios between recordings of a earthquake recorded, on volcano area and off-volcano (outside), would provide us information about the impact of subduction earthquakes on volcanoes. According (Linde and Sacks, 1998), magmatic activity is often affected by the occurrence of tectonic earthquakes near the volcano structure. For instance Sanchez and McNutt (2004) showed a clear volcanic response to the shaking from a large earthquake, observed in the intermediate-term (weeks to months) time scale. It consisted of a decline by at least 50% in the volcano seismicity rate. By using several independent methods to measure the seismicity rate at Mt. Wrangell volcano (Alaska, USA) before and after the main-shock, and applying rigorous statistical testing, Sanchez and McNutt (2004) concluded that the change in seismicity was a real effect of the large earthquake which occurred nearby in November 2002. They suggested that a depressurization of the volcanic plumbing system was responsible for the seismicity change. Earthquake volcano interactions have also been examined by Manga and Brodsky (2006); Sumner et al. (2007); Brodsky et al. (1998), these authors suggest that the passage of large seismic waves through a volcano may disrupt magma and bubbles in a pressurized system, leading to a process

called rectified diffusion. Rectified diffusion is a mechanism by which a strain wave can rapidly pump volatiles into a bubble and therefore increase the pressure in a closed system. The dynamic strain of either distant regional tectonic earthquakes or local volcanic tremor can be translated to static strain inside a magma chamber via this process (Brodsky et al., 1998).

Bibliography

Adams, N., De Silva, S., Self, S., Salas, G., Schubring, S., Permenter, J., and Arbesman, K. (2001). The physical volcanology of the 1600 eruption of huaynaputina, southern peru. *Bulletin of Volcanology*, 62:493–518.

Aki, K. (1957). Space and time spectra of stationary stochastic wave, with special reference to microtremors. *Bulletin Earthquake Research Institute*, 35:415–456.

Aki, K. and Richards, P. (2002). *Quantitative Seismology, 2nd Edition*. University Science Books, Sausalito (CA).

Alidibirov, M. and Dingwell, D. (1996). Magma fragmentation by rapid decompression. *Nature*, 380:146–148.

Alidibirov, M. and Dingwell, D. (2000). Three fragmentation mechanisms for highly viscous magma under rapid decompression. *Journal of Volcanology and Geothermal Research*, 100:413–421.

Almendros, J., Carmona, E., and Ibáñez, J. (2004). Precise determination of the relative wave propagation parameter of similar events using a small-aperture seismic array. *Journal of Geophysical Research*, 109:B11308, 15pp.

Almendros, J. and Chouet, B. (2003). Performance of the radial semblance method for the location of very long volcanic signals. *Bulletin of the Seismological Society of America*, 93:1890–1903.

Almendros, J., Chouet, B., and Dawson, P. (2001a). Spatial extent of a hydrothermal system at kilauea volcano hawaii, determined from array analysis of shallow long-period sismicity. part i: method. *Journal of Geophysical Research*, 106:13,565–13,580.

Almendros, J., Chouet, B., and Dawson, P. (2001b). Spatial extent of a hydrothermal system at kilauea volcano hawaii, determined from array analysis of shallow long-period sismicity. part ii: results. *Journal of Geophysical Research*, 106:13,581–13,597.

Battaglia, J. and Aki, K. (2003). Location of seismic events and eruptive fissures on the piton de la fournaise volcano using seismic amplitudes. *Journal of Geophysical Research*, 108 (B8):2364 (14PP) doi:10.1029/2002JB002193.

Battista, B. M., Knapp, C., McGee, T., and Goebel, V. (2007). Application of the empirical mode decomposition and hilbert-huang transform to seismic reflection data. *Geophys*, 72:2:H29–H37.

Bean, C. J., Lokmer, I., and O'Brien, G. S. (2008). Influence of near-surface volcanic structure on long-period seismic and moment tensor inversions simulated examples from mount etna. *Journal of Geophysical Research*, 113:B08308 (19PP) doi:10.1029/2007JB005468.

Berger, J., Davis, P., and Ekstrom, G. (2004). Ambient earth noise: A survey of the global seismographic network. *Journal of Geophysical Research*, 109:B11307.

Bienvenu, G. and Kopp, L. (1983). Optimality of high resolution array processing using eigensystem approach. *IEEE-ASSP*, 33:1235–1247.

Brodsky, E., Sturtevant, B., and Kanamori, H. (1998). Earthquakes, volcanoes, and rectified diffusion. *Journal of Geophysical Research*, 103:23,827–838.

Burgisser, A., Arbaret, L., Druitt, T., and Giachetti, T. (2011). Pre-explosive conduit conditions of the 1997 vulcanian explosions at soufriere hills volcano, montserrat: Ii. overpressure and depth distributions. *Journal of Volcanogy and Geothermal Research*, 199:193–205.

Burgisser, A., Poussineau, S., Arbaret, L., Druitt, T. H., Giachetti, T., and Bourdier, J.-L. (2010). Pre-explosive conduit conditions of the 1997 vulcanian explosions at soufriere hills volcano, montserrat: I. pressure and vesicularity distribution. *Journal of Volcanogy and Geothermal Research*, 194:27–41.

Capon, J. (1969). High-resolution frequency-wavenumber spectrum analysis. *Proceedings of the IEEE*, 57:(8):1408–1418.

Chouet, B. (1996). Long-period volcano seismicity: Its source and use in eruption forecasting. *Nature*, 380:309–316.

Chouet, B. (2003). Volcano seismology. *Pure appl. Geophys*, 160:739–788.

Chouet, B., Dawson, P., and Arciniega-Ceballos, A. (2005). Source mechanism of vulcanian degassing at popocatepetl volcano, mexico, determined from waveform inversion of very long period signals. *Journal of Geophysical Research*, 110:B07301 (20PP) doi:10.1029/2004JB003524.

Chouet, B. A. and Matoza, R. S. (2013). A multi-decadal view of seismic methods for detecting precursors of magma movement and eruption. *Journal of Volcanogy and Geothermal Research*, 252:108–175.

De Angelis, S. and Henton, S. (2011). On the feasibility of magma faracture wiwith volcanic conduits: Constraints from earthquake data and empirical modeling. *Geophysical Research Letters*, 38:L19310, 5pp.

De Barros, L., Bean, C. J., Lokmer, I., Saccoroti, G., Zuccarello, L., O'Brien, G. S., and Métaxian, J. (2009). Source geometry from exceptionally high resolution long period event observations at mt etna during the 2008 eruption. *Geophys Researh Letters*, 36:L24305 (5PP) doi:10.1029/2009GL041273.

De Barros, L., Lokmer, I., Bean, C., O'Brien, G., Saccorotti, G., Métaxian, J., Zuccarello, L., and Patané, D. (2011). Source mechanism of long period events recorded by a high density seismic network during the 2008 eruption on mt etna. *Journal of Geophysical Research - Solid Earth*, 116:B01304 (17PP) doi:10.1029/2010JB007629.

De la Cruz-Reyna, S. and Reyes-Davila, G. (2001). A model to describe precursory material-failure phenomena: applications to short-term forecasting at colina volcano, mexico. *Bulletin of Volcanology*, 63:297–308.

De Silva, S. L. and Francis, P. W. (1991). Volcanoes of the central andes. *Geological Magazine - Cambridge University Press*, 129:253–254.

De Silva, S. L. and Zielinsky, G. A. (1998). Global influence of the ad 1600 eruption of huaynaputina, peru. *Nature*, 393:455–458.

Del Pezzo, E., La Rocca, M., and Ibanez, J. (1997). Observations of high-frequency scattering waves using dense arrays at teide volcano. *Bulletin of the Seismological Society of America*, 87:1637–1647.

Di Lieto, B., Saccorotti, G., Zuccarello, L., La Rocca, M., and Scarpa, R. (2007). Continuous tracking of volcanic tremor at mount etna, italy. *Geophysical Journal International*, 169:699–705.

Dingwell, D. (1996). Physical properties of magma. *in E. Julius Dasch ed. Encyclopedia of Earth Sciences : MacMillan Reference USA, Simon and Schuster MacMillan, New York*, 2:817–820.

Druitt, T., Young, S. R., Baptie, B. J., Bonadonna, C., Calder, E. S., Clarke, A. B., Cole, P. D., Harford, C. L., Herd, R. A., Lockett, R., Ryan, G., and Voight, B. (2002). Episodes of cyclic vulcanian explosive activity with fountain collapse at soufriere hills volcano, montserrat. *Memoirs of the Geological Society of London*, 21:281–306.

Endo, E. and Murray, T. (1991). Real-time seismic amplitude measurement (rsam): A volcano monitoring tool. *Bulletin of Volcanology*, 53:533–545.

Ferro, A., Gambino, S., S., P., Falzone, G., Laudani, G., and Ducarme, B. (2011). High precision tilt observation at mt. etna volcano, itlay. *Acta Geophysica*, 59(3):618–632.

Flandrin, P., Rilling, G., and Gonçalves, P. (2004). Empirical mode decomposition as a filterbank. *IEEE Signal Processing Letters*, 11:(2) 112–114.

Friberg, P., Lisowski, S., Dricker, I., and Hellman, S. (2010). Earthworm in the 21st century. *Geophysical Research Abstracts*, 12:no.12, 654.

Furumoto, M., Kunitomo, T., Inoue, H., Yamada, I., Yamaoka, K., Ikami, A., and Fukao, Y. (1990). Twin sources of high-frequency volcanic tremor of izu-oshima, japan. *Geophysical Research Letters*, 17:25–27.

Garcia Yeguas, A., Almendros, J., Abella, R., and Ibanez, J. (2011). Quantitative analysis of seismic wave propagation anomalies in azimuth and apparent slowness at deception island volcano (antarctica) using seismic arrays. *Geophysical Journal International*, 184:801–815.

Goldstein, P. and Archuleta, R. (1987). Array analysis of seismic signal. *Geophysiical Research Letters*, 14:13–16.

Goldstein, P. and Chouet, B. (1994). Array measurements and modeling of sources of shallow volcanic tremor at kilauea volcano, hawaii. *Journal of geophysical research*, 99:B2: 2637 – 2652.

Hildreth, W. (1987). New perspectives on the eruption of 1912 in the valley of ten thousand smokes, katmai national park, alaska. *Bulletin of Volcanology*, 49:680–693.

Huang, N. E., Shen, Z., Long, S. R., Wu, M. C., Shih, H. H., Zheng, Q., Yen, N. C., Tung, C. C., and Liu, H. H. (1998). The empirical mode decomposition and the hilbert spectrum for nonlinear and nonstationary time series analysis. *Proceedings of the Royal Society of London A*, 454:903–995.

Iguchi, M., Yakiwara, H., Tameguri, T., Hendrasto, M., and Hirabayashi, J.-i. (2008). Mechanism of explosive eruption revealed by geophysical observations at the sakurajima, suwanosejima and semeru volcanoes. *Journal of Volcanology and Geothermal Research*, 179:1–9.

Inza, L., Mars, J. I., Métaxian, J.-P., O'Brien, G. S., and Macedo, O. (2011). Seismo-volcano source localization with triaxial broad-band seismic array. *Geophys Journal International*, 187:371–384.

Inza, L. A., Métaxian, J.-P., Mars, J. I., C.J., B., O'Brien, G. S., Macedo, O., and Zandomeneghi, D. (2013). Analysis of dynamics of vulcanian activity of ubinas volcano, using multicomponent seismic antennas. *Journal of Volcanogy and Geothermal Research*, Submitted:Submitted.

Jellinek, A. and Bercovici, D. (2011). Seismic tremors and magma wagging during explosive volcanism. *Nature*, 470:522–526.

Johnson, D. H. and Dudgeon, D. E. (1993). *Array Signal Processing - Concepts and Techniques*. Prentice Hall Signal Processing Series.

Johnson, J. and Aster, R. (2005). Relative partitioning of acoustic and seismic energy during strombolian eruptions. *Journal of Volcanology and Geothermal Research*, 148:334–354.

Kanamori, H., Given, J., and Lay, T. (1984). Analysis of seismic body waves excited by the mount st. helens eruption of may 18, 1980. *Journal of Geophysical Research*, 89:B3 1856–1866.

Kawakatsu, H., Kaneshima, S., Matsubayashi, H., Ohminato, T., Sudo, Y., Tutui, T., Uhira, K.and Yamasato, H., Ito, H., and Legrand, D. (2000). Aso-94: Aso seismic observation with broadband instruments. *Journal of Volcanology and Geothermal Research*, 101:129–154.

Krim, H. and Viberg, M. (1996). Two decades of array signal processing research: The parametric approach. *Signal Processing Magazine, IEEE*, 13:67–94.

Kumagai, H., Palacios, P., Maeda, T., Castillo, D. B., and Nakano, M. (2009). Seismic tracking of lahars using tremor signals. *Journal of Volcanology and Geothermal Research*, 183:112–121.

Kumagai, H., Placios, P., Ruiz, M., Yepes, H., and Kozono, T. (2011). Ascending seismic source during an explosive eruption at tungurahua volcano, ecuador. *Geophysical Research Letters*, 38:L01306, doi:10.1029/2010GL045944.

La Rocca, M., Galluzzo, D., Malone, S., McCausland, W., Saccoroti, G., and Del Pezzo, E. (2008). Testing small-aperture array analysis on well-located earthquakes, and application to the location of deep tremor. *Bulletin of Seismological Society of America*, 98:2:620–635.

La Rocca, M., Saccorotti, G., Del Pezzo, E., and Ibáñez, J. (2004). Probabilistic source location of explosion quakes at stromboli volcano estimated with double array data. *Journal of Volcanology and Geothermal Research*, 131:123–142.

Lacoss, R., Kelly, E., and Toksoz, M. (1969). Estimation of seismic noise structure using array. *Geophysics*, 34:21–38.

Lahr, J., Chouet, B., Stephens, C., Power, J., and R.A., P. (1994). Earthquake classification, location, and error analysis in a volcanic environment: implications for the magmatic system of the 1989-1990 eruptions at redoubt volcano, alaska. *Journal of Volcanology and Geothermal Research*, 62:137 – 151.

Lees, J. (2007). Seismic tomography of magmatic systems. *Journal of Volcanogy and Geothermal Research*, 167:37–56.

Linde, A. T. and Sacks, I. S. (1998). Triggering of volcanic eruptions. *Nature*, 395:888–890.

Lokmer, I., Bean, C. J., Saccoroti, G., and Patané, D. (2007). Moment-tensor inversion of lp events recorded on etna in 2004 using constraints obtained from wave simulation test. *Geophys Researh Letters*, 34:L22316 (6PP) doi:10.1029/2007GL031902.

Lokmer, I., O'Brien, G. S., De Barros, L., and Bean, C. (2010). High resolution spatio-temporal source inversion of a long period sequence recorded by a dense broadband network. *Geophysical Research Abstract*, 12:EGU2010 13706.

Longuet-Higging, M. (1950). A theory of the origin of microseisms. *Philosophical Transactions of the Royal Society A*, 234:(875):1–35.

Macedo, O., Métaxian, J., Taipe, E., Ramos, D., and Inza, L. A. (2009). Seismicity associated with the 2006-2008 eruption, ubinas volcano. *In: The VOLUME Project, edited by : Bean, C. J., Braiden, A. K., Lokmer, I., Martini, F., O'Brien, G. S.*, 1:pp. 262–270.

Manga, M. and Brodsky, E. (2006). Seismic triggering of eruptions in the far field: Volcanoes and geysers. *Annual Review of Earth and Planetary Sciences*, 34:263–291.

Manikas, A., Sleiman, A., and Dacos, I. (2001). Manifold studies of nonlinear antenna array geometries. *IEEE Transactions on singal processing*, 49 issue 3:497–506.

Marcos, S. (1998). *Les Méthodes à haute résolution: traitement d'antenne et analyse spectrale*. Hermes.

Mari, J., Glangeaud, F., and Coppens, F. (1997). *Signal Processing for Geophisics and Geologes*. TECHNIP,PARIS.

Mars, J. I., Glangeaud, F., and Mari, J. L. (2004). Advanced signal processing tools for dispersive waves. *Near Surface Geophysics*, 2(4):199–210.

McNutt, S. R. (2000). Seismic monitoring. *Encyclopedia of Volcanoes (H. Sigurdsson, B. Houghton, S.R. McNutt, H. Rymer and J. Stix eds.)*, Part VII:1095–1119.

McNutt, S. R. (2005). Volcanic seismology. *Annu Rev. Earth and Planet. Sci.*, 32:461–491.

Melnik, O. and Sparks, R. S. J. (2002). Dynamics of magma ascent and lava extrusion at soufriere hills volcano, montserrat (in the eruption of soufriere hills volcano, montserrat from 1995 to 1999). *Memoirs of the Geological Society of London*, 21:153–171.

Métaxian, J.-P., Lesage, P., and Dorel, J. (1997). Permanent tremor of masaya volcano, nicaragua: Wave field analysis and source location. *Journal of Geophysical Research*, 102:22,529–22,545.

Métaxian, J.-P., Lesage, P., and Valette, B. (2002). Locating sources of volcanic tremor and emergent events by seismic triangulation. *Geophys Researh Letters*, 107(B10):2243 (18PP).

Métaxian, J.-P., O'Brien, G., Bean, C., Valette, B., and Mora, M. (2009). Locating volcano-seismic signals in the presence of rough topography: wave simulations on arenal volcano, costa rica. *Geophys Journal International*, 179-3:1547–1557.

Miron, S., Le Bihan, N., and Mars, J. I. (2005). Vector-sensor music for polarized seismic sources localization. *EURASIP Journal on Applied Signal Processing*, 2005:74–84.

Miron, S., Le Bihan, N., and Mars, J. I. (2006a). High resolution vector-sensor array processing based on biquaternions. *IEEE Transactions on Signal Processing*, 54:1218–1229.

Miron, S., Le Bihan, N., and Mars, J. I. (2006b). Quaternion-music for vector-sensor array processing. *IEEE Transactions on Signal Processing*, 54:1218–1229.

Mora, M., Lesage, P., Valette, B., Alvarado, G., Leandor, C., Métaxian, J.-P., and Dorel, J. (2006). Shallow velocity structure and seismic site effects at arenal volcano, costa rica. *Journal of Volcanogy and Geothermal Research*, 152:121–139.

Morrissey, M. and Mastin, L. (2000). Vulcanian eruptions. *Encyclopedia of Volcanoes (H. Sigurdsson, B. Houghton, S.R. McNutt, H. Rymer and J. Stix eds.)*, Part IV:463–475.

Nakada, S. (2000). Hazards from pyroclastic flow and surges. *Encyclopedia of Volcanoes (Part VII: Volcanic Hazards, Hazel Rymer)*, 7:945–955.

Neuberg, J. (1998). Results from the broadband seismic network on montserrat. *Geophysical Research Letters*, 25:19:3661–3664.

Neuberg, J. and Pointer, T. (2000). Effects of volcano topography on seismic broad-band waveforms. *Geophys Journal International*, 143:239–248.

Neuberg, J. W., Tuffen, H., Collier, L., Green, D., Powell, T., and Dingwell, D. B. (2006). The trigger mechanism of low-frequency earthquakes on montserrat. *Journal of Volcanology and Geothermal Research*, 153:37–50.

Newhall, C. and Self, S. (1982). The volcanic explosivity index (vei): An estimate of explosive magnitude for historical volcanism. *Journal of Geophysical Research*, 87:1231–1238.

O'Brien, G. S. and Bean, C. J. (2004). A 3d discrete numerical elastic lattice method for seismic wave propagation in heterogeneous media with topography. *Geophysical Research Letters*, 31:L14608.1–L14608.4.

O'Brien, G. S., Lokmer, I., De Barros, L., Bean, C. J., Saccoroti, G., Métaxian, J.-P., and Patané, D. (2011). Time reverse location of seismic long period events recorded on mt etna. *Geophysical Journal International*, 184:452–462.

Ohminato, T., Chouet, B., Dawson, P., and Kedar, S. (1998). Waveform inversion of very long period impulsive signals associated with magmatic injection beneath kilauea volcano, hawaii. *Journal of Geophysical Research*, 103:23 823–23– 826.

Papale, P. (1999). Strain-induced magma fragmentation in explosive eruptions. *Nature*, 397:425–428.

Parfitt, E. A. and Wilson, L. (2008). *Fundamentals of Physical Volcanology*. Wiley-Blackwell.

Paulus, C. and Mars, J. I. (2006). New multicomponent filters for geophysical data processing. *IEEE Geosciences and Remote sensing*, 44:2260–2270.

Paulus, C. and Mars, J. I. (2010). Vector-sensor array processing for polarization parameters and doa estimation. *EURASIP Journal on Advances in Signal Processing*, 2010:Article ID 850265 (13PP) doi:10.1155/2010/850265.

Paulus, C., Mars, J. I., and Gounon, P. (2005). Wideband spectral matrix filtering for multicomponent sensors array. *Signal Processing*, 85:1723–1743.

Perrier, L., Métaxian, J.-P., Battaglia, J., and Garaebiti, E. (2012). Estimation of the near-surface velocity structure of the yasur-yenkahe volcanic complex, venuatu. *Journal of Volcanogy and Geothermal Research*, 227-228:50–60.

Ramos, V. (1999). Plate tectonic setting of the Andean cordillera:. *Episodes*, 22:183–190.

Rivera, M., Thouret, J.-C., Marino, J., Berolatti, R., and Fuentes, J. (2010). Characteristics and management of the 2006-2008 volcanic crisis at the ubinas volcano (peru). *Journal of Volcanology and Geothermal Research*, 198:19–34.

Rogers, J. (1995). Ssam real time seismic spectral amplitude measurement on pc and its application to volcano monitoring. *Bulletin of the Seismological Society of America*, 85:632–639.

Rost, S. and Thomas, C. (2002). Array seismology: Method and application. *Rev. Geophysics.*, 40:1008, 27PP.

Ruiz, M., Lees, J., and Johnson, J. (2005). Source constraints of tungurahua volcano explosion events. *Bulletin of Volcanology*, 68:5:480–490.

Saccorotti, G., Chouet, B., and Dawson, P. (2001). Wavefield properties of a shallow long-period event and tremor at kilauea volcano, hawaii. *Journal of Volcanology and Geothermal Research*, 109:163–189.

Saccorotti, G. and Del Pezzo, E. (2000). A probabilistic approach to the inversion of data from a seismic array and its application to volcanic signals. *Geophysical Journal International*, 143:249–261.

Saccorotti, G., Zuccarello, L., Del Pezzo, E., Ibáñez, J., and Gresta, S. (2004). Quantitative analysis of the tremor wavefield at etna volcano, italy. *Journal of Volcanology and Geothermal Research*, 136:223 – 245.

Sanchez, J. and McNutt, S. R. (2004). Unexepted response of mt. wrangell volcano, alaska, to the shaking from a large regional earthquake. a puzzle for intermediate term earthquake-volcano interactions. *Earth Sciences Research Journal*, 8:34–44.

Schmidt, R. O. (1986). Multiple emitter location and signal parameter estimation. *IEEE Transactions Antennas and Propagation*, 34(3):276–280.

Sébrier, M. and Soler, P. (1991). Tectonic and magmatism in the peruvian andes from late oligocene time to the present. *Geological Society of America Bulletin, Special Paper*, 265:259–278.

Self, S., Wilson, L., and Nairn, I. (1979). Vulcanian eruption mechanisms. *Nature*, 277:440–443.

Sigurdsson, H. (2000). *Encyclopedia of volcanoes*. Academic Press.

Simkin, T. and Siebert, L. (1994). *Volcanoes of the World*. Geoscience Press in association with Smithsonian Instituttion Global Volcanism, Tucson AZ.

Sparks, R. (1997). Causes and consequences of pressurusation in lava dome eruptions. *Earth and Planetary Science Letters*, 150:177–189.

Sparks, R. (2000). The causes and consequences of eruptions of andesite volcanoes. *Philosophical Transactions of the Royal Society A*, 358:1435–1440.

Sparks, R. (2003). Forecasting volcanic eruptions. *Earth and Planetary Science Letters*, 210:1–15.

Sparks, R., Huppert, H., Turner, J., Sakuyama, M., and M.J., O. (1984). The fluid dynamics of evolving magma chambers and discussion. *Philosophical Transactions of the Royal Society A*, 310:1514:511–534.

Spera, F. (2000). Physical properties of magma. *in Encyclopedia of Volcanoes (H. Sigurdsson, B. Houghton, S.R. McNutt, H. Rymer and J. Stix eds.)*, 1:171–190.

Stephens, C., Chouet, B., Page, R., and Lahr, J. (1994). Seismological aspects of the 1989-1990 eruptions at redoubt volcano, alaska: The ssam perspective: Miller t. and chouet b.a. (eds.) the 1989-1990 eruptions of redoubt, alaska. *Journal of Volcanogy and Geothermal Research*, 62:153–182.

Stoica, P. and Nehorai, A. (1989). Music, maximum likelihood, and cramer-rao bound. *IEEE Transactions Acoustic, Speech, and Signal Processing*, 37:(5):720–741.

Stoica, P. and Nehorai, A. (1991). *Advances in Spectrum Analysis and Array Processing, Vol II*. Prentice Hall Signal Processing Series.

Sumner, J., Rothery, D., Spiler, O., and Dingwell, D. (2007). Impact vesiculation - a new trigger for volcanic bubble growth and degassing in volcanic spatter. *eEarth*, 2:151–167.

Surono, Jousset, P., Boichu, M., Buongiorno, M., Budisantoso, A., Costa, F., and Andreastuti, S. (2012). The 2010 explosive eruption of java's merapi volcano - a '100-year' event. *Journal of volcanology and Geothermal Research*, 241-242:121–135.

Tarantola, A. and Valette, B. (1982). Inverse problems = quest for information. *Journal of geophysics*, 50:159–170.

Thomas, M. I. and Neuberg, J. W. (2012). What makes a volcano tick-a first explanation of deep multiple seismic sources in ascending magma. *Geology*, 40:351–354.

Thouret, J.-C., Davila, J., and Eissen, J.-P. (1999). Largest historic explosive eruption in the andes at huaynaputina volcano, south peru. *Geology*, 27:435–438.

Thouret, J.-C., Finizola, A., Fornari, M., Legeley-Padovani, A., Suni, J., and Frechen, M. (2001). Geology of el misti volcano near the city of arequipa, peru. *Geological Society American Bulletin*, 113:1593–1610.

Thouret, J.-C., Rivera, M., Worner, G., Gerbe, M., Finizola, A., M., F., and Gonzales, K. (2005). Ubinas: The evolution of the historically most active volcano in southern peru. *Bulletin of Volcanology*, 67:557–589.

Traversa, P., Lengliné, O., Macedo, O., Métaxian, J.-P., Grasso, J., Inza, A., and Taipe, E. (2011). Short term forecasting of explisions at ubinas volcano peru. *J. geophys. Res.*, 116:B11301, 15PP.

Trnkoczy, A. (1998). Understanding and setting sta/lta trigger algorithm parameters for the k2. *Application Note Kinemetrics*, 41:20p.

Tuffen, H. and Dingwell, D. (2005). Fault textures in volcanic conduits: evidence for seismic trigger mechanisms during silicic eruptions. *Bulletin of Volcanology*, 67:370–387.

Tuffen, H., Dingwell, D., and Pinkerton, H. (2003). Repeated fracture and healing of silicic magma generate flow banding and earthquakes? *Geology*, 31:1089–1092.

Voight, B. (1990). The 1985 nevado del ruiz volcano catastrophe: anatomy and retrospection. *Journal of Volcanology and Geothermal Research*, 44:349–386.

Wassermann, J. (1997). Locating the sources of volcanic explosions and volcanic tremor at stromboli volcano (italy) using beamforming on diffraction hyperboloids. *Physics of the Earth and Planetary Interiors*, 104:271–281.

Wassermann, J. (2012). *Volcano seismology, IASPEI New manual seismological observatory practice 2 (NMSOP-2) Chapter 13*. Potsdam : Deutsches GeoForschungsZentrum GFZ.

Wathelet, M., Jongmans, D.and Ohrnberger, M., and S., B.-C. (2008). Array performances for ambient vibrations on a shallow structure and consequences over vs inversion. *Journal of Seismology*, 12:1–19.

Wielandt, E. (2002). *International Geophysics, Seismometry Ch 18*. International Handbook of Earthquake and Engineering Seismology.

Wielandt, E. and Streckeisen, G. (1982). The leaf-spring seismometer: Design and performance. *Bulletin of the Seismological Society of America*, 72:2349–2367.

Withers, M., Aster, R., Young, C., Beiriger, J., Harris, M., Moore, S., and J., T. (1998). A comparison of select trigger algorithms for automated global seismic phase and event detection. *Bulletin of the Seismological Society of America*, 88:95–106.

Wong, K. T. and Zoltowski, M. D. (2000). Self-initiating music direction finding & polarization estimation in spatio-polarizational beamspace. *IEEE Transactions on Antennas and Propagation*, 48:671–681.

Yakoo, A., Tameguri, T., and Iguchi, M. (2009). Swelling of a lava plug associated with a vulcanian eruption at sakurajima volcano, japan, as revealed by infrasound record: case study of the eruption on january 2, 2007. *Bulletin of Volcanology*, 71:619–630.

Zobin, V., Reyes, G., Guevara, E., and Breton, M. (2009). Scaling relationship for vulcanian explosions derived from broadband seismic signals. *Journal of Geophysical Research*, 114:B03203, 14pp.

Appendix A

Matlab code to instrument correction

```
function datacor = ucd_transfer(data,zeros,poles,constant,fs,filtering)
%  Purpose: Instrument correction from zeros, poles, constant
%  data :  vector, seismic data
%  zeros:  vector with complex zeros of the instrument
%  poles:  vector with complex poles of the instrument
%  constant: constant value of the transfer function
%  fs   :  sample rate of the data
%  filtering: frequency band to perform the correction [f1 f2]
%
%  datacor : seismic data corrected

data       = reshape(data,1,numel(data));
poles      = reshape(poles,1,numel(poles));
zeros      = reshape(zeros,1,numel(zeros));
npts       = numel(data);
lendat     = 2^nextpow2(npts);

if lendat < 16384
    lendat = 16384;
end

wfreqs     = 2*pi*(0:lendat/2)*fs/(lendat/2);
fresp      = freqs( constant * poly(zeros), poly(poles), wfreqs);
ifresp     = 1./fresp;
ifresp(1)  = 0.0;
zdat11     = ( detrend(data.')).*tukeywin(npts,.2);
ifrespf = ([ real(ifresp(end:-1:2)) real(ifresp(1:end-1)) ] ...
             + 1i*[ -imag(ifresp(end:-1:2)) imag(ifresp(1:end-1))]);
zdat12 = real(ifft(ifftshift(fftshift(fft(zdat11.',lendat)).*(ifrespf))));
zdat13= sgolayfilt(zdat12,9,17); % smoothing filter
zdat13 = zdat13(1:npts);
zdat14= ( detrend(zdat13.')).*tukeywin(length(zdat13),.2);
```

```
33
34 % forward backward filter
35 [b,a] = butter(4,filtering/(fs*.5),'bandpass');
36 zdat14     = filter(b,a,zdat14);
37 zdat14     = filter(b,a,fliplr(zdat14));
38 datacor    = fliplr(zdat14);
```

Glossary

Epicenter or Epicentre is the point on the earth's surface vertically above the hypocenter (or focus), point in the crust where a seismic rupture begins., 164

Hypocenter or Hypocentre refers to the site of an earthquake or a ground explosion. Also commonly termed the focus. The epicenter is the point directly above it at the surface of the Earth., 164

Orogenic belts They are long, commonly arcuate tracts of highly deformed rock that develop during the creation of mountain ranges on the continents. The process of building an orogen, or orogenesis, occurs at convergent plate margins and involves intra-plate shortening, crustal thickening, and topographic uplift, 61

Pyroclasts Fragmentary material ejected during a volcanic eruption, including pumice, ash, and rock fragment. A fragment of magma, all solid fragments ejected from volcanoes, 64

Supersaturation It is defined as the difference between actual pressure and the pressure at which the concentration of dissolved volatiles would be in equilibrium with the co-existing vapor phase. The oversaturated required for nucleation corresponds to the energy that must be supplied to increase the surface area between two fluids., 43

Vesiculated In geology, vesiculated pertains to the formation of tiny gas bubbles in magma., 43

Vesiculation Nucleation and growth of gas bubbles in a magma. As dissolved gases are released from the magma, bubbles will begin to form. Bubbles frozen in a porous or frothy volcanic rock are called vesicles, and the process of bubble formation is called vesiculation or gas exsolution. The dissolved gases can escape only when the vapor pressure of the magma is greater than the confining pressure of the surrounding rocks. The vapor pressure is largely dependent on the amount of dissolved gases and the temperature of the magma., 44

Yagi antenna The Yagi antenna is a balanced traveling-wave structure, which has high directivity, gain, and front-to-back ratio. It is considered to be balanced because the voltage down the center of the antenna is constantly zero. The Yagi consists of three sections: the reflector, the driven element, and the directors., 86

Summary

In this thesis, we study the seismo-volcanic source localization using data recorded by new sensor arrays composed of three-component (3C) seismometers deployed on Ubinas stratovolcano (Peru). We develop a new framework (MUSIC-3C) of source localization method based on the well-known MUSIC algorithm. To investigate the performance of the MUSIC-3C method, we use synthetic datasets designed from eight broadband isotropic seismic sources located beneath the crater floor at different depths. The fundamental scheme of the MUSIC-3C method exploits the fact of the cross-spectral matrix of 3C array data, corresponding to the first seismic signal arrivals, provides of useful vector components (slowness, back-azimuth and incidence angle) from the seismic source. Application of the MUSIC-3C method on synthetic datasets shows the recovery of source positions. Real data used in this study was collected during seismic measurements with two seismic antennas deployed at Ubinas volcano in 2009, whose experiment conduced by volcanic teams of IRD-France (l'Institute de Recherche pour le Développment), Geophysics group University College Dublin Ireland and Geophysical Institute of Peru (IGP). We apply the MUSIC-3C algorithm to investigate wave fields associated with the magmatic activity of Ubinas volcano. These analysis evidence a complex mechanism of vulcanian eruptions in which their seismic sources are found at two separated sources located at depths of 300 m and 1100 m beneath the crater floor. This implies the reproduction of similar mechanisms into the conduit. Based on the eruptive mechanisms proposed for other volcanoes of the same type, we interpret the position of this sources as the limits of the conduit portion that was involved in the fragmentation process.

Keywords: ***3C seismic array processing, source localization, volcano monitoring.***

Résumé

Dans cette thèse, nous étudions le problème de la localisation de sources sismo-volcanique, à partir des données enregistrées par des réseaux de capteurs composés de nouveaux sismomètres à trois composantes (3C). Nous nous concentrerons sur le volcan Ubinas, l'un des plus actifs au Pérou. Nous développons une nouvelle approche (MUSIC-3C) basée sur la méthode MUSIC permettant de retourner les 3 paramètres utiles (lenteur, azimut et incidence). Pour valider notre méthodologie, nous analysons des sources synthétiques propagées en tenant compte de la topographie du volcan Ubinas. Dans cette expérience, les données synthétiques ont été générées pour plusieurs sources situées à différentes profondeurs sous le cratère Ubinas. Nous utilisons l'algorithme MUSIC-3C pour les relocaliser. Nous traitons également des données réelles provenant d'une expérience de terrain menée sur le volcan Ubinas (Pérou) en 2009 par les équipes de recherche de l'IRD-France (Institut de Recherche pour le Développment), UCD l'Irlande (projet VOLUME) et l'Institut de Géophysique du Pérou (IGP). Nous utilisons l'algorithme MUSIC-3C pour localiser les événements explosifs (type vulcanien), ce qui nous permet d'identifier et d'analyser les processus physiques de ces événements. Á la suite de cette analyse, nous avons trouvé deux sources pour chaque explosion situées à 300 m et 1100 m en dessous du fond du cratère actif. Basé sur les mécanismes éruptifs proposés pour d'autres volcans du même type, nous interprétons la position de ces sources ainsi que les limites du conduit éruptif impliqué dans le processus de fragmentation.

Mots-clés: ***Antenne sismique 3C, localisation des sources, surveillance des volcans.***